Mathematical Models in Water Filtration

James George Herterich

St Anne's College

University of Oxford

A thesis submitted for the degree of

Doctor of Philosophy
Mathematics

Trinity 2015

Abstract

Membrane filtration is a simple concept for water purification: water containing particulate contaminants is forced through a semi-permeable membrane that rejects the particulates leaving clean water to flow out. Nevertheless, there are many complex features of membrane filtration, the most important of which is the accumulation of the particulates at the membrane surface. This leads ultimately to fouling of the membrane and a reduction in the efficiency of the process. Concentration polarization is the precursor of fouling, that is, a high concentration of contaminants develops in front of the membrane without the contaminants attaching to each other or the membrane surface. However, several types of acute membrane fouling develop from the layer formed in concentration polarization, including internal fouling, pore blocking and caking. Addressing these and related problems has been at the forefront of membrane research since the process' inception.

In this thesis we develop mathematical models of aspects of crossflow and directflow filtration operating at constant flux. We begin by addressing questions related to the initial stages of concentration polarization in crossflow systems. In particular, we study the influence of particulates on the viscosity of the filtrate, and show how the filtration efficiency may be improved by tailoring the wall permeability to reduce the effects of osmosis. We then address the development of membrane fouling and caking in directflow systems: the transmembrane pressure difference, the possibility of elastic deformations during filtration, and the influence of these on the development of fouling and caking are all considered. We show that even small elastic effects can worsen fouling and suggest how the process can be operated to avoid this. We then discuss further opportunities for mathematical modelling in this area.

Acknowledgements

I would like to thank my supervisors Ian, Dominic, Robert and Nick for all their help during my studies, with special thanks to Ian and Dominic. I would also like to thank Danna for her continuous support, as well as everyone else from our cohort at Somerville College and beyond for making these years so enjoyable. I would like to thank all the members of OCCAM and OCIAM for making our work environment so special. Finally, I'd like to thank my family for getting me here!

This thesis is based on work supported by Award No. KUK-C1-013-04, made by King Abdullah University of Science and Technology (KAUST), and the Bracken Legacy, made available by the Department of Engineering Sciences, Oxford.

Contents

Chapter 1

Introduction

1.1 Motivation

The United Nations (UN) recognizes the human right to water, and that access to clean drinking water is essential to the realisation of all other human rights (United Nations General Assembly, 2010) and activities (Gleick, 1996). And yet, the World Health Organization (WHO) estimates that more than one billion people lack access to an improved water supply (World Health Organization, 2009), a figure supported by other studies (Gadgil, 1998; Gleick, 1998; Mintz et al., 2001; Shannon et al., 2008). Furthermore, millions of people die every year from water-related diseases, while many more drink water that is grossly contaminated (Gleick, 1998; Mintz et al., 2001; Shannon et al., 2008). For example, 88% of diarrhoeal deaths each year are caused by unsafe water, sanitation or hygiene, with 99% occurring in developing countries, 84% of which are children (World Health Organization, 2009). Addressing this problem is a target of the UN's Millennium Development Project (United Nations, 2015).

Water makes up over 70% of the Earth's surface. However, only 2.5% of this water is freshwater, and two thirds of that freshwater is locked up in glaciers and the ice caps (Figure 1.1). The remaining freshwater is found as groundwater and in lakes, rivers, in the soil and atmosphere, *etc.* Water treatment involves the cleaning and re-use of freshwater and wastewater, as well as making the vast quantities of sea water and brackish groundwater available to us as potable water after desalination. The WHO publishes guidelines for drinking-water quality, but in practice these guidelines vary throughout the world (World Health Organization, 2004).

Varying values of the recommended minimum daily water requirement per person

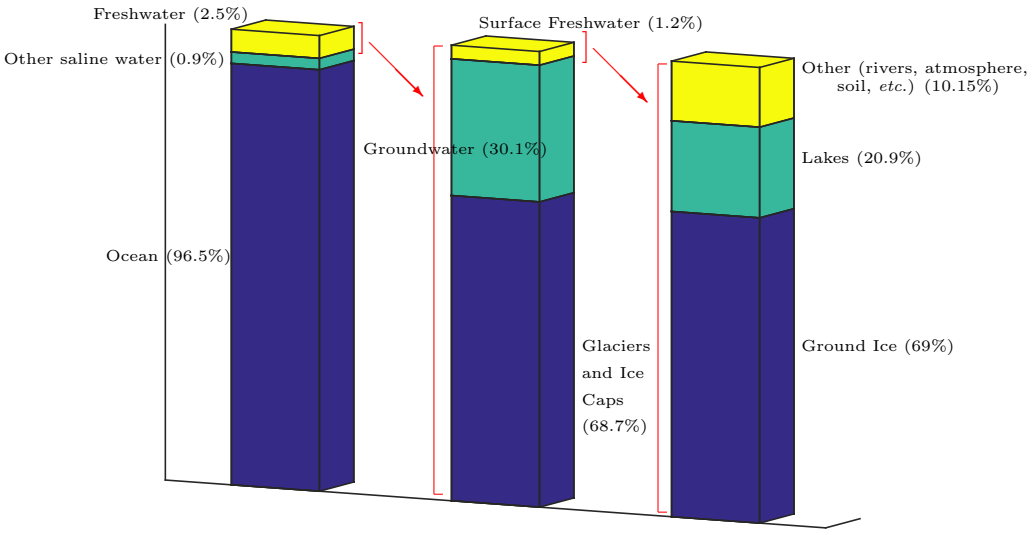

Figure 1.1: Water distribution on Earth. Only a small fraction is accessible as potable water in its current form. Graphic from data made available by the United States Geological Survey (2015).

have been proposed by a range of studies. The WHO and UNICEF define "reasonable access" as the availability within one kilometre of at least 20 litres per person per day (l/p/d) (World Health Organization, 2004). Others, including the UN, recommend a guaranteed access to 50 l/p/d to ensure basic needs and alleviate suffering (Gleick, 1996; Institute Water for Africa, 2015). However, the UN's Human Development Report in 2006 highlights the huge global inequality between rich and poor nations (Figure 1.2). Most European countries use 200–300 l/p/d, while the USA uses 575 l/p/d with some cities using in excess of 1000 l/p/d, in contrast to an average use in Mozambique of 10 l/p/d (Watkins, 2006).

The total global water production capacity by desalination in 2013 was 66.4 billion litres of water per day, and was expected to increase to 100 billion litres per day by 2015 (Ghaffour et al., 2013). Of this, approximately two thirds is produced by membrane processes while one third is produced by thermal and other processes. This equates to approximately 9.4 l/p/d globally, although many countries do not use any desalination processes, while others, such as Qatar and Kuwait, rely solely on it for domestic and industrial supplies (Ghaffour et al., 2013). The cost of desalination (capital and operating costs combined with subsidies and local incentives) has con-

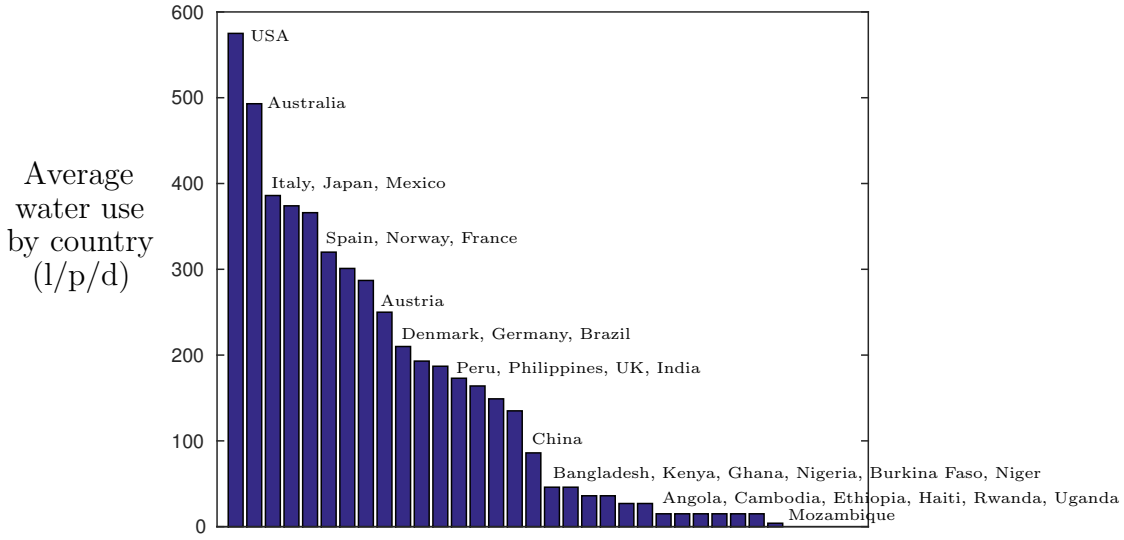

Figure 1.2: Average water use (litres per person per day) for various countries. Graphic from data made available by Data 360 (2015) and the UN's Human Development Report in 2006 (Watkins, 2006).

sistently fallen; however it is observed to scale linearly, in general, with the price of oil, typically ranging between \$ 0.5–4 per 1000 litres (Ghaffour et al., 2013; Mezher et al., 2011). The price range reflects the age of the technology; old filtration plants do not have pressure recovery devices that may reduce costs (Field, 2015).

Water treatment is improving our daily lives and, with growing concerns over pollution and water stress caused by climate change, will surely become even more important in the coming decades (Arnell, 1999; Gleick et al., 2014). By 2025, estimates suggest that 5 billion people will live in countries that experience water stress (Arnell, 1999) (see Figure 1.3). As such, an important area of increasing interest in science and engineering is the purification of contaminated water to produce clean, potable water. Combining better scientific and technological solutions with more effective resource management, improved efficiency, and conservation is required to increase the capacity and reduce the cost of providing safe and reliable water (Shannon et al., 2008).

1.2 Water Purification

Water purification concerns the removal of harmful suspended or dissolved solids (*e.g.*, heavy metals, salts), biological contaminants (viruses, bacteria), gases, and

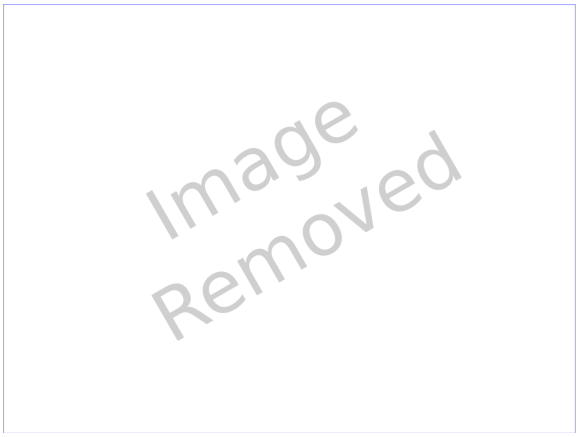

Figure 1.3: Predicted global water stress levels for the year 2025, compared with 1995.

other chemicals from water. There are many processes for water purification, some of which we will explain below. In this thesis, we shall focus on membrane filtration water treatment, with a detailed discussion of filtration in general in §1.3.

In distillation, contaminated water is boiled and its vapour condensed (Van der Bruggen and Vandecasteele, 2002). The water vapour is essentially pure and is cooled in a condenser, while the contaminants are concentrated in the unboiled liquid phase. The boiling (a water treatment process in its own right) kills bacteria, but other contaminating materials must be separated by the condensing process. However, this simple process has many drawbacks. For example, a large amount of energy is required to boil the water, while volatile contaminants with boiling points lower than water (*e.g.*, some pesticides) may not be removed (Free Drinking Water, 2015).

Sedimentation uses gravity to remove solids from water via settling of particles that are more dense than water. The (reduced) weight of the particles and fluid drag are important influences on the system. The efficiency of the process depends on the relative density of the particles and water (Yao et al., 1971). Hence this process is good for heavy solids, but may be time consuming or inefficient for particles that are close to neutrally buoyant. Sedimentation is often used as a pretreatment, where it can increase the efficiency of the full process, but has a significant capital cost (Howe and Clark, 2002).

The effective gravitational force for sedimentation may be increased by centrifugation in which the contaminated mixture is placed in a centrifuge and spun at high rates. The centripetal force causes the contaminants to move radially outwards, analogous to sedimentation but with enhanced 'gravity'. The process is efficient for

smaller particles and solids, but the energetic cost of rotation and maintenance is very high (Fakhrul-Razi et al., 2009).

An enhancement to sedimentation is brought about by coagulation and flocculation in which a chemical process is used to form a 'floc' or flake from smaller colloidal particles. A clarifying agent (an inorganic coagulant such as aluminium or iron salts) is introduced to the suspension, which adsorbs to the oppositely charged particles and reduces both the range and magnitude of the electric double-layer repulsive forces between the surfaces of each particle; the particles then adhere to form 'pin flocs' (coagulation) and grow in size through the shear forces caused by slow mixing to form larger flocs (Matilainen et al., 2010). These larger particles can sediment more quickly or can be removed more easily by other techniques, *i.e.*, membrane filtration (Leiknes, 2009). In doing so, some of the complicating factors in membrane filtration, such as particle aggregation at the membrane surface (to be discussed later), are reduced as the flocculation process removes the number of submicron particles near the membrane surface (Leiknes, 2009).

Ion exchange is the removal of (mainly higher valence) dissolved salts and minerals, such as calcium and magnesium, and is used, for example, for water softening. Contaminant cations and anionic complexes may be removed from water by ion exchange with resins or adsorption onto hydrous metal oxides (Clifford, 1999). This is typically a low energy process but requires pre- and post-treatment (*e.g.*, sedimentation, filtration) to achieve high efficiencies (Fakhrul-Razi et al., 2009).

The conventional activated sludge (CAS) process is a well-established biological process for wastewater treatment. Suspended flocs of microorganisms degrade wastewater aerobically, converting organic contaminants into carbon dioxide and water, and ammonia into nitrogen (Mayhew and Stephenson, 1997). CAS is a cheap and clean process (Fakhrul-Razi et al., 2009) where much of the biomass (the sludge) produced can be recycled (Mayhew and Stephenson, 1997). However, there is a large oxygen requirement for the process that necessitates the use of an electrical pump/blower to provide enough air (Fakhrul-Razi et al., 2009). An alternative to CAS is a membrane bioreactor (MBR) that combines biological oxidation with membrane separation (Pearce, 2011). This latter process has the advantage of intensifying the volume efficiency of the process and directly separating suspended matter from the treated water, though it involves a higher capital expense per unit throughput.

While we have reviewed some physical, chemical and biological processes involved in water treatment, this summary is by no means exhaustive. Other processes include adsorption, freeze-thaw evaporation, UV disinfection, sand filters, electrodeionization and many more, which are often used in combination with those mentioned above.

1.3 Membrane Filtration

Particles may be separated from a fluid by flowing the solution through a membrane that is permeable to the fluid phase but impermeable to particles and other contaminants; such membranes are said to be semi-permeable. This is a *filtration* process and is used to generate a large fraction of the world's treated water (Ghaffour et al., 2013). The contaminated fluid input is called the *feed*. The (clean) fluid output is called the *permeate* and the retained materials are called the *retentate*. Membrane separation is typically pressure-driven (Van der Bruggen et al., 2003). This means that a pressure difference, known as the *transmembrane pressure difference* (TMP), between the feed and permeate sides acts as a driving force for the water to pass through the membrane.

Membrane separation technology has become the preferred industrial method for purifying fluids such as water. Other processes, as discussed in §1.2, do not offer the same advantages all at once, which include highly selective separation, ambient operating temperatures, and continuous and economical operation (Bowen and Jenner, 1995a). Membrane separation processes can also separate a wide range of materials, such as dispersions of colloids and fine particles, biological materials and low molecular weight, non-volatile organics or pharmaceuticals, and dissolved salts (Bowen and Jenner, 1995a).

A common type of filtration device is the pressure driven capillary or hollow-fibre device (Figure 1.4). Here, filtration occurs in channel or tube units with membrane walls that are a single module in an array that make up the filtration device. Another configuration is a spiral-wound device where membrane sheets, separated by spacers, are wound around a central collector tube that the water permeates towards. Capillary or hollow-fibre devices have several advantages over spiral-wound devices: hydrodynamic efficiency, easier to clean without potential delamination, higher integrity (Pearce, 2011). In this thesis, we consider only capillary or hollow-fibre devices.

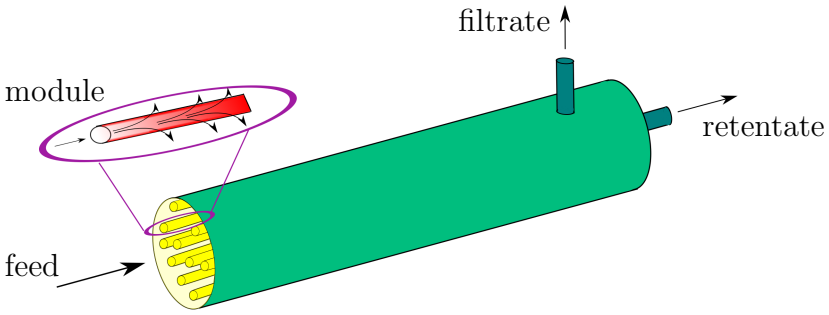

Figure 1.4: A pressure-driven capillary or hollow-fibre filtration device. The contaminated water (feed), enters into an array of tubes (modules) with porous walls (see the inset), and the the clean water (filtrate) exits at the end of the device with a separate exit for the retentate.

The process as described, where the contaminated water entering the module is drawn out by a pressure drop across the membrane, is known as *inside feed*. However, this process can also operate as *outside feed* where the feed and membrane active (separating) layer are on the outside of the hollow fibre and the permeate collects inside the hollow fibre. Each process has its advantages over the other. The inside feed provides greater protection to the membrane from damage, the hydrodynamics are easier to control, and the process can operate at higher velocities. The outside feed has a larger membrane area and can be cleaned by air scouring (Pearce, 2011). In this thesis, we consider only inside-feed processes.

Hollow-fibre inside-feed membranes may operate in a number of different configurations. Two of the most common setups are *dead-end* and *crossflow* filtration. In a dead-end configuration, the feed solution flows in an impermeable pipe, and the membrane is placed perpendicular to the flow, as in Figure 1.5(a). In a crossflow configuration, the feed solution flows in a pipe with membrane walls so that the filtration occurs tangential to the flow (driven by a pressure difference across the membrane), as in Figure 1.5(b). However, combinations or refinements of these two possibilities are also common (Pearce, 2011). Furthermore, the separating characteristics of the membrane can be tuned via poresize and other characteristics to retain almost everything except the water itself, or be more porous and retain macromolecules but not salts.

In both dead-end and crossflow configurations, the concentration of particles at the membrane surface (advected there by the flow) increases over time, leading to *fouling*. Forms of fouling include colloidal (pore blocking by particles), caking (layers of particles built up on the surface of the membrane), biological (biofilms), and others.

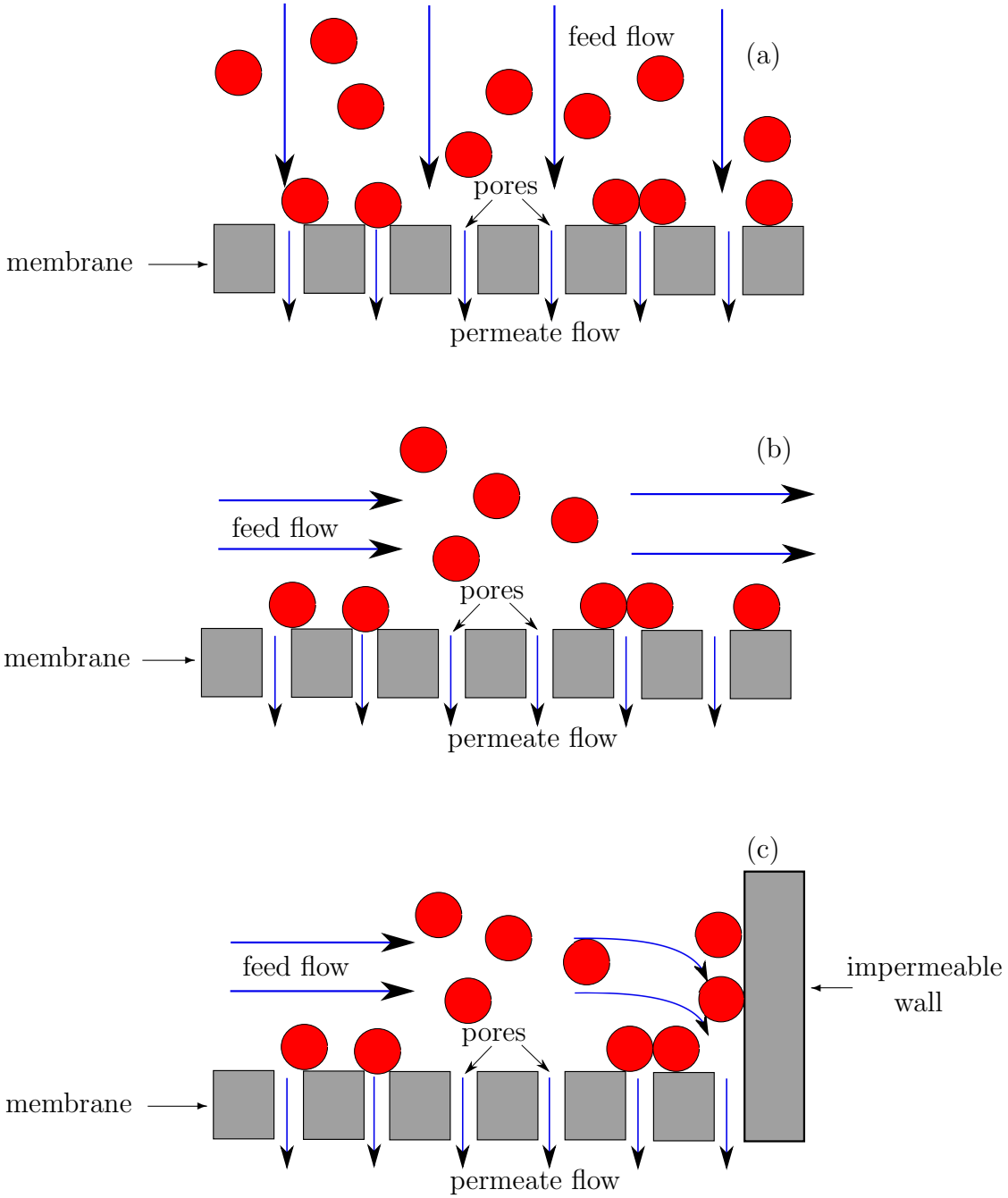

Figure 1.5: Schematics of (a) dead-end filtration, (b) crossflow filtration and (c) directflow filtration. The feed flow is perpendicular to the membrane in dead-end filtration and tangential to the membrane in crossflow filtration. Directflow filtration is crossflow with an impermeable capped end. In all cases, the water may pass through the pores but the contaminants are rejected.

Fouling can be classified as either *reversible*, where the fouling occurs on the membrane surface and can be removed (*i.e.*, caking), or *irreversible*, *e.g.*, where the fouling occurs within the membrane (by internal pore blocking), which generally cannot be removed except by the use of aggressive chemical agents (Guo et al., 2012). Fouling adds resistance to the flow so that either the flux is reduced when operating at constant pressure, or a larger pressure is required to maintain a constant flux (Davis, 1992; Guo et al., 2012).

In dead-end filtration, all of the contaminants are caught by the membrane and so a cake layer quickly develops. For crossflow systems, caking is also a problem. However, the large particle concentrations observed in dead-end filtration are mitigated by a tangential shear of the fluid that keeps the particle suspension flowing down the tube and inhibits the buildup of a thick cake (Davis, 1992).

Filtration velocities are usually smaller for crossflow than dead-end. This is because crossflow systems often require the ratio of the wall permeation velocity to the mean axial velocity to be small (Bowen and Jenner, 1995a). Although the filtration velocity may be smaller in crossflow than dead-end, this can be compensated by a large membrane area if the module is long and thin. In batch mode, fluid that is not filtered by the membrane is re-circulated and passes along the membrane again. In a continuous system there are multiple stages and the retentate from one stage is the feed to the next.

A refinement of crossflow that ensures all of the water is filtered in a single pass, while maintaining the useful shear, is *directflow* filtration. Directflow is similar to crossflow but with the end of the device capped, as in Figure 1.5(c). This can have a significant saving on energy for low-value products such as potable water. However, the concentration of particles increases dramatically further down the filter due to the capped end. In this thesis we consider only crossflow and directflow filtration processes.

1.3.1 Membranes

A membrane typically consists of a thin active layer on top of a thicker support layer. The active separating layer consists of pores large enough to allow the water molecules to pass through, but small enough to reject the contaminants (Figure 1.6(a)). The size of the pores therefore depends on the application and the material to be separated. The active layer is thin, approximately 0.1–10μm thick, to reduce resistance to

the flow. This active layer is usually supported by a thicker porous/web-structured substrate (10–200 μm thick) providing the membrane strength but negligible additional hydraulic resistance (Figure 1.6(b)) (Pearce, 2011; Probstein, 1989; Van der Bruggen et al., 2003).

The membranes themselves are traditionally made of organic polymers, but can also be made from inorganic ceramic materials. They must have relatively high permeability, high selectivity and mechanical stability (Van der Bruggen et al., 2003). The membrane structure (*e.g.* poresize, porosity) is determined by altering the casting solution or gelation conditions during manufacture (Lonsdale, 1982). The materials used have developed hugely over the past 60 years. The first generation of membranes were based on cellulose acetate, and used to filter sub-micron contaminants. However, they do not operate efficiently at temperatures above 50°C or with acids of pH less than 4 (Van der Bruggen et al., 2003; Garmash et al., 1995). The second generation of polyamide, polyacrylonitrile, and polysulfone membranes (Figures 1.6(c,d)), used to filter a wider range of contaminants, can withstand temperatures of up to 80°C and a wider pH range, and are still used today (Van der Bruggen et al., 2003; Garmash et al., 1995). The third generation is that of cost-effective ceramic membranes (Figures 1.6(e,f)), many of which use an inorganic or carbon substrate covered with an active ZrO_2 microporous layer, among other materials (Van der Bruggen et al., 2003; Pearce, 2011). This type of membrane can withstand the full pH range, temperatures up to 300°C and pressures up to 15 bar (Garmash et al., 1995).

More recent, and popular, developments in membranes include thin-film composite membranes, hollow-fibre membranes and ceramic membranes. Composite membranes consist of multi-layer membranes: a dense polymer coating on a support film. Here the rejecting layer can be 10 times thinner than cellulose acetate membranes. This gives high rejection, performing well at rejecting low molar mass organics, with high flux rates (Probstein, 1989). Hollow-fibre membranes are self-supporting membranes, and are commonly used. As such, the membrane area can be increased while maintaining a small volume (Clifton et al., 1984). Ceramic membranes have been studied and used for some time now (Garmash et al., 1995). They are made of inorganic nanomaterials such as aluminium, titanium or silicon carbide (Kim and Van der Bruggen, 2010). Due to the structure of the material, they have been used for gas separation, when temperatures are very high or when acids and corrosive fluids are involved. However, they are becoming increasingly popular in water filtration. The ceramic material can withstand higher pressures (up to 100 bar) with little deformation, the

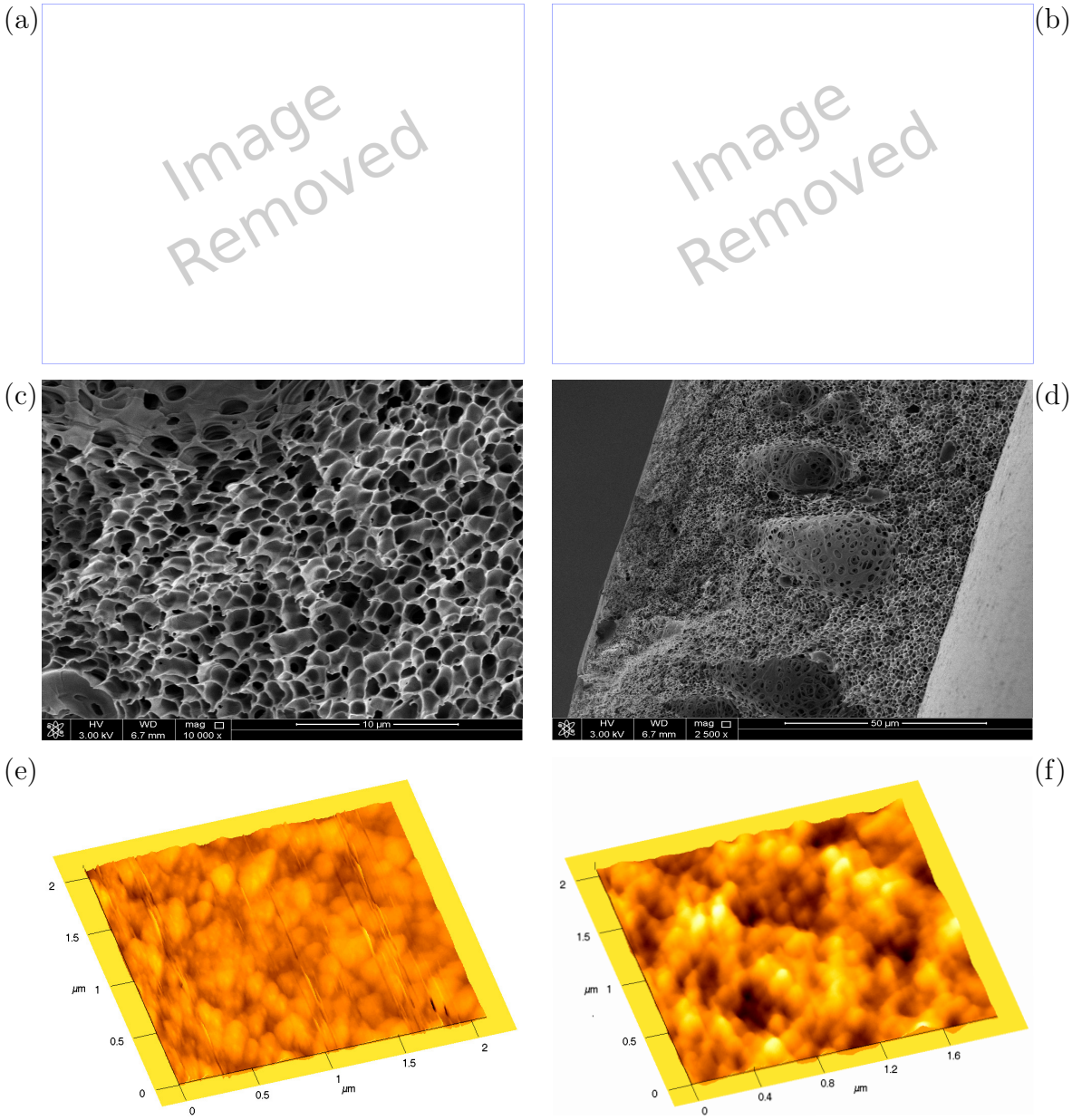

Figure 1.6: Scanning electron microscope (SEM) and atomic force microscope (AFM) images of membranes. (a) SEM image of a PES membrane surface in which the porous structure is clearly observable. (b) Typical fibre cross-section of a PES membrane: filtration occurs by the active separation layer, with support and protection layers behind it. (c) and (d) SEM images of polymeric ultrafiltration membranes. (e) and (f) AFM 3D images of 50 nm and 100 nm, respectively, ceramic nanofiltration membranes. Figures (c)–(f) courtesy of Nidal Hilal, University of Swansea (Hilal, 2015).

poresize distribution is usually more uniform, and they preserve their properties at temperatures up to 1000°C (Garmash et al., 1995).

The future development of membrane materials is currently concerned with using nano-materials. These offer flux and energy improvements, greater mechanical stability and are cost effective. Carbon nanotubes have been studied as a membrane filtration material, where graphene sheets are rolled up into cylinders of nanoscale diameter with an extremely smooth surface (Goh et al., 2013). Their crystalline and smooth structure enhances the flow (Mishra and Ramaprabhu, 2011), with molecular dynamic modelling showing that the flux can be several orders of magnitude greater than conventional pores, meaning that less energy is required and fouling is reduced (Goh et al., 2013). Furthermore, the flow may be controlled with an electric field by altering, spatially or temporally, the charge distribution on the carbon nanotube. This can be used to increase the flow of water molecules through the membrane, and inhibit ion transport to the membrane (Banerjee et al., 2007). The latter can also be enhanced by chemical functionalization of the tube ends. However, application for potable water production is not expected in the near or medium term.

An interesting filtration material that has been studied is plant xylem (Boutilier et al., 2014). This offers an inexpensive, readily available, disposable material that is effective at pathogen removal for niche point-of-use water filtration, particularly in developing countries or regions without reliable access to clean water. The xylem part of a tree branch is simply fastened to a tube, and hydrostatic pressure forces the water though it. This process utilizes the structures/matrix that trees use to transport fluid from root to leaves. The xylem vessels and tracheids (internal pathways) force the water to pass through pit membranes, that is, a porous medium with pores of around 500 nm. This is effective at removing various pathogens such as *E. coli*, but it has yet to be scaled up and pilot tested.

1.3.2 Types of filtration

There are five major types of membrane filtration: reverse osmosis, forward osmosis, nanofiltration, ultrafiltration and microfiltration. These differ by membrane material and poresize, the size and charge of the materials being filtered, and the hydraulic pressures exerted (Van der Bruggen et al., 2003).

Before discussing each filtration type, an important distinction needs to be made regarding the permeation process, *i.e.*, how the membrane controls the separation

of different species. Two such models are *solution–diffusion* and *pore-flow*. In the solution–diffusion model, the feed solution dissolves in the membrane material and passes through the membrane by diffusing down a concentration gradient. The clean water is separated from the contaminants by the ability, rate and amount of each material to dissolve into, and diffuse through, the membrane. The solution–diffusion model applies to reverse-osmosis and forward-osmosis membranes (Duan et al., 2014; Wang et al., 2010; Wijmans and Baker, 1995). The pore-flow model uses a pressure-driven flow through small pores that separates via size exclusion, and applies to nanofiltration, ultrafiltration and microfiltration membranes (Wijmans and Baker, 1995). The need for the two models was a topic of debate for many years, with the difference between them related to the permanence of the pores. For the solution–diffusion model, at the molecular scale the polymer has a dynamic free volume but there is no interconnected pore all through the membrane. However, the free volume (pores) in the pore-flow model are relatively fixed (Wijmans and Baker, 1995).

Reverse osmosis is a simple but important process used in filtration, for particles larger than 0.1 nm at pressures of 5–120 bar (Van der Bruggen et al., 2003; Hyflux Membranes, 2012). The mechanism behind reverse osmosis is as follows. Suppose we have a tube containing salty water, at the bottom of which is a membrane impermeable to salt but permeable to water, as in Figure 1.7. This is a dead-end filter, but the process applies equally to crossflow. In contact and directly below the membrane is a reservoir of freshwater. If there is no difference in hydrostatic pressure across the membrane, then the freshwater will flow into the salty water by osmosis (*i.e.*, the difference in chemical potentials, and hence osmotic pressures, on either side of the membrane generates a flow in order to achieve thermodynamic equilibrium, discussed in more depth in §2.2.2). However, if the osmotic pressure is exceeded by an opposing hydrostatic pressure across the membrane, then the flow is reversed and some of the water from the salty water solution flows into the freshwater (Williams, 1969). This process gradually removes some of the freshwater from the salty water solution, leaving behind a salt solution at higher concentration. A more in-depth discussion of reverse osmosis is given in §2.2.

Forward osmosis, as opposed to reverse osmosis, uses the osmotic pressure as the driving force for filtration. Here, the solution on the permeate side, known in this process as the *draw solution*, has a higher chemical potential than the contaminated feed solution, so that the freshwater is drawn across the membrane, *e.g.*, an NaCl feed solution with an $MgCl_2$ draw solution. As such the filtration process dilutes the draw

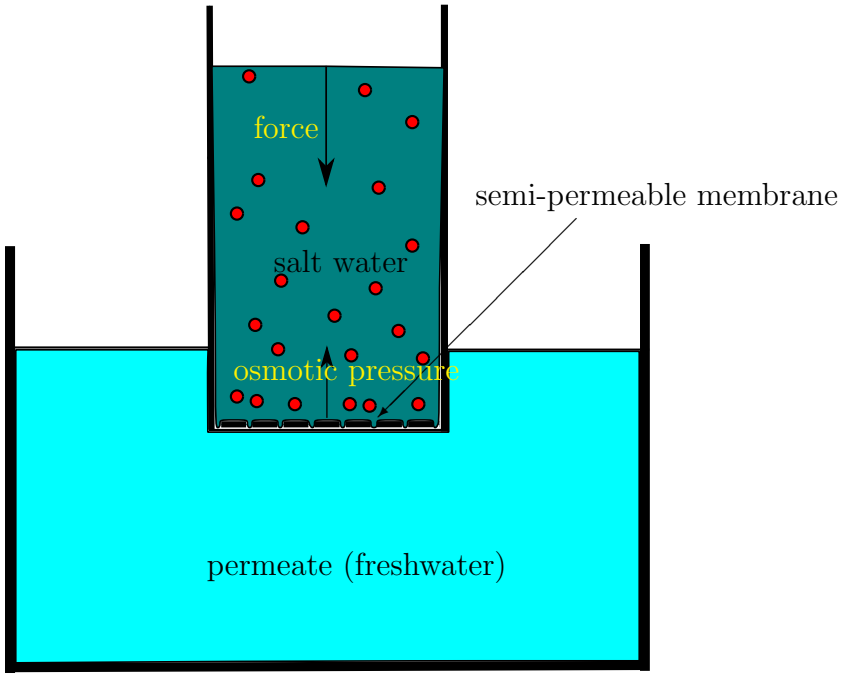

Figure 1.7: Schematic of reverse osmosis where a semi-permeable membrane filters freshwater from salt water. A force on the salt water solution overcomes the osmotic pressure to filter clean freshwater through the membrane.

solution and it must be re-concentrated: this may be achieved by reverse osmosis. While this may make forward osmosis seem somewhat redundant, the draw solution may be chosen to be energetically easier and/or safer to filter than the original feed solution. An advantage of forward osmosis is that no hydraulic pressures are required in the first stage of the process and the regeneration can, depending upon the draw used, be dependent upon low grade energy (Cath et al., 2006; Field, 2015). We do not consider forward osmosis in this thesis.

There is no fundamental difference between microfiltration, ultrafiltration and nanofiltration. They are all hydrodynamic processes that use a sieve process (structured poresizes, size exclusion and applied hydraulic pressure) to filter particles larger than those filtered by reverse osmosis. Here the smallest poresize corresponds to the contaminants to be filtered (Van der Bruggen et al., 2003). Each method is used to filter particles of different size, but also has some unique characteristics.

Nanofiltration uses crossflow filtration for particles of size 1–10 nm, a poresize range between reverse osmosis and ultrafiltration, and at pressures of 3–20 bar (Hyflux Membranes, 2012; Van der Bruggen et al., 2003). Nanofiltration membranes also have a surface charge in the presence of a feed solution. This generates an electric potential

Technique	Poresize	Pressure	Contaminants Filtered
Reverse Osmosis	0.1–1 nm	5-120 bar	metal ions, aqueous salts, pesticides/herbicides, sugars
Nanofiltration	1–10 nm	3-20 bar	pesticides/herbicides, sugars, endotoxin/pyrogen, natural organic matter
Ultrafiltration	0.01–1μm	0.1-5 bar	natural organic matter, viruses, colloidal silica, asbestos
Microfiltration	0.1–10 μm	0.1-2 bar	bacteria, yeast cells, oil emulsion

Table 1.1: Typical poresize and operating pressure ranges, and materials filtered by different filtration techniques (Hyflux Membranes, 2012; Van der Bruggen et al., 2003).

that retains ions smaller than the poresize, known as Donnan exclusion (Van der Bruggen et al., 2003).

Ultrafiltration membranes filter particles in the size range 10 nm–1 μm at pressures of 0.1–5 bar (Bowen and Jenner, 1995a; Hyflux Membranes, 2012; Van der Bruggen et al., 2003). The macrosolute concentrations in typical ultrafiltration feed solutions usually have negligible osmotic pressures, except at the membrane surface where concentrations become significantly higher (Bowen and Jenner, 1995a).

Microfiltration membranes filter particles in the size range 0.1–10 μm at pressures of 0.1–2 bar (Bowen and Jenner, 1995a; Hyflux Membranes, 2012; Van der Bruggen et al., 2003). These membranes have the largest permeability and so operate at the lowest applied pressure (Van der Bruggen et al., 2003).

Table 1.1 gives an account of each type of filtration technique, the typical poresize, operating pressure, and common particles/contaminants they are used to filter. Again, each of these membrane filtration processes is operated, usually, in one of two configurations: dead-end and crossflow (Figure 1.5).

1.3.3 Challenges in Membrane Filtration

In membrane filtration systems, the action occurs near the membrane surface: the fluid flows towards the walls, due to the imposed pressure difference across it, as well as along the channel, advecting particles towards the walls. Particles may not pass through the wall, and so collect there. This buildup of particles is moderated by diffusion towards the centre of the channel. The resulting particle concentration

profile, which is higher at the walls than in the bulk near the centre, is known as concentration polarization (CP) (Vasan and Field, 2006; Zydney, 1997). The key challenge, with regard to all types of filtration, is to moderate the buildup of particles at the membrane surface and their influence on filtration.

There are many adverse effects of CP, including a greater propensity for blockage of the membrane pores, restricting flow through the permeable walls (Song and Elimelech, 1995), and an increased osmotic pressure (Hoek et al., 2002). The latter acts to reduce the pressure difference across the membrane, thereby affecting the filtration performance (Guo et al., 2012). When concentration polarization occurs, the pressure is increased to maintain the flux. However, this only provides temporary relief: the flux brings more solute to the membrane, increasing cake thickness (increasing resistance) and osmotic pressure, thereby reducing the flux (Bowen and Jenner, 1995a). The transition from CP to cake formation has been analysed, with consolidation of the particles occurring when sufficient fluxes slow down particle redispersion to form a stagnant layer (Chen et al., 1997).

A concentration-polarization layer begins to form almost immediately after the beginning of filtration (Aimar et al., 1991). However, it is generally reversible: stopping the flow allows the particles to diffuse away from the membrane (Aimar et al., 1991). Nevertheless, it is important that this is done before the concentration becomes high enough for the particles to stick together and deposit on the membrane surface, forming a cake that requires additional measures to remove it. Furthermore, the cake adds a resistance to the flow via a frictional drag to the fluid that is be filtered by the membrane (Bacchin et al., 2002).

During cake formation the membrane pores are often fouled via pore blocking. Whereas the cake layer adds to the resistance of the membrane, pore blocking changes the flow properties through the membrane itself. The signature decline in flux over time varies depending on the different ways in which blocking occurs (Hermia, 1982). These include complete blocking, intermediate blocking and internal blocking, as shown in Figure 1.8. Complete blocking occurs when particles that are larger than the poresize reach the membrane and seal a pore completely, stopping all flow through the pore (Figure 1.8(a)). Intermediate blocking occurs when a particle can seal a pore completely, partially or land on an inactive part of the membrane (Figure 1.8(b)). Internal blocking occurs when particles smaller than the poresize enter the membrane and adsorb to the membrane walls, restricting flow, and may eventually stop the flow through the pore altogether (Figure 1.8(c)). Models of the effective flux in

each of these types of blocking have been developed and the coupling between them examined (Cheng et al., 2011; Field et al., 1995; Field and Wu, 2011; Griffiths et al., 2014; Ho and Zydney, 2000), with each type possessing a unique signature response (developing over time) for influx against permeate flux.

The *critical flux* hypothesis for microfiltration states that there exists a start-up flux below which flux decline does not occur (Field et al., 1995). In other words, fouling does not occur below this flux, but does occur above it. The critical flux depends on many effects, especially hydrodynamics. Since the rate of fouling increases with the transmembrane pressure difference, operating at a lower pressure difference is required (Field et al., 1995). The tangential velocity has also been shown to be important, with a critical ratio of permeate flux to mass transfer (a critical Péclet number) existing (Bacchin, 2004). Furthermore, in models with caking and intermediate blocking, the critical flux is related to the (square root of the) shear stress (Field and Wu, 2011).

A number of procedures are implemented to stop or mitigate against the onset of irreversible fouling. In the water industry, the feed-filtration process usually runs for a period of 20 minutes. During this time, a cake layer forms at the surface of the membranes. The feed-flow is then switched off and a pump on the permeate side of the membrane runs for a short period, about 30 seconds, at a high pressure in the opposite direction, known as a *backflush* (Figure 1.9) (Remize et al., 2010). Backflushing breaks up the cake layer, mixing it back into the bulk suspension. This procedure is repeated periodically: the process alternates between feed-filtration and short backflushes (backflushing must be short since the relatively clean permeate water is consumed and becomes re-contaminated). However, backflushing does not always completely remove the cake or particles that block the membrane. In particular its effectiveness decreases with time so that a more robust chemical clean must be performed on the membrane every few days (Le-Clech et al., 2006; Remize et al., 2010). Over months, possibly years, the membrane becomes unusable and must be replaced.

When operating at constant flux, the driving pressure (pump pressure) increases due to fouling of the membrane, cake growth and concentration polarization. Although the backflush removes the cake and CP layers, reducing the operating pressure, the gradual increase in membrane fouling means that the overall pressure trend is increasing (Ye et al., 2011).

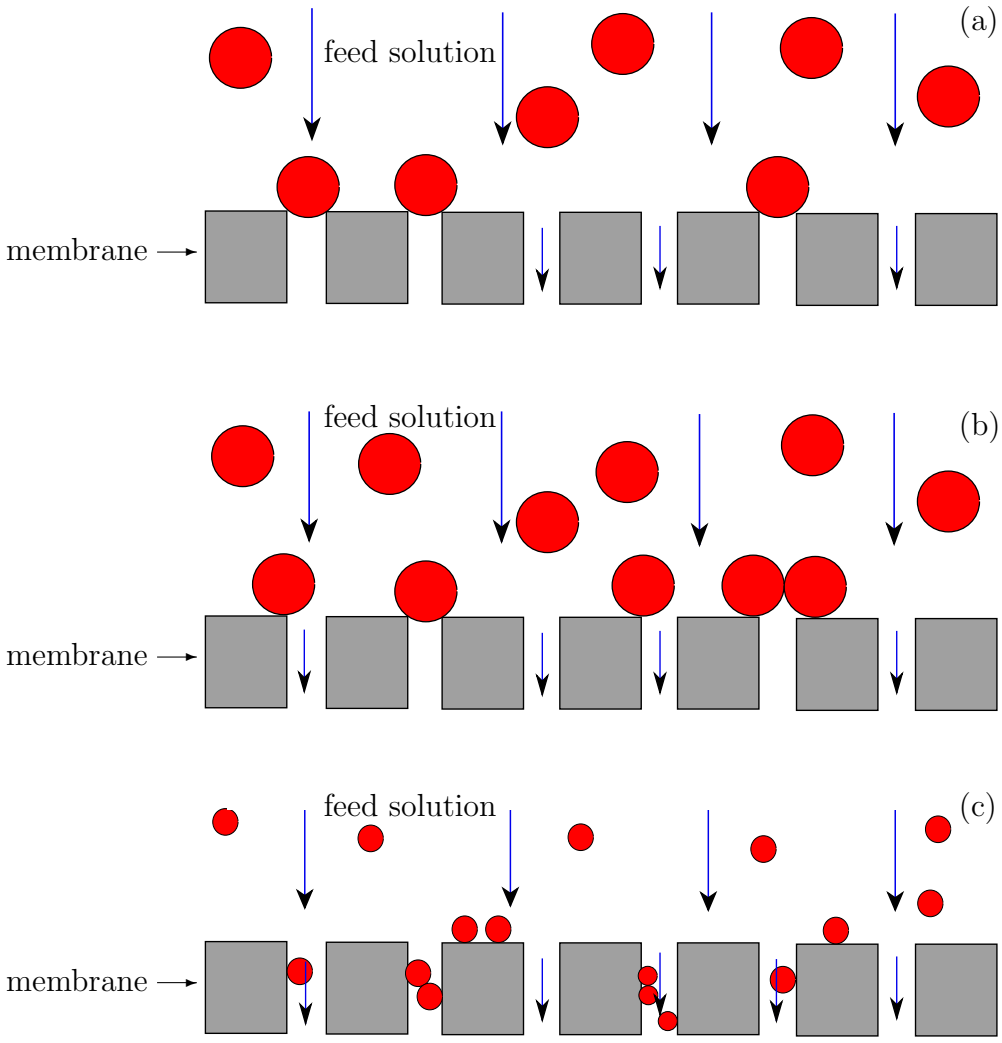

Figure 1.8: Pore blocking via three mechanisms: (a) complete blocking where the particles are larger than the poresize and seal a pore completely, (b) intermediate blocking where a particle can seal a pore completely, partially or land on an inactive part of the membrane, and (c) internal blocking where particles smaller than the poresize enter the membrane and adsorb to the membrane walls, constricting flow.

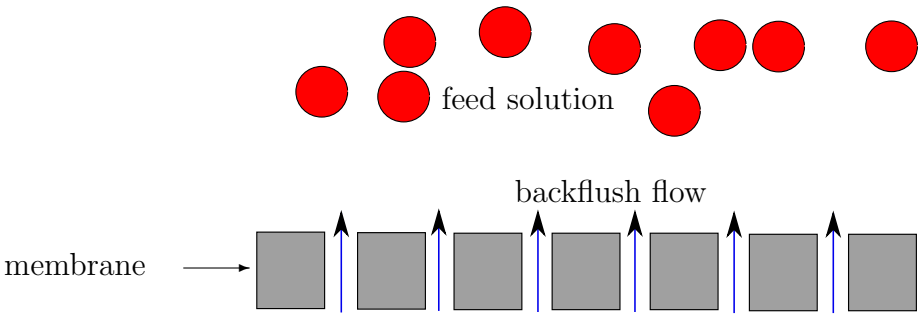

Figure 1.9: The rejected contaminants on the membrane surface may be removed, and resuspended in the solution, via a backflush. Here, the direction of flow is reversed from the permeate side to break up and remove the contaminants from the membrane surface.

During the entire filtration process, the membranes are subject to varying amounts of stress. This can have a detrimental effect on the structure of the membrane, including increases in the typical poresize (She et al., 2012). This may result in increased fouling of the membrane, and potentially failure of the membrane to filter contaminants if, for example, the material yield stress is exceeded.

1.4 Thesis Outline

The aim of this thesis is to develop and analyse mathematical models of various aspects of water filtration. We study crossflow membrane filtration systems, in a 2D channel and a 3D tube. Our goals are first to understand the mechanics underlying the processes involved and then to suggest improvements that might increase filtration efficiency.

The thesis is broadly split into two themes: conventional crossflow filtration (Chapters 2–4) and directflow filtration (Chapters 5–7). Furthermore, we consider different aspects of fouling during filtration. In Chapters 2–4, we are concerned with the precursor of fouling, specifically concentration polarization; how CP affects the flow parameters and filtration efficiency. In Chapters 5–7, we consider caking and (irreversible) internal fouling of the membrane; how these mechanisms evolve over time and, again, affect the flow and filtration efficiency. For the reader's ease we will refer to reversible fouling by its specific forms, *i.e.*, concentration polarization and caking, and refer to irreversible fouling, *i.e.*, internal pore blocking of the membrane, as

membrane fouling or, simply, fouling. Furthermore, we consider only insoluble solids (particulates) as the contaminants.

In Chapter 2, we discuss the tools required to model crossflow systems. This includes the governing equations for fluid flow and particle transport, incorporating osmotic pressure. We also discuss the appropriate constitutive relations (*e.g.*, concentration-dependent viscosity and diffusivity, and the Kozeny–Carman relation).

In Chapter 3, we study the effect of a concentration-dependent viscosity on the transport of a dilute suspension of particles in 2D crossflow. An asymptotic expansion gives insight into the response of the system at constant flux and the effect of the initial concentration profile. In Chapter 4, we consider the effect of osmotic pressure in 2D crossflow and show how this may be ameliorated by tailoring the membrane permeability. We determine a geometry that optimizes the filtration efficiency and energy cost of the system.

We then consider aspects of directflow filtration. Motivated by the generic pressure and fouling increases observed during membrane filtration over time, we consider caking, (irreversible) fouling, and membrane deformation. In Chapter 5, we study the flow through a directflow unit, both inside the tube, as well as on the permeate side. We show that in this scenario the transmembrane pressure difference may be approximately constant along the membrane.

In Chapter 6, we study the effects of linear-elastic membrane deformation in a cross-section of a 3D directflow tube. We study elastic deformations of the membrane and cake layers and show that these may reduce the effectiveness of the system, via pore expansion. We also show that in certain situations the energy efficiency may increase due to increases in permeability. In Chapter 7, we consider the dynamic evolution of membrane fouling and cake layer development, where periodic backflushing is performed. We determine operating strategies (*e.g.*, frequency of backflushing) that maximize the permeability of the membrane but do not permit fouling.

In Chapter 8, we summarize our findings and discuss the implications for membrane filtration and possibilities for future work.

Chapter 2

Theory of Membrane Filtration

2.1 Introduction

Contaminated water is, at its simplest, a suspension of particles and other contaminants in water, and so fluid mechanics plays a fundamental role in filtration. One of the most common forms of water filtration is crossflow membrane filtration (CFF) (Bowen and Jenner, 1995a; Davis, 1992), whose fluid-mechanical principles are relatively simple: particle-laden water enters a specially designed module (a channel) with permeable walls that allow the fluid, but not the suspended particles, to pass through to the permeate side. The fluid flows both towards the walls and along the channel, the former advecting particles towards the walls, as in Figure 2.1. The particles exhibit concentration polarization, which has many adverse effects for filtration as discussed in §1.3.3.

In this chapter, we discuss the fundamental principles of fluid mechanics and particle suspension dynamics necessary to model aspects of the membrane filtration process. We consider the macroscale modelling (fluid mechanics, particle transport, reverse osmosis, *etc*), fundamental microscale properties (osmotic pressure and constitutive relations for how properties vary with the concentration of impurities), as well as relevant membrane properties.

2.1.1 Scalings, parameters and typical values

Here, we consider parameter values at which filtration operates and determine the typical values of the governing parameters. We consider values representative of crossflow filtration of small particles such as viruses, as considered in DiLeo et al. (1992).

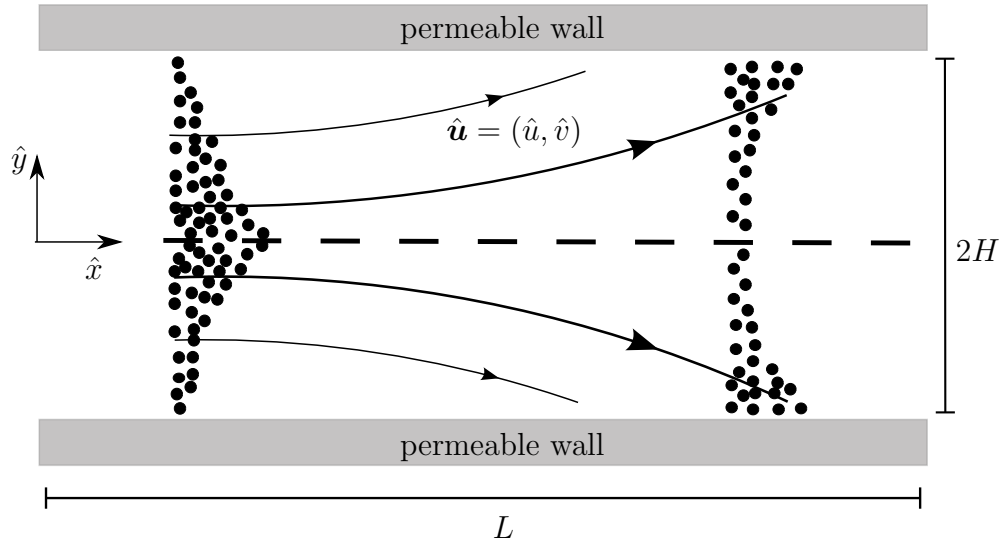

Figure 2.1: Schematic of a channel with permeable walls. The channel has length L and width $2H$. The fluid velocity field is $\hat{\boldsymbol{u}} = (\hat{u}, \hat{v})$ from left to right and is allowed to permeate out through the semi-permeable channel walls. Particles entrained in the fluid with some distribution at the inlet are advected by the flow and diffuse by Brownian motion, collecting at the channel walls (exhibiting concentration polarization), which are impermeable to the particles.

In crossflow filtration, there are many geometric and physical scales to consider. The channel has a typical length, L, and height, $2H$, as in Figure 2.1. For conventional membrane-filtration devices, these lengths are of the order, $H = 100 - 1000\,\mu$m and $L \sim 1\,$m (DiLeo et al., 1992; Pearce, 2011). The fluid has a typical velocity, $U = 0.1 - 1\,$m/s, for a flow with a typical shear rate of $1200\,\mathrm{s}^{-1}$ (DiLeo et al., 1992), in response to a pressure drop, P. The fluid flux, Q, is the amount of fluid that passes through a tube cross-section per unit time; as such Q may have units m^2/s or m^3/s depending on whether it is 2D or 3D. For a channel, $Q = HU = \mathcal{O}\left(10^{-5} - 10^{-3}\right)\mathrm{m}^2/\mathrm{s}$, and for a circular tube of radius R, $Q = \pi R^2 U = \mathcal{O}\left(10^{-9} - 10^{-6}\right)\mathrm{m}^3/\mathrm{s}$. The contaminants (particulates) have a typical concentration, Φ, and exert a typical osmotic pressure, Π.

Furthermore, there are many intrinsic parameters of the system. The fluid has a density, ρ, and viscosity, μ. The density and viscosity of water are $\rho = 1000\ \mathrm{kg}/\mathrm{m}^3$ and $\mu \sim 1\ \mathrm{m\,Pa\,s}$, respectively (Acheson, 1990). The diffusivity, D, of the particles is a macroscopic property characterising Brownian motion in the fluid (Guazzelli and Morris, 2012). For nanometric viruses, typically with a radius of the order $a = 10\,$nm, the diffusion constant is of the order $D = \mathcal{O}\left(10^{-11}\right)\ \mathrm{m}^2/\mathrm{s}$, by the Stokes–Einstein relation (Guazzelli and Morris, 2012). The permeability, k, of a porous medium is

a measurement of how much fluid flows through it at a given pump pressure: typically $k = \mathcal{O}(10^{-16})\,\mathrm{m}^2$ for a membrane (Shipley et al., 2010). Some of the parameters may depend on the others, *e.g.*, $\mu = \mu(\phi)$.

We can determine the number of dimensionless parameters in our model using the Buckingham Pi-theorem (Howison, 2005). Our model contains ten independent variables: length, L [m], width, H [m], flux, $Q = HU$ [m^2/s], hydrostatic pressure, P [Pa], osmotic pressure, Π [Pa], volume fraction, ϕ [ ], viscosity, μ [Pa s], diffusivity, D [m^2/s], density, ρ [kg], and permeability, k [m^2]; with three independent physical dimensions: length, time and mass. The Buckingham Pi-theorem tells us that we then have seven dimensionless parameters, some of which we describe below.

The volume fraction, ϕ, is a dimensionless number that measures the volume ratio of the contaminants (particulates) in the feed solution compared to the contaminants and liquid. Hence, $0 \leq \phi \leq 1$. In Chapter 3 we consider the dilute limit where $\phi \ll 1$.

An important dimensionless parameter that represents the geometry of the channel is the aspect ratio, δ, defined by

$$\delta = \frac{H}{L}. \tag{2.1}$$

For a long and thin channel, $\delta = \mathcal{O}(10^{-4} - 10^{-3}) \ll 1$. We will exploit $\delta \ll 1$ to simplify the governing equations in what follows.

The Reynolds number measures the ratio of inertial to viscous forces for a fluid flow. In a thin channel (*i.e.*, $\delta \ll 1$) the required pressure scaling results in a scaled version of the Reynolds number (with factor δ^2), known as the reduced Reynolds number (Howison, 2005),

$$\mathrm{Re} = \delta^2 \frac{\rho U L}{\mu}. \tag{2.2}$$

The reduced Reynolds number (2.2) is of the order $\mathrm{Re} = \mathcal{O}(10^{-3})$, so inertial forces may be neglected.

The Péclet number measures the ratio of advection to diffusion of a quantity to be transported. In this thesis, this is the transport of particles in a fluid. Analogously to the Reynolds number, we use a scaled version of the Péclet number (with factor δ^2) that takes into account the small aspect ratio of the channel (Howison, 2005). We call this the reduced Péclet number

$$\mathrm{Pe} = \delta^2 \frac{U L}{D}. \tag{2.3}$$

The reduced Péclet number (2.3) is of the order $\mathrm{Pe} = \mathcal{O}(10^2)$ (where D is calculated via Stokes–Einstein (Guazzelli and Morris, 2012)), which is rather large, but since $\delta\,\mathrm{Pe}$ is small, Pe is not asymptotically large for a thin-channel flow. A smaller Péclet number may be achieved by a slower flow, of order cm/s (Gabelman and Hwang, 1999). Furthermore, as discussed in §1.3.3, membrane fouling is linked to a critical Péclet number, given by $\mathrm{Pe}_{\mathrm{crit}} = J\delta_{\mathrm{bl}}/D$, where J is the permeate flux and δ_{bl} is the particle concentration-polarization boundary-layer thickness (Bacchin, 2004). In channel flow with a flux of order HU and assuming a boundary layer thickness of δH, then for a range of typical particle sizes, the critical Péclet number can range from $0.1 - 100$. Operating below the critical flux ensures that fouling does not develop. As such, we will assume an order-one Péclet number because operating under this condition allows for the richest particle dynamics in the channel.

The Darcy number measures the ratio of the permeability of a porous medium to the cross-sectional area (Batchelor et al., 2002). We use a scaled version of the Darcy number (with factor δ^{-5}) that we call the reduced Darcy number,

$$\mathrm{Da} = \frac{k}{\delta^5 L^2}. \tag{2.4}$$

The reduced Darcy number (2.4) can vary from $0.01 - 100$; we will assume an order-one quantity for simplicity. In Chapter 4 we consider the limit of a small effective permeability.

The relative importance of the osmotic pressure is determined by the ratio of the osmotic pressure to the fluid pressure, Π/P. In ultrafiltration and microfiltration, osmotic pressures are negligible. However, in nanofiltration and reverse osmosis, the osmotic and fluid pressures become comparable (Bowen and Jenner, 1995a). Since $\mathrm{Re} \ll 1$, we use a Stokes-equation scaling for the pressure drop in a channel, $P = \mu U/\delta^2 L \sim 1\,\mathrm{kPa}$, however the absolute pressure is typically $100\,\mathrm{kPa}$ (Bowen and Jenner, 1995a). The typical osmotic pressure, Π, is given by the Morse equation for a dilute suspension of particles, $\Pi = iRT/N_A V^*$ (Amiji and Sandmann, 2003; Casassa and Markovitz, 2004). Here, i is the van't Hoff factor providing a measure of the effect of the solute on various colligative properties of the solution ($i = 1$ for viruses), $R = 8.314\ \mathrm{J/mol\,K}$ is the gas constant, T the absolute temperature (taken to be room temperature $\approx 300\,\mathrm{K}$). Avogadro's number, N_A, and the volume of a single contaminant particle, $V^* = 4\pi a^3/3\,\mathrm{m}^3$, play a role via the conversion from density to volume fraction. Hence, for particles sizes in the range $a = 1 - 10\,\mathrm{nm}$ (as

in reverse osmosis and nanofiltration, see Table 1.1), the osmotic pressure is of the order $\Pi = \mathcal{O}(1 - 100\,\mathrm{kPa})$ – crucially, Π can be the same order as P.

2.2 Reverse Osmosis

As discussed in §1.3.2, reverse osmosis is a process whereby an applied hydrodynamic pressure difference, Δp, overcomes the osmotic pressure difference, $\Delta\pi$, to filter a fluid through a semi-permeable membrane. The fluid flux, J, is given by

$$J \propto \Delta p - \Delta\pi, \tag{2.5}$$

where $\Delta p - \Delta\pi$ is known as the *transmembrane pressure difference* (TMP) (Wijmans and Baker, 1995). In this section we discuss the osmotic pressure, π, and deduce the above form of the TMP for reverse-osmosis membranes via the solution–diffusion model.

2.2.1 Osmotic pressure

The *osmotic pressure* is an expression of properties of concentrated colloidal dispersions. It describes various colloidal interaction forces that affects their transport by a fluid. From the perspective of the molecular–kinetic theory of heat, suspended particles influence (even slightly) the movement of the liquid, due to the Brownian motion of the liquid molecules. As a result, if the particles are caught by a membrane filter, with the fluid moving around them, then they exert a pressure on the fluid. This pressure is the osmotic pressure (Einstein, 1956). Osmotic pressures can be large, even at dilute limits. Sea water, for example, contains only around 1.4 moles per litre of ions and yet can generate osmotic pressures of up to 25–30 atmospheres (Deboeuf et al., 2009).

The osmotic pressure, π, is defined thermodynamically to be the negative derivative of the Helmholtz free energy with respect to volume at constant pressure (Brady, 1993). As well as particle size and physio-chemical properties, including ionic strength and zeta potential, the osmotic pressure is a function of the volume fraction of particles, $\pi = \pi(\phi)$. The osmotic pressure is not affected by the solvent itself, and may be derived just from mechanical considerations via macroparticle equations of motion (Brady, 1993). It is given by a combination of entropic pressure, van der Waals

interaction and electrostatic interactions (Bacchin et al., 2002; Bowen and Williams, 2001),

$$\pi(\phi) = \pi_{ent}(\phi) + \pi_{vdW}(\phi) + \pi_{ele}(\phi) + \pi_{ext}. \tag{2.6}$$

The analytic expressions for each term in Eq. (2.6) are summarized in Bacchin et al. (2002); the entropic pressure term, π_{ent}, arises from Hall's equation for hard spheres (Hall, 1972), the van der Waals term, π_{vdW}, arises from the change in the van der Waals free energy with the number of solvent molecules (Jönsson and Jönsson, 1996), the electrostatic interactions term, π_{ele}, arises from double-layer interactions (Bowen and Jenner, 1995b), and π_{ext} is due to any extra interactions between particles (Bowen and Williams, 2001).

For small volume fractions, the entropic pressure dominates, and for larger volume fractions, the electrostatic interactions dominate. However, in each case, there is a critical volume fraction at which the van der Waals surface interactions dominate and reduce the osmotic pressure (Bacchin et al., 2002).

The dominance of the electrostatic interaction at higher volume fractions provides an explanation for the transition from a concentration polarization dispersion layer to a fouling solid state. The attraction forces cause the particles to coagulate, described as a "negative diffusion". This also applies to suspensions of larger particles, such as in microfiltration, when osmotic pressures are lower (Bacchin et al., 2002).

For dilute suspensions, $\phi \ll 1$, where the entropic pressure dominates, the osmotic pressure is approximated by

$$\pi(\phi) = a_1\phi + a_2\phi^2 + a_3\phi^3 + \cdots, \tag{2.7}$$

where $a_1 = iRT/N_A V^*$ is given by van't Hoff's law (Bowen and Jenner, 1995a; Deboeuf et al., 2009). This approximation agrees with the small-ϕ asymptotic expression of the analytic calculation of π (2.6) in Bacchin et al. (2002). Furthermore, it is the standard expression for the osmotic pressure at low concentrations found in the literature.

We will see that the osmotic pressure reduces the efficiency of the water filtration process. It is an increasing function of volume fraction (for small ϕ), and an important component in models as concentration polarization results in high concentrations at the membrane walls. Furthermore, the osmotic pressure influences other suspension transport properties such as gradient diffusivity (Bowen and Williams, 2001), as will briefly be discussed in §2.5.2.

2.2.2 Reverse osmosis

Here, we deduce the form of the TMP (2.5) for reverse-osmosis membranes which operate at the molecular scale via a solution–diffusion mechanism, as opposed to the pressure driven pore-flow model for which the form in (2.5) naturally arises as an extension to Darcy's equation.

The solution–diffusion mechanism allows for the contaminants to dissolve into the membrane and diffuse down a concentration gradient. The osmotic pressure arises from the tendency of the solvent to flow towards a higher solute concentration, *i.e.*, up the concentration gradient, in order to reach a state of concentration equilibrium (equilibrium of chemical potentials). This pressure is independent of the membrane, and depends only on the solution (Probstein, 1989).

We assume that the flux, J, of a contaminant across the membrane may be modelled by Fickian diffusion so that

$$J = -D\nabla c, \tag{2.8}$$

where c is the molar concentration of a contaminant and D is the diffusivity (Kedem and Katchalsky, 1957; Wijmans and Baker, 1995). Permeation in membranes is driven by pressure, temperature, concentrations, *etc.*, which are all related to the change in chemical potential, μ, across the membrane. The chemical potential has the form

$$\mu = \mu^0 + RT \ln(\gamma c) + n_v \left(p - p^0\right), \tag{2.9}$$

where R is the gas constant, T the absolute temperature, γ the activity coefficient, n_v is the molar volume of water, and p the pressure, with μ^0 the chemical potential of pure water at pressure p^0 (Kedem and Katchalsky, 1957; Wijmans and Baker, 1995). For a diffusion model, the pressure-driven permeation is observed to have continuity of pressure and chemical potential at the salty water–membrane interface, and continuity of chemical potential at the membrane–permeate interface. However, for solution–diffusion membranes, the pressure remains the same in the membrane but drops discontinuously at the membrane–permeate interface (Wijmans and Baker, 1995).

A pressure difference across the membrane exists so that the chemical potential (2.9) is continuous. The osmotic pressure difference may be determined as the pressure difference across the membrane such that the flux (2.8) is zero. This results in a

representation of the concentration gradient across the membrane, so that the flux reads

$$J \approx \frac{DK}{l} c_i \frac{n_v}{RT} \left(\Delta p - \Delta \pi\right), \tag{2.10}$$

where K is the ratio of activity constants, and experimentally the quantity $-n_v \left(\Delta p - \Delta \pi\right) / RT$ is observed to be small compared to the pressure difference, Δp (Wijmans and Baker, 1995). Taking the membrane constant $A = DKc_i n_v / lRT$, the flux of water through the membrane is proportional to the TMP, given by

$$J = A \left(\Delta p - \Delta \pi\right). \tag{2.11}$$

The above expression for the fluid flux across the membrane (2.11) resembles Darcy's law, with the fluid pressure replaced by the difference in fluid and osmotic pressures. We see here the potential concentration polarization has to limit the flux though the membrane, where the osmotic pressure can be high enough such that $\Delta p - \Delta \pi = 0$, as observed in experiments with sub-macromolecule particles that produce high osmotic pressures (Bowen and Jenner, 1995a).

2.3 Fluid Mechanics

In this section, we briefly describe how the full Navier–Stokes equations can be reduced to the Stokes equations using assumptions that are valid for crossflow membrane filtration. We also discuss the relevant boundary conditions and Darcy's law for flow in a porous medium.

The classical solution describing laminar flow in a channel with porous walls was given by Berman (1953). Here, a uniform permeation velocity at the wall is assumed to make the analysis tractable. However, it has long been recognized that a constant permeation velocity is an unrealistic assumption (Brian, 1965). Many models were developed for the fluid flow but contained assumptions that are not in general valid. These models, reviewed by Ilias and Govind (1993), usually assume one or more of the following: an approximated flow field, constant or piecewise constant permeation velocity, an osmotic pressure but no axial pressure drop, use of an effective permeability, or constant parameters (*e.g.*, viscosity, diffusivity *etc.*). Despite these limitations, they continue to be used in the literature (Bowen et al., 1996; Karode, 2001; Keir and Jegatheesan, 2014; Li et al., 1998; Meireles et al., 2015).

In §2.3.1, 2.3.2 and 2.5, we address many of the issues within these models for a channel with porous walls. We make rational simplifications (small reduced Reynolds number and thin channel) that will allow us to make progress solving the resulting system, rather than making unfounded approximations.

2.3.1 Governing equations

The motion of an incompressible liquid is usually described by the unsteady incompressible Navier–Stokes equations. These equations represent conservation of mass and momentum for a fluid, and account for the inertial, viscous and surface body forces that act on a fluid. The fluid velocity is written $\boldsymbol{u} = (u, v)$ in 2D. The Navier–Stokes equations may be written as

$$\nabla \cdot \boldsymbol{u} = 0, \tag{2.12a}$$

$$\rho \left[\frac{\partial \boldsymbol{u}}{\partial t} + (\boldsymbol{u} \cdot \nabla)\, \boldsymbol{u} \right] = \boldsymbol{f} - \nabla p + \nabla \cdot \left(\mu \left[\nabla \boldsymbol{u} + (\nabla \boldsymbol{u})^T \right] \right), \tag{2.12b}$$

where the density, ρ, is assumed constant and $\boldsymbol{f}$ is an external body force (Guazzelli and Morris, 2012; Batchelor, 1967, Chapter 3).

The Navier–Stokes equations (2.12) can be simplified for crossflow filtration systems. First, we assume that there is no external force, $\boldsymbol{f} = \boldsymbol{0}$ (gravity is negligible). Second, we study the system in steady state, $\partial \boldsymbol{u}/\partial t = 0$. This is a reasonable assumption for crossflow systems if fouling and caking do not occur, *i.e.*, below the critical flux (Field et al., 1995). Third, we can use the geometry of a thin channel ($\delta \ll 1$). This gives us the small reduced Reynolds number (2.2) as verified for typical parameter values in §2.1.1. This means that the viscous forces dominate the inertial forces in the flow, and so the $(\boldsymbol{u} \cdot \nabla)\, \boldsymbol{u}$ term in the Navier–Stokes momentum equation (2.12b) is small compared with the other terms.

These assumptions combine to give a simplified flow, the thin-layer Stokes equations (or lubrication equations (Reynolds, 1886)),

$$\frac{\partial u}{\partial x} + \frac{\partial v}{\partial y} = 0, \tag{2.13a}$$

$$\frac{\partial}{\partial y} \left(\mu \frac{\partial u}{\partial y} \right) = \frac{\partial p}{\partial x}, \tag{2.13b}$$

$$0 = \frac{\partial p}{\partial y}. \tag{2.13c}$$

In fact, the y-momentum equation (2.13c) tells us that $\partial p/\partial y = \mathcal{O}(\delta^2) \ll 1$: the pressure depends only on the axial position, x, so that $p = p(x)$ to leading order, as is familiar from lubrication theory and other thin-layer models of fluid flow (Oron et al., 1997). Thus the $\partial/\partial x$ on the RHS of (2.13b) becomes $\mathrm{d}/\mathrm{d}x$. In Chapter 3, we consider the case of a concentration-dependent viscosity, $\mu = \mu(\phi)$.

In Chapter 4, we consider a constant viscosity, μ, for simplicity. Here, the momentum equation (2.13b) may be simplified further to give the familiar lubrication equations,

$$\frac{\partial u}{\partial x} + \frac{\partial v}{\partial y} = 0, \tag{2.14a}$$

$$\mu \frac{\partial^2 u}{\partial y^2} = \frac{\mathrm{d}p}{\mathrm{d}x}. \tag{2.14b}$$

In filtration, the flow inside the porous wall is usually described by Darcy's law (Oxarango et al., 2004). Darcy's law is the simplest relation between velocity, $\boldsymbol{u}$, and pressure, p, in a porous medium (Ockendon et al., 2003), giving

$$\nabla \cdot \boldsymbol{u} = 0, \tag{2.15a}$$

$$\boldsymbol{u} = -\frac{k}{\mu} \nabla p. \tag{2.15b}$$

These equations may be justified by homogenization of the Stokes equations (Chamsri, 2013). The fluid entering the porous medium can only occupy the pore space, which makes up a fraction (the porosity, $\varphi \in (0, 1)$) of the medium. Hence, the actual fluid velocity is larger than the Darcy velocity,

$$u_{avg} = \varphi u, \tag{2.16}$$

where u_{avg} is the Darcy velocity.

2.3.2 Boundary conditions

The thin-layer Stokes equations (2.13) require a reduced set of boundary conditions in comparison to the full Navier–Stokes equations. Due to the highest derivative of each variable in (2.13), we need two boundary conditions for the axial velocity, u, one for the transverse velocity, v, and one for the fluid pressure, p. The channel geometry is oriented such that $x = 0$ and $x = L$ are the entrance and exit to the

channel, respectively, and $y = 0$ is the centre of the channel with the permeable walls at $y = \pm H$ (Figure 2.1).

Usually a channel has identical porous membrane walls on each side. As such, the system is naturally symmetric about $y = 0$ (the dashed line in Figure 2.1). Along this line of symmetry, the axial velocity, u, is symmetric and the transverse velocity, v, is zero, *i.e.*,

$$\frac{\partial u}{\partial y} = v = 0 \qquad \text{at} \qquad y = 0. \tag{2.17}$$

We therefore need only consider the behaviour in the half-channel given by $0 \leq x \leq L$ and $0 \leq y \leq H$.

Membrane filtration systems concern the flow of water over a permeable boundary. If the boundary is a smooth impermeable wall, a *no-slip* condition is appropriate, meaning the velocity of the fluid at the boundary is the same as the velocity of the boundary itself. However, a permeable boundary contains pores that allows the fluid to pass through, and adds a surface roughness. Beavers and Joseph (1967) investigated the appropriate boundary condition to apply for a viscous fluid at a naturally permeable boundary as they found that the assumption of no-slip was insufficient. Motivated by experiments, Beavers and Joseph (1967) wrote the tangential, or *slip*, velocity boundary condition as

$$\frac{\partial u}{\partial y} = \frac{\alpha}{k^{1/2}} \left(u - \bar{U} \right) \qquad \text{at} \qquad y = H, \tag{2.18}$$

where u is the tangential velocity, $\bar{U}$ the mean tangential filtrate velocity in the porous medium, k is the permeability of the porous medium and α is a dimensionless constant dependent on the structure of the porous medium. The fluid is governed by the Stokes equations within the channel, and Darcy's law within the porous medium. Since the porosity changes discontinuously at the permeable boundary, there is a boundary layer solution in the porous medium. The fluid flows faster at a permeable boundary than a solid boundary. The slip boundary condition (2.18), in the limit of small k, is justified mathematically by Saffman (1971).

As mentioned previously, crossflow filtration systems typically have $\delta \ll 1$ and hence the ratio of the wall permeation velocity to the mean axial velocity is small. This results in a small or even negligible slip coefficient at the boundary with a porous wall (Bowen and Jenner, 1995a), confirmed by experiments using a microfiltration

system (Shipley et al., 2010), even up to surface porosities of 80% (Schmitz and Prat, 1995). We therefore use the no-slip condition at a permeable wall, which reads

$$u = 0 \qquad \text{at} \qquad y = H. \tag{2.19}$$

Other studies have looked at the effects of a large slip coefficient. This is relevant once Reynolds numbers and permeabilities become too high, or fouling becomes relevant to the process (Altena and Belfort, 1984; Bowen and Jenner, 1995a; Schmitz and Prat, 1995).

For the pore-flow model in nanofiltration, ultrafiltration and microfiltration, the permeate flow is driven by the *transmembrane pressure difference* across the membrane (Wijmans and Baker, 1995). As such, the transverse fluid flow, v, through the channel walls (*i.e.*, membranes) is given by the difference in fluid pressure and osmotic pressure across the membrane,

$$v = \kappa(\Delta p - \Delta\pi) \qquad \text{at} \qquad y = H, \tag{2.20}$$

where $\kappa = k/\mu b$ is the spatially varying effective permeability, related to the wall permeability, k, fluid viscosity, μ, and wall thickness, b. The quantity $\Delta p = p(x, H) - p_{\text{outer}}$ is the difference between the hydrodynamic pressure, p, in the channel at the wall and the pressure outside the channel, p_{outer} (assumed constant), on the permeate side. Similarly, $\Delta\pi = \pi(x, H) - \pi_{\text{outer}}$ is the osmotic pressure difference across the wall, where π is the osmotic pressure due to particles in the channel, and π_{outer} is that due to particles outside the channel. Assuming complete rejection of particles at the channel wall, *i.e.*, a perfect filter, we take $\pi_{\text{outer}} = 0$. The functional form of the osmotic pressure, π, was discussed in §2.2.1. The form of Eq. (2.20) was justified in §2.2.2 for reverse-osmosis membranes from arguments based on irreversible thermodynamics relating to the solution–diffusion model.

At the inlet of the channel we impose a constant fluid flux, $2Q$. We therefore write

$$\int_0^H u \, \mathrm{d}y = Q \qquad \text{at} \qquad x = 0, \tag{2.21}$$

using the symmetry of the system about $y = 0$. We will see later that the imposition of a constant fluid influx results in a boundary condition for the pressure gradient at the inlet, $x = 0$. We assume that the end of the channel is open so that the pressure at the outlet is the same as the pressure outside the channel from the membrane,

$$p = p_{\text{outer}} \qquad \text{at} \qquad x = L. \tag{2.22}$$

This provides a reference pressure at the channel exit for the condition on the pressure gradient at the inlet.

2.4 Particle Suspensions

The interesting phenomena that occur during membrane filtration are largely due to the dynamics of the particle suspension. In this section we discuss the transport of a particle suspension by a fluid flow.

2.4.1 Governing equations

The concentration of a particle suspension, given by the volume fraction, ϕ, is conserved in a fluid flow. Assuming no sources or sinks, the continuity equation states that the rate of change of ϕ is given by the change in the local mass flux, $\boldsymbol{j}$,

$$\frac{\partial \phi}{\partial t} + \nabla \cdot \boldsymbol{j} = 0. \tag{2.23}$$

The total flux, $\boldsymbol{j}$, for a particle suspension in a fluid flow has two components: an advective flux, $\boldsymbol{j}_a$, and a diffusive flux, $\boldsymbol{j}_d$ (Ockendon et al., 2003). The advective term represents a mass transfer by the flow carrying the particles, and is given by

$$\boldsymbol{j}_a = \boldsymbol{u}\phi, \tag{2.24}$$

with $\boldsymbol{u}$ the fluid velocity. The diffusion term models the Brownian motion of a concentration of particles, moving from regions of high concentration to low concentration. Hence the flux associated with diffusion, known as Fick's law, is proportional to the negative concentration gradient,

$$\boldsymbol{j}_d = -D\nabla\phi, \tag{2.25}$$

where D is the diffusivity. The diffusivity may also depend on the properties of the flow, including the concentration, $D = D(\phi)$.

The total flux is given by $\boldsymbol{j} = \boldsymbol{j}_d + \boldsymbol{j}_d$. The conservation equation (2.23) then reads

$$\frac{\partial \phi}{\partial t} + \boldsymbol{u} \cdot \nabla\phi = \nabla \cdot (D\nabla\phi), \tag{2.26}$$

since the fluid is incompressible (2.12a). Eq. (2.26) is known as the *advection–diffusion equation*. In steady state, the equation reads,

$$\boldsymbol{u} \cdot \nabla\phi = \nabla \cdot (D\nabla\phi). \tag{2.27}$$

As with the fluid equation in §2.3.1, we can exploit the thin-channel approximation, $\delta \ll 1$, to simplify this equation,

$$u\frac{\partial \phi}{\partial x} + v\frac{\partial \phi}{\partial y} = \frac{\partial}{\partial y}\left(D\frac{\partial \phi}{\partial y}\right). \tag{2.28}$$

The axial-diffusion term, $\frac{\partial}{\partial x}\left(D\frac{\partial \phi}{\partial x}\right)$, is of order $\mathcal{O}(\delta^2)$ (Howison, 2005) and hence is neglected in the equation.

2.4.2 Boundary conditions

The advection–diffusion equation (2.28) requires three boundary conditions to be fully solved. As with the fluid flow in §2.3.2, we assume an axial symmetry for the particle concentration, ϕ, about $y = 0$, written as

$$\frac{\partial \phi}{\partial y} = 0 \qquad \text{on} \qquad y = 0, \tag{2.29}$$

so that we need only consider the behaviour in the half-channel $0 \leq x \leq L, 0 \leq y \leq H$.

Since particles are completely rejected by the wall we apply the no-flux boundary condition (Bacchin et al., 2002; Davis and Sherwood, 1990)

$$\boldsymbol{j} \cdot \boldsymbol{n} = v\phi - D\frac{\partial \phi}{\partial y} = 0 \qquad \text{on} \qquad y = H, \tag{2.30}$$

where $\boldsymbol{n}$ is the outward normal to the wall.

Finally, the particles enter the channel with some distribution through the cross-section

$$\phi(0, y) \equiv \Phi(y). \tag{2.31}$$

The functional form of $\Phi(y)$ is yet to be specified. In general, the inlet condition (2.31) will not satisfy the no-flux boundary condition (2.30). However, a small boundary layer region is present in which the concentration accordingly adjusts.

2.4.3 Particle migration

Ordinarily, one expects Brownian motion to move particles from high concentrations to low concentrations. However, a small but finite Reynolds number can result in other forms of diffusion, and indeed particle migration, that counteract ordinary diffusion.

When the particles in a suspension are sufficiently large ($> 10\mu$m, *i.e.*, non-colloids) that Brownian forces do not play a significant role, another form of diffusion arises in shear flow. This experimentally observed phenomenon, known as *shear-induced diffusion*, is caused by particle interactions: a lateral velocity component is generated, resulting in irreversible self-diffusion (Guazzelli and Morris, 2012). The diffusivity is proportional to $a^2\dot{\gamma}$, where $\dot{\gamma}$ is the shear rate (Leighton and Acrivos, 1987). This diffusion process results in a migration of particles from regions of high shear rate to low shear rate, known as *shear-induced migration*. In Poiseuille flow, particles migrate from the walls to the centre line, generating a larger concentration (Guazzelli and Morris, 2012).

When small, but finite, particle Reynolds numbers are considered, *tubular pinch* may occur. First reported experimentally, a rigid sphere in a laminar flow is subject to radial fluid forces resulting in displacement outwards from the centre of the tube, and inwards from the walls, to an equilibrium radial position (Segre and Silberberg, 1962). The preferred radial position is at approximately 0.6 tube radii from the axis. This annular region of high particle concentration is attributed to the inertia of the fluid (Cox and Brenner, 1968). However, the phenomenon is still not fully understood (Di Carlo et al., 2009; Hood et al., 2015).

In this thesis, we do not consider these particle migration effects. We assume small enough particle sizes (colloids) and Reynolds numbers that Fickian diffusion dominates.

2.5 Constitutive relations

Two important physical parameters are the fluid viscosity, μ, and the particle diffusivity, D. These parameters are often taken as constants, but in practice depend on many local properties of the fluid such as temperature, density, shear rate, *etc.* Here, we consider their dependence on the particle concentration, ϕ. Another important parameter is the permeability of the membrane, k, which may be related to the membrane structure. Here we consider a relation where the permeability is expressed in terms of the porosity and poresize of the membrane.

2.5.1 Concentration-dependent viscosity

The effect of a dilute ($\phi \ll 1$) suspension of rigid spheres on the viscosity was first studied by Einstein (1956). The calculation is based on the energy dissipated in the liquid by the mechanical work done by the sphere. The result is that the effective viscosity of a dilute suspension, $\mu(\phi)$, is related to that of the pure fluid, μ_0, by

$$\mu(\phi) = \mu_0 \left(1 + \frac{5}{2}\phi\right), \tag{2.32}$$

known as the *Einstein viscosity* (Guazzelli and Morris, 2012). This appears in the Stokes equation (2.13b), coupling the fluid flow to the particle concentration. Further terms in this expansion, when pair–particle interactions are included, may be found (Batchelor and Green, 1972) but are not used in this thesis.

Our discussion so far is valid for a dilute suspension, and holds for the early stages of the buildup of a concentration-polarization layer. It should be noted that the assumption of a Newtonian fluid remains valid when considering a thin-cake layer. The concentrated fluid is also treated as an effective Newtonian fluid with a viscosity dependent on the local concentration of the suspension (Davis and Leighton, 1987).

2.5.2 Concentration-dependent diffusivity

Brownian motion is the random movement of a (colloid) particle due to the thermal molecular movement of the fluid, and results in diffusion: particles move from regions of high concentration to low concentration. The equilibrium condition, that the free energy must vanish, gives the Stokes–Einstein equation for the diffusivity, D_0, as

$$D_0 = \frac{k_B T}{6\pi\mu_0 a}, \tag{2.33}$$

where k_B is Boltzmann's constant, T is the temperature and a is the particle radius (Einstein, 1956; Guazzelli and Morris, 2012; Song and Elimelech, 1995).

The Stokes–Einstein equation may be generalized to include both hydrodynamic and colloid particle interactions, that is valid for all particle volume fractions. The hydrodynamic interactions are determined by the effect of neighbouring particles on the Stokes drag force on a single particle, and the colloid particle interactions are determined by the osmotic pressure (Batchelor, 1976; Bowen and Williams, 2001;

Elimelech et al., 1995). For a dilute ($\phi \ll 1$) mono-disperse colloidal suspension, the effective diffusivity, $D(\phi)$, is given by

$$D(\phi) = D_0 \left(1 + \chi \, \phi\right), \tag{2.34}$$

where D_0 is the Stokes–Einstein relation (2.33), and the constant χ is a virial coefficient, a type-specific constant accounting for particle–particle interactions (see Batchelor (1976) and Elimelech et al. (1995) for tabulated values from the literature). The diffusivity appears in the advection–diffusion equation (2.28).

2.5.3 Kozeny–Carman relation

A membrane filter is a porous medium consisting of interconnected open pores, allowing fluid to flow through. The structural properties of the membrane determine how conducive it is to flow. We will relate the *permeability*, k, of the membrane to its *porosity*, φ, and *poresize*, a, with the commonly used Kozeny–Carman relation (Coussy, 2011; Xu and Yu, 2008). For a generic porous media, the Kozeny–Carman relation reads

$$k = \frac{\varphi^3}{(1-\varphi)^2} \frac{a^2}{36\tau}, \tag{2.35}$$

where τ is the *tortuosity*. The permeability appears in Darcy's law (2.15b).

The porosity, φ, of a porous medium is a measure of the amount of free space in the medium. In other words, it is the fraction of the total volume that is not material, with $\varphi \in (0, 1)$. It is through this porous free space that the fluid flows in a porous medium.

The poresize, a, of the membrane determines the particle sizes that can be effectively rejected by the membrane, and hence filtered. It is the pores at the inner surface of the membrane that are most important since the particles are caught here. Most membranes are asymmetric with a support layer consisting of larger pores (Figure 1.6). Throughout this thesis, we assume that the pores on the inner surface are of equal size and are equidistributed.

The permeability, k, of a porous medium measures how amenable the porous medium is to fluids passing through. It depends only on the geometry of the pores (Ockendon et al., 2003). Conceptually related to the permeability is the tortuosity, τ, measuring how curved the paths through the porous medium are, or in a sense a measurement of

diffusion in the porous medium (Van Brakel and Heertjes, 1974) (for cylindrical pores the tortuosity is the path length through the active layer of the membrane divided by the thickness of the active layer).

2.6 Summary

The governing equations for a flow of particles in a channel with membrane walls, with a small reduced Reynolds number and thin-channel approximation, from §2.3.1 and 2.4.1, read

$$\frac{\partial u}{\partial x} + \frac{\partial v}{\partial y} = 0, \tag{2.36a}$$

$$\frac{\partial}{\partial y}\left(\mu(\phi)\frac{\partial u}{\partial y}\right) = \frac{\mathrm{d}p}{\mathrm{d}x}, \tag{2.36b}$$

$$u\frac{\partial \phi}{\partial x} + v\frac{\partial \phi}{\partial y} = \frac{\partial}{\partial y}\left(D(\phi)\frac{\partial \phi}{\partial y}\right). \tag{2.36c}$$

The boundary conditions, from §2.3.2 and 2.4.2, read

$$\frac{\partial \phi}{\partial y} = \frac{\partial u}{\partial y} = v = 0 \quad \text{on} \quad y = 0, \tag{2.37a}$$

$$u = 0 \quad \text{on} \quad y = H, \tag{2.37b}$$

$$v = \kappa(\Delta p - \Delta\pi) \quad \text{on} \quad y = H, \tag{2.37c}$$

$$v\phi - D(\phi)\frac{\partial \phi}{\partial y} = 0 \quad \text{on} \quad y = H, \tag{2.37d}$$

$$\int_0^H u \,\mathrm{d}y = Q \quad \text{at} \quad x = 0, \tag{2.37e}$$

$$p = p_{\text{outer}} \quad \text{at} \quad x = L, \tag{2.37f}$$

$$\phi \equiv \Phi(y) \quad \text{at} \quad x = 0. \tag{2.37g}$$

The osmotic pressure (2.7) takes the form

$$\pi(\phi) = iRT/N_A V^* \phi. \tag{2.38}$$

In this study, the functional form of $\Phi(y)$ (yet to be prescribed) will be crucial.

In Chapter 3 we shall study the effect of variations in μ due to ϕ. For a dilute suspension, the concentration-dependent viscosity (2.32) takes the form

$$\mu(\phi) = \mu_0\left(1 + \frac{5}{2}\phi\right), \tag{2.39}$$

and the concentration-dependent diffusivity (2.34) takes the form

$$D(\phi) = D_0 \left(1 + \chi \, \phi\right). \tag{2.40}$$

In Chapter 4 we shall study we shall study spatial variations in κ.

In both chapters, the amount of fluid that passes through the walls,

$$F = 2 \int_0^L v(x, H) \, \mathrm{d}x, \tag{2.41}$$

is a quantity of significant practical interest since this provides a measure of the efficiency of the filtration process. We begin now to study crossflow filtration systems.

Chapter 3

Concentration-Dependent Viscosity

Summary

The transport of a dilute suspension of particles through a channel with porous walls is analysed, accounting for the concentration dependence of the viscosity. In particular, we study two cases of fluid permeation through the porous channel walls: (i) at a constant flux, and (ii) dependent on the pressure drop across the wall. We also consider the effect of mixing the suspension first rather than injecting at a point. We do this by considering inlet concentration distributions of different widths. We find that a pessimal (worst possible) *inlet distribution width exists that maximizes the required hydrodynamic pressure for a constant fluid flux. The effect of an external hydrodynamic pressure, to compensate for the reduced transmembrane pressure difference due to osmotic pressure, is investigated.*

A paper based on the contents of this chapter has been published:
J. G. Herterich, I. M. Griffiths, R. W. Field, D. Vella,
The effect of a concentration-dependent viscosity on particle transport in a channel flow with porous walls,
AIChE Journal **60(5)** (2014): 1891-1904

3.1 Introduction

A crossflow filtration system consists of a feed solution of fluid with contaminants (often particulates) flowing tangentially to a porous membrane. This membrane allows the fluid to pass through (the filtrate) but rejects the particulates (the retentate), as depicted in Figure 1.5(b). The filtration is driven by two pressure differences across the membrane: (i) the hydrodynamic pressure difference that is conducive to filtration, and (ii) the osmotic pressure difference that mitigates against filtration. This is a reverse-osmosis procedure, as described in §1.3.2. The osmotic pressure on the filtrate side is generally close to zero while that on the feed side may be large due to the concentration polarization (CP) that occurs. The phenomenon of CP, as discussed in §1.3.3, is the observed large particle-concentration near the membrane surface compared to that in the bulk flow. CP is one of the main limitations of the efficacy of water filtration since the relatively high osmotic pressure on the feed side of the membrane reduces the effective pressure (*cf.* Eq. (2.20)) that drives filtration (Song and Elimelech, 1995).

The transition from concentration polarization to deposition (fouling) on the membrane is of great importance to the lifetime of membranes. Bacchin et al. (2002) model this by a toggle that changes the equations for the permeate flux and wall concentration depending on which is taking place. This toggle is implemented via a critical concentration: below this critical value, concentration polarization occurs, but once above it, there is sufficiently high concentration for particle deposition to occur as well as concentration polarization (*i.e.*, there is some irreversible solidification as a gel or cake formation). The type of driving phenomena may alter the outcome and the critical flux for the transition between concentration polarization and deposition is linked to the local Péclet number, as discussed in §1.3.3.

Mass transport of particle suspensions to membranes have become important in other areas such as tissue engineering. The setup is similar to that of membrane filtration: flow in a tube with porous membrane walls, with analogous equations. However, in tissue engineering, part of the challenge is often to deliver the particles (*e.g.* nutrients) to the membrane walls, often with an equal distribution (Griffiths et al., 2013; Shipley and Waters, 2011).

The fluid velocity in a channel with porous walls has been analysed for a constant viscosity, membrane permeability, and permeation velocity (Probstein, 1989). The solution is a Poiseuille-like parabolic profile decreasing in magnitude along the channel

for the axial component. The transverse component has a cubic dependence on cross-channel position that is proportional to the permeation flux (Hurwitz, 1989). More generally, the axial flow rate in the channel decreases with flow through the porous walls. When combined with advection by the transverse flow, the resultant flow transporting particles is conducive to concentration polarization at the walls (Kostoglou and Karabelas, 2009). The limits of this and similar fluid models are described in §2.3. Specifically in this chapter we address the limits of a constant liquid viscosity and constant permeation velocity. We retain the assumption of a constant membrane permeability as this is a reasonable filtration condition until fouling becomes relevant.

A complicating factor in water filtration using membranes is the dependence of the liquid viscosity on particle concentration. The liquid viscosity is often taken as a constant in models of filtration, but in practice depends on many local properties of the fluid such as its temperature, density and shear rate. Of particular concern is the effect of a concentration-dependent viscosity on crossflow filtration, as discussed in §2.5.1. This becomes important because of the CP layer near the membrane surface, as well as the general spatial variability of the concentration in the channel.

The permeate flux, concentration-dependent viscosity and CP are strongly interrelated near the membrane. They combine to slow down the flow and increase CP (Bacchin et al., 2002; Gill et al., 1988). Davis and Sherwood (1990) consider the convection–diffusion equation for particles in a steady-state boundary layer with a concentration-dependent viscosity and diffusivity given by Davis and Leighton (1987). This model assumes that, outside the boundary layer, the bulk concentration of particles is constant. Physically, this may be achieved in a system in which the Péclet number is large so that advection dominates diffusion. A similarity solution in the boundary layer is obtained in this case. Bowen and Williams (2001) consider a full numerical solution to the Navier–Stokes and convective–diffusion equations for crossflow ultrafiltration with a concentration-dependent viscosity and diffusivity using a Thomas algorithm. Their results show the significant effect various parameters have on concentration polarization and the rate of filtration.

In this chapter we consider a pressure-driven fluid flow with advection and diffusion of particles in a thin channel with porous walls. We extend the fluid permeation velocity to depend on the pressures, both hydrodynamic and osmotic, in the channel that is required for reverse osmosis. We study the particular case of a *dilute* suspension of identical and neutrally buoyant particles and consider a bulk concentration with a specified cross-stream distribution entering the channel. As such, we assume that

deposition of particles on the membrane does not occur. Determining the critical concentration before fouling occurs, defined in Bacchin et al. (2002), is beyond the scope of this work; rather, our aim is to understand the early stages of particle buildup that ultimately results in concentration polarization, which is of considerable interest to the membrane industry (Ockendon, 1991).

We study the steady flow (*i.e.*, constant in time) and examine its variations in space arising due to the local particle concentration and permeation flux through the channel walls. The fluid (but not particles) may pass through the porous walls so that the walls act as perfect filters, and we do not consider the possibility that particles may block pores when they reach the walls. As such, we assume that the permeability is constant. The effects of a concentration dependence of the viscosity of the fluid are analysed. However, a constant diffusivity is shown to be asymptotically appropriate for a dilute suspension. The form of the channel fluid flow as in Probstein (1989) is retrieved as a leading-order solution that does not have a particle concentration dependence, and the higher-order concentration-dependent solution is determined. The case of a pressure-dependent permeation flux is considered, where the hydrodynamic and osmotic pressures drive the filtration. We are particularly interested in the pressures required for a constant inlet fluid flux due to the concentration-dependent viscosity.

We provide a mathematical description of the problem, applying a thin-channel approximation to the governing equations to derive a coupled system of nonlinear partial differential equations (PDEs). These equations are simplified by examining the asymptotic limit of a dilute suspension of particles. Analytic results are obtained at leading order, with numerical results at the next order (where the dilute particle suspension and flow interact). We also consider the effects of an outer pressure, that is, a pressure outside the channel that affects the transmembrane pressure difference. Order-one Péclet numbers are taken so that the advection and diffusion of particles in the channel are equally important, to provide the greatest generality for the particle dynamics in the channel.

3.2 Modelling

We consider a two-dimensional channel of length L, with porous walls located at $\hat{y} = \pm H$, as depicted in Figure 3.1. Fluid is injected into the channel at $\hat{x} = 0$ at

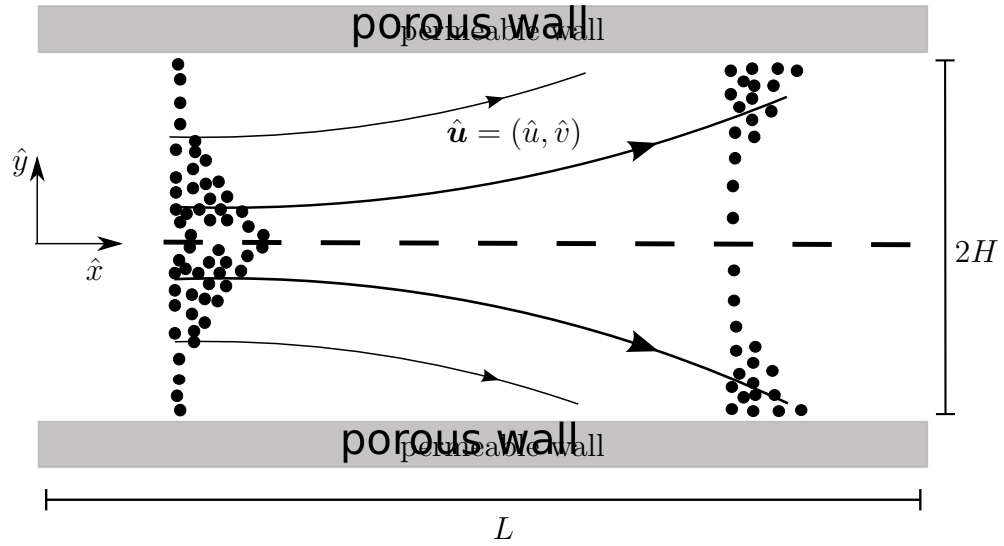

Figure 3.1: Schematic of a channel with permeable walls. The channel has length L and width $2H$. The fluid velocity field is $\hat{\boldsymbol{u}} = (\hat{u}, \hat{v})$ from left to right and is allowed to permeate out through the channel walls. Particles entrained in the fluid with some distribution at the inlet are advected by the flow and diffuse by Brownian motion, collecting at the channel walls.

a fixed flow rate, $2\hat{Q} = 2HU\,(\mathrm{m}^2/\mathrm{s})$, and with a given concentration distribution of particles. The velocity field within the fluid is $\hat{\boldsymbol{u}} = (\hat{u}, \hat{v})$, with $\hat{u}$ the axial component and $\hat{v}$ the transverse component. In such a configuration the solvent (particle-free) viscosity, μ_0, will play a key role in determining the flow profile.

The typical parameter values are as given in §2.1.1. This means that we have a small aspect ratio, $\delta = H/L \ll 1$ (2.1), a small reduced Reynolds number, Re (2.2), and an order-one Péclet number, Pe (2.3). We assume that this Péclet number is sufficiently small so that fouling does not occur, as discussed in §2.1.1. Furthermore, we note that the particles, of size a, are in principle subject to Brownian diffusion ($\hat{D} = k_B T/6\pi\mu_0 a$ (Song and Elimelech, 1995)) and shear-induced diffusion ($a^2\dot{\gamma}$ (Leighton and Acrivos, 1987), for shear rate $\dot{\gamma} = U/H$), as discussed in §2.4.3. However, for $a < 1\,\mu$m, as we shall consider, Brownian diffusivity dominates and we neglect shear-induced diffusion.

The particles in the channel are described by their volume fraction, $\phi(\hat{x}, \hat{y})$. The volume fraction of particles at the inlet, $\hat{x} = 0$, is prescribed by $\phi(\hat{x} = 0, \hat{y}) = \Phi(\hat{y})$ for some function Φ. We wish to understand how the volume fraction, $\phi(\hat{x}, \hat{y})$, changes with distance along the channel as a result of the fluid flow, and how it influences the flow. The viscosity of the fluid, $\hat{\mu}$, is assumed to be dependent on the volume fraction, writing $\hat{\mu} = \hat{\mu}(\phi)$, the functional form of which has been discussed in §2.5.1.

3.2.1 Governing equations

The steady flow of a fluid with a small reduced Reynolds number in a thin channel is derived in §2.3.1. The fluid flow is governed by the steady Stokes equations, representing conservation of mass and momentum of the fluid,

$$\boldsymbol{\nabla} \cdot \hat{\boldsymbol{u}} = 0, \tag{3.1a}$$

$$\boldsymbol{\nabla} \cdot \left(\hat{\mu}(\phi) \left[\boldsymbol{\nabla} \hat{\boldsymbol{u}} + (\boldsymbol{\nabla} \hat{\boldsymbol{u}})^T \right] \right) = \boldsymbol{\nabla} \hat{p}, \tag{3.1b}$$

where $\hat{p}$ is the hydrodynamic fluid pressure. For a dilute suspension, $\phi \ll 1$, the concentration-dependent viscosity (2.32) is given by the Einstein viscosity (Guazzelli and Morris, 2012),

$$\hat{\mu}(\phi) = \mu_0 \left(1 + \frac{5}{2} \phi \right), \tag{3.2}$$

as discussed in §2.5.1.

The flow advects the particles down the channel, but they also diffuse within the channel. The particle volume fraction is governed by the steady advection–diffusion equation,

$$\hat{\boldsymbol{u}} \cdot \boldsymbol{\nabla} \phi = \boldsymbol{\nabla} \cdot \left(\hat{D}(\phi) \boldsymbol{\nabla} \phi \right), \tag{3.3}$$

as derived §2.4.1. We discussed the particle diffusivity, $\hat{D}(\phi)$, which also depends on volume fraction, in §2.5.2. For a dilute suspension, the concentration-dependent diffusivity (2.34) is given by

$$\hat{D}(\phi) = D_0 \left(1 + \chi \, \phi \right), \tag{3.4}$$

where the constant χ is a virial coefficient, a type-specific constant accounting for particle-particle interactions (Batchelor, 1976; Elimelech et al., 1995).

3.2.2 Boundary conditions

Let us now consider the boundary conditions to which the governing equations (3.1) and (3.3) are subjected, as in §2.3.2 and 2.4.2. The flow and particle distribution are assumed to be symmetric about the axis of the channel, that is,

$$\frac{\partial \phi}{\partial \hat{y}} = \frac{\partial \hat{u}}{\partial \hat{y}} = \hat{v} = 0 \qquad \text{on} \qquad \hat{y} = 0. \tag{3.5}$$

Henceforth we shall consider only the behaviour in the half channel $0 \leq \hat{x} \leq L$, $0 \leq \hat{y} \leq H$. We consider the two permeation fluxes through the porous channel walls, $\hat{\mathcal{V}} := \hat{v}(\hat{x}, H)$, that are most often found in practical applications. First the case when $\hat{\mathcal{V}}$ is a constant, say $\hat{\mathcal{V}}^*$, is considered. In the absence of significant osmotic effects, this type of permeation flux has been achieved by having a flow of fluid (recirculated filtered fluid) outside the channel so that the pressure difference across the membrane is constant along the wall (Sandblom, 1978). Secondly we consider the case where $\hat{\mathcal{V}}$ is proportional to the net driving force (*i.e.*, the transmembrane pressure difference). At the wall, we therefore have one of the two possible boundary conditions for the transverse velocity,

$$\hat{v}(\hat{x}, H) = \hat{\mathcal{V}} = \begin{cases} \hat{\mathcal{V}}^* = \text{constant} & \text{(Case 1)}, \\ \hat{\kappa}\,(\Delta\hat{p} - \Delta\hat{\pi}) & \text{(Case 2)}, \end{cases} \tag{3.6}$$

respectively, where $\hat{\kappa}$ is a constant of proportionality that is related to the solvent viscosity and the permeability of the porous wall and its thickness (*cf.* Darcy's law). Here the term $\Delta\hat{p} = \hat{p}(\hat{x}) - \hat{p}_{\text{outer}}$ is the hydrodynamic pressure difference across the membrane, which is measured relative to the pressure outside the channel, $\hat{p}_{\text{outer}}$ (*i.e.*, the reference pressure). In the following sections we assume that the outer pressure is zero,

$$\hat{p}_{\text{outer}} = 0. \tag{3.7}$$

This assumption will be relaxed in §3.5. Similarly, $\Delta\hat{\pi} = \hat{\pi} - \hat{\pi}_{\text{outer}}$ where $\hat{\pi}$ is the osmotic pressure due to particles in the channel and $\hat{\pi}_{\text{outer}}$ is that due to particles outside the channel. We assume complete rejection of particles at the channel wall,

$$\hat{\pi}_{\text{outer}} = 0. \tag{3.8}$$

The osmotic pressure difference across the porous wall is, in general, a function of the volume fraction of particles at the surface of the porous wall, as discussed in §2.2.1.

In §2.3.2 we discussed the need for a slip boundary condition at the porous wall. Remarking that it has been found that slip is not significant for a wide range of membranes (Shipley et al., 2010), we adopt a no-slip boundary condition,

$$\hat{u}(\hat{x}, H) = 0, \tag{3.9}$$

as also adopted by Bowen and Williams (2001).

Since particles are rejected by the membrane but fluid may permeate, a no-flux boundary condition for the particles at the channel walls is applied. This may be written as (Bacchin et al., 2002; Davis and Sherwood, 1990)

$$\hat{v}\phi - \hat{D}\frac{\partial \phi}{\partial \hat{y}} = 0 \qquad \text{on} \qquad \hat{y} = H. \tag{3.10}$$

Two final conditions close the system. At the inlet we impose a constant flow, $\hat{Q}$,

$$2\hat{Q} = \int_{-H}^{H} \hat{u}\,\mathrm{d}\hat{y} = 2\int_{0}^{H} \hat{u}\,\mathrm{d}\hat{y} \qquad \text{at} \qquad \hat{x} = 0. \tag{3.11}$$

At the outlet the pressure is assumed to be constant; without loss of generality we may set this outlet pressure to zero, *i.e.*,

$$\hat{p} = 0 \qquad \text{at} \qquad \hat{x} = L, \tag{3.12}$$

matching the outer pressure condition (3.7). This corresponds to the common setup in which the hydrodynamic outlet pressure and pressure outside the channel walls are equal. We also note that the appropriate outlet boundary condition for a directflow configuration is $\hat{u} = 0$ at $\hat{x} = L$. However, we could in principle choose the outlet pressure such that there is no net outflow (Karode, 2001). While these conditions are not identical, the overall behaviour in both cases will be similar, except in a small region near the outlet.

3.2.3 Thin-channel approximation

We suppose that the channel is thin so that the aspect ratio $\delta = H/L \ll 1$. We exploit the smallness of δ, non-dimensionalizing the system by letting

$$\begin{aligned}
&\hat{x} = Lx, && \hat{y} = \delta L y, && \hat{u} = \frac{\hat{Q}}{H}u,\\
&\hat{v} = \delta\frac{\hat{Q}}{H}v, && \hat{\mu} = \mu_0\mu, && \hat{p} = \frac{\hat{Q}\mu_0}{\delta^2 HL}p,\\
&\hat{\kappa} = \frac{\delta^3 L}{\mu_0}\kappa, && \hat{\pi} = \frac{\hat{Q}\mu_0}{\delta^2 HL}\pi, && \hat{D} = D_0 D,
\end{aligned} \tag{3.13}$$

in which the dimensional variables appear with a hat, and μ_0 is the viscosity of the solvent in the absence of particles, and D_0 is the constant Brownian diffusivity for a particle in the absence of the effects of surrounding particles. Conservation of mass motivates the transverse velocity scaling being chosen to be a factor of δ times the

axial velocity scaling. However, note that the total fluid permeate may be order unity (despite the small velocity at each point) because of the length of the channel. Substituting the non-dimensionalization (3.13) into equations (3.1) and (3.3) and retaining only leading-order terms in δ provides the equations for the volume fraction in a thin-channel flow with a concentration-dependent viscosity,

$$\frac{\partial u}{\partial x} + \frac{\partial v}{\partial y} = 0, \tag{3.14a}$$

$$\frac{\partial}{\partial y}\left(\mu(\phi)\frac{\partial u}{\partial y}\right) = \frac{\partial p}{\partial x}, \tag{3.14b}$$

$$0 = \frac{\partial p}{\partial y}, \tag{3.14c}$$

$$\mathrm{Pe}\left(u\frac{\partial \phi}{\partial x} + v\frac{\partial \phi}{\partial y}\right) = \frac{\partial}{\partial y}\left(D(\phi)\frac{\partial \phi}{\partial y}\right). \tag{3.14d}$$

Here Pe is the (reduced) Péclet number,

$$\mathrm{Pe} = \delta^2 \frac{UL}{D_0} = \delta \frac{\hat{Q}}{D_0}. \tag{3.15}$$

The Péclet number measures the rate of advection of particles down the channel compared with the diffusion across the channel. As discussed earlier, the viscosity $\mu(\phi)$ is assumed to be a known function. We note that (3.14c) implies that the hydrodynamic pressure is, to leading order, a function of x only, *i.e.*, $p = p(x)$ (Oron et al., 1997). Note also that equation (3.14d) indicates that there is no axial particle diffusion present at leading order.

The dimensionless boundary conditions, to leading order, to be used in determining the solution to (3.14) are as follows,

$$\frac{\partial \phi}{\partial y} = \frac{\partial u}{\partial y} = v = 0 \qquad \text{on } y = 0, \tag{3.16a}$$

$$v(x,1) = \mathcal{V} = \begin{cases} \mathcal{V}^* & (\text{Case 1}), \\ \kappa\,(p - \Delta\pi) & (\text{Case 2}), \end{cases} \tag{3.16b}$$

$$u(x,1) = 0, \tag{3.16c}$$

$$\mathrm{Pe}\, v\phi - \frac{\partial \phi}{\partial y} = 0 \qquad \text{on } y = 1, \tag{3.16d}$$

$$\int_0^1 u \,\mathrm{d}y = 1 \qquad \text{at } x = 0, \tag{3.16e}$$

$$p = 0 \qquad \text{at } x = 1. \tag{3.16f}$$

The two cases in Equation (3.16b) refer to the two distinct permeation fluxes as described in (3.6): constant, $\mathcal{V}^*$, and pressure-dependent, and will be treated separately. Finally, we specify the volume fraction profile at the inlet

$$\phi(0, y) = \Phi(y), \tag{3.17}$$

for some $\Phi(y)$. Two natural types of injection that should be compared are (i) uniform injection across $0 \leq y \leq 1$ and (ii) point injection. To capture both of these we consider a normalized particle distribution at the inlet that is Gaussian in nature, of the form:

$$\phi(0, y) = \Phi(y) = \frac{\exp\left(\dfrac{-y^2}{2\sigma^2}\right)}{\sqrt{\dfrac{\pi}{2}}\,\sigma\,\mathrm{erf}\left(\dfrac{1}{\sqrt{2}\sigma}\right)}. \tag{3.18}$$

Here σ is a constant that reflects the width of the distribution. The uniform inlet volume fraction arises in the limit $\sigma \to \infty$, whilst point injection at the centre $y = 0$ corresponds to $\sigma \to 0$; intermediate values of σ give different pulse widths.

Eqns. (3.14) subject to boundary conditions (3.16) and inlet condition (3.17) define our problem mathematically.

3.2.4 Model solution

Our aim is to determine the change in particle volume fraction, ϕ, as we move down the channel, *i.e.*, the variation with y of $\phi(x, y)$ as x increases. Integrating the momentum equation (3.14b), and making use of the symmetry and no-slip conditions (3.16a,c) gives

$$u(x, y) = -\frac{\mathrm{d}p}{\mathrm{d}x} \int_y^1 \frac{\tilde{y}}{\mu\big(\phi(x, \tilde{y})\big)}\,\mathrm{d}\tilde{y}. \tag{3.19}$$

Substituting (3.19) into the continuity equation (3.14a), integrating and applying (3.16a) gives

$$v(x, y) = \frac{\partial}{\partial x}\left\{\frac{\mathrm{d}p}{\mathrm{d}x}\left(y \int_y^1 \frac{\tilde{y}}{\mu\big(\phi(x, \tilde{y})\big)}\,\mathrm{d}\tilde{y} + \int_0^y \frac{\tilde{y}^2}{\mu\big(\phi(x, \tilde{y})\big)}\,\mathrm{d}\tilde{y}\right)\right\}. \tag{3.20}$$

The transverse fluid velocity at the channel wall, $\mathcal{V}$, is then given by

$$v(x, 1) = \mathcal{V} = \frac{\partial}{\partial x}\left\{\frac{\mathrm{d}p}{\mathrm{d}x}\left(\int_0^1 \frac{\tilde{y}^2}{\mu\big(\phi(x, \tilde{y})\big)}\,\mathrm{d}\tilde{y}\right)\right\}. \tag{3.21}$$

Treating $\mathcal{V}$ as given by the two behaviours of the permeation flux of interest in (3.16b), and expanding the derivative in equation (3.21) results in two ordinary differential equations (ODEs) for the hydrodynamic pressure, $p(x)$, of the form

$$\frac{\mathrm{d}^2 p}{\mathrm{d}x^2} - \frac{B(x)}{A(x)}\frac{\mathrm{d}p}{\mathrm{d}x} - \frac{1}{A(x)}\mathcal{V} = 0, \tag{3.22}$$

(one for each $\mathcal{V}$ case in Eq. (3.16b)) where

$$A(x) = \int_0^1 \frac{\tilde{y}^2}{\mu\big(\phi(x,\tilde{y})\big)}\,\mathrm{d}\tilde{y}, \tag{3.23a}$$

$$B(x) = \int_0^1 \frac{\tilde{y}^2}{\mu\big(\phi(x,\tilde{y})\big)^2}\frac{\partial \mu\big(\phi(x,\tilde{y})\big)}{\partial x}\,\mathrm{d}\tilde{y}. \tag{3.23b}$$

Equations (3.19) and (3.20) give the axial and transverse velocities in terms of the volume fraction, ϕ, and hydrodynamic pressure, p. These may be substituted into the advection–diffusion equation (3.14d) and, with the ODE for the hydrodynamic pressure (3.22), they provide two coupled integro-differential equations for ϕ and p (for each permeate flux case), which are difficult to solve numerically. However, in the next section we are able to make further analytical progress by exploring the limit of a dilute suspension, $\phi \ll 1$.

3.3 Asymptotics for a Dilute Suspension

The coupled nonlinear system of equations (3.14) can be simplified by considering a dilute suspension of particles,

$$\phi(x,y) = \epsilon\,\phi_1(x,y) \tag{3.24}$$

with $\epsilon \ll 1$ and ϕ_1 assumed to be $\mathcal{O}(1)$. The small parameter ϵ represents the dilution of the particles in the fluid.

The osmotic pressure difference across the porous wall, in the dilute limit, is a linear function of the particle volume fraction at the wall (Williams, 1969)

$$\Delta\pi = \epsilon\pi_0\phi_1(x, y=1) + \mathcal{O}\left(\epsilon^2\right), \tag{3.25}$$

where π_0 is a reference osmotic pressure related to the van't Hoff factor, as discussed in §2.2.1. In the dilute limit, the leading-order effect of volume fraction on viscosity is given by the Einstein viscosity (3.2),

$$\mu(\phi) = 1 + \frac{5}{2}\epsilon\,\phi_1 + \mathcal{O}\left(\epsilon^2\right). \tag{3.26}$$

Finally, the asymptotic expression for the effective diffusivity, $D(\phi)$, for a dilute mono-disperse suspension is given by (3.4),

$$D(\phi) = 1 + \epsilon\,\chi\,\phi_1 + \mathcal{O}\left(\epsilon^2\right). \tag{3.27}$$

We exploit the dilute approximation by expanding the hydrodynamic pressure and velocity components as

$$p(x) = p_0(x) + \epsilon\,p_1(x) + \mathcal{O}\left(\epsilon^2\right), \tag{3.28a}$$

$$u(x,y) = u_0(x,y) + \epsilon\,u_1(x,y) + \mathcal{O}\left(\epsilon^2\right), \tag{3.28b}$$

$$v(x,y) = v_0(x,y) + \epsilon\,v_1(x,y) + \mathcal{O}\left(\epsilon^2\right). \tag{3.28c}$$

Substituting these expressions into the advection–diffusion equation for ϕ, (3.14d), the lowest-order terms are at $\mathcal{O}(\epsilon)$, and so this forms an equation for ϕ_1 in terms of the leading-order velocities u_0 and v_1:

$$\mathrm{Pe}\left(u_0\frac{\partial\phi_1}{\partial x} + v_0\frac{\partial\phi_1}{\partial y}\right) = \frac{\partial^2\phi_1}{\partial y^2}. \tag{3.29}$$

We note that the Brownian diffusivity, D_0, enters through the Péclet number. The concentration-dependent term in the diffusivity (3.27) appears at a higher order, $\mathcal{O}(\epsilon^2)$ in this case. This plays no role in the first-order correction to the fluid flow. As a result, we need only consider a constant particle diffusivity, D_0, here. In the dilute limit, the symmetry and no-flux boundary conditions from (3.16a) and (3.16d) read

$$\frac{\partial\phi_1}{\partial y} = 0 \qquad \text{on } y = 0, \tag{3.30a}$$

$$\mathrm{Pe}\,\mathcal{V}_0\,\phi_1 - \frac{\partial\phi_1}{\partial y} = 0 \qquad \text{on } y = 1, \tag{3.30b}$$

where $\mathcal{V}_0 = v_0(x,1)$ is the leading-order permeation flux at the porous channel walls. The inlet condition is

$$\phi_1(0,y) = \Phi(y), \tag{3.31}$$

for a normalized Gaussian function $\Phi(y)$ of the form given by equation (3.18).

The expression for the axial velocity given by (3.19) may be expanded in powers of ϵ, using the viscosity and pressure expansions (3.26) and (3.28a), to give

$$u(x,y) = \frac{\mathrm{d}p_0}{\mathrm{d}x}\frac{(y^2-1)}{2} + \epsilon\left(\frac{\mathrm{d}p_1}{\mathrm{d}x}\frac{(y^2-1)}{2} + \frac{\mathrm{d}p_0}{\mathrm{d}x}\int_y^1 \frac{5}{2}\,\tilde{y}\phi_1(x,\tilde{y})\,\mathrm{d}\tilde{y}\right) + \mathcal{O}\left(\epsilon^2\right). \tag{3.32}$$

Similarly for the transverse velocity, given by (3.20), we find

$$v(x,y) = \frac{\mathrm{d}^2 p_0}{\mathrm{d}x^2}\frac{(3y-y^3)}{6} + \epsilon\frac{\partial}{\partial x}\left\{\frac{\mathrm{d}p_1}{\mathrm{d}x}\frac{(3y-y^3)}{6} - \frac{\mathrm{d}p_0}{\mathrm{d}x}\left[y\int_y^1 \frac{5}{2}\,\tilde{y}\phi_1(x,\tilde{y})\,\mathrm{d}\tilde{y} + \int_0^y \frac{5}{2}\,\tilde{y}^2\phi_1(x,\tilde{y})\,\mathrm{d}\tilde{y}\right]\right\} + \mathcal{O}\left(\epsilon^2\right). \tag{3.33}$$

Equations (3.32) and (3.33) determine the leading-order and order-ϵ components of the velocities u and v. As expected in the dilute limit, the presence of particles does not affect the leading-order problem; their effect is only felt at the next order.

The two cases for the boundary condition for v at $y = 1$ (3.16b) take the form $\mathcal{V} = \mathcal{V}_0 + \epsilon\mathcal{V}_1$ where

$$\mathcal{V} = \mathcal{V}_0 + \epsilon\mathcal{V}_1 = \begin{cases} \mathcal{V}^* & \text{(Case 1)}, \\ \kappa p_0 + \epsilon\kappa\left[p_1 - \pi_0\phi_1(x, y=1)\right] & \text{(Case 2)}. \end{cases} \tag{3.34}$$

Thus there is no $\mathcal{O}(\epsilon)$ correction to the permeation flux for the case of constant outflow, *i.e.*, $\mathcal{V}_1 = 0$ in this case. However, for the pressure-dependent permeation flux, the leading-order outflow is proportional to the leading-order pressure difference across the membrane, and the $\mathcal{O}(\epsilon)$ outflow is related to the $\mathcal{O}(\epsilon)$ hydrodynamic pressure *and* the osmotic pressure.

3.4 Results

3.4.1 Leading-order velocities

Examining the $\mathcal{O}(1)$ velocity terms in the expansions (3.32) and (3.33), we find the leading-order velocity components $\boldsymbol{u_0} = (u_0, v_0)$,

$$u_0(x,y) = \frac{\mathrm{d}p_0}{\mathrm{d}x}\frac{(y^2-1)}{2}, \tag{3.35a}$$

$$v_0(x,y) = \frac{\mathrm{d}^2 p_0}{\mathrm{d}x^2}\frac{(3y-y^3)}{6}. \tag{3.35b}$$

Note that the axial velocity, u_0, depends quadratically on the transverse coordinate, y, and the transverse velocity, v_0, depends cubically on y. Similar channel velocities may be found in the literature (*e.g.*, see Hurwitz (1989) and Probstein (1989) for the case of a constant permeation flux). If the hydrodynamic pressure gradient, $\mathrm{d}p_0/\mathrm{d}x$, were constant, the leading-order velocities (3.35) would correspond precisely to Poiseuille flow. However, here we have the added interest that $\mathrm{d}p_0/\mathrm{d}x$ may be a function of x.

This means that, while the profile remains parabolic, its magnitude may vary due to the spatially varying hydrodynamic pressure gradient. This variation must be determined case by case by considering the leading-order flow through the channel wall, $\mathcal{V}_0$, given by the ODEs:

$$v_0(x,1) = \mathcal{V}_0 = \frac{1}{3}\frac{\mathrm{d}^2 p_0}{\mathrm{d}x^2} = \begin{cases} \mathcal{V}^* & \text{(Case 1)}, \\ \kappa p_0 & \text{(Case 2)}. \end{cases} \tag{3.36}$$

We note that, in solving for the leading-order hydrodynamic pressure p_0 from the ODEs in (3.36), the constraints of constant flux at the channel inlet (3.16e), and zero pressure at the outlet (3.16f) and outside the channel ($p^0_{\text{outer}} = 0$) are applied, which, for the leading-order problem, read as

$$\int_0^1 u_0 \,\mathrm{d}y = 1, \qquad \text{at } x = 0, \tag{3.37a}$$

$$p_0 = 0, \qquad \text{at } x = 1. \tag{3.37b}$$

In the following we consider each of these two cases for flow out of the the porous wall, in turn.

3.4.1.1 Case 1: Constant permeation flux

In the case of constant flow through the porous walls, $\mathcal{V}_0 \equiv \mathcal{V}^* = \text{constant}$, the ODE for the leading-order hydrodynamic pressure (3.36) with conditions (3.37) has solution

$$p_0 = 3(1-x)\left[1 - \frac{1}{2}\mathcal{V}^*(x+1)\right]. \tag{3.38}$$

This function decreases with $\mathcal{V}^*$ for all x, *i.e.*, the greater the permeation flux the lower the required hydrodynamic pressure to maintain a constant flux. The leading-order flow then reads

$$\boldsymbol{u_0} = (u_0, v_0) = \left(\frac{3}{2}(1-y^2) - \frac{3}{2}\mathcal{V}^* x(1-y^2), \frac{1}{2}\mathcal{V}^*(3y - y^3)\right), \tag{3.39}$$

from (3.35). The leading-order axial velocity $u_0 = u_0(x,y)$ and the transverse velocity $v_0 = v_0(y)$ are dependent on the magnitude of the flow through the walls. In the case of no permeation flux (impermeable walls), $\mathcal{V}^* = 0$, Eq. (3.39) reduces simply to Poiseuille flow.

There is a maximum allowable constant permeation flux, $\mathcal{V}^*_{\text{max}}$, for which there is a positive net axial flow at the end of the channel; in this limiting case, all the fluid

injected at the inlet passes through the porous walls. Exceeding this permeation flux results in *backflow* from the channel outlet into the channel. The value of $\mathcal{V}^*_{\max}$ is obtained by equating the influx of fluid with the flux through the channel walls, given by integrating the velocity v_0 (3.39) along the channel wall at $y = 1$, resulting in a maximum permeation flux of $\mathcal{V}^*_{\max} = 1$. As mentioned previously, another filtration process in which the flow is zero at the end of the channel (dead-end flow) is directflow filtration (Pearce, 2011).

3.4.1.2 Case 2: Pressure-dependent permeation flux

We now determine leading-order solutions for the velocities and pressure for a pressure-dependent permeation flux. When the permeation flux through the wall is proportional to the hydrodynamic pressure, p, and osmotic pressure, π, then at leading order only the hydrodynamic pressure is significant, $\mathcal{V}_0 = \kappa p_0$, as seen from Eq. (3.34). The leading-order transverse flow at $y = 1$ (3.36) gives an ODE for the leading-order hydrodynamic pressure

$$\frac{1}{3}\frac{\mathrm{d}^2 p_0}{\mathrm{d}x^2} = \kappa p_0. \tag{3.40}$$

This ODE, subject to the boundary conditions (3.37), has solution

$$p_0 = \sqrt{\frac{3}{\kappa}}\,\mathrm{sech}\sqrt{3\kappa}\,\sinh\left[\sqrt{3\kappa}(1-x)\right]. \tag{3.41}$$

From this equation, we observe that the pressure, p_0, decreases with κ for all x and, as is the case for uniform permeation flux, the greater the permeation flux through the channel walls, the lower the required hydrodynamic pressure to achieve a constant influx. Substituting (3.41) into (3.35) determines the leading-order velocity field, (u_0, v_0). We note that, as $\kappa \to 0$ (in the limit of impermeable walls), $p_0 \to 3(1-x)$, and we recover Poiseuille flow, as expected. The components of the leading-order velocity field are shown in Figure 3.2 for $\kappa = 1$. We observe that the leading-order axial velocity u_0 retains its parabolic profile along the channel though the amplitude decreases exponentially, because of the permeation of fluid through the channel walls. The leading-order transverse fluid velocity v_0, which has a cubic profile about $y = 0$, also decreases in magnitude along the channel. This indicates the tendency of the fluid to move towards the porous walls of the channel but with an exponentially decaying rate along the channel.

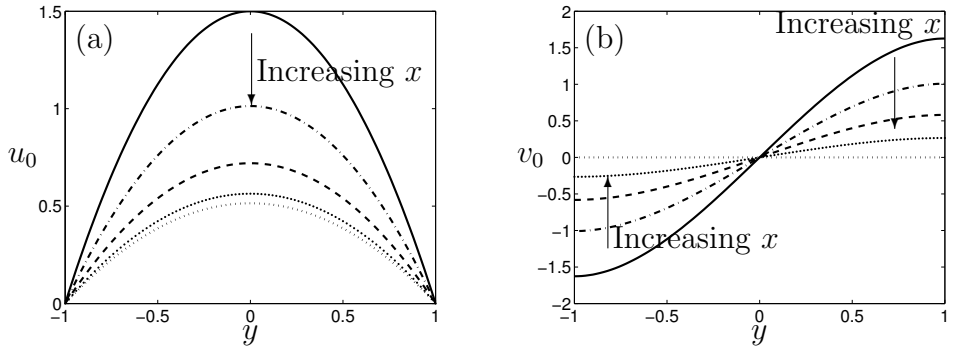

Figure 3.2: Profiles of the leading-order velocities for pressure-dependent permeation flux with $\kappa = 1$ so that $\mathcal{V}_0 = p_0$: (a) axial velocity, u_0, and (b) transverse velocity, v_0. In each, the profiles are shown at $x = 0$ (solid), $x = 0.25$ (dot-dashed), $x = 0.5$ (dashed), $x = 0.75$ (dotted) and $x = 1$ (skinny-dotted).

3.4.2 Numerical results for volume fraction

Having seen that the leading-order velocity fields and pressure gradient can be determined analytically in the two cases of interest, we now turn our attention to determining the volume fraction profile, ϕ_1. Recall that the advection–diffusion equation (3.29), with u_0 and v_0 given by our previous analysis, must be solved subject to the boundary conditions (3.30) and the Gaussian inlet particle distribution (3.31). We note that this initial condition does not satisfy the no-flux boundary condition (3.16d) and so there is a small transient over which this relaxes to a configuration that satisfies the boundary conditions. However, we choose to employ this inlet condition as it provides a simple expression that elucidates the effect of a non-uniform particle volume fraction distribution, and we do not expect the behaviour in the small transient to have an effect on the global system dynamics. This system is solved numerically, implementing a finite difference scheme in MATLAB (see Appendix A for details). As an illustrative example, Figure 3.3 depicts how an initial distribution in the channel develops downstream of the injection point, with $\sigma^2 = 0.05$, $\mathrm{Pe} = 3$, for the cases of: no permeation at the wall; constant permeation flux; and pressure-dependent permeation flux (with $\kappa = 1$).

For the case of an impermeable wall, $\mathcal{V}^* = 0$, we observe that the initial distribution spreads until it is essentially uniform across the width of the channel (Figure 3.3(a)). With permeation through the porous wall, particles still diffuse away from the centreline but now collect near the wall. This buildup of particles at the porous walls is known as concentration polarization (Song and Elimelech, 1995). In particular, for

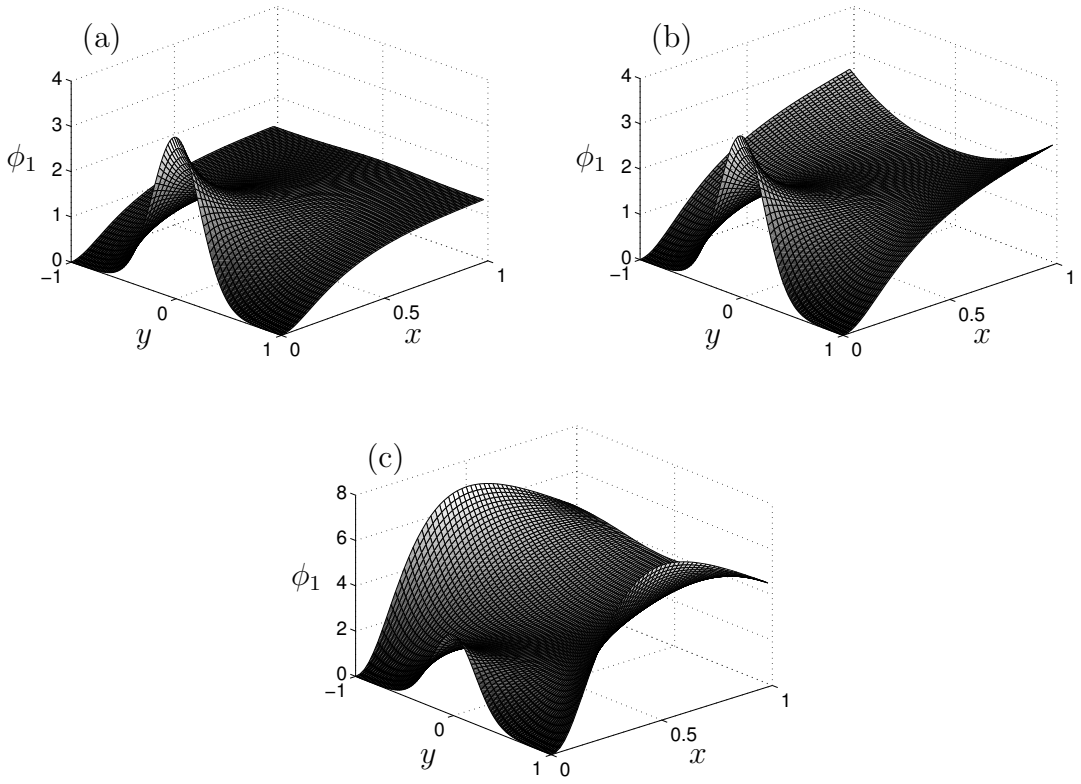

Figure 3.3: Profiles of the particle volume fraction ϕ_1 in the channel given by the solution to (3.29) with velocities (3.35). (a) No permeation, $\mathcal{V}^* = 0$, ϕ_1 tends to a uniform state in the channel, (b) constant permeation, $\mathcal{V}^* = 0.25$, with p_0 given by (3.38), and (c) pressure-dependent permeation with p_0 given by (3.41). In (b) and (c) permeation flux results in particles collecting at the boundaries. In all computations, $\mathrm{Pe} = 3$, $\sigma^2 = 0.05$, and for (c), $\kappa = 1$.

the case of constant permeation, the volume fraction of particles at the wall increases monotonically along the length of the channel (Figure 3.3(b)). We note that, since the particles are initially localized in the centre of the channel ($y = 0$) where the transverse velocity is low as in Equation (3.39), the transport of particles to the walls is slower than we would expect if the particles were injected with a uniform distribution. When permeation is proportional to the pressure, the volume fraction at the walls is greatest about half way along the channel, as in Figure 3.3(c). This is as a result of the transverse flow, which becomes smaller near the end of the channel after which point diffusion acts to move particles away from the wall.

3.4.3 Order-ϵ velocities

Having computed the leading-order velocity components, u_0 and v_0, and volume-fraction distribution ϕ_1, we are now in a position to compute the perturbation to the fluid flow caused by the presence of particles, *i.e.*, the $\mathcal{O}(\epsilon)$ corrections to the fluid velocity. From the axial and transverse velocities, (3.32) and (3.33) respectively, we have

$$u_1(x,y) = \frac{\mathrm{d}p_1}{\mathrm{d}x}\,\frac{(y^2-1)}{2} + \frac{\mathrm{d}p_0}{\mathrm{d}x}\int_y^1 \frac{5}{2}\,\tilde{y}\phi_1(x,\tilde{y})\,\mathrm{d}\tilde{y}, \tag{3.42a}$$

$$v_1(x,y) = \frac{\partial}{\partial x}\left\{\frac{\mathrm{d}p_1}{\mathrm{d}x}\frac{(3y-y^3)}{6} - \frac{\mathrm{d}p_0}{\mathrm{d}x}\left[y\int_y^1 \frac{5}{2}\,\tilde{y}\phi_1(x,\tilde{y})\,\mathrm{d}\tilde{y} + \int_0^y \frac{5}{2}\,\tilde{y}^2\,\phi_1(x,\tilde{y})\,\mathrm{d}\tilde{y}\right]\right\}. \tag{3.42b}$$

We note that a perturbation to the velocity, u_1, in principle affects the flux of fluid into the channel. However, the condition of constant fluid influx (3.16e), considering (3.37a), demands that,

$$\int_0^1 u_1(0,y)\,\mathrm{d}y = 0. \tag{3.43}$$

To ensure that this condition is satisfied we must solve for a perturbation to the hydrodynamic pressure at the inlet $x = 0$,

$$\mathcal{P} := p_1(0) \neq 0. \tag{3.44}$$

The value of $\mathcal{P}$ indicates how much harder we must push the liquid in the presence of particles to obtain the same fluid influx as would be obtained for a configuration in the absence of particles. The hydrodynamic pressure perturbation, p_1, may be found

from the perturbed permeation flux, $\mathcal{V}_1$, out of the channel wall using the transverse velocity (3.33) at $y = 1$,

$$\frac{\mathrm{d}}{\mathrm{d}x}\left\{\frac{1}{3}\frac{\mathrm{d}p_1}{\mathrm{d}x} - \frac{\mathrm{d}p_0}{\mathrm{d}x}\int_0^1 \frac{5}{2}\,\tilde{y}^2\,\phi_1(x,\tilde{y})\,\mathrm{d}\tilde{y}\right\} = \mathcal{V}_1. \tag{3.45}$$

Here $\mathcal{V}_1 = 0$ for the case of constant permeation flux through the channel walls and $\mathcal{V}_1 = \kappa\,(p_1 - \pi_0\phi_1)$ when the permeation flux is pressure-dependent, see Eq. (3.34). For each case we may substitute for p_0 in equation (3.45) and solve subject to

$$p_1(0) = \mathcal{P}, \qquad p_1(1) = 0, \tag{3.46a,b}$$

and the flux condition (3.43) is applied to find $\mathcal{P}$.

By considering the initial volume fraction distribution given by (3.18) we may determine the dependence of $\mathcal{P}$ on the width of the distribution, σ. This gives us insight into the pressures required to transport a fixed flux of fluid containing a given distribution of particles through the channel for the two distinct cases of permeation flux through the channel walls, $\mathcal{V}_1$.

3.4.3.1 Case 1: Constant permeation flux

When there is constant flow through the boundary, $\mathcal{V} = \mathcal{V}^*$, and so, at order ϵ, $\mathcal{V}_1 = 0$. In this case, the ODE (3.45) to determine the order-ϵ pressure, p_1, becomes

$$\frac{1}{3}\frac{\mathrm{d}^2p_1}{\mathrm{d}x^2} - \frac{\mathrm{d}}{\mathrm{d}x}\left\{\frac{\mathrm{d}p_0}{\mathrm{d}x}\int_0^1 \frac{5}{2}\,\tilde{y}^2\phi_1(x,\tilde{y})\,\mathrm{d}\tilde{y}\right\} = 0, \tag{3.47}$$

which has solution

$$\begin{aligned} p_1 =& \mathcal{P}(1-x) + 3\int_0^x \left[\frac{\mathrm{d}p_0(\tilde{x})}{\mathrm{d}\tilde{x}}\int_0^1 \frac{5}{2}\,\tilde{y}^2\phi_1(\tilde{x},\tilde{y})\,\mathrm{d}\tilde{y}\right]\,\mathrm{d}\tilde{x} \\ &- 3x\int_0^1 \left[\frac{\mathrm{d}p_0(\tilde{x})}{\mathrm{d}\tilde{x}}\int_0^1 \frac{5}{2}\,\tilde{y}^2\phi_1(\tilde{x},\tilde{y})\,\mathrm{d}\tilde{y}\right]\,\mathrm{d}\tilde{x}, \end{aligned} \tag{3.48}$$

where we have applied the boundary conditions (3.46). Upon imposing the flux condition (3.43), the input pressure perturbation, $\mathcal{P}$, is related to the particle volume fraction through

$$\begin{aligned} \mathcal{P} =& \frac{15}{2}\left\{\frac{\mathrm{d}p_0(0)}{\mathrm{d}x}\left(\int_0^1 \tilde{y}^2\phi_1(0,\tilde{y})\,\mathrm{d}\tilde{y} - \int_0^1\int_{\tilde{y}}^1 y'\phi_1(0,y')\,\mathrm{d}y'\,\mathrm{d}\tilde{y}\right)\right. \\ &\left. - \int_0^1 \left[\frac{\mathrm{d}p_0(\tilde{x})}{\mathrm{d}\tilde{x}}\int_0^1 \tilde{y}^2\phi_1(\tilde{x},\tilde{y})\,\mathrm{d}\tilde{y}\right]\,\mathrm{d}\tilde{x}\right\}. \end{aligned} \tag{3.49}$$

We note that this relationship is non-local, depending on the behaviour of the particles along the entire length of the channel. Substituting for $\mathcal{P}$ into (3.48) provides the pressure perturbation, p_1. Along with ϕ_1, this allows us to calculate the perturbations to the velocity field u_1 and v_1 using the order-ϵ velocities (3.42).

In Figure 3.4(a) we illustrate the pressure for the profile ϕ_1 with $\sigma^2 = 0.05$ and $\mathrm{Pe} = 3$, as shown in Figure 3.3(b). As expected, the pressure perturbation is positive for all x: the hydrodynamic pressure in the channel required to maintain the same fluid influx as the case in which no particles are present is increased as a result of the increase in viscosity. The perturbation to the axial velocity, u_1, is shown in Figure 3.4(b). Recall that the leading-order axial velocity here is a Poiseuille profile, decreasing in magnitude as we move down the channel. We see that, in regions of high particle volume fraction, u_1 is negative and so the total axial velocity, u, is decreased by the presence of particles, while in regions of lower particle volume fraction u_1 is positive and so the total axial velocity is increased (*cf.* Figure 3.3(b)). By conservation of mass, (3.14a), a perturbation in the axial velocity results in a perturbation in the transverse velocity, v. There is an accumulation of particles near the walls, *i.e.*, the region of high volume fraction moves to the walls. As a result, the location of the position of maximum retardation in the transverse direction (caused by the perturbation to the flow) moves towards the walls as we move down the channel (Figure 3.4(b)). Hence, while the perturbed transverse velocity, v_1 (3.42b), initially increases, since there is no perturbed permeation through the walls, *i.e.*, $v_1(x, 1) = 0$, the fluid must ultimately be transported back towards the centre of the channel; this is signified by a change in sign of v_1 further along the channel, as seen in Figure 3.4(c).

The relationship between the pressure perturbation at the inlet, $\mathcal{P}$, and the width of the particle distribution, σ, for various constant permeation fluxes, $\mathcal{V}^*$, is shown in Figure 3.5. Since the addition of particles increases the viscosity of the fluid, and the hydrodynamic pressure gradient is related to the viscosity through the momentum equation (3.14b), we expect that a greater hydrodynamic pressure will be required to maintain a constant influx. However, we find that that there is a *critical value* of σ that maximizes the additional pressure, $\mathcal{P}_{\mathrm{pess}}$. This means, surprisingly, that there is an inlet particle distribution width that requires the largest additional (perturbed) pressure, while the pressure perturbation increases as the permeation flux increases (Figure 3.6(a)). The pessimal value of the distribution width, σ_{pess}, decreases linearly with permeation flux, $\mathcal{V}^*$ (Figure 3.6(b)). The values of σ around this pessimal pressure perturbation reflect inlet distributions that have significant volume fraction

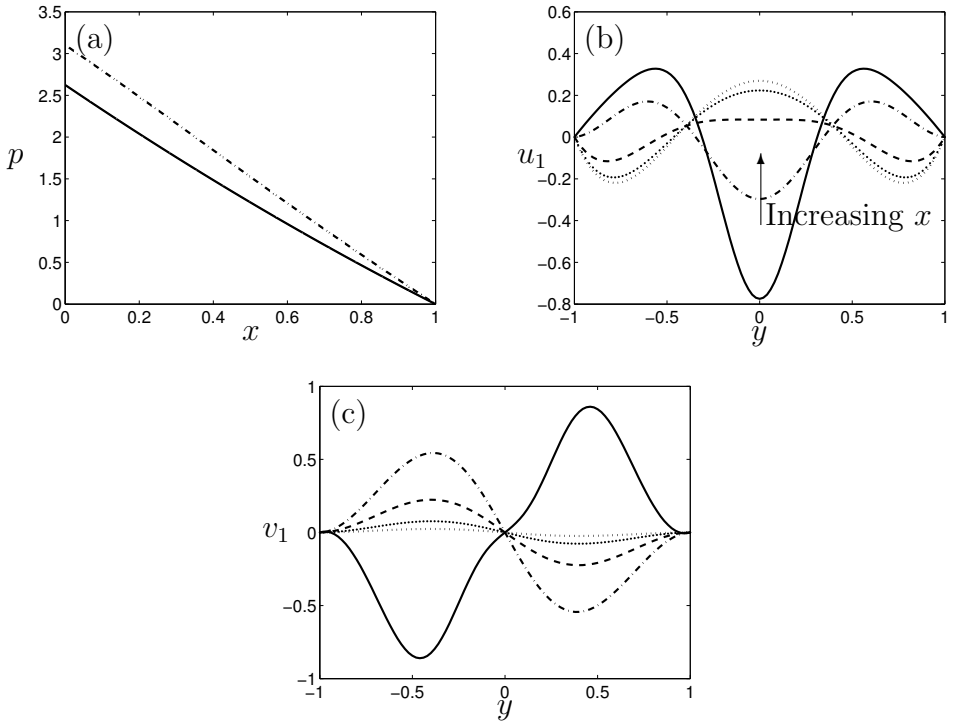

Figure 3.4: Pressure and order-ϵ velocity profiles given by (3.42) for the case of constant permeation flux through the channel walls, $\mathcal{V}^* = 0.25$. (a) The hydrodynamic pressure, $p = p_0 + \epsilon p_1$, for $\epsilon = 0.05$ (dot-dashed) is plotted with the leading-order term, p_0 (solid). (b) Profile of the order-ϵ axial velocity perturbation, u_1. (c) Profile of order-ϵ transverse velocity perturbation, v_1. In (b) and (c) $x = 0$ (solid), $x = 0.25$ (dot-dashed), $x = 0.5$ (dashed), $x = 0.75$ (dotted) and $x = 1$ (skinny-dotted). In all computations, Pe $= 3$, $\sigma^2 = 0.05$.

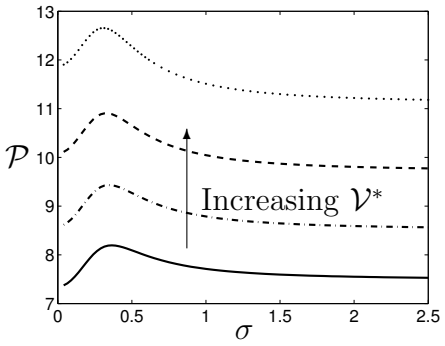

Figure 3.5: Variation of the pressure perturbation parameter $\mathcal{P}$ given by (3.49) with σ for the case of constant permeation flux: $\mathcal{V}^* = 0$ (solid), $\mathcal{V}^* = 0.2$ (dot-dashed), $\mathcal{V}^* = 0.4$ (dashed) and $\mathcal{V}^* = 0.6$ (dotted). As σ increases, $\mathcal{P}$ tends to a constant, with a non-trivial behaviour showing a critical value of σ that maximizes $\mathcal{P}$. Note that $\mathcal{P} \to 15/2$ as $\sigma \to \infty$ when $\mathcal{V}^* = 0$. In the computations, Pe $= 3$.

gradients across the channel. Hence the viscosity has a significant gradient in the channel, globally, and thus the particles have a greater effect on the resulting flow. It is found that both 'thinner' and 'fatter' volume fraction distributions require less additional pressure to maintain a constant fluid influx: for larger values of σ, the volume fraction distribution is more uniform and so there is less variation to the flow due to the concentration-dependent viscosity, whereas for smaller values of σ the volume fraction is largely confined to a small region that does not significantly affect the viscosity for large regions of the channel.

In the case of no flow through the porous walls (impermeable walls, $\mathcal{V}^* = 0$) there is an analytic asymptote for $\mathcal{P}$ as $\sigma \to \infty$, namely $\mathcal{P} \to 15/2$ (see Figure 3.5, solid line). This may be calculated using the expression for p_0 from (3.38) and the equation for $\mathcal{P}$ (3.49), since in the limit $\sigma \to \infty$, $\phi_1 \equiv 1$. However, in the case of porous walls, concentration polarization along the channel walls results in ϕ_1 no longer being spatially independent along the channel. This precludes the analytical calculation of the asymptote, $\mathcal{P}_{\text{asym}}$, that is observed numerically in the limit $\sigma \to \infty$, (Figure 3.5). The value of $\mathcal{P}_{\text{asym}}$ increases with the magnitude of the permeation flux, with $\mathcal{P}_{\text{asym}} < \mathcal{P}_{\text{pess}}$ as expected (Figure 3.6(a)).

Although the leading-order hydrodynamic pressure, p_0, required to maintain a constant influx decreases with increasing permeation flux, it is observed in Figure 3.5 that the $\mathcal{O}(\epsilon)$ hydrodynamic pressure, $\mathcal{P}$, increases with increasing permeation flux. This arises as a result of there being no $\mathcal{O}(\epsilon)$ permeation flux in this case. Particles aggregate at the walls because of the leading-order permeation flux; by increasing the

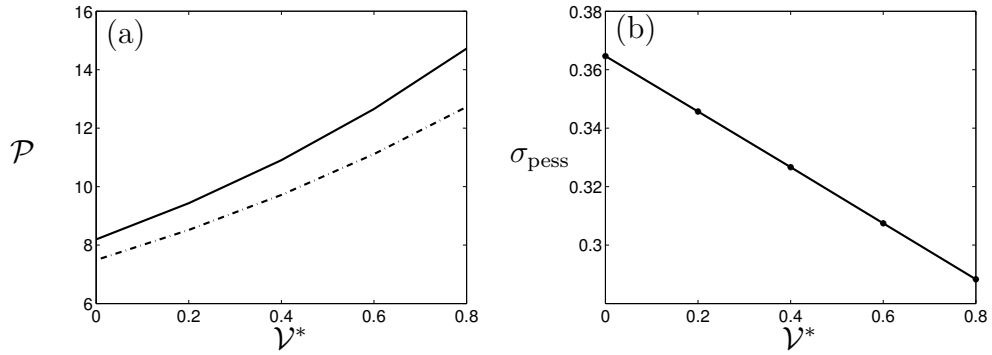

Figure 3.6: (a) The pessimal pressure perturbation, $\mathcal{P}_{\text{pess}}$ (solid), and the asymptotic pressure perturbation, $\mathcal{P}_{\text{asym}}$ (dot-dashed), as $\sigma \to \infty$, for the case of a constant permeation flux $\mathcal{V} = \mathcal{V}^*$, and (b) the distribution width resulting in the pessimal pressure, σ_{pess}. In the computations, Pe = 3.

permeation flux, $\mathcal{V}^*$, this increases the accumulation of particles at the wall, and thus the local viscosity, so more pressure is required to advect these particles along the channel.

3.4.3.2 Case 2: Pressure-dependent permeation flux

When there is a pressure-dependent flow through the porous channel walls, the $\mathcal{O}(\epsilon)$ permeation flux through the walls is given by $\mathcal{V}_1 = \kappa\,[p_1 - \pi_0\phi_1(x, y = 1)]$. The ODE for the hydrodynamic pressure (3.45), with boundary conditions (3.46), then becomes

$$\frac{\mathrm{d}^2 p_1}{\mathrm{d}x^2} - 3\kappa p_1 = 3g(x), \tag{3.50a}$$

$$p_1(0) = \mathcal{P}, \tag{3.50b}$$

$$p_1(1) = 0, \tag{3.50c}$$

where

$$g(x) := \frac{\mathrm{d}}{\mathrm{d}x}\left\{\frac{\mathrm{d}p_0}{\mathrm{d}x}\int_0^1 \frac{5}{2}\,\tilde{y}^2\phi_1(x,\tilde{y})\,\mathrm{d}\tilde{y}\right\} - \kappa\pi_0\phi_1(x,1). \tag{3.51}$$

The homogeneous adjoint problem to (3.50) only permits the trivial zero solution; the Fredholm Alternative Theorem (Keener, 2000) then implies that the ODE with boundary conditions given in (3.50) has a unique solution. This solution can be found

using the method of variation of parameters, giving

$$\begin{aligned} p_1 =& \mathcal{P}\cosh\left(\sqrt{3\kappa}x\right) + 3\int_0^x \left[\cosh\left(\sqrt{3\kappa}[x-\tilde{x}]\right)\frac{\mathrm{d}p_0(\tilde{x})}{\mathrm{d}\tilde{x}}\int_0^1 \frac{5}{2}\,\tilde{y}^2\phi_1(\tilde{x},\tilde{y})\,\mathrm{d}\tilde{y}\right]\,\mathrm{d}\tilde{x} \\ &+ \sqrt{\frac{3}{\kappa}}\frac{\mathrm{d}p_0(0)}{\mathrm{d}x}\sinh\left(\sqrt{3\kappa}x\right)\left(\int_0^1\int_{\tilde{y}}^1 \frac{5}{2}\,y'\phi_1(0,y')\,\mathrm{d}y'\,\mathrm{d}\tilde{y} - \int_0^1 \frac{5}{2}\,\tilde{y}^2\phi_1(0,\tilde{y})\,\mathrm{d}\tilde{y}\right) \\ &- \sqrt{3\kappa}\,\pi_0\int_0^x \phi_1(\tilde{x},1)\sinh\left(\sqrt{3\kappa}[x-\tilde{x}]\right)\,\mathrm{d}\tilde{x}, \end{aligned} \tag{3.52}$$

where we have imposed the boundary condition (3.50b) and flux condition (3.43). Imposing the final boundary condition (3.50c), we determine the relationship between the additional pressure, $\mathcal{P}$, and the particle distribution ϕ_1

$$\begin{aligned} \mathcal{P} =& \sqrt{\frac{3}{\kappa}}\tanh\sqrt{3\kappa}\,\frac{\mathrm{d}p_0(0)}{\mathrm{d}x}\left(\int_0^1 \frac{5}{2}\,\tilde{y}^2\phi_1(0,\tilde{y})\,\mathrm{d}\tilde{y} - \int_0^1\int_{\tilde{y}}^1 \frac{5}{2}\,y'\phi_1(0,y')\,\mathrm{d}y'\,\mathrm{d}\tilde{y}\right) \\ &- 3\,\mathrm{sech}\sqrt{3\kappa}\int_0^1 \left[\cosh\left(\sqrt{3\kappa}[1-\tilde{x}]\right)\frac{\mathrm{d}p_0(\tilde{x})}{\mathrm{d}\tilde{x}}\int_0^1 \frac{5}{2}\,\tilde{y}^2\phi_1(\tilde{x},\tilde{y})\,\mathrm{d}\tilde{y}\right]\,\mathrm{d}\tilde{x} \\ &+ \sqrt{3\kappa}\,\pi_0\,\mathrm{sech}\sqrt{3\kappa}\int_0^1 \phi_1\left(\tilde{x},1\right)\sinh\left(\sqrt{3\kappa}[1-\tilde{x}]\right)\,\mathrm{d}\tilde{x}. \end{aligned} \tag{3.53}$$

Given ϕ_1 we may solve (3.53) for $\mathcal{P}$. The pressure perturbation, p_1, and the $\mathcal{O}(\epsilon)$ velocities u_1 and v_1 follow immediately from (3.52) and (3.42).

We illustrate the resulting behaviour by considering the injection of particles with distribution width $\sigma = \sqrt{0.05}$, so that ϕ_1 is as shown in Figure 3.3(c). The reference osmotic pressure is taken to be $\pi_0 = 0.1$ here. We note that, while the quantitative results are affected by changes in π_0, the qualitative features are unaffected and as such we choose to hold the parameter constant in the results presented here. The behaviour of p_0 and p_1 and the osmotic pressure are then as shown in Figure 3.7(a). We observe that the hydrodynamic pressure perturbation, p_1, is positive corresponding to an increase in the total hydrodynamic pressure in the channel. However, there is an axial position beyond which the osmotic pressure, $\Delta\pi > 0$ (3.25), exceeds the hydrodynamic pressure perturbation. This is unavoidable since $p_1 = 0$ at $x = 1$ (3.16f), and has an impact on the permeation flux observed.

The flow perturbation u_1 is shown in Figure 3.7(b). Near the entrance to the channel, u_1 is negative in the centre of the channel where there is a high volume fraction so the total axial flow is lower than the leading-order (particle-free) flow; in regions of low particle volume fraction, u_1 is positive and so the total axial flow is greater than in the absence of particles, similar to the case of constant permeation flux. However, further down the channel u_1 is negative across the entire channel. This is due to the

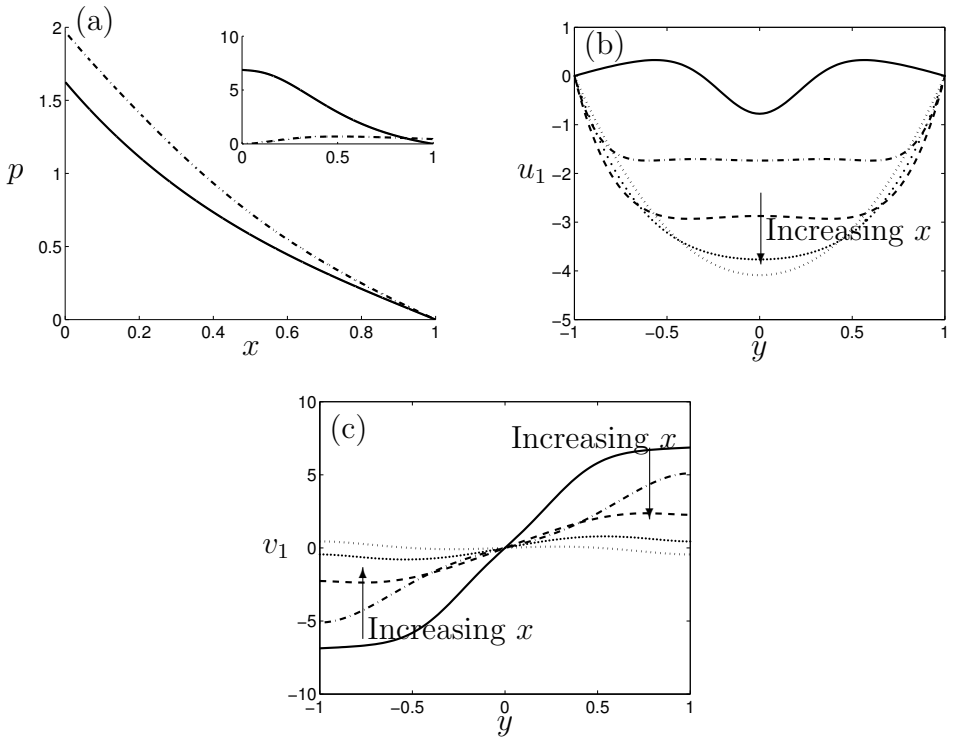

Figure 3.7: Pressure and order-ϵ velocity profiles given by (3.42) for the case of pressure-dependent permeation flux through the channel walls, $\mathcal{V}_1 = \kappa\,[p_1 - \pi_0\phi_1(x,1)]$. (a) The hydrodynamic pressure, $p = p_0 + \epsilon p_1$, for $\epsilon = 0.05$ (dot-dashed) is plotted with the leading-order term, p_0 (solid). The inset shows the pressure perturbation, p_1 (solid), and the osmotic pressure (dot-dashed) in the channel. (b) Profile of order-ϵ axial velocity perturbation, u_1. (c) Profile of order-ϵ transverse velocity perturbation, v_1, at $x = 0$ (solid). In (b) and (c) $x = 0.25$ (dot-dashed), $x = 0.5$ (dashed), $x = 0.75$ (dotted) and $x = 1$ (skinny-dotted). In all computations, Pe $= 3$, $\sigma^2 = 0.05$ and $\pi_0 = 0.1$.

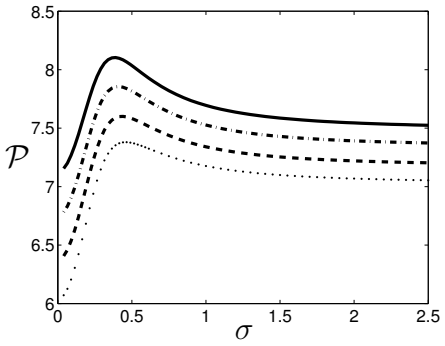

Figure 3.8: Variation of the pressure perturbation parameter, $\mathcal{P}$, given by (3.53) with σ for the case of pressure-dependent permeation flux through the channel walls, $\mathcal{V}_1 = \kappa\,[p_1 - \pi_0\phi_1(x,1)]$ with $\kappa = 0.25$ (solid), $\kappa = 0.5$ (dot-dashed), $\kappa = 0.75$ (dashed) and $\kappa = 1$ (dotted). As σ increases $\mathcal{P}$ tends to a constant, again with a non-trivial behaviour showing a critical σ at which $\mathcal{P}$ is maximized. In the computations, $\mathrm{Pe} = 3$ and $\pi_0 = 0.1$.

order-ϵ transverse permeation flux, which causes fluid to be removed from the channel. In this case, the perturbation to the transverse velocity, v_1, (see Figure 3.7(c)) increases the total transverse velocity towards the walls over the entire length of the channel. This induces an additional fluid flux through the channel walls which also advects particles towards the walls, increasing the osmotic pressure due to concentration polarization up to the point where it exceeds the hydrodynamic pressure (see Figure 3.7(a)). This excess osmotic pressure results in a net inward flow (classic osmosis), which is undesirable in filtration because it reduces the amount of pure water that is produced by filtration. Hence, near the end of the channel this osmotic inflow is unavoidable, when $p_{\mathrm{outer}} = 0$. However, since the particles in the channel do not affect the leading-order flow, there is no osmotic inflow of fluid at leading order, and the outflow through the channel walls tends to zero at the end of the channel (since $p = 0$ at $x = 1$).

The relationship between $\mathcal{P}$ and σ is shown in Figure 3.8 for different constants of proportionality, κ, for the pressure-dependent permeation flux. A similar functional relationship to Case 1 for constant permeation flux is observed, specifically the existence of a pessimal distribution of particles. As for Case 1 when $\mathcal{V}^* \neq 0$ there is no simple analytical asymptote as $\sigma \to \infty$. The value of the distribution width, σ_{pess}, resulting in the pessimal pressure perturbation increases linearly with κ (Figure 3.9(a)). However, the pessimal pressure perturbation, $\mathcal{P}_{\mathrm{pess}}$, is observed to decrease with κ, in an approximately linear fashion (provided κ exceeds a certain value, $\kappa \approx 0.3$) as in

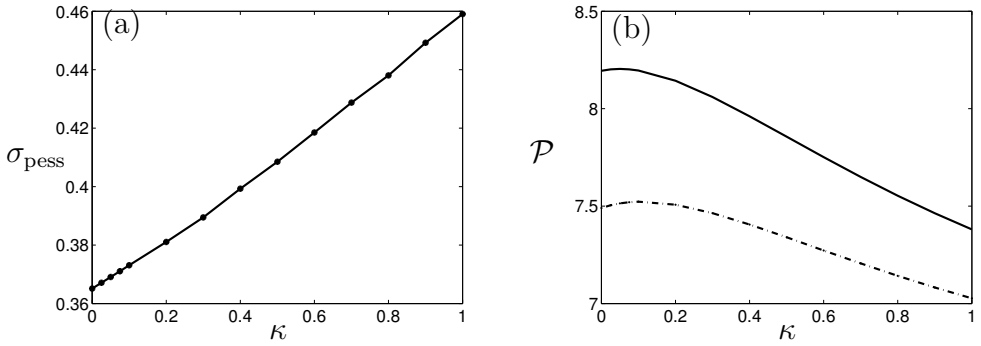

Figure 3.9: (a) The distribution width resulting the the pessimal pressure, σ_{pess}, and (b) the pessimal pressure perturbation, $\mathcal{P}_{\text{pess}}$ (solid), and the asymptotic pressure perturbation, $\mathcal{P}_{\text{asym}}$ (dot-dashed), as $\sigma \to \infty$, for different channel wall permeabilities, κ. In the computations, $\text{Pe} = 3$ and $\pi_0 = 0.1$.

Figure 3.9(b). Similarly to Case 1, the leading-order hydrodynamic pressure in the channel (3.41) is reduced by the permeation flux. However, this case differs in that the asymptote for $\mathcal{P}$, $\mathcal{P}_{\text{asym}}$, decreases as $\sigma \to \infty$ as the permeation flux through the channel walls increases (via an increase in wall permeability in κ). This decrease is approximately linear for $\kappa \gtrsim 0.3$, as in Figure 3.9(b). Hence, less pressure is required to ensure a constant influx of fluid for higher wall permeabilities when particles are present in the channel. This result is a consequence of the osmotic component of $\mathcal{P}$, which becomes increasingly negative with κ and so causes the reduction in the pressure perturbation. This suggests that the component of the channel for which there is a net fluid outflow, and which acts as an effective filter, is shorter because more fluid is lost through the walls earlier in the channel. This reduces the hydrodynamic pressure, p, required to maintain a given fluid influx.

3.4.4 Total Permeate

A quantity of particular interest is the total flux of fluid that flows out through the porous walls, F. This is given by the integral of the transverse velocity along the wall,

$$\begin{aligned} F &= 2\int_0^1 v(x,1)\,\mathrm{d}x, \\ &= 2\int_0^1 \Big(v_0(x,1) + \epsilon v_1(x,1)\Big)\,\mathrm{d}x = F_0 + \epsilon F_1. \end{aligned} \tag{3.54}$$

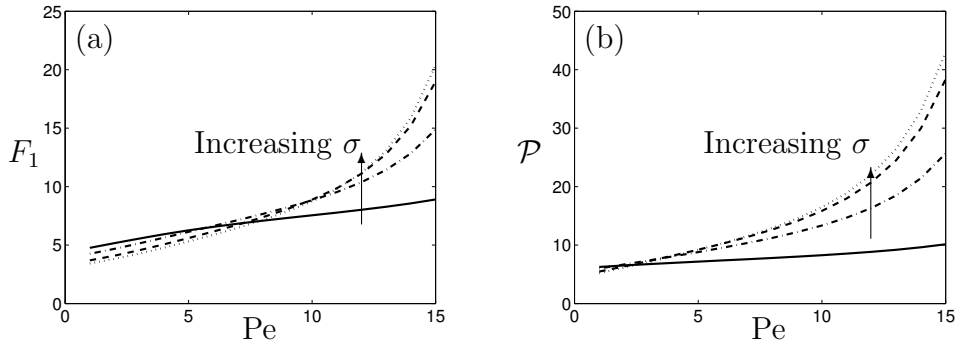

Figure 3.10: (a) Order-ϵ flux through the channel walls as a function of Péclet number, Pe. (b) Pressure perturbation parameter, $\mathcal{P}$, against Péclet number. In each, we have $\sigma = 0.2$ (solid), $\sigma = 0.4$ (dot-dashed), $\sigma = 0.75$ (dashed), and $\sigma = 1.5$ (skinny-dotted). In the computations, $\kappa = 1$ and $\pi_0 = 0.1$.

(Here the factor of two is due to the symmetry of the system about $y = 0$.) This is easily calculated for the constant permeation-flux case since here $\mathcal{V} = \mathcal{V}^*$ for all $0 \leq x \leq 1$, and so the total fluid flux passing through the porous walls is simply $F = 2\mathcal{V}^*$.

For the pressure-dependent permeation flux case, the leading-order total flux may also be calculated analytically as $F_0 = 2\left(1 - \operatorname{sech}\sqrt{3\kappa}\right)$, an increasing function of κ as would be expected. However, the order-ϵ term must be calculated numerically. The interesting feature of the order-ϵ term, F_1, is that it is dependent on the particles in the flow. In addition, there is an osmotic inflow of fluid towards the end of the channel that reduces the net permeate flux. Consequently, both the inlet distribution width, σ, and the Péclet number, Pe, influence the result (Figure 3.10(a)). For lower Péclet numbers, more localized distributions (lower values of σ) result in larger fluxes, but for larger Péclet numbers, more spatially uniform distributions (larger values of σ) produce larger fluxes. Analysing the pressure perturbation parameter, $\mathcal{P}$, with Péclet number (Figure 3.10(b)), we see that, as the Péclet number is increased, a greater pressure is required to maintain a constant influx. Since an increase in Péclet number also increases the permeation flux, this suggests a direct correspondence between hydrodynamic pressure and permeation flux, as one would expect.

3.5 Pressure Outside the Channel

In the previous section we concluded that it is an inevitable consequence of the osmotic pressure that an $\mathcal{O}(\epsilon)$ flux of fluid *enters* the channel through its walls in a pressure-

dependent permeation flux. In water filtration, this effect, at any order, is undesirable. Here we consider a modified setup that eliminates this inflow by setting the pressure outside the channel, p_{outer}, to be a non-zero constant while holding $p_{\text{end}} = 0$. This can be achieved by pressurizing the bath of clean filtered fluid outside the membrane. The effective total transmembrane pressure may then be written as

$$\Delta p - \Delta\pi = p_0(x) - p_{\text{outer}} + \epsilon\left[p_1(x) - \pi_0\phi_1(x,1)\right]. \tag{3.55}$$

We retain, without loss of generality, the condition that the fluid pressure, p, is zero at the end of the channel. By choosing p_{outer} appropriately we can ensure that the effective total transmembrane pressure remains non-negative over the entire length of the channel.

Osmotic pressure is again negligible in the leading-order problem and the leading-order permeation flux is given here by $\mathcal{V}_0 = \kappa(p_0 - p_{\text{outer}})$ (*cf.* equation (3.34)). The leading-order transverse flow at $y = 1$ (3.36) gives an ODE for the leading-order pressure

$$\frac{1}{3}\frac{\mathrm{d}^2 p_0}{\mathrm{d}x^2} = \kappa(p_0 - p_{\text{outer}}), \tag{3.56}$$

which on application of boundary conditions (3.37) yields

$$p_0(x) = p_{\text{outer}}\left[1 - \operatorname{sech}\sqrt{3\kappa}\,\cosh\left(\sqrt{3\kappa}x\right)\right] + \sqrt{\frac{3}{\kappa}}\operatorname{sech}\sqrt{3\kappa}\,\sinh\left(\sqrt{3\kappa}\,[1-x]\right). \tag{3.57}$$

The leading-order velocities (u_0, v_0) may be calculated by substituting (3.57) into equation (3.35). These, in turn, may be used to calculate the volume fraction of particles, ϕ_1, in the channel by solving the advection–diffusion equation (3.29) with boundary conditions (3.30) and inlet condition (3.31).

The hydrodynamic pressure (3.57) increases with p_{outer} as smaller transmembrane pressure differences reduce the permeation flux: with more fluid remaining in the channel, a higher hydrodynamic pressure is required to maintain a constant influx. However, since the permeation flux is reduced, concentration polarization is reduced. But, with $p = 0$ at $x = 1$, if $p_{\text{outer}} > 0$ there is a point in the channel at which $p < p_{\text{outer}}$ and so there is an induced leading-order permeation influx from the outside into the channel through the channel walls. This inflow does not occur at leading order with $p_{\text{outer}} = 0$. Hence, a positive outer pressure decreases particle collection at the wall but results in a backflow.

Conversely, if $p_{\text{outer}} < 0$ then the pressure difference across the membrane is increased, increasing the permeation flux which in turn decreases the required hydrodynamic pressure, (3.57). Here we do not have an influx of fluid into the channel at any position at leading order if p_{outer} is larger in magnitude than the osmotic pressure (order-ϵ). However, since the permeation flux is increased, there is a greater concentration polarization effect. Hence, a negative outer pressure ensures a number of outcomes. Firstly, no fluid re-enters into the channel from the walls (backflow). From a water-filtration perspective this means that none of the filtered water re-enters the channel. Secondly, we increase the permeation flux at the walls resulting in more fluid being filtered. The penalty in doing so is the extra energy required to generate the negative external pressure and also the increase in particle collection at the walls.

The leading-order total permeate, F_0, for a non-zero p_{outer}, reads

$$F_0 = 2\left(1 - \operatorname{sech}\sqrt{3\kappa}\right) - 2\sqrt{\frac{\kappa}{3}}\, p_{\text{outer}} \tanh\sqrt{3\kappa}, \tag{3.58}$$

using (3.54). We note that F_0 is a decreasing function of p_{outer} for all κ, and the critical point ($F_0 = 0$) beyond which there is a net influx occurs when

$$p_{\text{outer}} = \sqrt{\frac{3}{\kappa}}\ \tanh\frac{\sqrt{3\kappa}}{2}. \tag{3.59}$$

Furthermore, the order-ϵ total permeate, F_1, is a decreasing function of the outside pressure for all Pe and σ.

3.5.1 Order-ϵ outer pressure

We wish to choose the outer pressure to avoid any re-entry of fluid into the channel through the walls. In the previous section we saw that this might be achieved by using a sufficiently large negative outer pressure. However, we also want to reduce the energy required to generate this additional pressure, so it is the 'optimum' outer pressure that is of interest. Since re-entry is an order-ϵ effect due to the osmotic pressure, we assume that p_{outer} is $\mathcal{O}(\epsilon)$. Now the leading-order pressure is given by equation (3.41) and F_0 does not depend on p_{outer} and remains as in the case of $p_{\text{outer}} = 0$, that is, $F_0 = 2\left(1 - \operatorname{sech}\sqrt{3\kappa}\right)$. Also, since F_0 differs between the cases of an outer pressure and no outer pressure, a better comparison of how the particles affect the flow is to consider an outer pressure that is of order ϵ.

As the leading-order problem remains unchanged, and the re-entry is a result of the osmotic pressure exceeding the hydrodynamic pressure near the exit of the channel,

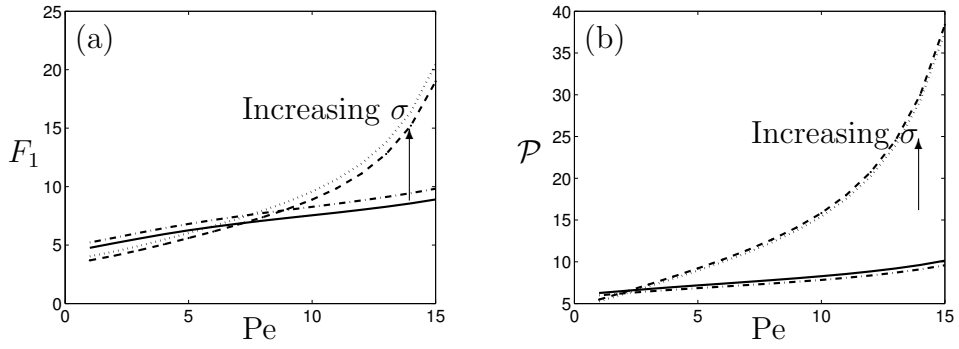

Figure 3.11: (a) Order-ϵ flux through the channel walls as a function of Péclet number, Pe. We see that the order-ϵ outer pressure increases the fluid flux. (b) Pressure perturbation parameter, $\mathcal{P}$, as a function of Péclet number. We see that the order-ϵ outer pressure decreases the pressure perturbation parameter. In each we take zero outer pressure and order-ϵ outer pressure for $\sigma = 0.2$ (solid and dot-dashed respectively) and $\sigma = 0.75$ (dashed and skinny-dotted, respectively). In all computations, $\kappa = 1$ and $\pi_0 = 0.1$.

we take p_{outer} to be equal and opposite to the osmotic pressure at the exit of the channel, that is

$$p_{\text{outer}} = -\epsilon\pi_0\phi_1(1,1). \tag{3.60}$$

The transmembrane pressure difference now reads

$$\Delta p - \Delta\pi = p_0(x) + \epsilon\left\{p_1(x) - \pi_0[\phi_1(x,1) - \phi_1(1,1)]\right\}. \tag{3.61}$$

This leads to a modification to the $\mathcal{O}(\epsilon)$ pressure given by equation (3.52) and the pressure perturbation given by equation (3.53). In this case the terms $\phi_1(\tilde{x},1)$ in the final term of each equation are replaced with $\phi_1(\tilde{x},1) - \phi_1(1,1)$.

The choice of outer pressure that negates the osmotic effect does indeed prevent any influx of fluid from outside the channel through the walls, with transverse velocity giving a permeation flux out of the channel at each point along the wall. This results in a greater $\mathcal{O}(\epsilon)$ permeate flux F_1 as seen in Figure 3.11(a) as well as a reduction in the pressure perturbation $\mathcal{P}$ as in Figure 3.11(b).

By choosing p_{outer} (3.60) in this way we ensure that no fluid re-enters into the channel from the walls. However, in terms of the energy penalty in doing so, the analysis here provides a mechanism for determining the minimum suction pressure required to ensure that no filtered fluid re-enters the channel, thus optimizing the filtration operation if the actual outlet gauge is zero ($p = 0$ at $x = 1$). For a positive outlet pressure, p_{outer} could be zero or even positive.

3.6 Conclusion

The flow and particle distribution for a dilute suspension in a channel flow with porous walls has been described. Allowing permeation (either constant or pressure dependent) through the porous walls reduces the pressure required for the fluid to flow at a constant influx. This wall permeation also contributes to the transport of particles from the centre of the channel to the channel walls, leading to concentration polarization when the walls are impermeable to particles. The presence of particles reduces the flow velocity by increasing the viscosity of the fluid.

We considered the effect of varying the width of an inlet pulse of particles in the cross-stream channel direction. Beginning with a very narrow pulse (relatively highly concentrated in a small region around the centre of the channel), we observe that, as this pulse width increases, it initially becomes harder to push the particles and fluid with the same influx, that is, a higher inlet hydrodynamic pressure is required. This is attributed to the size of the region of the channel occupied by the particles: for small widths the particles do not affect a significant region of the channel to alter the fluid flow; however, as this pulse width increases, the particles affect a greater proportion of the fluid and so a greater pressure is required to transport the particles with a constant fluid influx. Interestingly, however, this increase in pressure *reverses* as the width of the inlet distribution of particles surpasses a critical value and it becomes easier (less pressure is required) to transport the particles. We attribute this observation to the lower gradients of particle volume fraction in the channel, since the particles are now more uniformly distributed. Thus overall, we observe a critical, *pessimal* value of the inlet distribution width that *maximizes* the additional pressure required.

In the case of pressure-dependent permeation flux, concentration polarization results in the osmotic pressure exceeding the hydrodynamic pressure at the end of the channel. This leads to a backflow (an inward flow) from the porous channel walls. In a filtration system, this situation of pure fluid entering the channel contaminated by particles is undesirable yet unavoidable due to the condition of equal outlet pressure and pressure outside the channel (the permeate side).

Finally, we analysed the effect of applying a constant outer pressure to the channel walls in an effort to eliminate the occurrence of clean water re-entry. A positive outer pressure decreases concentration polarization at the channel walls, but again there is an unavoidable influx of fluid through the channel walls. A negative outside

pressure increases the permeation flux, with no influx, but at the cost of increased concentration polarization and energy expenditure. Applying an outer pressure that is equal and opposite to the osmotic pressure at the end of the channel negates the influx caused by osmosis. Since the magnitude of the outer pressure is small, it is a reasonable compromise in terms of additional energy required to prevent the re-entry of fluid into the channel.

The results presented here provide new observations into a model problem related to water filtration that may offer insight into operating strategies. In the next chapter, we consider a filtration setup to counteract backflow due to the osmotic pressure; we tailor the wall permeability to maximize filtration efficiency.

Chapter 4

Tailoring Wall Permeabilities

Summary

The buildup of particulate contaminants at the walls of crossflow membrane filtration systems can be detrimental to the operation of such systems because of, amongst other things, the osmotic backflow it may induce. In this chapter, we propose a strategy to avoid the negative effects of backflow due to osmosis by using 2D channels bounded by walls with a combination of permeable and impermeable segments. We show that preventing flow through the final portion of the channel can increase the efficiency of filtration and we determine the configuration that maximizes efficiency. Our analysis uses a combination of numerical techniques and asymptotic analysis in the limit of low wall permeabilities. Finally, we consider how the energy cost of filtration depends on the Péclet number and show that the energy cost per unit of filtered water may be minimized by choosing both the Péclet number and the permeable fraction appropriately.

A paper based on the contents of this chapter has been published:
J. G. Herterich, D. Vella, R. W. Field, N. P. Hankins, I. M. Griffiths,
Tailoring wall permeabilities for enhanced filtration,
Physics of Fluids **27(5)** (2015): 053102

4.1 Introduction

In the previous chapters we have discussed the many adverse effects of concentration polarization during crossflow membrane filtration. These include a greater propensity for blockage of the membrane pores, thus restricting flow through the permeable walls (Song and Elimelech, 1995), as well as an increased osmotic pressure (Bowen and Jenner, 1995a; Hoek et al., 2002), which acts to reduce the effective transmembrane pressure and may even draw clean water into the channel, reducing filtration performance. Here we consider a setup to address the increased osmotic pressure that may occur. We tailor the permeability of the permeable walls so that the osmotic pressure does not become significant, *i.e.*, large enough to draw water into the channel, via an impermeable wall section (Figure 4.1). Novel experiments are ongoing for membrane fabrication using thin-film composites that control the permeability via patterned compositions (Badalov et al., 2015). Furthermore, studies in solute transport in thin porous tubes have shown that the solute concentration delivered to the permeable wall can be controlled by varying the permeability (Griffiths et al., 2013).

However, to remove particles from the wall, some previous works have focused on the effect of manipulating the fluid flow, for example, by increasing shear rate (Hoek et al., 2002) or vortex mixing (Bellhouse and Lewis, 1988), as well as many other methods (Hilal et al., 2005; Wakeman and Williams, 2002; Wang et al., 1994). These may involve a structural change to the channel, such as furrowed or dimpled wall surfaces to produce the vortex mixing, resulting in complicated fluid flows. Here we consider low Reynolds numbers flows and impose a structural change to the channel that does not overcomplicate the flow. This structural change is to alter the wall permeability to block that part of the permeable wall that may otherwise result in relatively high osmotic pressures that draw fluid into the channel from the permeate side. Operating in a slow flow regime results in a greater deposition of particles at the membrane surface (Field and Pearce, 2011). As in the previous chapter, we do not consider deposition (to be addressed in Chapters 5–7); the concentration polarization observed represents the early stages of particle buildup that may ultimately lead to deposition and cake formation.

Again we consider a crossflow membrane filtration system with a flow from left to right induced by a pressure gradient (Figure 4.1). As discussed in previous chapters, membrane filtration systems utilize a higher fluid pressure to overcome the osmotic

pressure, ensuring sustained water filtration. The rationale for altering the wall permeabilities stems from considering the hydrodynamic pressure within a channel with walls of uniform permeability. As discussed in Chapter 3, fluid permeates out of the wall (leaving particles behind) at a rate, $\hat{\mathcal{V}}$, that depends on the overall effective transmembrane pressure difference, $\Delta\hat{p} - \Delta\hat{\pi}$, where $\Delta\hat{p}$ is the difference between the hydrodynamic pressure in the channel at the wall and the pressure outside the channel, and $\Delta\hat{\pi}$ is the osmotic pressure difference across the permeable membrane wall (Bowen and Jenner, 1995a; Hoek et al., 2002). Motivated by Darcy's law we write

$$\hat{\mathcal{V}} = \hat{\kappa}(\Delta\hat{p} - \Delta\hat{\pi}), \tag{4.1}$$

where $\hat{\kappa} = k/\mu b$ is the spatially varying effective permeability, related to the wall permeability, k, fluid viscosity, μ, and wall thickness, b (*cf.* §2.2). We assume that the filter is perfect, *i.e.*, complete rejection of particles occurs at the channel wall. If the osmotic pressure exceeds the fluid pressure, then the flow is reversed and clean water flows into the channel, a process we call *backflow*.

Backflow of clean water into the channel is very inefficient for the filtration process; energy has been used in extracting the clean water, only for it to re-enter the contaminated flow. Since the region most prone to this osmotic backflow is the end (where $\Delta\hat{p}$ is smallest), as identified in the previous chapter, it is natural to consider whether replacing the permeable wall with an impermeable wall in this region would eliminate the backflow. However, the size of this impermeable region needs to be carefully chosen: too short and backflow will still occur, too long and there is insufficient opportunity for clean water to flow out. Both of these scenarios compromise filtration efficiency. For example, consider a system with permeable walls throughout, with constant pressure gradient and a constant osmotic pressure. Eq. (4.1) implies that filtration occurs when $\hat{p} > \hat{\pi}$, and backflow occurs when $\hat{\pi} > \hat{p}$ (Figure 4.2a). If we set the permeability to be zero beyond a certain point in the channel (ignoring the changes this will induce in the pressure for this illustrative example), then the region where backflow by osmosis was previously active has been modified so that this no longer occurs and thus the amount of net fluid filtered increases (Figure 4.2b).

For simplicity we take the fluid pressure at the end of the channel to be equal to the fluid pressure outside the channel (on the permeate side of the permeable wall), which we may set equal to zero without loss of generality. As a result, any significant non-zero osmotic pressure near the end of the channel will result in a backflow

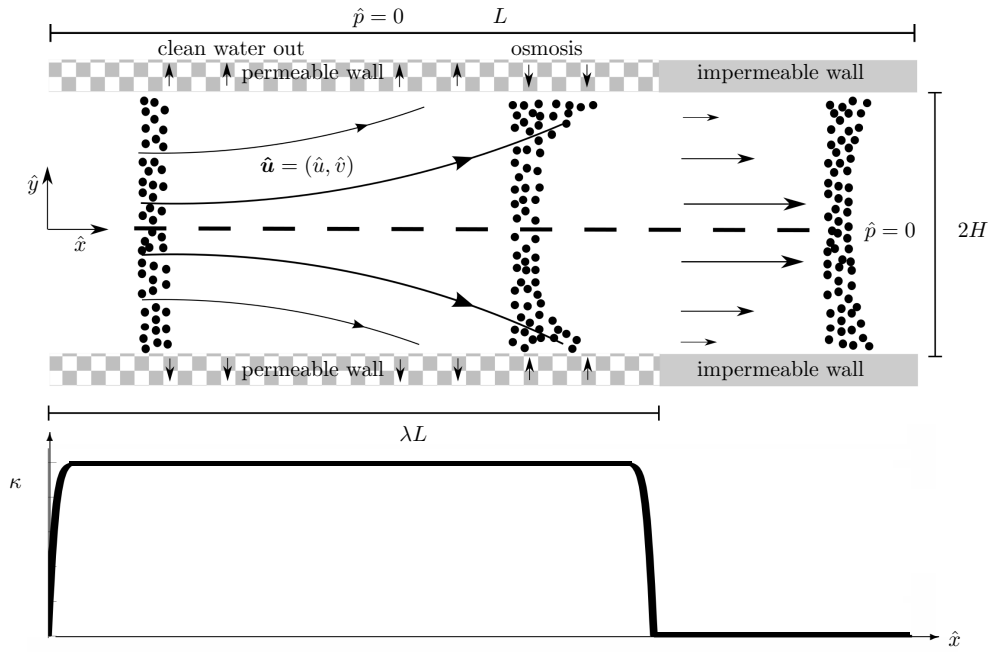

Figure 4.1: Above: schematic of a channel module containing a suspension of particles. The suspension enters from the left and flows along the channel. The walls are a permeable membrane for a section of the channel and impermeable towards the end of the channel, as depicted in the sketch of the permeability, κ, of the channel (below). Particles are advected towards the wall by the flow, increasing the osmotic pressure at the walls, and diffuse back into the channel when the walls are impermeable. If the osmotic pressure exceeds the fluid pressure, osmosis occurs. In the impermeable-walled region, there is no flow through the walls.

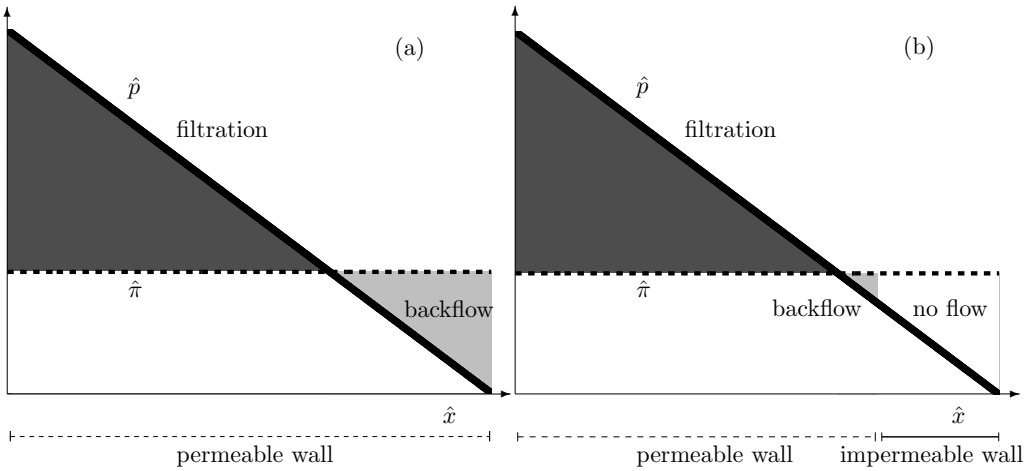

Figure 4.2: Schematic showing the hydrodynamic pressure (solid black), $\hat{p}$, and osmotic pressure (dashed black), $\hat{\pi}$, as functions of the distance along the channel. The sign of $\hat{p}-\hat{\pi}$ determines whether filtration (dark grey) or backflow (light grey) occurs. (a) For a spatially uniform permeability, the effect of backflow significantly decreases the efficiency of filtration. (b) Introducing an impermeable region (no flow, white) reduces backflow and increases the net filtration.

(*cf.* Eq. (4.1)). We note that simply shortening the channel will not remedy this inevitable flow reversal (since wherever the end is open, the pressure difference is zero). An alternative approach would be to take a positive reference pressure at the end of the channel and/or a negative reference outer pressure, as explored in §3.5. However, keeping these additional pressure differences in place during operation in a membrane filtration device may require additional energy. Our proposed setup of partially blocking the end of the module offers a simple way of resolving this issue.

Energy cost is an important consideration for filtration devices. The input energy is required for pumping the flow and creating the pressure in the filtration device. Although the volume filtered increases with crossflow velocity, the power requirement for the pump can increase by as much as the cube of the crossflow velocity (Xi and Geissen, 2001). This results in a trade-off between input energy and filtration output.

In this chapter, we examine the advantages of using a spatially varying wall permeability in order to optimize the efficacy of filtration. We examine in detail, using numerical and asymptotic techniques, a channel that has a permeable region followed by an impermeable region. This illustrates the significant effect that backflow due to osmosis can have on a system where the hydrodynamic pressure and osmotic pres-

sure are of the same order of magnitude. We also consider the impact of a variable permeability on the energy cost for filtration.

4.2 Mathematical Modelling

We model the input fluid as a dilute suspension of neutrally buoyant small particles, typically tens of nanometres in radius. The fluid flows into a 2D channel of length L, at a controlled rate with areal flux $2\hat{Q}$. The walls of the channel are positioned at $\hat{y} = \pm H$ (Figure 4.1). The walls comprise a region of uniform non-zero permeability followed by a region that is impermeable. On the outside of the channel, and at the end of the channel ($\hat{x} = L$), the fluid pressure is constant; we take this value to be our pressure datum. Upon entering the channel, the suspension is advected down the channel and towards the permeable walls; at the wall, the suspended particles are rejected allowing only clean water to flow out. The rate at which clean fluid (the permeate) flows through the permeable walls is proportional to the effective transmembrane pressure difference, as seen in Eq. (4.1). Fluid that does not pass through the walls, together with the rejected particles (forming the retentate), leaves the channel at the open end, $\hat{x} = L$. We consider the steady-state (time-independent) operation of the system.

For suspensions with large volume fractions, both the fluid viscosity, μ, and particle diffusivity, D, will be significantly altered by the presence of particles, as were discussed in the previous chapter for the case of a dilute suspension. However, for simplicity, and to highlight the fundamental aspects of this problem, we neglect such effects, taking μ and D to be constant. As in Chapter 3, we take the typical parameter values as given in §2.1.1.

4.2.1 Governing equations

A steady flow $\hat{\boldsymbol{u}} = (\hat{u}, \hat{v})$ in a thin-channel, with a small Reduced Reynolds number and constant viscosity, is governed by the Stokes equations (2.14) as derived in §2.3.1,

$$\boldsymbol{\nabla} \cdot \hat{\boldsymbol{u}} = 0, \tag{4.2a}$$

$$\mu \boldsymbol{\nabla}^2 \hat{\boldsymbol{u}} = \boldsymbol{\nabla} \hat{p}, \tag{4.2b}$$

where $\hat{p}$ is the fluid pressure. The particle volume fraction, $\hat{\phi}$, is governed by the steady advection–diffusion equation,

$$\hat{\boldsymbol{u}} \cdot \boldsymbol{\nabla} \hat{\phi} = D \ \boldsymbol{\nabla}^2 \hat{\phi}, \tag{4.3}$$

as derived in §2.4.1.

4.2.2 Boundary conditions

In the previous chapter we studied a range of inlet particle distributions; it was shown that a well mixed distribution is far from the pessimal distribution in terms of the pressure perturbation (Figure 3.8). Furthermore, a well mixed (*i.e.*, uniform) inlet distribution over the cross-section is a reasonable assumption for these systems,

$$\hat{\phi}(0, \hat{y}) \equiv \Phi_0, \tag{4.4}$$

where Φ_0 is a constant.

We assume that the fluid flow and particle concentration are symmetric about the x-axis of the channel, that is,

$$\frac{\partial \hat{\phi}}{\partial \hat{y}} = \frac{\partial \hat{u}}{\partial \hat{y}} = \hat{v} = 0 \qquad \text{on } \hat{y} = 0, \tag{4.5}$$

and so we need only consider the behaviour in the half-channel $0 \leq \hat{x} \leq L, 0 \leq \hat{y} \leq H$. This assumption will be relaxed later in §4.6.

The fluid flow through the (permeable) channel walls is again given by the effective transmembrane pressure difference,

$$\hat{v}(\hat{x}, H) = \hat{\mathcal{V}}(\hat{x}) = \hat{\kappa}(\hat{x})(\Delta\hat{p} - \Delta\hat{\pi}) \qquad \text{on} \qquad \hat{y} = H, \tag{4.6}$$

as in Eq. (4.1) and the previous chapter, where $\hat{\kappa}(\hat{x})$ is now the spatially varying effective permeability to be specified later, $\Delta\hat{p}(\hat{x}, H) = \hat{p} - \hat{p}_{\text{outer}}$ is the difference between the hydrodynamic pressure in the channel at the wall and the pressure outside the channel, $\hat{p}_{\text{outer}}$ (assumed constant). We assume that the end of the channel is open so that the pressure at the outlet, $\hat{p}_{\text{end}} = \hat{p}_{\text{outer}}$. Similarly, $\Delta\hat{\pi} = \hat{\pi} - \hat{\pi}_{\text{outer}}$ is the osmotic pressure difference across the wall where $\hat{\pi}$ is the osmotic pressure due to particles in the channel and $\hat{\pi}_{\text{outer}}$ is that due to contaminating particles outside the channel. Again, we assume complete rejection of particles at the channel wall, so

that $\hat{\pi}_{\text{outer}} = 0$. The osmotic pressure is, in general, a function of the volume fraction of particles at the surface of the permeable wall

$$\hat{\pi}(x)|_{\hat{y}=H} = \Pi\Phi_0 \; \hat{\phi}(\hat{x}, \hat{y} = H), \tag{4.7}$$

as discussed in §2.2.1.

As in the previous chapter, and commonly used in the literature, we use a no-slip boundary condition (Bowen and Williams, 2001),

$$\hat{u}(\hat{x}, H) = 0, \tag{4.8}$$

and a no-flux boundary condition (Bacchin et al., 2002; Davis and Sherwood, 1990),

$$\hat{\mathcal{V}}\hat{\phi} - D\frac{\partial \hat{\phi}}{\partial \hat{y}} = 0 \qquad \text{on } \hat{y} = H, \tag{4.9}$$

at the membrane wall. Again we note that the inlet condition (4.4) will not satisfy this boundary condition, in general, and a small boundary layer region is present in which the concentration appropriately adjusts.

At the inlet we impose a constant inlet flow, $2\hat{Q}$,

$$2\hat{Q} = \int_{-H}^{H} \hat{u} \, \mathrm{d}\hat{y} = 2\int_{0}^{H} \hat{u} \, \mathrm{d}\hat{y} \qquad \text{at } \hat{x} = 0. \tag{4.10}$$

The above boundary conditions suffice to solve the problem.

From a practical point of view, the amount of fluid filtered through the walls,

$$\hat{F} = 2\int_{0}^{L} \hat{\mathcal{V}} \, \mathrm{d}\hat{x}, \tag{4.11}$$

is of interest.

4.2.3 Non-dimensionalization and thin-channel approximation

Since our system is dependent on the competing forces of hydrodynamic pressure and osmotic pressure, and we have shown these to be of the same order for our system, it is natural to scale $\hat{p}$ and $\hat{\pi}$ in the same way; Eq. (4.7) indicates that the natural scaling

choice is $\Pi\Phi_0$; L and $H = \delta L$ are used to non-dimensionalize lengths as appropriate, where $\delta = H/L \ll 1$ is the aspect ratio. We thus let

$$\begin{aligned} \hat{x} &= Lx, & \hat{y} &= \delta L y, & \hat{\phi} &= \Phi_0 \phi, & \hat{\pi} &= \Pi\Phi_0 \pi, \\ \hat{u} &= \frac{\hat{Q}}{\delta L} u, & \hat{v} &= \frac{\hat{Q}}{L} v, & \hat{p} &= \Pi\Phi_0 p + \hat{p}_{\text{outer}}, & \hat{\kappa} &= \frac{D}{\Pi\Phi_0 \delta L}\kappa, \end{aligned} \tag{4.12}$$

where the scalings of u, v arise in order to balance the equations and to eliminate $\hat{Q}$ from the influx condition. Hence the velocity scale is $U = \hat{Q}/\delta L$. Substituting the scalings (4.12) into Eqns. (4.2) and (4.3), and retaining only leading-order terms in $\delta \ll 1$ provides the governing equations for the system

$$\frac{\partial u}{\partial x} + \frac{\partial v}{\partial y} = 0, \tag{4.13a}$$

$$\text{Pe}\mathcal{D}\frac{\partial^2 u}{\partial y^2} = \frac{\partial p}{\partial x}, \tag{4.13b}$$

$$0 = \frac{\partial p}{\partial y}, \tag{4.13c}$$

$$\text{Pe}\left(u\frac{\partial \phi}{\partial x} + v\frac{\partial \phi}{\partial y}\right) = \frac{\partial^2 \phi}{\partial y^2}, \tag{4.13d}$$

for $0 \le x \le 1$ and $0 \le y \le 1$ with the channel walls at $y = \pm 1$ (with symmetry about $y = 0$). Here $\text{Pe} = \delta\hat{Q}/D$ is the reduced Péclet number, a measure of the ratio of advection to diffusion of the particles in a thin channel, and $\mathcal{D} = \mu D/\delta^4 L^2 \Pi\Phi_0$ is a dimensionless number. We note that $1/\mathcal{D} = b(\delta^4 L^2 \Pi\Phi_0/\mu b)/D$ so that $\mathcal{D}$ is identified as an inverse Péclet number where the velocity scale is the Darcy velocity across a membrane of thickness b with permeability scaling like a length squared, $\delta^4 L^2$. Hence $\text{Pe}\mathcal{D}$ represents a ratio of Péclet numbers. By our parameter estimations, $\text{Pe}\mathcal{D}$ is an order-one quantity. The Péclet number is estimated in §2.1.1 to be $\text{Pe} = 10^2$; however, it is noted that this is not asymptotically large, *i.e.*, $\delta\text{Pe} \ll 1$. Throughout this chapter, we take the Péclet number to be an order-one quantity as this regime produces the richest dynamics. The influx, $\hat{Q}$, that has been scaled out of the problem appears in the Péclet number. This affects the fluid flow in Eq. (4.13b), and the particles in Eq. (4.13d).

Note that there is no axial diffusion term in the leading-order advection–diffusion equation (4.13d) due to the thin-channel approximation ($\delta \ll 1$). The y-momentum equation (4.13c) indicates that the pressure is a function of x only, *i.e.*, $p = p(x)$, as expected from lubrication theory and other thin-layer models of fluid flow (Oron et al.,

1997). Furthermore our non-dimensionalization means that the osmotic pressure at the walls from Eq. (4.7) now reads

$$\pi(x) = \phi_w(x), \tag{4.14}$$

where we have introduced $\phi_w(x) = \phi(x, y = 1)$ to denote the particle concentration at the wall.

The dimensionless boundary conditions read

$$\begin{aligned}
&\text{Symmetry:} && \frac{\partial \phi}{\partial y} = \frac{\partial u}{\partial y} = v = 0 && \text{on } y = 0, && (4.15a)\\
&\text{No axial wall slip:} && u = 0 && \text{on } y = 1, && (4.15b)\\
&\text{Permeate flow:} && \mathcal{V} = \frac{\kappa(x)}{\mathrm{Pe}}\,(p - \phi_w) && \text{on } y = 1, && (4.15c)\\
&\text{Perfect filtering of particles:} && \mathrm{Pe}\ \mathcal{V}\ \phi - \frac{\partial \phi}{\partial y} = 0 && \text{on } y = 1, && (4.15d)\\
&\text{Fluid influx:} && \int_0^1 u\,\mathrm{d}y = 1 && \text{at } x = 0, && (4.15e)\\
&\text{Fixed outlet pressure:} && p = 0 && \text{at } x = 1, && (4.15f)\\
&\text{Inlet condition:} && \phi \equiv 1 && \text{at } x = 0. && (4.15g)
\end{aligned}$$

The influx, $\hat{Q}$, appears again through the Péclet number in the boundary conditions, affecting the flow in Eq. (4.15c) and the particles in Eq. (4.15d). This non-dimensionalization results in four free parameters: the Péclet number, Pe, the permeability, κ, the permeable wall fraction, λ, and a dimensionless number, $\mathcal{D}$. From §4.3 on, we fix $\mathcal{D} = 1$ and investigate the effects of varying λ with each of κ and Pe in turn.

4.2.4 Solution of flow problem

The system of equations (4.13a,b) with boundary conditions (4.15a,b) can be solved immediately to give the flow within the channel. The axial and transverse velocities are given by

$$u(x, y) = \frac{1}{\mathrm{Pe}\mathcal{D}} \frac{\mathrm{d}p}{\mathrm{d}x} \frac{y^2 - 1}{2}, \qquad v(x, y) = \frac{1}{\mathrm{Pe}\mathcal{D}} \frac{\mathrm{d}^2 p}{\mathrm{d}x^2} \frac{3y - y^3}{6}, \tag{4.16a,b}$$

respectively, where the factor $1/\mathrm{Pe}\mathcal{D}$ represents the scaling for the ratio of Péclet numbers. This is a classic result and can be found in many textbooks (Probstein, 1989).

The hydrodynamic pressure in the channel is then determined by the boundary condition (4.15c) and Eq. (4.16b), resulting in an ordinary differential equation (ODE) for p

$$\frac{1}{3}\frac{\mathrm{d}^2 p}{\mathrm{d}x^2} = \mathcal{D}\kappa(x)\left(p - \phi_w\right). \tag{4.17}$$

The boundary conditions (4.15e,f) translate to conditions on the pressure

$$\left.\frac{\mathrm{d}p}{\mathrm{d}x}\right|_{x=0} = -3\mathrm{Pe}\mathcal{D}, \qquad p(1) = 0. \tag{4.18a,b}$$

For convenience we restate the governing equation for ϕ

$$\mathrm{Pe}\left(u\frac{\partial\phi}{\partial x} + v\frac{\partial\phi}{\partial y}\right) = \frac{\partial^2\phi}{\partial y^2}, \tag{4.19}$$

with boundary conditions

$$\left.\frac{\partial\phi}{\partial y}\right|_{y=0} = 0, \qquad \mathrm{Pe}\ \mathcal{V}\ \phi - \left.\frac{\partial\phi}{\partial y}\right|_{y=1} = 0, \qquad \phi(0,y) \equiv 1. \tag{4.20a,b,c}$$

The coupling between p and ϕ in the ODE for the pressure (4.17) and the advection–diffusion equation for the volume fraction (4.19) makes analytical progress difficult, if not impossible. We therefore resort to numerical solution of Eqns. (4.17) and (4.19) subject to the boundary conditions (4.18) and (4.20). We use a finite difference scheme for the equations within a shooting method (p and ϕ are coupled, and we know $p(1)$ but not $p(0)$: we choose a $p(0)$ and solve the system, check the value of $p(1)$, and update a new $p(0)$ using a secant method - this is repeated until the correct value of $p(1)$ is obtained).

We normalize the amount of fluid filtered through the walls (Eq. (4.11)) by the influx, $2\hat{Q}$, giving the efficiency of the filtration process as

$$E = \frac{\hat{F}}{2\hat{Q}} = F. \tag{4.21}$$

where (noting the symmetry in the flow)

$$F = \int_0^1 \mathcal{V}\,\mathrm{d}x, \tag{4.22}$$

is the dimensionless flux through one wall. In dimensionless form, the efficiency, E, is the same as the net flux through one of the walls, F, as the flow has dimensionless flux 1. In this chapter we will distinguish between the two, as appropriate.

Since the wall velocity is proportional to κ (Eq. (4.15c)), we expect more fluid to be filtered with larger κ. However, we consider the re-scaled efficiency, E/κ, to compare systems of different permeability.

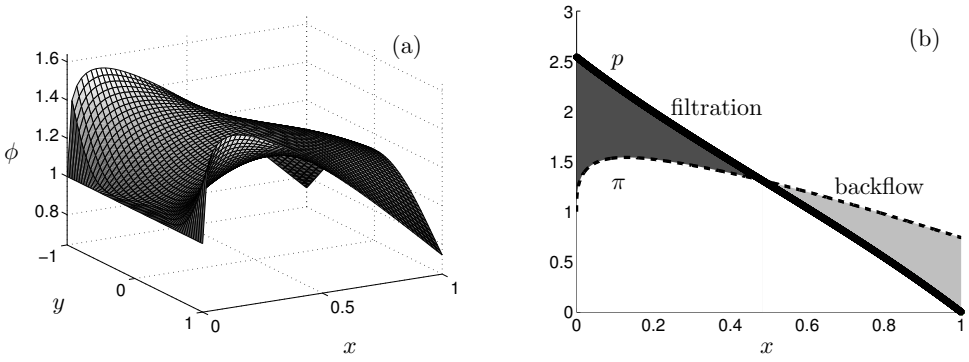

Figure 4.3: (a) Particle concentration in a channel with uniformly permeable walls. Concentration polarization occurs close to the inlet but the concentration falls off with x due to concentration polarization-induced osmotic backflow and diffusion. (b) The difference in hydrodynamic pressure (solid), p, and osmotic pressure (dashed), π, determines the regions of filtration and backflow as in Eq. (4.15c): the dark shaded region indicates filtration; the light shaded region indicates backflow. Here $\mathcal{D} = 1$, Pe $= 1$ and $\kappa_0 = 1$.

4.3 Uniformly Permeable Walls

We first consider a channel in which the walls are uniform with constant permeability, *i.e.*, $\kappa(x) = \kappa_0 =$ constant for $0 \leq x \leq 1$. We solve the coupled pressure ODE (4.17) and advection–diffusion equation (4.19), subject to the boundary conditions (4.18) and (4.20), numerically using a finite difference method. For convenience, from now on we fix $\mathcal{D} = 1$ since it is an order-one number.

Figure 4.3a shows that the system exhibits concentration polarization (CP) in the channel: in regions where filtration occurs ϕ is larger close to the wall than in the bulk flow. In practice CP may lead to blocking of the pores of the permeable walls, a reduced permeability of the walls, and hence a reduction in the proportion of water that is filtered. We do not consider this effect here, focusing instead on the effects arising further down the channel; here CP is significantly reduced for two reasons. Firstly, the channel loses fluid due to the permeable walls. This reduces the advection of particles and so the particles that have collected at the walls (CP) begin to diffuse away, leading to a more uniform particle distribution in the channel. Secondly, the osmotic pressure exceeds the hydrodynamic pressure drawing fluid into the channel from outside (Figure 4.3b).

Both CP and backflow are undesirable effects when striving to maximize filtration efficiency and so in the next section we show how spatially variable permeability of the walls may mitigate these issues and increase the net filtration.

4.4 A Variable Permeability Channel

We begin by considering a canonical example of a channel with a single region of permeable wall for $0 \leq x < \lambda$ and a single region of impermeable wall for $\lambda \leq x \leq 1$ where $\lambda \in (0, 1)$ (Figure 4.1). This is motivated by the idea of blocking the permeable walls of the channel towards the end to prevent inflow (see §4.1). While we might imagine setting the permeability to be constant in the permeable region and zero in the impermeable region, the discontinuity in κ results in a discontinuity in the second derivative of the pressure and thus in the transverse flow velocity, v (Eqns. (4.17) and (4.16b), respectively). This affects the advection–diffusion of the particles via the no-flux boundary condition (4.20b). In reality, this discontinuity could be absorbed by revisiting our neglection of $\mathcal{O}(\delta)$ terms but this is not particularly enlightening for our analysis. Instead, we choose a functional form for the permeability that rapidly but smoothly varies between the permeable and impermeable regions:

$$\kappa(x) = \kappa_0 \tanh\big(A\ x\big) \tanh\big[A\ (\lambda - x)\big]\ \theta(\lambda - x), \tag{4.23}$$

where κ_0 and A are constants representing the unblocked permeability and the width of the transition region, respectively, and θ is the Heaviside function. We note that the functional form of the permeability in Eq. (4.23) is not a C^1 function. However, we do not take any derivatives of $\kappa(x)$ in our analysis and so this does not affect the numerics. We vary the maximum value, $\kappa(x) = \kappa_0$, to analyse the dependence of the permeate flux on the permeability. Here we take $A = 500$ to provide a close approximation to a step function while allowing our numerical scheme to resolve the rapid variations in x. Note that when λ is small, the width of the transition region becomes important. For some small λ the growth of the permeability does not attain the maximum value, κ_0, before it transitions back to zero. In these cases, we normalize the function by dividing by the maximum value obtained by $\tanh\big(A\ x\big) \tanh\big[A\ (\lambda - x)\big]$.

4.4.1 λ and κ_0–dependency

Here, we fix the Péclet number, $\mathrm{Pe} = 1$, and vary the strength of the permeability, κ_0, and the fraction of permeable wall region, λ. We solve the coupled pres-

sure ODE (4.17) and advection–diffusion equation (4.19) numerically, subject to the boundary conditions (4.18) and (4.20), using finite differences, with κ given by (4.23).

As in the case of the uniformly permeable channel, the particle concentration, ϕ, exhibits CP in the permeable region $x < \lambda$ (Figure 4.4a). Also, as was seen in the uniformly permeable channel case, the flow is reduced in the channel by loss of fluid through the membrane: diffusion then acts to smooth out the CP further down the channel.

In the impermeable region $x \geq \lambda$, the particles are able to diffuse back to an approximately uniform distribution across the channel (though with a higher concentration than at the origin, Eq. (4.20c), because of the permeation of fluid through the permeable walls). The distribution becomes uniform because the transverse velocity disappears, due to the impermeable walls. This is expected since the advection–diffusion equation for the particle distribution, Eq. (4.19), becomes a diffusion equation with zero-flux boundary conditions.

The choice of λ may significantly affect the net flux filtered through the permeable walls, F (4.22) (compare Figure 4.3b and Figure 4.4b). If λ is close to unity, then the backflow region is significant, reducing the net flux through the permeable wall. However, if λ is too small, then we reduce the region available for filtration. There is therefore a critical (optimal) value, $\lambda = \lambda^*$, that maximizes the efficiency of filtration, E (4.21), found by a numerical search of λ (Figure 4.5a).

An increase to the wall permeability increases the transport of fluid through the wall (see Eq. (4.15c)). As such, the accumulation of particles at the wall (CP) increases as well. The resulting increase in osmotic pressure leads to backflow occurring closer to the entrance of the channel. The optimal fraction of permeable wall, λ^*, thus decreases with κ_0, as does the optimal re-scaled efficiency, E^*/κ_0, as seen in Figures 4.5b and 4.5c. Here, we use the previously mentioned re-scaled efficiency, E^*/κ_0, to compare the systems, however now scaled with the maximum value of the varying permeability, κ_0. Hence the decrease in E^*/κ_0 with κ_0 is attributed to the larger osmotic pressure that occurs when more particles are advected to the wall.

4.4.2 Asymptotics for small permeability

The numerical results in the previous section give an insight into the behaviour of our system. We now seek to gain a deeper understanding by finding analytical expres-

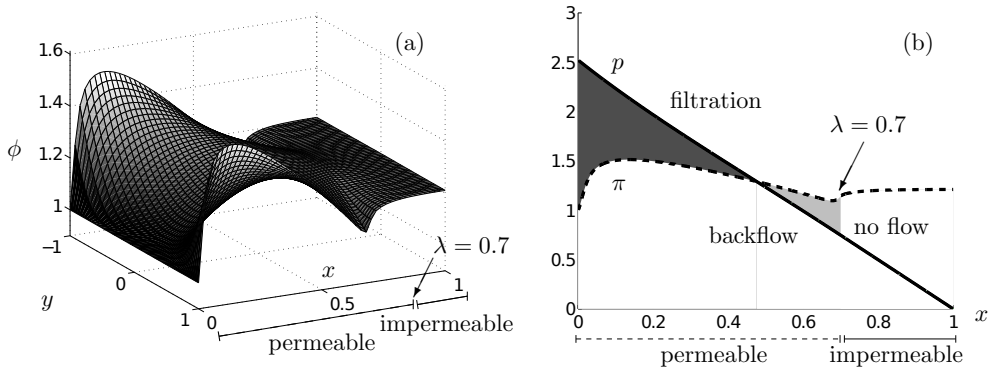

Figure 4.4: (a) Particle concentration in a channel with permeable walls of varying permeability (4.23) with $\lambda = 0.7$. Concentration polarization occurs in the permeable region and diffusion to a uniform concentration occurs in the impermeable region. (b) The difference in hydrodynamic (solid), p, and osmotic (dashed), π, pressures determine the regions of filtration and backflow. The dark shaded region indicates filtration, the light shaded region indicates backflow, and there is no flow in the white region between p and π. Here $\mathcal{D} = 1$, $\mathrm{Pe} = 1$ and $\kappa_0 = 1$.

sions for the parameter dependencies in the asymptotic regime of small permeability, $\kappa_0 \ll 1$. This corresponds to a crossflow filtration system with a very small filtration velocity. While this is less relevant to filtration applications it gives insight into the qualitative behaviour of the system that holds even at higher permeabilities.

When the channel walls are impermeable ($\kappa_0 = 0$), the flow in the channel (4.17) is given by a constant pressure gradient, $\mathrm{d}p/\mathrm{d}x = -3\mathrm{Pe}\mathcal{D}$ by Eq. (4.18a), and so the velocities in Eq. (4.16) read, $u = 3(1-y^2)/2 \equiv u_0$ and $v = 0$ (*i.e.*, Poiseuille flow). By (4.19) the volume fraction remains uniform throughout, $\phi \equiv 1$. We consider the small-permeability limit, $\kappa_0 \ll 1$, as a perturbation of this uniform, unidirectional flow state with the aim of understanding the general curve shape shown in Figure 4.5a. We perturb the variables as follows

$$p = p_0 + \kappa_0\, p_1, \qquad u = u_0 + \kappa_0\, u_1, \qquad v = \kappa_0\, v_1, \qquad \phi = 1 + \kappa_0\, \phi_1, \qquad \pi = 1 + \kappa_0\, \pi_1, \tag{4.24a,b,c,d,e}$$

where $\pi_1 = \phi_1(x, y = 1)$ in (4.24e) is obtained from Eq. (4.14). Eq. (4.17) at leading and first order gives

$$\frac{\mathrm{d}^2 p_0}{\mathrm{d}x^2} = 0, \qquad \frac{\mathrm{d}^2 p_1}{\mathrm{d}x^2} - 3\mathcal{D}p_0 + 3\mathcal{D} = 0, \tag{4.25a,b}$$

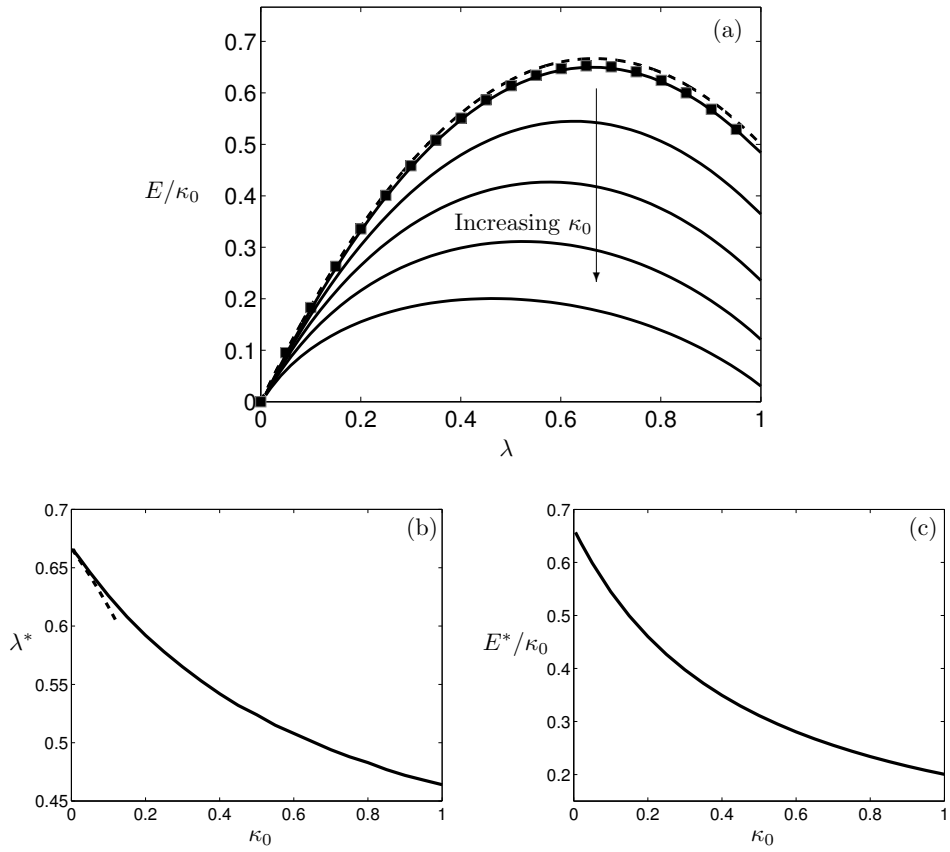

Figure 4.5: (a) Dependence of re-scaled efficiency of filtration through the permeable walls, E/κ_0, on the permeable fraction of the wall, λ, for $\kappa_0 = \{0.01, 0.1, 0.25, 0.5, 1\}$ (solid curves). E/κ_0 is maximized by an optimal value of $\lambda = \lambda^*$, decreasing with κ_0. The dashed black curve and the squares show respectively the leading-order and first-order asymptotic results (4.28b), for $\kappa_0 = 0.01$. (b) The optimal permeable wall fraction, λ^*, that maximizes the efficiency of filtration, E/κ_0, of clean water out versus wall permeability, κ_0. The asymptotic result, to order κ_0 (dashed line), for this decreasing function, matches the numerics for $\kappa_0 \ll 0.01$. (c) The re-scaled optimal efficiency, the efficiency at the optimal λ, decreases with κ_0. Here $\mathrm{Pe} = 1$ and $\mathcal{D} = 1$.

respectively. Eqns. (4.25a,b) must be solved subject to the boundary conditions

$$\left.\frac{\partial p_0}{\partial x}\right|_{x=0} = -3\mathrm{Pe}\mathcal{D}, \qquad p_0(1) = 0, \qquad \left.\frac{\partial p_1}{\partial x}\right|_{x=0} = 0, \qquad p_1(1) = 0, \quad \text{(4.26a,b,c,d)}$$

using Eq. (4.18), which gives

$$p_0 = 3\mathrm{Pe}\mathcal{D}\,(1-x)\,, \qquad p_1 = -\frac{3}{2}\mathcal{D}\left[\mathrm{Pe}\mathcal{D}x^3 + (1-3\mathrm{Pe}\mathcal{D})x^2 + 2\mathrm{Pe}\mathcal{D} - 1\right]. \tag{4.27a,b}$$

The leading order solution (4.27a) is Poiseuille flow in a channel with impermeable walls, as expected. The filtration efficiency, (4.21), is given as a function of λ by

$$E = \int_0^\lambda \mathcal{V}\,\mathrm{d}x = \int_0^\lambda \frac{\kappa_0}{\mathrm{Pe}}\,(p-\pi)\,\mathrm{d}x, \tag{4.28a}$$

$$= \frac{\kappa_0\,\lambda}{\mathrm{Pe}}\left(3\mathrm{Pe}\mathcal{D} - 1 - \frac{3\mathrm{Pe}\mathcal{D}\,\lambda}{2}\right) + \frac{\kappa_0^2}{\mathrm{Pe}}\int_0^\lambda (p_1-\pi_1)\,\mathrm{d}x, \tag{4.28b}$$

using (4.15c, 4.24a,d, 4.27a). The first term in Eq. (4.28b) (proportional to κ_0) explains the quadratic dependence on λ observed in the efficiency of filtration (Figure 4.5a). As such, the leading-order efficiency of filtration is

$$\frac{E_0}{\kappa_0} = \lambda\left(3\mathcal{D} - \frac{1}{\mathrm{Pe}} - \frac{3\mathcal{D}\,\lambda}{2}\right), \tag{4.29}$$

which is shown as the dashed curve in Figure 4.5a. The leading-order efficiency (of order κ_0) may be negative. This reflects the significant osmotic pressure that may occur in the small-permeability limit. To ensure that E_0 (4.29) is positive we must have a condition relating $\mathrm{Pe}, \mathcal{D}$ and λ, the fluid and geometric parameters of the system. This can be written as either

$$\mathrm{Pe}\mathcal{D} > \frac{1}{3\left(1-\frac{\lambda}{2}\right)}, \qquad \text{or} \qquad \lambda < 2\left(1 - \frac{1}{3\mathrm{Pe}\mathcal{D}}\right), \tag{4.30}$$

where $0 \le \lambda \le 1$, $\mathrm{Pe} > 0$ and $\mathcal{D} > 0$, that is, a condition on the flow depending on the geometry or a condition on the geometry depending on the desired flow.

The value of λ that maximizes E_0, $\lambda^*_{\mathrm{asymp}}$, is given by

$$\lambda^*_{\mathrm{asymp}} = 1 - \frac{1}{3\mathrm{Pe}\mathcal{D}}. \tag{4.31}$$

The order-κ_0 result may be calculated numerically and matches the result in Figure 4.5b for $\kappa_0 = 0.01$. Note that $\lambda^*_{\mathrm{asymp}} < 1$ meaning that the greatest net filtration occurs when some part of the wall section is impermeable. This makes sense as osmotic induced backflow is inevitable in this system, as discussed earlier.

The osmotic term $\pi_1 = \phi_1$ that appears in (4.28b) is determined by substituting the perturbation (4.24d) into the advection–diffusion equation (4.19) and boundary conditions (4.20). The resulting order-κ_0 equations are,

$$\frac{\partial \phi_1}{\partial x} = \frac{2}{3\ \mathrm{Pe}\ (1-y^2)} \frac{\partial^2 \phi_1}{\partial y^2}, \tag{4.32a}$$

$$\frac{\partial \phi_1}{\partial y} = 0 \qquad \text{on } y = 0, \tag{4.32b}$$

$$\mathrm{Pe}\ v_1 - \frac{\partial \phi_1}{\partial y} = 0 \qquad \text{on } y = 1, \tag{4.32c}$$

$$\phi_1 = 0 \qquad \text{at } x = 0. \tag{4.32d}$$

These equations for ϕ_1 may in principle be solved by separation of variables. However, the resulting parabolic cylinder functions are complicated and do not give much insight to the solution. We therefore solve the problem numerically. The efficiency of filtration, E, can now be calculated from (4.28b) for various values of λ. The order-κ flux captures the shape of E as a function of λ (Figure 4.5a). Including the $\mathcal{O}(\kappa_0^2)$ correction provides an almost indiscernible result from the full numerical solution when $\kappa_0 = 0.01$.

4.4.3 λ and Pe–dependency

The permeability is a structural part of the membrane filtration module that plays an important role in filtration; once the module is made, it cannot easily be changed. However, the Péclet number, $\mathrm{Pe} = \delta \hat{Q}/D$, is dependent on the flow rate which may easily be adjusted by the pump used in a device. This parameter is important for the transport of particles in the flow and hence heavily influences the osmotic pressure. By varying the Péclet number, we are not considering changes to the particles, *e.g.*, radius. It is the influx that is being changed, not the diffusivity.

To investigate the role of Pe, we solve the coupled pressure ODE (4.17) and advection–diffusion equation (4.19), subject to the boundary conditions (4.18) and (4.20), numerically using finite differences. The wall permeability, κ, is again given by (4.23) with $\kappa_0 = 1$ and the Péclet number is varied, together with λ. In §4.4.1, we observed an optimal value, λ^*, for the efficiency of filtration (Figure 4.5a), that decreases with κ_0 (Figure 4.5b). We now observe a similar behaviour, *i.e.*, the presence of an optimal value for the efficiency of filtration as we vary the Péclet number. As we increase Pe, the optimal value, λ^*, increases (Figure 4.6a), *i.e.*, a larger fraction of

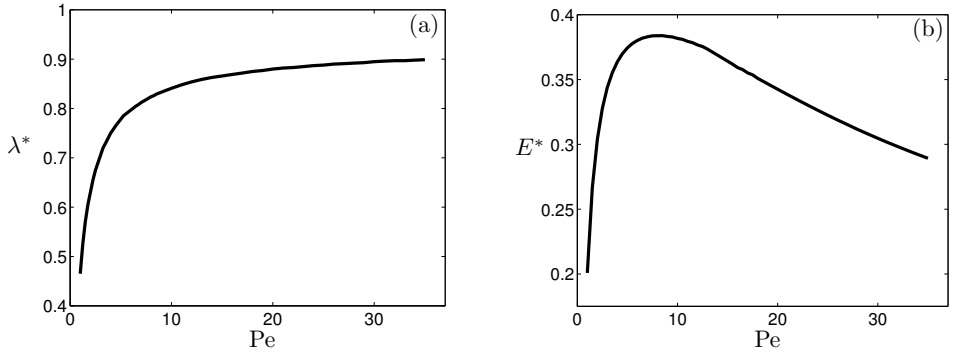

Figure 4.6: (a) The optimal permeable wall fraction, λ^*, as a function of the Péclet number, Pe, increases rapidly for Pe $\lesssim 10$ and asymptotes for larger values. (b) The optimal flux, E^*, corresponding to the optimal fraction of permeable wall, λ^*, for each Pe, results in a global optimal result that maximizes filtration. Here $\kappa_0 = 1$ and $\mathcal{D} = 1$.

permeable wall maximizes the efficiency of filtration. This can be explained by considering the pressure in the channel: the pressure gradient at the entrance is dependent on the flux, and hence on Pe (4.18a), resulting in greater pressures in the channel as we increase Pe. Furthermore, λ^* asymptotes to a value less than 1 as Pe $\to \infty$ because backflow is inevitable at the end of the channel since the hydrodynamic pressure vanishes (4.18b).

The optimal filtration efficiencies, E^*, corresponding to the optimal fraction of permeable wall, λ^*, as Pe varies exhibits an optimum (Figure 4.6b). This provides the global maximum efficiency for both λ and Pe. This may be explained by considering the particle distribution in the channel; as we begin to increase the Péclet number, advection is dominating, however, a boundary layer at the wall exists when Pe $\gg 1$. This boundary layer produces larger particle concentrations and concentration gradients at the walls, which leads to a large osmotic pressure that increases further with Pe. This competes with the large pressure in the channel and a turning (critical) point occurs, reducing the efficiency, and thus leading to an optimum.

4.4.4 Energy

We have analysed the efficiency of a filtration module composed of a region of permeable wall followed by an impermeable-walled region. However, filtration efficiency does not necessarily imply energy efficiency. In a filtration setup, the power requirement for a feed pump scales like $\hat{P} = \hat{Q}\left(\hat{p}(0) - \hat{p}(L)\right)/e$ (Parameshwaran et al., 2001; Xi and Geissen, 2001) where $\hat{Q}$ is the influx, $\hat{p}(0) - \hat{p}(L)$ is the pressure difference in the channel, and e is the pump efficiency (a constant for a given pump). Since power corresponds to the quantity of energy ($\hat{T}$) consumed per unit time, we equate the energy with the power multiplied by the time taken to filter an areal volume, V, of fluid, $\hat{t}_f = V/\hat{Q}E$, giving

$$\hat{T} = \hat{P}\hat{t}_f = \frac{\left[\hat{p}(0) - \hat{p}(L)\right]V}{Ee}. \tag{4.33}$$

In dimensionless form, scaling $\hat{T} = (\Pi\Phi_0 V/e)T$, the energy cost (input) required for filtration scales like

$$T \sim \frac{p(0) - p(1)}{E} = \frac{p(0)}{E}, \tag{4.34}$$

since, in our case, $p(1) = 0$. This is a balance between how hard we push the fluid (pressure difference applied) and the filtration efficiency, E. The harder we push and/or the less efficient the system, the more energy that is consumed to filter a given amount of fluid.

The Péclet number plays an important role in the energy cost of the system, directly affecting the pressure (Eq. (4.18a)) and velocity (Eq. (4.16)) of the fluid. For any given variable-permeability channel with a permeable-region fraction, λ, an optimal value for the Péclet number, Pe^*, exists that minimizes the energy expended (Figure 4.7a). This optimal value increases with λ, indicating that channels that comprise a higher fraction of permeable-wall region must operate at higher Péclet numbers to minimize energy cost (Figure 4.7b). Finally, an optimum value of λ (using the corresponding Pe^*) exists for which the energy is globally minimized (Figure 4.7c). This is also seen as the dashed line in Figure 4.7a. When $\kappa_0 = 1$ we find that the global optimal operating conditions are $\lambda \approx 0.5$ and $\mathrm{Pe} \approx 1.05$ (Figure 4.7b,c). We note that this optimization can yield significant advantages with, for instance, an energy saving of up to 50% when operating in this optimal regime when compared to a setup with $\lambda = 0.1$ (Figure 4.7c).

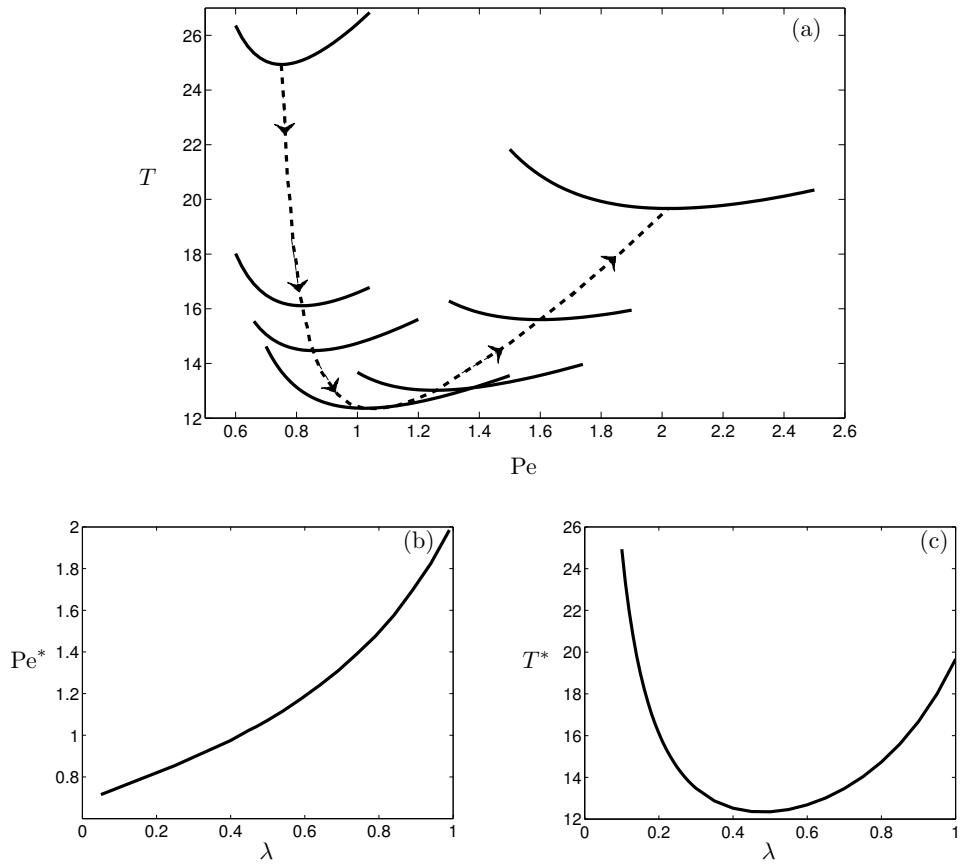

Figure 4.7: (a) The energy T varies with Péclet number Pe for $\lambda = 0.1, 0.2, 0.25, 0.45, 0.65, 0.85, 1$ (solid curves with λ increasing in the direction of the arrows) giving an optimal value (along the dashed line) for each value of λ. (b) The Péclet number that minimizes the energy cost, Pe^*, increases with λ. (c) The minimal energy cost, T^*, for each λ evaluated at the optimal Péclet number from (b) showing a global minimum. In all cases, $\kappa_0 = 1$ and $\mathcal{D} = 1$.

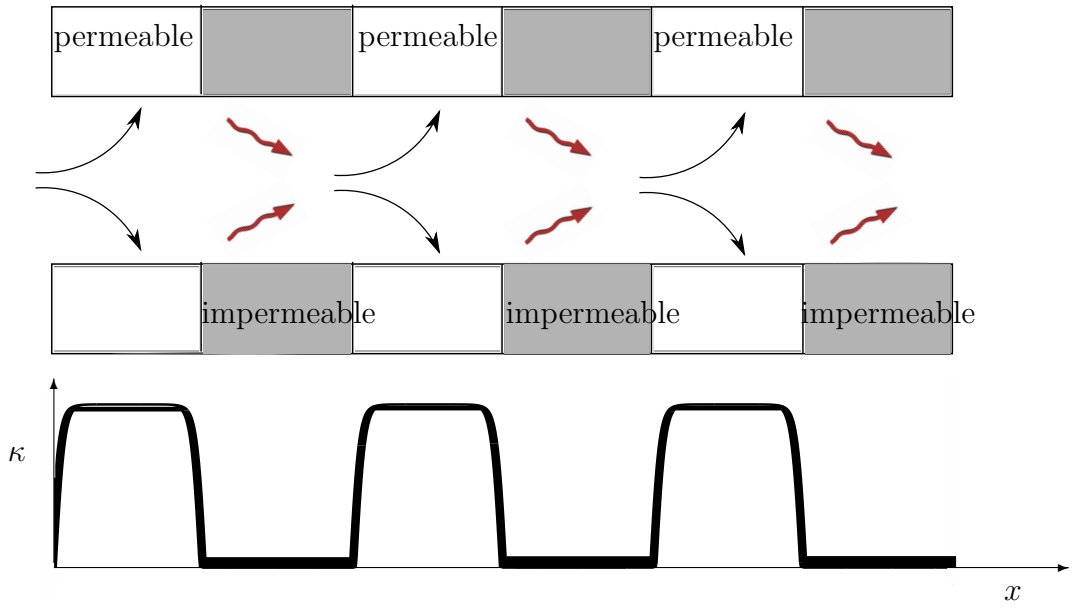

Figure 4.8: Sketch of a *Zebra Channel*. The walls are periodically permeable and impermeable. The total permeable section takes us a fraction λ of the wall length and the total impermeable region takes up a fraction $1 - \lambda$ of the wall length. The particles follow the arrows in the sketch. In impermeable regions, they are advected towards the walls, and in impermeable regions, they diffuse back to the bulk of the flow. Below is a sketch of the permeability, κ, of the channel walls.

4.5 Zebra Channel

We can advance the system of a channel with a single permeable region followed by an impermeable region by fitting a sequence of such permeable/impermeable striped regions, that we call a *Zebra Channel*, to form a chain of permeable and impermeable wall regions as in Figure 4.8. This allows us to exploit the diffusion of particles at the wall in the impermeable region, reducing CP and encouraging a uniform concentration across the channel, before re-entering a permeable region.

We perform the same analysis as for the varying permeability channel, taking n to be the number of stripes in the Zebra Channel. Using the same permeable to impermeable region ratio, λ, in each stripe, we ensure that the total total fraction of the channel wall that is permeable is the same regardless of the number of stripes, n, but the permeable region is split up differently within the channel. We use a more general version for the permeability to Eq. (4.23)

$$\kappa(x) = \kappa_0 \tanh\left(A\ x\right) \tanh\left[A\ \left(\frac{\lambda}{n} - x\right)\right]\ \theta\left(\frac{\lambda}{n} - x\right), \tag{4.35}$$

for each stripe region (of one permeable and one impermeable section).

Again, we solve the coupled pressure ODE (4.17) and advection–diffusion equation (4.19) numerically, subject to the boundary conditions (4.18) and (4.20), using finite differences with the varying permeability appropriate for the zebra-like striping (4.35). We determine an optimal ratio, λ^*, that maximizes the net filtration (Figure 4.9(a)). As the number of such permeable/impermeable stripes increases, the optimal value, λ^*, increases. This suggests that by allowing the particles to diffuse from a CP configuration towards a uniform concentration we can use more of the channel wall as a filter.

However, for the optimal ratio of permeable/impermeable stripes, we observe that as the number of stripes, n, increases then the corresponding optimal rescaled efficiency, E^*/κ_0, decreases (Figure 4.9(b)). This means that the optimal zebra channel filters less fluid the more stripes we fit into the channel. This may be explained by considering the pressure in the channel: as the fluid pressure drops further down the channel, the transmembrane pressure, $p - \phi_w$, drops for permeable regions further down the channel (for $n > 1$) resulting in a reduced flow through the wall, Eq. (4.15c). Yet, by creating an impermeable section closer to the inlet in the channel, we are losing the larger filtration pressures that give a greater flow of filtered water though the membrane.

4.5.1 Asymptotics for small permeability

The asymptotics for small permeabilities described in 4.4.2 hold in this more general case. However, calculating the filtration efficiency, (4.21), requires dividing the region up into n sections and considering the sections that are permeable,

$$E = \sum_{j=0}^{n-1} \int_{\frac{j}{n}}^{\frac{j+\lambda}{n}} \mathcal{V}\,\mathrm{d}x = \sum_{j=0}^{n-1} \int_{\frac{j}{n}}^{\frac{j+\lambda}{n}} \frac{\kappa_0}{\mathrm{Pe}}\,(p-\pi)\,\mathrm{d}x, \tag{4.36a}$$

$$= \frac{\kappa_0\ \lambda}{\mathrm{Pe}}\ \left(3\mathrm{Pe}\mathcal{D} - 1 - \frac{3\mathrm{Pe}\mathcal{D}}{2}\left(\frac{n-1+\lambda}{n}\right)\right) + \frac{\kappa_0^2}{\mathrm{Pe}}\ \sum_{j=0}^{n-1} \int_{\frac{j}{n}}^{\frac{j+\lambda}{n}} (p_1 - \pi_1)\,\mathrm{d}x, \tag{4.36b}$$

using (4.15c, 4.24a,d, 4.27a), with p_1 given in Eq. (4.27b) and $\pi_1 = \phi_1$ (4.24e) determined by solving the system (4.32).

The first term in Eq. (4.36b) (proportional to κ_0) matches that in Eq. (4.28b) for $n = 1$. The leading-order efficiency of filtration for the Zebra Channel is given by

$$\frac{E_0}{\kappa_0} = \frac{\lambda}{\mathrm{Pe}} \left(3\mathrm{Pe}\mathcal{D} - 1 - \frac{3\mathrm{Pe}\mathcal{D}}{2} \left(\frac{n-1+\lambda}{n} \right) \right), \tag{4.37}$$

analogously to Eq. (4.29) for $n = 1$. Again, the leading-order efficiency in the small-permeability (of order κ_0) limit may be negative. To ensure that E_0 (4.37) is positive we must again have a condition relating $\mathrm{Pe}, \mathcal{D}$ and λ, the fluid and geometric parameters of the system as in (4.30). For the case of n stripes, this can be generalized as either

$$\mathrm{Pe}\mathcal{D} > \frac{1}{3\left(1 - \frac{n-1+\lambda}{2n}\right)}, \qquad \text{or} \qquad \lambda < 2n \left(1 - \frac{n-1}{2n} - \frac{1}{3\mathrm{Pe}\mathcal{D}} \right), \tag{4.38}$$

where $0 \leq \lambda \leq 1$, $\mathrm{Pe} > 0$, $\mathcal{D} > 0$ and $n \geq 1$.

The value of λ that maximizes E_0, $\lambda^*_{\mathrm{asymp}}$, in the Zebra Channel may be calculated by solving $\mathrm{d}(E_0/\kappa_0)/\mathrm{d}\lambda = 0$ in Eq. (4.37). To leading order, this gives

$$\lambda^*_{\mathrm{asymp}} = \begin{cases} n\left(\frac{1}{2} - \frac{1}{3\mathrm{Pe}\mathcal{D}}\right) + \frac{1}{2}, & \text{for } n \leq \dfrac{3\mathrm{Pe}\mathcal{D}}{3\mathrm{Pe}\mathcal{D} - 2}, \\ 1, & \text{for } n > \dfrac{3\mathrm{Pe}\mathcal{D}}{3\mathrm{Pe}\mathcal{D} - 2}, \end{cases} \tag{4.39}$$

noting that λ^* cannot exceed 1 by construction. The expressions matches that in Eq. (4.31) for $n = 1$.

We note that for $n > 1$ we can get situations when the greatest net filtration occurs when $\lambda = 1$, *i.e.*, when the whole wall is permeable. This again may be explained by the loss of permeable regions nearer the inlet of the channel where the transmembrane pressure difference is higher, resulting in greater filtration. The result is telling us the importance of utilising these regions for filtration; the larger n is, the closer λ is to 1, and with a larger n we have more of these impermeable sections, but also they begin to occur closer to the inlet, where the transmembrane pressure difference is highest.

4.6 Asymmetric Zebra Channel

In the previous section, we have demonstrated how a Zebra Channel may address the problem of backflow due to osmosis near the end of the channel. In this section, we now consider a setup that also addresses the CP that still occurs in the osmotic backflow regions. We consider one channel wall, of unit dimensionless length, with

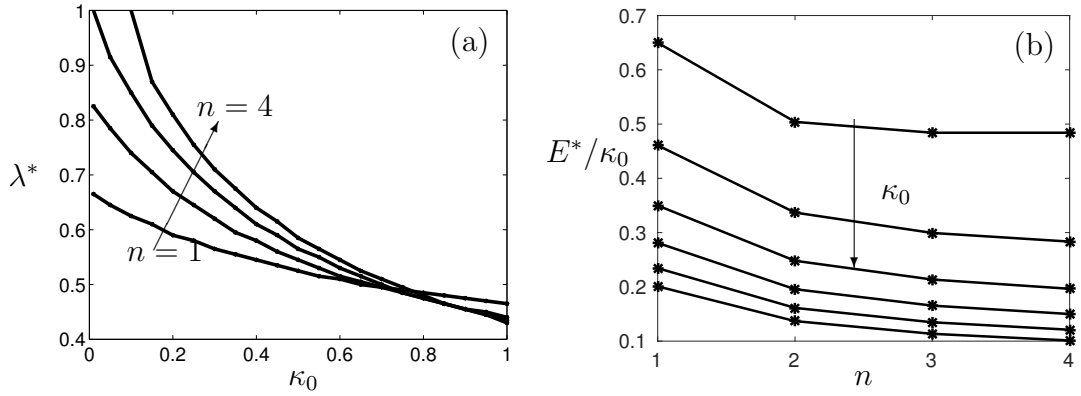

Figure 4.9: (a) The optimal ratio of permeable to impermeable wall components, λ^*, that maximizes flux of clean water out, F, versus wall permeability, κ_0 for $n = 1, 2, 3$ and 4 Zebra Channel segments. The $n = 1$ case corresponds to that in Figure 4.5b. (b) The optimal rescaled efficiency, E^*/κ_0, against number of zebra segments, n, for $\kappa_0 = 0.01, 0.2, 0.4, 0.6, 0.8, 1$. We take $\mathcal{D} = 1$ and $\mathrm{Pe} = 1$.

permeable and impermeable stripes that are of equal length, Λ, so that the number of stripes along the wall is $N = 1/\Lambda$ (which need not be an integer). We choose the permeable and impermeable regions of the opposing wall to be out of phase (Figure 4.10). We call this an *Asymmetric Zebra Channel*; the functional form of the varying permeability on each wall is analogous to that in Eq. (4.35) (but with equal sized permeable/impermeable regions). We note that in this setup there is always a part of a channel wall that is permeable on one side and closed on the other. This means that exactly half of the total channel walls available is permeable. For a given Λ we have $N^* = \mathrm{ceil}(1/\Lambda)$ permeable/impermeable sections in the channel, where $\mathrm{ceil}(x)$ denotes the ceiling function.

In this setup, the particles in the flow are originally advected towards the permeable wall before being advected across the channel to the other wall as the permeability switches. This process is repeated, with particles advected back and forth, for as many such stripes as we have in the channel. As a result, the overall particle concentration at the permeable regions of the walls (and hence the osmotic pressure) is reduced. Indeed, we would expect that the buildup of particles and any resulting contribution towards blocking and caking will be diminished in such a configuration, thus enhancing the lifetime of the membrane filtration system.

We again solve the governing equations (4.13). However, we no longer have the axial symmetry property for the flow and particle concentration since the permeability of our channel walls is out of phase. Symmetry breaking means that (4.15a) no longer

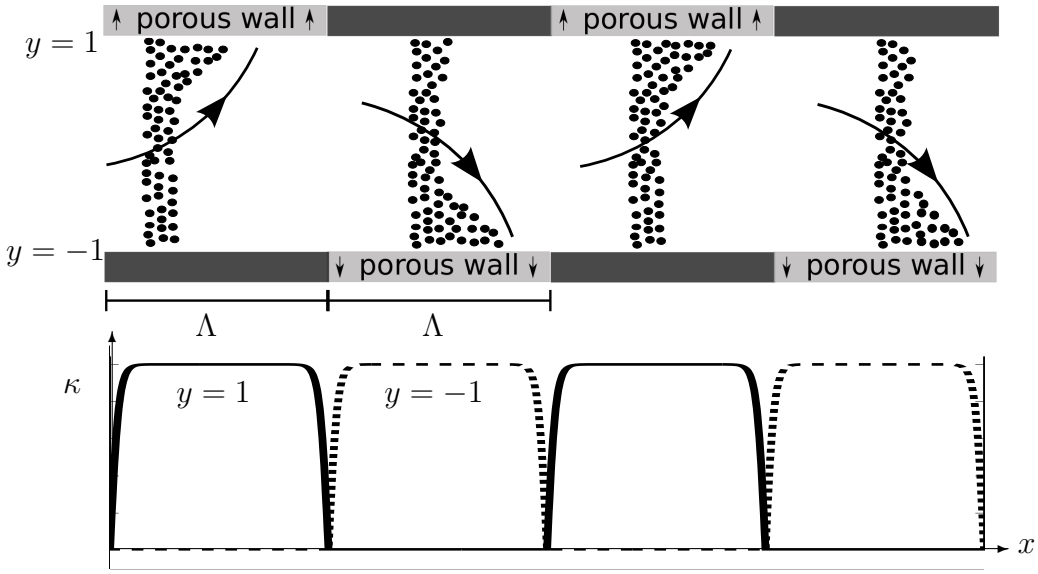

Figure 4.10: Schematic of a channel with fluid laden with particles entering from the left. The walls are alternately permeable and impermeable in the channel for a length Λ, as seen in a sketch of the permeability, κ, of the channel beneath. The solid line indicates the wall permeability at the wall located at $y = 1$ and the dashed line corresponds to the wall permeability at the wall located at $y = -1$.

applies. Instead we impose the following asymmetric boundary conditions

No axial slip:	$u = 0$	on $y = \pm 1$,	(4.40a)
Permeate flux:	$\mathcal{V}_\pm = \dfrac{\kappa_\pm(x)}{\mathrm{Pe}}\,(p - \phi_{w\pm})$	on $y = \pm 1$,	(4.40b)
Perfect filtering of particles:	$\mathrm{Pe}\ \mathcal{V}_\pm \phi - \dfrac{\partial \phi}{\partial y} = 0$	on $y = \pm 1$,	(4.40c)
Fluid influx:	$\displaystyle\int_0^1 u \,\mathrm{d}y = 1$	at $x = 0$,	(4.40d)
Fixed outlet pressure:	$p = 0$	at $x = 1$,	(4.40e)
Inlet condition:	$\phi \equiv 1$	at $x = 0$,	(4.40f)

where (4.40b) and (4.40c) will vary depending on which wall is permeable as $\kappa_\pm$ is zero on one wall section on one side, and takes a form as in (4.35) on the other side, alternating as stripes change, and $\mathcal{V}_\pm$ and $\phi_{w\pm}$ are the permeate flux and the particle concentation at either wall, $y = \pm 1$, respectively.

We solve for the axial velocity, u, using the x-momentum equation (4.13b) with the no-slip boundary conditions (4.40a), to obtain the same form of u as before (4.16a)

$$u(x, y) = \frac{1}{\mathrm{Pe}\mathcal{D}} \frac{\mathrm{d}p}{\mathrm{d}x} \frac{y^2 - 1}{2}. \tag{4.41}$$

However, the transverse velocity differs from (4.16b) due to the breaking of symmetry and the fluid is filtered alternatingly from each wall, now given by

$$v(x,y) = \frac{1}{\mathrm{Pe}\mathcal{D}} \frac{\mathrm{d}^2 p}{\mathrm{d}x^2} \frac{3y - y^3 \pm 2}{6}, \tag{4.42}$$

using (4.13a) and (4.40b), where the ± 2 term corresponds to regions of the channel wall in which the impermeable wall is located at $y = \mp 1$ respectively. The hydrodynamic pressure in the channel is determined by the permeate-flux boundary condition for the transverse velocity, (4.40b). Using Eq. (4.42) at $y = \pm 1$ and the boundary condition (4.40b) again results in an ODE for the hydrodynamic pressure

$$\frac{2}{3} \frac{\mathrm{d}^2 p}{\mathrm{d}x^2} = \mathcal{D}\kappa_{\pm}(x) \left(p - \phi_{w\pm}\right). \tag{4.43}$$

Here, we are implicity choosing the appropriate permeability, $\kappa_{\pm}(x)$, and wall concentration, $\phi_{w\pm}$, to be the permeable side in the channel as we solve in the asymmetric Zebra Channel. It differs from the earlier pressure ODE (4.17) by the factor of two on the left hand side. This accounts for the fact that half the total available channel wall is permeable and half is impermeable. It affects the system by reducing the pressure gradient in the channel. As there is half the permeable wall availabe in each section, less fluid can be filtered in the area and so the pressure gradient is halved.

We solve the coupled advection–diffusion equation, (4.13d), and ODE for the pressure, (4.43), numerically for spatially varying permeability using finite differences, subject to the boundary conditions (4.40c-f). The particle concentration, ϕ, exhibits CP in the permeable regions and the particles are advected across the channel as the permeability switches at the walls (Figure 4.11(a)). The osmotic pressures at both walls exceed the hydrodynamic pressure, p, for some portion of the channel (Figure 4.11(b)), which results in a backflow by osmosis.

The total flux, F, behaves in a surprising manner as we vary the number of stripes in the channel, N (Figure 4.12). In particular we observe a peak in the rescaled efficiency, E/κ_0, when N is an integer, N^*, that is, when we fit an integer number of permeable and impermeable regions into the Asymmetric Zebra Channel. These apparent local optima may be explained by considering the effects of our placement of the permeable and impermeable regions. At a permeable wall, particles accumulate due to advection, but, as we move down the channel, the hydrodynamic pressure difference decreases, and so the particle concentration will fall as the influence of back-diffusion becomes more prominent. If we switch to an impermeable wall too late (choose Λ too large) then the pressure will fall too low resulting in a weaker

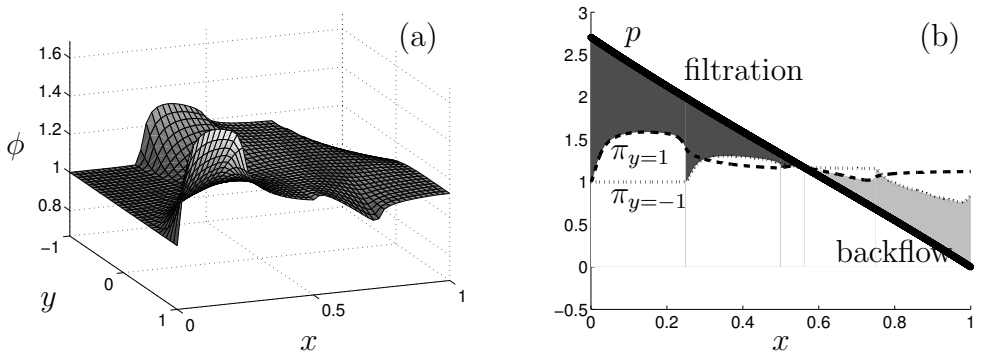

Figure 4.11: (a) Particle concentration in an Asymmetric Zebra Channel with alternating permeable walls of spatially varying permeability (4.23) with $\Lambda = 0.25$. The particle concentration is advected to the permeable wall and induces CP. (b) The difference in hydrodynamic pressure, p, (solid) and osmotic pressures, π, at each wall (the dashed curve corresponds to the wall at $y = 1$ and the dotted curve corresponds to the wall at $y = -1$). The dark shaded region indicates filtration and the light shaded region indicates backflow. Here we take $\mathcal{D} = 1$, $\mathrm{Pe} = 1$ and $\kappa_0 = 1$.

outflow. If we switch too early (Λ too small) then we increase the likelihood of the wall becoming permeable again before particles have had a chance to diffuse away during the impermeable region, thus reducing the permeate flux when the wall becomes permeable again. Switching when $1/\Lambda = N \in \mathbb{N}$ results in a locally maximized flux.

4.6.1 Asymptotics for small permeability

The analysis for the Asymmetric Zebra Channel follows the same approach as for the Zebra Channel. However we now substitute the pressure and volume fraction perturbations in Eq. (4.24) into (4.43), subject to boundary conditions (4.26). The leading- and first-order ODEs in κ_0 are

$$\frac{\mathrm{d}^2 p_0}{\mathrm{d}x^2} = 0, \qquad \frac{\mathrm{d}^2 p_1}{\mathrm{d}x^2} - \frac{3}{2}\mathcal{D}p_0 + \frac{3}{2}\mathcal{D} = 0, \tag{4.44a,b}$$

and the boundary conditions (4.26) are restated below

$$\left.\frac{\partial p_0}{\partial x}\right|_{x=0} = -3\mathrm{Pe}\mathcal{D}, \qquad p_0(1) = 0, \qquad \left.\frac{\partial p_1}{\partial x}\right|_{x=0} = 0, \qquad p_1(1) = 0, \tag{4.45a,b,c,d}$$

to give

$$p_0 = 3\mathrm{Pe}\mathcal{D}\,(1-x)\,, \qquad p_1 = -\frac{3}{4}\left(\mathrm{Pe}Dx^3 + (1-3\mathrm{Pe}D)\,x^2 + 2\mathrm{Pe}D - 1\right). \tag{4.46a,b}$$

As expected the form of p_0 in Eq. (4.46a) corresponds to Poiseuille flow in a channel with impermeable walls, as in the Zebra Channel (4.27a). The pressure perturbation

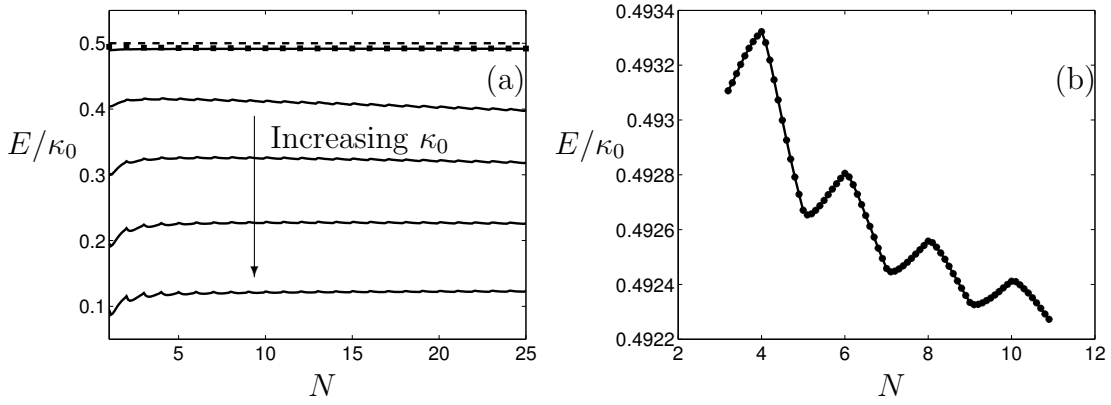

Figure 4.12: (a) Rescaled efficiency through the asymmetric zebra permeable walls, E/κ_0, against the inverse of the length of the permeable region, Λ, for $\kappa_0 = \{0.01, 0.1, 0.25, 0.5, 1\}$ where the direction of increasing κ_0 is indicated. The dashed black line and the squares show the leading-order and first-order asymptotic results (4.49), respectively, for a small κ_0, shown with $\kappa_0 = 0.01$. (b) A close-up of the the first-order solution with the presence of peaks for $\kappa_0 = 0.01$, where the dots match the squares in (a) illustrating the contribution of the particles to the effect of the local maxima. We take $\mathcal{D} = 1$ and $\mathrm{Pe} = 1$.

due to the asymmetric permeable channel regions (4.46b) is half that of the Zebra Channel case (4.27b), as expected from the form of the pressure ODEs, *cf.* (4.17), and (4.43).

The total flux of fluid through the Asymmetric Zebra Channel walls with permeable region of length Λ is given by

$$F = \int_0^1 \mathcal{V}_+ \,\mathrm{d}x - \int_0^1 \mathcal{V}_- \,\mathrm{d}x, \tag{4.47}$$

where $\mathcal{V}_\pm = v(x, y = \pm 1)$, which replaces (4.22), and noting that $\mathcal{V}_-$ is a negative fluid *velocity*. As there is always a permeable channel wall region on one side of the channel, there is filtration occuring for every value of x, and we can write (4.47) as

$$F = \int_0^1 \mathcal{V}_+ \,\mathrm{d}x - \int_0^1 \mathcal{V}_- \,\mathrm{d}x = \int_0^1 \frac{\kappa_0}{\mathrm{Pe}} \left(2p - \pi_{w+} - \pi_{w-}\right) \,\mathrm{d}x, \tag{4.48}$$

where $\pi_{w+} = \pi(x, y = 1)$ and $\pi_{w-} = \pi(x, y = -1)$ are the osmotic pressure at either wall. The efficiency is given by $E = F$ (4.21). Substituting the perturbations (4.24), with the pressure given in (4.46), the efficiency is given asymptotically as

$$E = \kappa_0 \, \frac{1}{\mathrm{Pe}} \, \left(\frac{3\mathrm{Pe}\mathcal{D}}{2} - 1\right) + \kappa_0^2 \, \left(\int_0^1 \left[(p_1 - \pi_1)\right]_{y=-1} \,\mathrm{d}x + \int_0^1 \left[(p_1 - \pi_1)\right]_{y=1} \,\mathrm{d}x\right). \tag{4.49}$$

The order-κ_0 efficiency (4.49) is a constant that is independent of Λ (Figure 4.12), since the total length of the channel walls that is permeable is the same regardless of the value of Λ. As such, the leading order behaviour, where the particle concentration is constant, $\phi_0 \equiv 1$, does not explain the behaviour of the observed peaks in Figure 4.12(a). That behaviour must be determined by the perturbation to the particle concentration, and hence osmotic pressure, at the walls given by the order-κ_0 efficiency in (4.49).

The term $\pi_1 = \phi_1$ is determined by substituting the perturbation expansion (4.24d) into the advection–diffusion equation (4.13d), the asymmetric boundary condition (4.40c), and the zero inlet condition, $\phi_1(0, y) = 0$. The resulting order-κ_0 equations are

$$\frac{\partial \phi_1}{\partial x} = \frac{2}{3\ \mathrm{Pe}\ (1 - y^2)} \frac{\partial^2 \phi_1}{\partial y^2}, \tag{4.50a}$$

$$\frac{\partial \phi_1}{\partial y} = \mathrm{Pe}\ v_1 \phi_1, \qquad y = \pm 1, \tag{4.50b}$$

$$\phi_1 = 0, \qquad x = 0. \tag{4.50c}$$

These equations must be solved numerically for ϕ_1. The flux (4.49) can now be calculated for various values of Λ. The order-κ_0^2 flux captures the local optima behaviour observed in the the full numerical solution (Figure 4.12). As the leading-order term is independent of Λ, this suggests that the local optima behaviour is a result of the movement of particles in the channel, *i.e.*, that an integer number of permeable and impermeable regions in the Asymmetric Zebra Channel corresponds to a natural frequency for the advection of particles both across and down the channel.

Finally, we note that as we increase the Péclet number, via increasing the inlet flux, $\hat{Q}$, the leading-order measure of net filtration tends to a constant

$$\frac{E}{\kappa_0} \sim \frac{3}{2}\mathcal{D}, \qquad \text{as} \qquad \mathrm{Pe} \to \infty, \tag{4.51}$$

for low wall permeabilities, maximizing the efficiency to leading order.

4.7 Conclusions

In this chapter, we have explored the idea of tailoring the wall permeability in a permeable channel to optimize the amount of fluid that is filtered. This addresses deleterious problems in filtration such as backflow due to osmosis and energy cost for

the case where the outlet pressure is the same as the permeate side pressure. We consider the early stages of particle buildup in which filtration is compromised by an osmotic pressure opposing the filtration process. Further study is required to address later-stage mechanisms such as deposition, fouling and cake formation; aspects of these will be addressed in Chapters 5–7 as we develop a model to explain the gradual increase in pressure over time during filtration.

We introduced a channel with walls composed of permeable and impermeable regions. An optimum permeable wall fraction that maximizes the net flux of fluid filtered at the walls is found. This optimum arises as a result of the competing effects of hydrodynamic pressure, allowing filtration, and osmosis, causing a flow of the filtered fluid back into the channel. The optimum is a design parameter that is a decreasing function of the permeability; this indicates that setups composed of walls with higher permeability are optimized with smaller permeable regions. This is due to larger permeabilities resulting in larger filtration velocities, inducing a greater transport of particles to the wall and thus causing osmotic backflow to occur earlier in the channel. Our numerical results match an asymptotic result for small wall permeabilities.

Similar optima are found when varying the Péclet number. However, here the optimal permeable wall fraction increases with the Péclet number, due to the dependence of the pressure on this parameter. An asymptote occurs due to the inevitable backflow at the end of the channel. An optimal Péclet number that maximizes filtration efficiency exists due to a boundary layer at the wall that increases the osmotic pressure.

We considered the effect of the Péclet number on the energy cost of filtration. We find that, given a certain fraction of permeable wall, an optimal value for the Péclet number exists that minimizes the energy to filter a given quantity of liquid. Furthermore that optimal Péclet number increases with the fraction of the wall that is permeable. Given this, an optimal fraction of permeable wall exists that minimizes the energy.

We generalize the idea of segmenting the wall permeability to that of a striped series of permeable and impermeable regions. The efficiency increases as concentration polarization is reduced periodically; the concentration diffuses towards a uniform profile in the impermeable regions. However, we have introduced impermeable regions to sections of the pipe where the transmembrane pressure is at its greatest, *i.e.*, near the entrance of the pipe. This greatly reduces the efficiency of filtration. The overall effect is to reduce the efficiency of filtration.

An asymmetric version of the striped regions is considered. The result is a series of local optima in the efficiency for the striping pattern. These optima coincide with integer multiples of stripes in the channel, and is shown to be a particle effect in the asymptotic limit of a small permeability. This suggests a resonance effect in the system, however, further work is required to fully understand this observation.

As stated, the model presented is suitable for the early stages in a filtration process, before caking, blocking and fouling occur. By increasing the efficiency of the filtration process at this stage, we expect this to have favourable repercussions later on in the process by significantly reducing the volume of fluid to be filtered at higher pressures.

Chapter 5

Directflow Filtration

Summary

During filtration at constant flux, the transmembrane pressure is observed to increase gradually over time. In this chapter and the following two chapters we form a model that combines fluid flow, poroelasticity, fouling, and caking to explain this phenomenon via elasticity-induced pore expansion; we study this in the context of directflow filtration. In this chapter, we consider only the fluid flow in a directflow device, which is composed of a series of individual modules. The flux through each tube is coupled to the others, and we focus on this coupling for both 2D channels and 3D tubes. The quantity of interest is the transmembrane pressure difference, which we show is approximately constant along the length of the membrane under certain conditions. This result will be a useful simplification in the subsequent chapters.

5.1 Overview

During filtration, the driving pressure required to filter fluid at a constant flux increases over time. This increase is attributed to caking and fouling. At regular intervals a backflush is performed, removing the cake layer and decreasing the driving pressure for the next period of filtration. However, experimental results show that backflushing does not return the pressure to the baseline value (at the start of filtration), as in Figure 5.1 (Delgrange-Vincent et al., 2000; Ye et al., 2011). In fact, after each backflush, the new driving pressure is greater than that at the start of

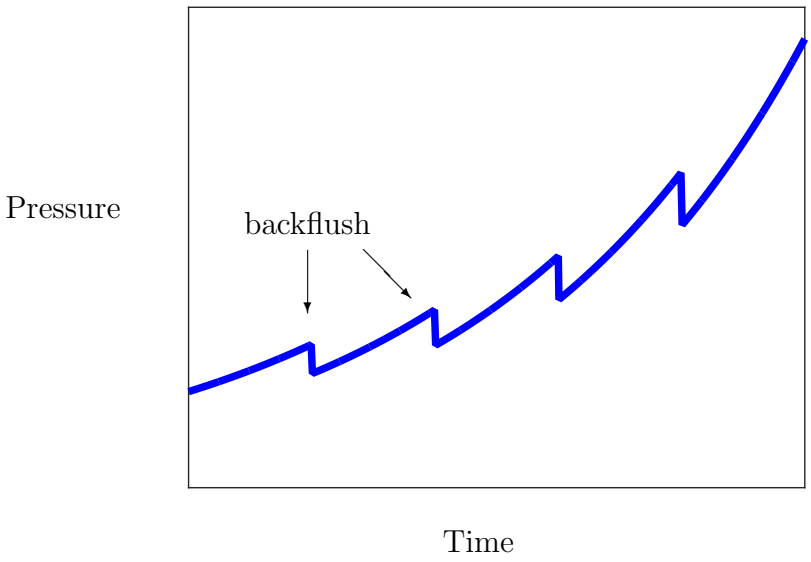

Figure 5.1: Sketch of the driving pressure over time in a directflow device operating at constant flux. A cake layer builds up over time, increasing the pressure. At regular intervals, backflushing is performed, removing the cake layer and reducing the filtration pressure. This causes the regular drops in pressure, which do not return the pressure to its baseline value.

the previous filtration run. Furthermore, the increase over each subsequent run is larger than that in the previous run. As a result, the filtration process becomes less energetically efficient with time. The analogue of this pressure-time *signature* when operating at constant pressure has also been reported: the flux gradually declines over time with only partial recovery in the flux of filtered fluid after backflushing (Hong et al., 2005).

We argue that these experimental results can be explained by the elastic deformation of the membrane during filtration. The pores initially reject the particles, causing a cake layer to grow. However, the membrane is deformed by the stress of the fluid flow and cake layer; the pores increase in size and allow internal, irreversible fouling of the membrane. A pressure increase is then required to maintain a constant fluid flux. After backflushing, the cake layer is removed but most particles caught in the pores remain (Remize et al., 2010). The process for this multi-stage model is summarized in the flow chart in Figure 5.2.

In this chapter, we study the flow in a directflow module (a single tube in the array of the directflow device). We make an observation about the flow that allows us to simplify the model to a 2D cross-section of the tube. In Chapter 6, the poroelastic

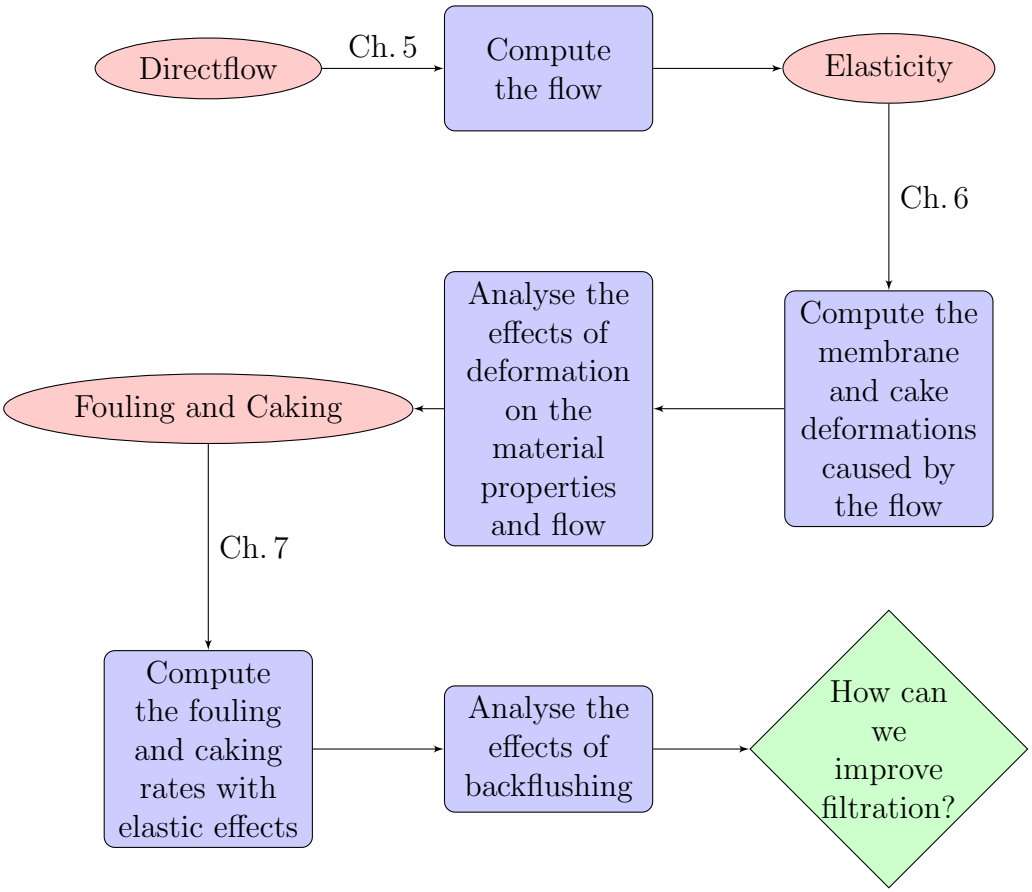

Figure 5.2: Flow chart mapping out the significant steps to be taken in the remaining chapters. The three major sections are: analysing the flow in a directflow device (this chapter), modelling the elastic response of a membrane and cake layer due to the flow (Chapter 6), and modelling the time evolution of fouling and caking, with backflushing (Chapter 7).

deformations of the membrane and cake layer are analysed, as well as their effect on the material properties (*e.g.*, membrane poresize) and flow (*e.g.*, membrane permeability). In Chapter 7, we study the rates of fouling and caking due to a constant flux of particles into the tubes, with periodic backflushes and incorporating elasticity effects. This enables us to consider how we may improve filtration effectiveness and efficiency.

5.2 Introduction

In Chapters 3 and 4, we discussed models of two features of the usual configuration of crossflow filtration. An alternative form of crossflow filtration is directflow filtration,

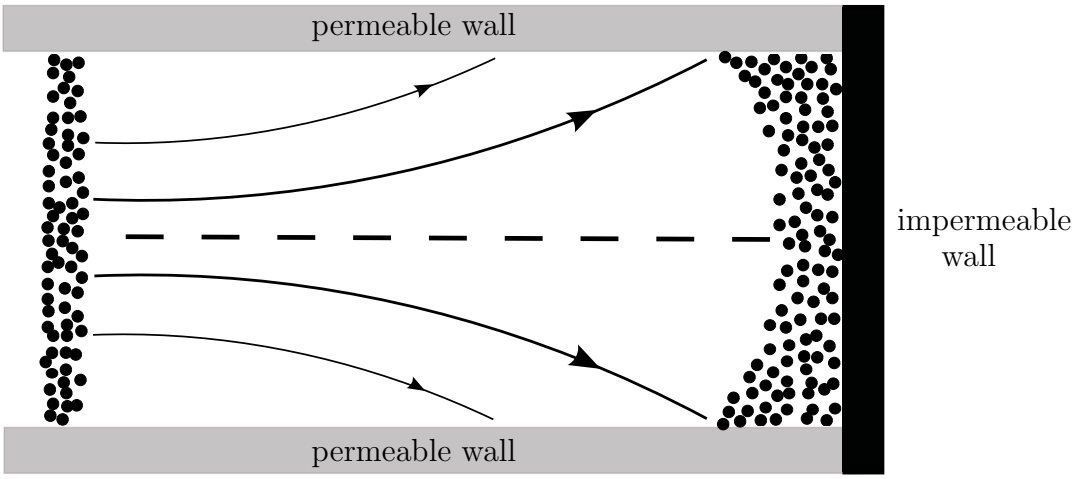

Figure 5.3: A schematic of the feed in a channel during directflow filtration. The channel has porous walls and an impermeable capped end. The contaminated water (particulate feed) enters the channel and builds up at the walls, especially at the impermeable end.

as in Figure 5.3. Here, again the device consists of long and thin tubes or channels with permeable membrane walls. However, rather than the retentate being able to flow out of the end of the tube, each tube has an impermeable capped end. The impermeable cap forces all the fluid to pass through the permeable walls. The clean water on the permeate side then flows out of the device and all the contaminants (particles) either remain within the tube or within the pores of the membrane. The capped end does not allow for re-circulation of the feed. As a result, the particle concentration builds up from the capped end, resulting in fouling: pore blocking and caking. Removing these particles requires frequent backflushing. In the case of constant driving pressure, these mechanisms contribute towards resistance to flow and a decline in the permeate flux. In the case of constant flux, the pressure (and hence power required to operate the device) increases, as in crossflow and dead-end filtration.

There are many advantages to directflow filtration. In particular, it is a simple setup that does not require re-circulation (batch mode) or a continuous system where the retentate from one stage is the feed for the next, as in more traditional crossflow systems. This results in lower pressure drops across the system and makes it possible to use much finer feed channels (Pearce, 2011). Furthermore, the directflow setup requires little maintenance (Ravazzini et al., 2005). Empirical observations suggest that the feed and permeate flows can result in a constant transmembrane pressure

difference (TMP) (Pearce, 2011). The same flux of fluid is thus filtered through each point along the membrane (Pearce, 2013). We will try to understand this for a directflow device operating at constant inlet flux, which is the condition of most interest to industry.

In regular crossflow, an analytical expression for the pressure drop along the channel/tube has been derived assuming a constant wall permeability (Karode, 2001). This expression includes a free parameter, f, that measures the fractional recovery (ratio of permeate flux to influx). The capped end of a directflow module means that all the fluid entering the tube is filtered by the membrane, *i.e.*, $f = 1$. It is possible to set $f = 1$ in the result of Karode (2001) so that a pseudo-directflow process is in operation. However, this still differs from a capped end directflow setup: the exit to the channel/tube is open (at $p = 0$) so that the flow is fundamentally different to that with a capped end, and this study does not consider the flow on the permeate side or the effect of other modules. Similarly, other studies of solute transport in a thin porous tube with variable wall permeability examine situations of zero net axial flux at the exit (Griffiths et al., 2013).

Hurwitz (1989) considered the flow inside a single porous tube with a capped end. The flow was solved asymptotically in the limits of low permeability and low Reynolds number. However, the coupling that results from the flow on the permeate side was not considered.

In this chapter, we develop a mathematical model of the flow in a directflow filter. We consider only the fluid mechanics in this setup and ignore the transport or effect of particles. We model the feed and permeate flow in a single filter (both 2D and 3D) of the directflow device. The flow obeys the usual thin-layer flow equations with a transmembrane pressure difference across the membrane boundary. We show that this transmembrane pressure difference is approximately constant along much of the membrane, confirming the intuition of those who work in the field (Pearce, 2013).

5.3 Directflow

5.3.1 Setup

We begin by considering a 2D analogue of the directflow device. We consider the flow in a single 2D channel (one module in the array that constitutes the device),

of typical length L and width $2H$, with permeable walls. The permeability of the channel walls, $\hat{k}$, is constant, and the end of the channel is capped (impermeable), as in Figure 5.4. A fixed flux, $2\hat{Q}$, of fluid enters the channel (Region 1), passes through the membrane walls at the side, and into the permeate region (Region 2). For an isolated channel we would just consider Region 1 inside the channel and a quiescent bath outside. In reality, other channels are nearby so the flow in Region 2 must be considered. Since the end of the channel is blocked, all of the fluid must eventually flow through the permeable walls from Region 1 into Region 2: a flux $\hat{Q}$ through each side of the channel by symmetry. We envisage an array of such channels with a centre–centre separation $2(H + D)$ and so impose a symmetry condition at $\hat{x} = \pm(H + D)$.

Typically, for hollow-fibre membrane module configurations, $L = 1.5$m and $2H = 0.7 - 1$mm, so that the aspect ratio, $\delta \ll 1$. The channel spacing range is $D = 0.2 - 2.5$mm; this range covers values that are both smaller and larger than the width of the channel. The Reynolds number is 1000, however, the reduced Reynolds number (Eq. (2.2)) is small (Pearce, 2011).

The fluid velocity field in the $(\hat{x}, \hat{z})$ directions is $\hat{\boldsymbol{u}} = (\hat{u}(\hat{x}, \hat{z}), \hat{w}(\hat{x}, \hat{z}))$, while the pressures in Regions 1 and 2 are $\hat{p}$ and $\hat{q}$ respectively. The quantity of most interest is $\hat{p} - \hat{q}$ at $\hat{x} = \pm H$, that is, the transmembrane pressure difference (TMP).

5.3.2 Governing equations

Since the reduced Reynolds number is small and the channel is thin, the fluid flow will obey the thin-layer flow equations (*cf.* §2.3.1). Axial symmetry in the 2D channel means that we need only solve the system for $(\hat{x}, \hat{z}) \in ([0, H + D], [0, L])$.

We non-dimensionalize lengths with the height of the channel, L, and use the small aspect ratio, $\delta = H/L \ll 1$. Similarly, the velocities are scaled with the typical axial velocity, W:

$$\begin{aligned} \hat{z} &= Lz, & \hat{x} &= \delta L x, & \hat{w} &= W w, & \hat{u} &= \delta W u, \\ \hat{p} &= \frac{\mu W}{\delta^2 L} p, & \hat{q} &= \frac{\mu W}{\delta^2 L} q, & \hat{Q} &= \delta W L Q, & \hat{k} &= \delta^5 L^2 \kappa. \end{aligned} \tag{5.1}$$

In this model, we allow for variations in the dimensionless flux, Q, the effective membrane permeability, κ, and the parameter $l = D/\delta L$ characterizing the inter-module separation.

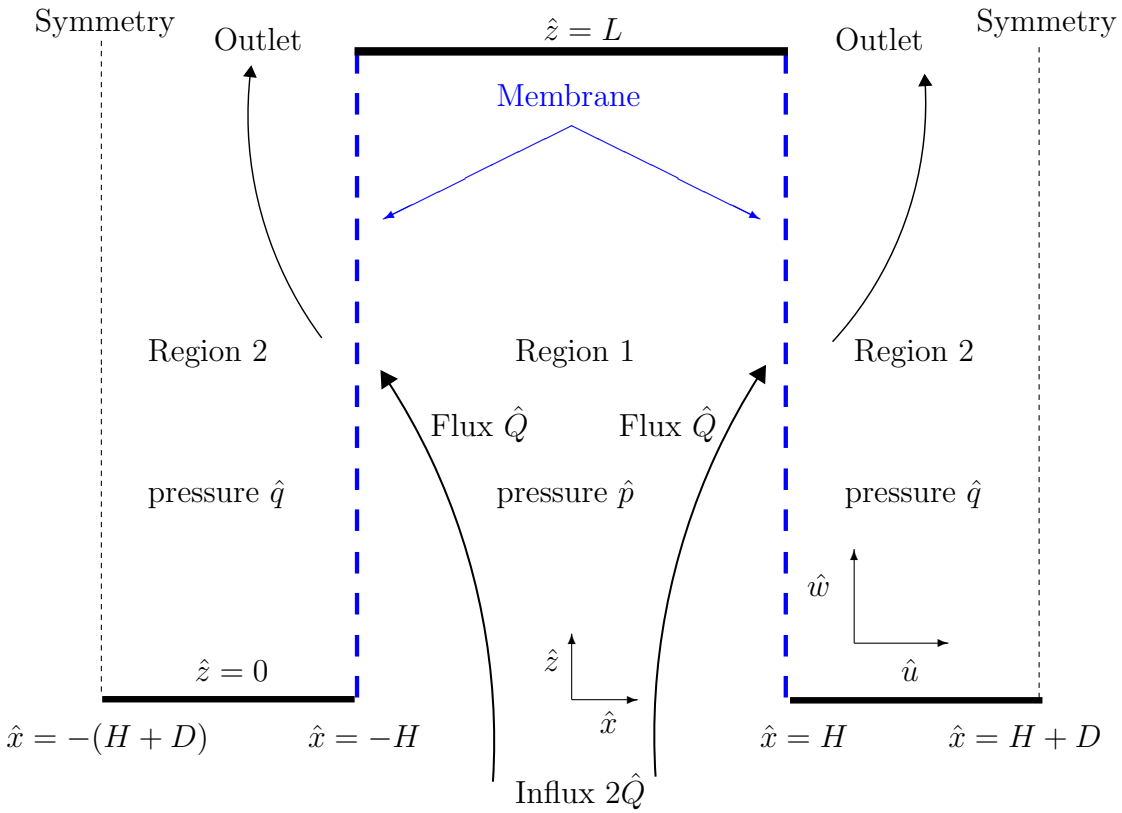

Figure 5.4: A schematic of a directflow capsule. Solid lines denote impermeable walls, the blue dashed lines are permeable walls, and the skinny-dashed line indicates symmetry in the flow. Flow enters from the bottom, passes through the permeable walls and then continues to the outlet. We label the inside of the membrane-walled channel as Region 1 and outside as Region 2. In a typical device, there is a series of such channels lined up together. This results in a symmetry of the flow at each side, outside of the channel. The flow follows the black arrows. The (spatially variable) pressure inside the channel is $\hat{p}$ and outside the channel is $\hat{q}$.

In Region 1 ($0 < x < 1$ and $0 < z < 1$), we have the thin-layer flow equations

$$\frac{\partial u}{\partial x} + \frac{\partial w}{\partial z} = 0, \tag{5.2a}$$

$$\frac{\partial^2 w}{\partial x^2} = \frac{\mathrm{d}p}{\mathrm{d}z}. \tag{5.2b}$$

These equations are subject to boundary conditions (a reduced set since the thin-layer equations reduce the order of the Stokes equations) that reflect the symmetry of the flow, the influx of fluid, no flux through the impermeable end, no-slip at the porous wall, and a filtration velocity that is proportional to the transmembrane pressure difference and permeability of the membrane, *i.e.*,

Symmetry:	$\dfrac{\partial w}{\partial x} = u = 0,$	on $x = 0,$	(5.3a)
No axial wall slip:	$w = 0,$	on $x = 1,$	(5.3b)
Permeate flow:	$u = \kappa\,(p - q)\,,$	on $x = 1,$	(5.3c)
Fluid influx:	$\displaystyle\int_0^1 w\,\mathrm{d}x = Q,$	at $z = 0,$	(5.3d)
No fluid outflux:	$w = 0,$	at $z = 1.$	(5.3e)

As the end is capped all injected fluid must pass through the membrane, and so

$$\int_0^1 u\,\mathrm{d}z = Q \qquad \text{at} \qquad x = 1. \tag{5.4}$$

In this model, there is a transverse flow, u, at the capped end, $z = 1$. In reality, there is a no-slip condition, $u = 0$, here. However, in the case of a long and thin channel (or tube) with a small reduced Reynolds number, this no-slip condition influences the flow only in a boundary layer of size δ near the capped end (Hurwitz, 1989). Hence, we neglect this effect in our model.

In Region 2 ($1 < x < 1 + l$ and $0 < z < 1$), the fluid also obeys the thin-layer flow equations

$$\frac{\partial u}{\partial x} + \frac{\partial w}{\partial z} = 0, \tag{5.5a}$$

$$\frac{\partial^2 w}{\partial x^2} = \frac{\mathrm{d}q}{\mathrm{d}z}. \tag{5.5b}$$

The boundary conditions reflect the symmetry of the flow, the impermeable bottom, a fixed outlet pressure, no-slip at the porous wall, and continuity of velocity across

the membrane, *i.e.*,

$$\begin{aligned}
&\text{Symmetry:} && \frac{\partial w}{\partial x} = u = 0, && \text{on } x = 1 + l, && (5.6a)\\
&\text{No axial wall slip:} && w = 0, && \text{on } x = 1, && (5.6b)\\
&\text{Permeate flow:} && u = \kappa\,(p - q)\,, && \text{on } x = 1, && (5.6c)\\
&\text{No fluid flux:} && w = 0, && \text{at } z = 0, && (5.6d)\\
&\text{Fixed outlet pressure:} && q = 0, && \text{at } z = 1. && (5.6e)
\end{aligned}$$

The permeate-flow boundary conditions (5.3c) and (5.6c) are the same, reflecting continuity of flux across the membrane.

5.3.3 Flow in a directflow device

The system of equations (5.2), (5.3), (5.5), and (5.6), can be solved analytically. Using both sets of symmetry and no axial wall slip conditions (Eqns. (5.3a,b) and (5.6a,b)), we can find the fluid velocities in terms of the pressures. In Region 1 we have

$$w = \frac{1}{2}\frac{\mathrm{d}p}{\mathrm{d}z}(x^2 - 1), \tag{5.7a}$$

$$u = \frac{1}{6}\frac{\mathrm{d}^2p}{\mathrm{d}z^2}(3 - x^2)x, \tag{5.7b}$$

while in Region 2,

$$w = \frac{\mathrm{d}q}{\mathrm{d}z}\left[\frac{1}{2}x^2 - (1+l)x + l + \frac{1}{2}\right], \tag{5.8a}$$

$$u = \frac{\mathrm{d}^2q}{\mathrm{d}z^2}\left[-\frac{1}{6}x^3 + \frac{1}{2}(1+l)x^2 - \left(l + \frac{1}{2}\right)x - \frac{1}{3}(1+l)^3 + \left(l + \frac{1}{2}\right)(l+1)\right]. \tag{5.8b}$$

In each region, we find a Poiseuille profile for the axial velocity, and a transverse velocity that is proportional to the second pressure derivative and cubic in the coordinate x. These are as expected with flow in a channel with porous walls, as seen in Chapters 3 and 4, and in Hurwitz (1989) and Probstein (1989). However, we shall see that pressure itself is affected by the capped end of the channel.

Using the axial velocities in (5.7a) and (5.8a), we can rewrite some of the boundary conditions of the system. The fluid influx condition (5.3d) becomes

$$\left.\frac{\mathrm{d}p}{\mathrm{d}z}\right|_{z=0} = -3Q. \tag{5.9}$$

The conditions of no flux of fluid through the capped end in Region 1 (5.3e), and an impermeable bottom in Region 2 (5.6d), become

$$\left.\frac{\mathrm{d}p}{\mathrm{d}z}\right|_{z=1} = 0, \qquad \left.\frac{\mathrm{d}q}{\mathrm{d}z}\right|_{z=0} = 0, \tag{5.10}$$

respectively.

Substituting the transverse velocity expressions, (5.7b) and (5.8b), into the boundary conditions for the permeate flux through the membrane, (5.3c) and (5.6c), gives a set of second-order ordinary differential equations (ODEs) for the pressures, p and q. Along with the two boundary conditions each, from (5.6e), (5.9) and (5.10), the system reads

$$\frac{1}{3}\frac{\mathrm{d}^2 p}{\mathrm{d}z^2} = \kappa\,(p-q)\,, \qquad \left.\frac{\mathrm{d}p}{\mathrm{d}z}\right|_{z=0} = -3Q, \qquad \left.\frac{\mathrm{d}p}{\mathrm{d}z}\right|_{z=1} = 0, \tag{5.11a}$$

$$\frac{l^3}{3}\frac{\mathrm{d}^2 q}{\mathrm{d}z^2} = \kappa\,(q-p)\,, \qquad \left.\frac{\mathrm{d}q}{\mathrm{d}z}\right|_{z=0} = 0, \qquad q(z=1) = 0. \tag{5.11b}$$

The system of ODEs (5.11) may be solved analytically. The pressures on either side of the membrane may be written as

$$p(z) = \frac{1}{1+l^3}\left[l^3\mathcal{M}(z) + 3Q(1-z) + \mathcal{M}_0\right], \tag{5.12a}$$

$$q(z) = \frac{1}{1+l^3}\left[-\mathcal{M}(z) + 3Q(1-z) + \mathcal{M}_0\right], \tag{5.12b}$$

where

$$C_1 = \sqrt{3\kappa\left(1+\frac{1}{l^3}\right)}, \tag{5.13a}$$

$$\mathcal{M}(z) = \operatorname{sech}(C_1)\left[\mathcal{M}_0\cosh(C_1 z) + \frac{3Q}{C_1}\sinh(C_1(1-z))\right], \tag{5.13b}$$

$$\mathcal{M}_0 = \frac{3Q}{C_1}\left[\frac{1}{l^3}\coth(C_1) + \operatorname{csch}(C_1)\right]. \tag{5.13c}$$

We can consider the behaviour of these pressures for different separation distances, l. When $l = 1$, there is a negative pressure gradient on both sides of the membrane (p are q and decreasing, as seen in Figure 5.5(a)) with the pressure in Region 1 larger than the pressure in Region 2. This means that there is a flow of fluid in the z-direction on each side of the membrane. When $l = 10$, the outside pressure, q, is effectively zero everywhere (Figure 5.5(b)), equivalent to a quiescent bath (*i.e.*, unaffected by the flow from the channel).

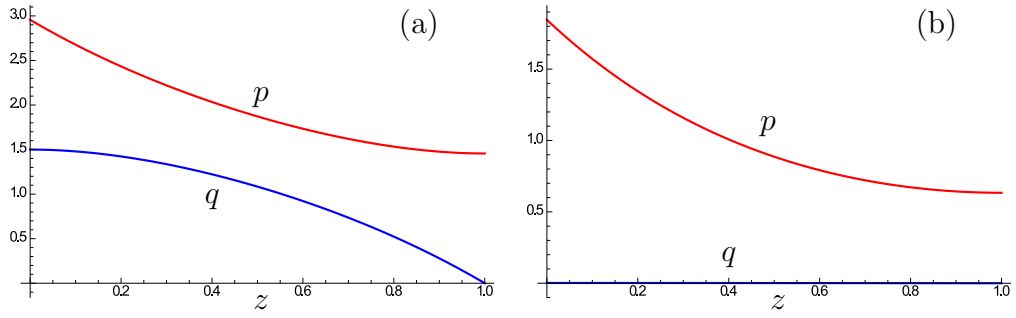

Figure 5.5: The fluid pressure inside the channel, p (red), and outside the channel, q (blue). Here the permeability is $\kappa = 1$ and the flux is $Q = 1$, with separation distances (a) $l = 1$ and (b) $l = 10$.

In fact the quantity of real interest is not p and q separately but rather the TMP, that is, $p - q$. This quantity is simply given by the function $\mathcal{M}$ (5.13b). We investigate the effect on the TMP of variations in the flux, Q, the permeability, κ, and the separation distance, l, as shown in Figure 5.6.

As Q increases, the TMP (5.13b) increases linearly at each point along the membrane. In general, the TMP has a parabolic shape so that more of the fluid is filtered near the entrance and capped end (Figure 5.6(a)). For small values of Q, the TMP is approximately constant along the membrane. When Q is larger, the TMP retains the qualitative shape, but varies to a larger degree along the membrane.

The TMP has the same qualitative shape as we vary κ (Figure 5.6(b)). However, here, higher pressures are required for smaller permeabilities. This is expected because in directflow under constant flux, all the fluid must be filtered through the membrane. The variation between minimum and maximum TMP increases with κ.

The separation of the channels, given by the value of l, is important in determining the TMP (Figure 5.6(c)). For $l > 1$, the section of the membrane walls nearer the entrance of the channel has the largest TMP. Here, the separation distance is larger than the channel width, $D > H$, but note that the permeate flow is still in a thin channel as the problem is scaled with the length of the channel, $L \gg H$. The TMP decreases monotonically, as the permeate side behaves like a quiescent bath. We see that for $l = 1$ (*i.e.*, $D = H$), the TMP acquires a parabolic shape, similar to variations in the other parameters. For $l < 1$, when the channels are relatively close to each other ($D < H$), the TMP is dominant at the impermeable capped end. This informs us that the force felt on the fluid in one channel by that in a channel nearby reduces the TMP. This forces the majority of filtration to occur further down the

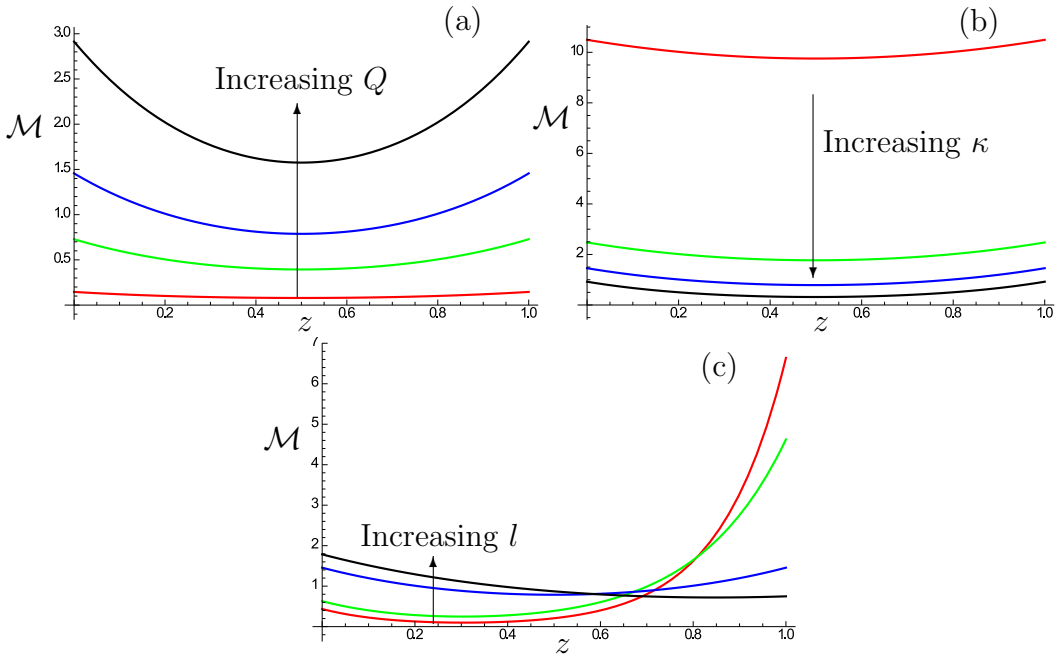

Figure 5.6: The transmembrane pressure difference, $\mathcal{M}(z) = (p-q)|_{x=1}$, in a capped channel for various values of (a) flux, Q, (b) permeability, κ, and (c) separation distance, l. In each figure, the varying quantity takes the values $0.1, 0.5, 1, 2$, plotted in red, green, blue and black respectively, with the other quantities taking the value 1.

channel: a situation to be avoided since a large area of the membrane is not being utilized.

We have seen that for a range of parameter values, the TMP is larger at the entrance and capped end of the channel with a dip in the middle section (a parabolic-like shape). As such, the heuristic first approximation that the TMP is constant along the membrane is reasonable for these parameter values; though we recognize that it may deviate to a large degree (a greater difference in minimum and maximum TMP) under different conditions. The parameter regime for which the TMP is approximately constant along the channel is for small fluxes, small permeabilities and separation distances that are the same size as the width of the channel.

The pump-driving pressure at the entrance to the module is given by (5.12a) at $z = 0$,

$$p(0) = \frac{3Q\left\{C_1 + \left[2 + \left(l^3 + \frac{1}{l^3}\right)\cosh C_1\right]\operatorname{csch} C_1\right\}}{(1+l^3)C_1}, \tag{5.14}$$

where C_1 is given by (5.13a), and so depends on the flux, Q, permeability, κ, and separation distance, l. The driving pressure linearly increases with flux, as expected. For both permeability and separation distance the driving pressure decreases with

these parameters. This is because a greater pressure is required to force the fluid through the walls when the permeability is small. The behaviour with separation distance, l, is explained via the transmembrane pressure difference in the system (Figure 5.6(c)). As l is decreased, more of the fluid passes through a smaller area of the membrane, and so a higher pressure is required. When l is large so that the other channels have a small effect on the flow, the pressure difference (5.13b) takes a similar form to that of the channel with full fractional recovery ($f = 1$) in Karode (2001), and the zero net exit flux in Griffiths et al. (2013). This is expected since they both model the flow in a long and thin channel with constant permeability. However, they cannot be exactly the same as the models are fundamentally different due to the capped end boundary condition versus an open exit.

5.4 3D Pipe

We now consider the 3D cylindrical analogue of the directflow device illustrated in Figure 5.4. The axisymmetric coordinates are now (r, z) where the radial coordinate r replaces the Cartesian x and the z-coordinate remains unchanged. The radius of Region 1 is R, and dimensionally, the $\hat{r}$ component is in the range $[0, R]$. We non-dimensionalize by scaling with R so that $r \in [0, 1]$, and now $l = D/R$. The arrangement of these pipes in the directflow device is now a 2D array, and so the analogous symmetry condition, at a constant r, is no longer appropriate. Depending on the packing of the tubes (square, hexagonal, *etc.*), the curve of symmetry between the pipes may be complicated. However, we will assume for simplicity that the symmetry condition may be applied at a constant radius, $r = 1 + l$.

The analogous dimensionless equations to (5.2), (5.3), (5.5), and (5.6) for a cylindrical geometry may easily be written down. In Region 1, the fluid obeys the thin-layer flow equations,

$$\frac{1}{r}\frac{\partial}{\partial r}(ru) + \frac{\partial w}{\partial z} = 0, \tag{5.15a}$$

$$\frac{1}{r}\frac{\partial}{\partial r}\left(r\frac{\partial w}{\partial r}\right) = \frac{\mathrm{d}p}{\mathrm{d}z}, \tag{5.15b}$$

for $0 < r < 1$ and $0 < z < 1$, where $u = \boldsymbol{u} \cdot \boldsymbol{e}_r$ and $w = \boldsymbol{u} \cdot \boldsymbol{e}_t$. The boundary condi-

tions read, by analogy with (5.3):

$$\text{Symmetry:} \qquad \frac{\partial w}{\partial r} = u = 0, \qquad \text{on } r = 0, \tag{5.16a}$$

$$\text{No axial wall slip:} \qquad w = 0, \qquad \text{on } r = 1, \tag{5.16b}$$

$$\text{Permeate flow:} \qquad u = \kappa\,(p - q)\,, \qquad \text{on } r = 1, \tag{5.16c}$$

$$\text{Fluid influx:} \qquad 2\pi \int_0^1 wr\,\mathrm{d}r = Q, \qquad \text{at } z = 0, \tag{5.16d}$$

$$\text{No fluid flux:} \qquad w = 0, \qquad \text{at } z = 1. \tag{5.16e}$$

In Region 2, the fluid again obeys the thin-layer flow equations,

$$\frac{1}{r}\frac{\partial}{\partial r}\,(ru) + \frac{\partial w}{\partial z} = 0, \tag{5.17a}$$

$$\frac{1}{r}\frac{\partial}{\partial r}\left(r\frac{\partial w}{\partial r}\right) = \frac{\mathrm{d}q}{\mathrm{d}z}, \tag{5.17b}$$

for $1 < r < 1 + l$ and $0 < z < 1$. For this region, the boundary conditions read,

$$\text{Symmetry:} \qquad \frac{\partial w}{\partial r} = u = 0, \qquad \text{on } r = 1 + l, \tag{5.18a}$$

$$\text{No axial wall slip:} \qquad w = 0, \qquad \text{on } r = 1, \tag{5.18b}$$

$$\text{Permeate flow:} \qquad u = \kappa\,(p - q)\,, \qquad \text{on } r = 1, \tag{5.18c}$$

$$\text{No fluid flux:} \qquad w = 0, \qquad \text{at } z = 0, \tag{5.18d}$$

$$\text{Fixed outlet pressure:} \qquad q = 0, \qquad \text{at } z = 1. \tag{5.18e}$$

As in the 2D case, the flow in the single module, given by (5.15)–(5.18), can be solved analytically. Using both sets of symmetry and no axial wall slip conditions (Eqns. (5.16a,b) and (5.18a,b)), we can solve for the fluid flow in terms of the pressure gradient. In Region 1, we find

$$w = \frac{1}{4}\frac{\mathrm{d}p}{\mathrm{d}z}(r^2 - 1), \tag{5.19a}$$

$$u = \frac{1}{16}\frac{\mathrm{d}^2p}{\mathrm{d}z^2}(2r - r^3), \tag{5.19b}$$

similar to Hurwitz (1989), although the pressure will take a different form since we consider the combined flow in Regions 1 and 2. In Region 2, we find

$$w = \frac{1}{4}\frac{\mathrm{d}q}{\mathrm{d}z}\left[r^2 - 2(1+l)^2 \log\, r - 1\right], \tag{5.20a}$$

$$u = \frac{1}{16}\frac{\mathrm{d}^2q}{\mathrm{d}z^2}\Bigg[2r - r^3 + (1+l)^2\left(-2r + 4r\log\, r - (1+l)^2\left(-\frac{3}{r} + \frac{4}{r}\log\,(1+l)\right) - \frac{2}{r}\right)\Bigg]. \tag{5.20b}$$

The constant flux condition (5.16d) may be rewritten as

$$\left.\frac{\mathrm{d}p}{\mathrm{d}z}\right|_{z=0} = -\frac{8Q}{\pi}, \tag{5.21}$$

using (5.19a). The conditions of no flux of fluid through the capped end in Region 1 (5.16e), and an impermeable bottom in Region 2 (5.18d), become

$$\left.\frac{\mathrm{d}p}{\mathrm{d}r}\right|_{z=1} = 0, \qquad \left.\frac{\mathrm{d}q}{\mathrm{d}r}\right|_{z=0} = 0, \tag{5.22}$$

respectively, using (5.19a) and (5.20a).

Again, the permeate flux through the membrane, (Eqns. (5.16c) and (5.18c)), give a set of second-order ordinary differential equations (ODEs) for the pressures, p and q. These equations have two boundary conditions each, given by (5.18e), (5.21) and (5.22)

$$\frac{1}{16}\frac{\mathrm{d}^2 p}{\mathrm{d}z^2} = \kappa\,(p-q)\,, \qquad \left.\frac{\mathrm{d}p}{\mathrm{d}z}\right|_{z=0} = -\frac{8Q}{\pi}, \qquad \left.\frac{\mathrm{d}p}{\mathrm{d}z}\right|_{z=1} = 0, \tag{5.23a}$$

$$-\frac{\Lambda}{16}\frac{\mathrm{d}^2 q}{\mathrm{d}z^2} = \kappa\,(p-q)\,, \qquad \left.\frac{\mathrm{d}q}{\mathrm{d}z}\right|_{z=0} = 0, \qquad q(z=1) = 0, \tag{5.23b}$$

where $\Lambda = \Lambda(l)$ is given by

$$-\Lambda(l) = 1 - 4(1+l)^2 + [3 - 4\log(1+l)](1+l)^4 < 0. \tag{5.24}$$

The ODEs (5.23) may be solved analytically, where the pressures, p and q, in the 3D pipe may be written as

$$p(z) = \frac{1}{1+\Lambda}\left[\Lambda\mathcal{N}(z) + \frac{8Q}{\pi}(1-z) + \mathcal{N}_0\right], \tag{5.25a}$$

$$q(z) = \frac{1}{1+\Lambda}\left[-\mathcal{N}(z) + \frac{8Q}{\pi}(1-z) + \mathcal{N}_0\right]. \tag{5.25b}$$

where

$$C_2 = \sqrt{16\kappa\left(1+\frac{1}{\Lambda}\right)}, \tag{5.26a}$$

$$\mathcal{N}(z) = \operatorname{sech}(C_2)\left[\mathcal{N}_0\cosh(C_2 z) + \frac{8Q}{\pi C_2}\sinh(C_2(1-z))\right], \tag{5.26b}$$

$$\mathcal{N}_0 = \frac{C_2 Q}{2\pi\kappa(\Lambda+1)}\coth(C_2) + \frac{8Q}{\pi C_2}\operatorname{csch}(C_2). \tag{5.26c}$$

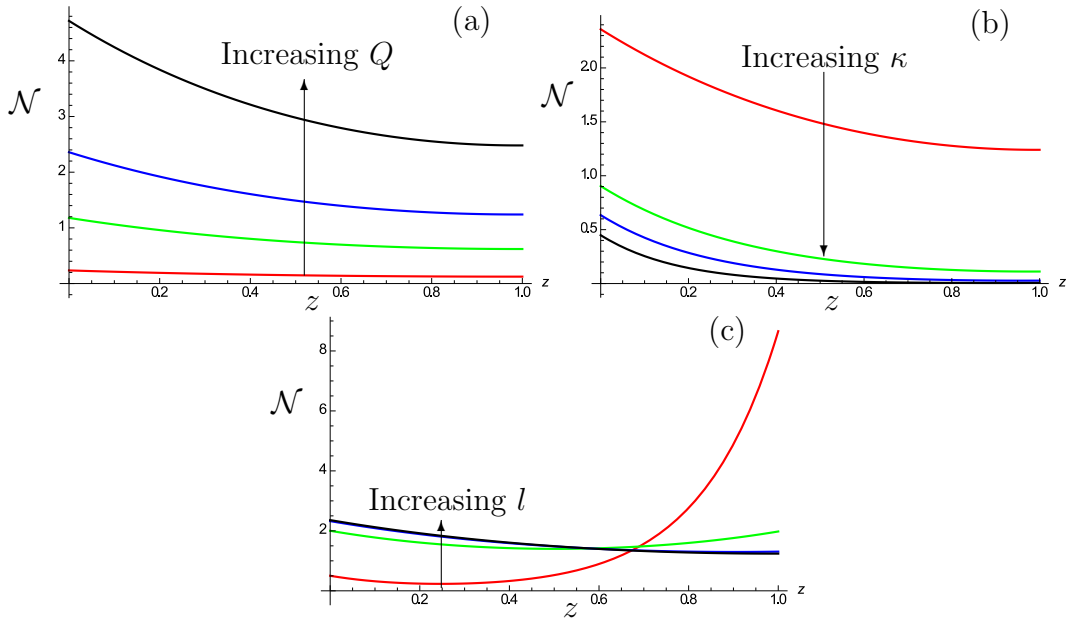

Figure 5.7: The transmembrane pressure difference, $\mathcal{N}(z) = (p-q)|_{r=1}$, in a capped circular cylinder for various values of (a) flux, Q (with $l = 1, \kappa = 0.1$), (b) permeability, κ (with $Q = 1, l = 1$), and (c) separation distance, l (with $Q = 1, \kappa = 0.1$). In each figure, the varying quantity takes the values $0.2, 0.5, 1, 2$, plotted in red, green, blue and black respectively.

The TMP in the 3D pipe (Figure 5.7), given by the function $\mathcal{N}(z) = (p-q)|_{r=1}$ (5.26b), behaves similarly to that of the 2D channel, *cf.*, Figure 5.6. Again, the TMP appears to be larger at either end of the channel with a dip in the middle. In this case, however, the TMP at the entrance is typically larger than that at the capped end, except for very small separation distances, l (Figure 5.7(c)). In order to achieve an approximately constant TMP, the permeability and flux must be low and the separation distance similar to the width of tube ($D \sim H$).

5.5 Conclusions

The slow flow in a directflow device may be solved analytically for a 2D channel and a 3D pipe. The quantity of most practical interest is the transmembrane pressure difference (TMP) across the membrane. In both the 2D and 3D cases, we observe that the TMP is larger at the entrance and capped end of the membrane, with a dip in the middle. The relative difference between the maximum and minimum TMP varies depending on the parameters, from within a few percent for low permeabilities and narrow gaps, to 80% for large permeabilities and larger gaps. This observation

remains relatively consistent as we change parameters such as the influx and the separation distance of each channel/tube. This confirms an experimental observation, assuming a low permeability and low flux, that for flow in a directflow device the TMP is approximately constant in the device (Pearce, 2013). The 2D channel has a wider range of parameter values for which the TMP is approximately constant than the 3D pipe.

We use the observation of an approximately constant TMP to simplify the analysis in the next chapters. There, we will consider elastic effects of the membrane to explain the observed increase in pressure during operation of a directflow filtration setup, and relate it to fouling of the membrane.

We finish our study of directflow by noting that in a practical device we may wish to pack in as many directflow modules as possible. This will increase the overall membrane area and thus improve filtration performance. However, we have observed that the module separation distance influences the size of the membrane region in which most filtration occurs: the fluid is filtered relatively evenly (low variation in TMP) along the membrane provided the separation distance is not too small, *i.e.*, less than the width of each module in the array. However, for small separation distances (large packing of modules), most of the fluid is filtered in a small area near the capped end. This area decreases as we reduce the separation distance, *i.e.*, as we pack modules more tightly. As such, the operating pressure increases dramatically, with high energy costs and a large portion of the membrane area not utilized efficiently.

Chapter 6

Elasticity Effects in Filtration

Summary

During filtration, the membrane and cake layer experience stress from the fluid flow and each other, resulting in deformation. We model this as a fluid flow through porous media sharing an interface. We study a 2D cross-section through the device for simplicity, and quantify the membrane expansion, cake layer contraction, and the resulting effect on the material properties (porosity, poresize and permeability). These results will be useful in the next chapter when fouling and cake development are studied.

6.1 Introduction

At the beginning of the previous chapter, we discussed the observed increase in pressure and fouling during filtration. These observations lead us to believe that the membrane pores are somehow growing larger over time, a process that is depicted in Figure 6.1. This would allow more particles to foul the membrane, but that is not reversible by periodic backflushes. One possible mechanism for this growth of pores is the elastic deformation of the membrane in response to the applied internal pressure. The pores may expand or rupture, allowing larger particles into the membrane to cause further fouling or, in the worst-case scenario, passage of the contaminants (particles) through the membrane. In this chapter, we consider the role and influence of elasticity in filtration at constant flux, to quantify this possibility.

The idea of elastic deformation resulting in increased fouling has previously been considered from a different perspective: the deformation of the contaminant itself,

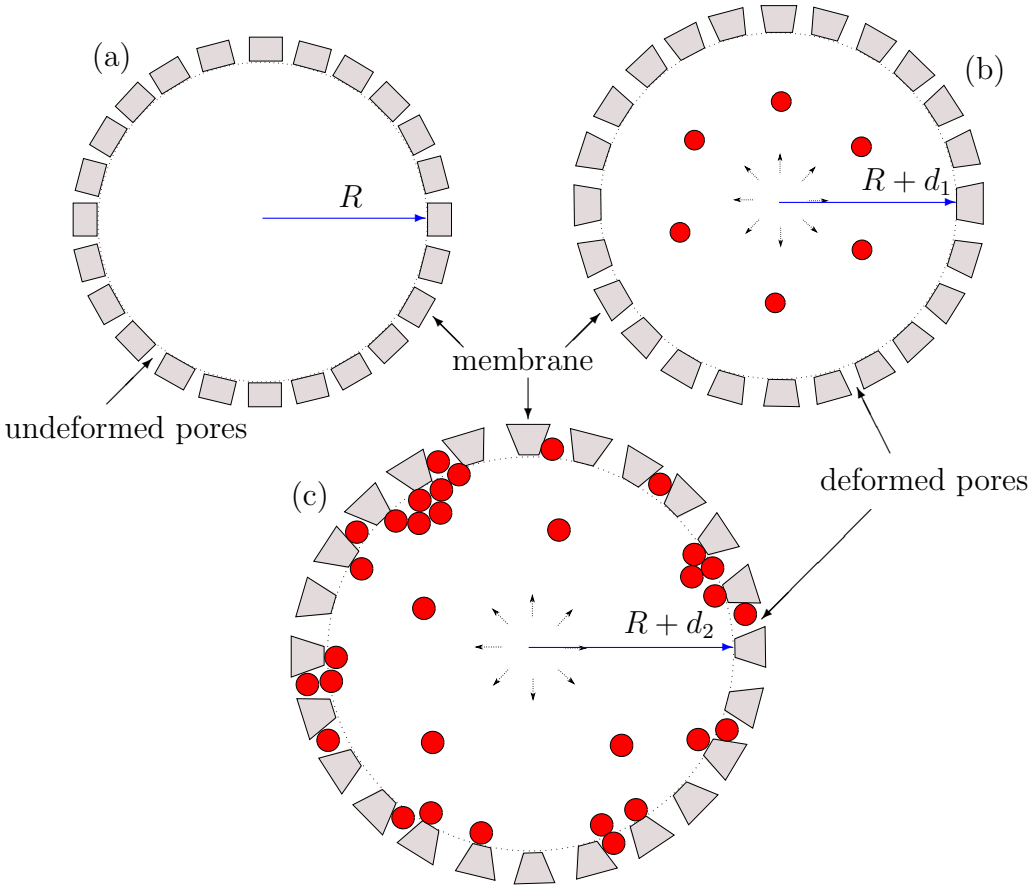

Figure 6.1: Schematic illustrating the expansion of a pore as fouling and caking occur. (a) The pores are initially uniform in size and undeformed, with tube radius R. (b) A fluid flow through the membrane exerts a stress that deforms the membrane, inducing an increase in poresize. The tube radius increases by a small amount d_1. (c) Fouling of the pores and the build up of a cake layer results in higher pressures, and hence further deformation of the membrane, by $d_2 > d_1$, and to a larger poresize. The pressure required must increase to maintain a constant fluid flux through the membrane. The greater the fouling and thicker the cake layer, the greater the deformation.

TMP	Operating condition
0.7 bar	stable, low fouling
1.4–3 bar	no active layer deformation or fibre damage
3–6 bar	typical pressure rating
3–10 bar	elastic strain region
10–15 bar	fibre burst and collapse

Table 6.1: Allowable transmembrane pressures (Chou et al., 2013; Pearce, 2011).

whether a bacteria or macromolecule (Madaeni, 1999; Sadr Ghayeni et al., 1999). This has been demonstrated using a flexible polymer in ultrafiltration. Here, the polymers are stretched in the flow to the point that its projected cross-sectional area is smaller than the pore, thus allowing the polymer to pass through the pore (Nguyen and Neel, 1983). However, recent studies illustrate that the membrane itself may deform under high pressures, leading to increased fouling as the poresizes increase (She et al., 2012). The stress-strain relationship for hollow-fibre membranes has been characterized into three zones: elastic strain, transitional strain and plastic strain. The elastic strain region is valid for pressures of up to 10 bar (Chou et al., 2013), and hence is a factor for all types of filtration (see Table 1.1). Transitional and plastic strain occur at higher pressures. Table 6.1 provides details for allowable pressures during filtration (there is considerable variation based on individual membrane material and structure). Cake deformation has also been studied, where soft colloids/deformable particles are considered. However, the cake is observed to compress under pressure (Guo et al., 2012; Hwang and Hsueh, 2003). In the next chapter, we will see that this leads to an interesting coupling in which the membrane expands while the cake layer contracts.

There are many studies of viscous flow in an elastic cylinder (with thin walls). Typically the flow is coupled to a tube law that relates the deformed radius to the fluid pressure (Whittaker et al., 2010). Various models have led to the design and control of important processes, *e.g.*, reducing wall shear stress on, and improving mass transport to, an artery wall during blood flow (Wang and Tarbell, 1992), and controlling the deformation field in soft-robotics (Elbaz and Gat, 2014). However, the walls in such systems are impermeable, and so qualitatively different to membrane filtration. Furthermore, the tube law does not allow for a descriptive account of the deformation within the membrane, that is, how the membrane structure is altered.

In this chapter, we treat the membrane and cake layer as two different elastic porous media that share a surface; one is a solid material with pores (membrane) and the

other a collection of particles (cake layer). We consider a range of cake thicknesses and degrees of fouling, but not how they change in time. This chapter focuses purely on the quasi-static elastic response during filtration and we consider the time evolution of cake growth and fouling in the next chapter. Here, we analyse the deformation in each medium, and how this affects their properties, *e.g.*, porosity, poresize, permeability. This gives insight into the changes in behaviour of the flow and particle deposition, and explains the observed pressure and fouling increases. We determine how each porous medium contributes to the driving pressure of the system. For simplicity we neglect osmotic pressure effects here, as may be relevant in microfiltration (Bowen and Jenner, 1995a).

6.2 Setup

In Chapter 5, we studied the flow in a directflow filtration system. A key result is that the transmembrane pressure difference (TMP) is, to a first approximation, constant along the membrane. Since the TMP is approximately constant, the same flux, Q/L, must be filtered per unit length of the tube. This motivates us to simplify our model of the membrane deformation in the filter tube by considering a cross-sectional slice of the tube. We therefore consider an axisymmetric plane-strain elastic model (so that $e_{zz} = 0$) for the deformation of the membrane and cake layer. We shall use linear elasticity throughout this analysis. The results will be of interest in the next chapter where we will discuss the evolution of fouling and cake growth.

Our model problem is depicted schematically in Figure 6.2. The wall of the tube constitutes the porous membrane; we denote its Young's modulus, E_{m}, and Poisson ratio, ν_{m}. Initially (*i.e.*, before deformation), the membrane has internal radius R and thickness d_{m}. During filtration, a flux of fluid, Q, from a source at the centre of the tube, flows radially towards and through the membrane with a velocity $\hat{v}(r)$. We take the pressure outside the annulus to be the pressure datum. We assume the flow is in a quasi-steady state and occurs at low Reynolds number, with a constant viscosity, μ. Particles are deposited on the membrane and build up to form a cake layer. We assume that this cake layer is also a poroelastic medium with Young's modulus, E_{c}, and Poisson ratio, ν_{c}. As the fluid passes though this layer, it rejects the particles it is carrying thereby contributing additional particles that increase the thickness of the cake, d_{c}. Inside the annular membrane and cake regions, $\hat{r} < R - d_{\mathrm{c}}$,

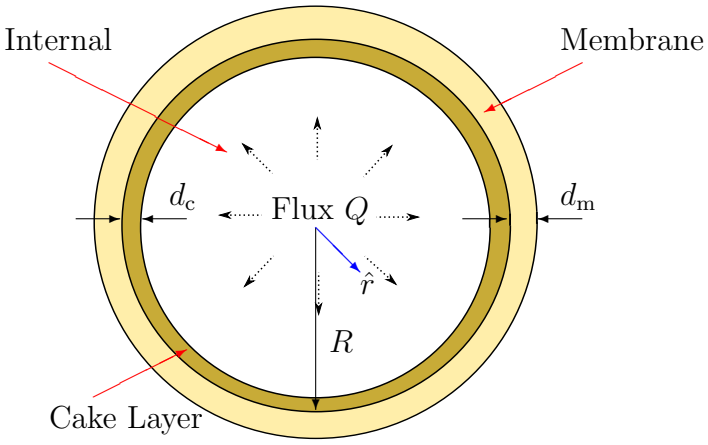

Figure 6.2: Cross-section through a cylindrical module. The filter has an undeformed internal radius R. A fluid flux, Q, flows radially from the centre of the tube with radial velocity $\hat{v}$. The membrane thickness is d_m and cake thickness is d_c.

is void space. In the context of linear elasticity, R is equivalently the undeformed and deformed membrane radius.

The flow deforms the membrane and cake layer by (small) amounts, which we denote by $\hat{u}_m$ and $\hat{u}_c$ respectively. This deformation affects the material properties of the membrane, and hence the rate of fouling and cake growth. In particular, the poresize of the membrane may grow as it deforms. Some particles, if smaller than the pores, may enter and foul the membrane. This fouling reduces the flux of fluid through the membrane at a constant pressure. To maintain the flux, the pressure must be increased. Thence the deformation of the membrane and poresize increase, thereby starting a cyclic process of further increasing of the pressure and fouling.

6.3 Parameter Values

For the remainder of this chapter and the next we shall fix the parameter values of the system, unless otherwise stated. We discuss here typical parameter values appropriate for the undeformed state, and hence for the linearly elastic deformed state also. The tube has an internal radius $R = 10^{-3}\,\mathrm{m}$ and the membrane thickness is $d_m = 10^{-4}\,\mathrm{m}$ (Pearce, 2011) (*i.e.*, the dimensionless membrane thickness $\delta_m = 10^{-1}$). The filtration velocity is of the order of centimetres per second, say $4 \times 10^{-2}\,\mathrm{m/s}$, corresponding to a flux into the annulus of $Q = 4\pi \times 10^{-8}\,\mathrm{m^3/s}$, similar to those in a range of filtration experiments (Gabelman and Hwang, 1999; Shipley et al., 2010).

We take a typical particle size to be $4 - 5\,\mu$m, representative of microfiltration. To have maximum permeability whilst still rejecting particles, the undeformed poresize, $\hat{a}_0$, must be chosen to be as large as possible without allowing for fouling; we thus take $\hat{a}_0 = 3.98 \times 10^{-6}\,$m. Specifically, we choose this $\hat{a}_0$ so that a small deformation may lead to fouling. We note that we may take values that are an order of magnitude lower, *e.g.*, $\hat{a}_0 = 0.1\,\mu$m, *etc* (Lateef et al., 2013). However, our purpose here is to understand whether the proposed mechanism works, so we will not compare a wide range of values.

The membrane properties are taken to be those of hollow-fibre membranes. The (undeformed) membrane permeability for microfiltration is of the order, $\hat{k}_{\mathrm{m},0} = 10^{-16}\,\mathrm{m}^2$ (Shipley et al., 2010). Given the poresize and permeability, the porosity may be determined by relations such as Kozeny–Carman (2.35); giving $\varphi_{\mathrm{m},0} \simeq 0.35$. Typical values for the Young's modulus of a hollow fibre membrane are of the order $10^7\,$Pa (Qin and Chung, 1999); we take $E_{\mathrm{m}} = 6 \times 10^7\,$Pa. We choose a Poisson ratio, $\nu_{\mathrm{m}} = 0.3$, although a large range including negative values (*e.g.*, honeycomb and carbon nanotube structures) are reported (Ma et al., 2003, 2010).

To the author's knowledge, parameter values for the cake layer are not available. As such, the cake-layer properties are chosen for convenience, guided by some intuition. A value for cake permeability is difficult to determine as the cake layer is a collection of loose particles packed at the membrane surface, whose packing is non-trivial and beyond the scope of this work. Nevertheless, it is reasonable to consider a large $\hat{k}_{\mathrm{c},0}$ when caking is beginning, with smaller values later on when the cake compacts more. Since the cake layer represents a collection of particles of similar size to the membrane poresize, we assume that it has a similar (undeformed) permeability to the membrane, $\hat{k}_{\mathrm{c},0} = 10^{-16}\,\mathrm{m}^2$. We take the porosity, $\varphi_{\mathrm{c},0} = 0.4$, to be a bit larger than the membrane as it is not a solid material. Analogously, we take the Young's modulus to be an order of magnitude lower than the membrane, $E_{\mathrm{c}} = 10^6\,$Pa. Finally, we take the Poisson ratio to be lower than the membrane, $\nu_{\mathrm{c}} = 0.2$, meaning that the cake layer is, in a sense, a softer material. A Poisson ratio of 0.2 has been measured for a closely packed colloidal crystal, and used in the modelling of a colloidal gel (Style and Peppin, 2011).

6.4 Fluid Mechanics

The fluid velocity, $\hat{v}$, is governed by the steady axisymmetric incompressible Stokes equations in the tube (the central void) and Darcy's law in a porous media, as in §2.3.1. The velocity in Darcy's equation is the Darcy velocity, given by the fluid velocity scaled with the porosity. We will use the same notation, $\hat{v}$, for simplicity but the distinction will be assumed. We use the Kozeny–Carman relation (2.35) to relate the permeability of each porous medium to its structural properties (porosity and poresize). For the membrane, we assume that its permeability, $\hat{k}_{\mathrm{m}}$, has a further dependence that is linear with the fraction of open pores, N,

$$\hat{k}_{\mathrm{m}} = \left(\hat{k}_{\mathrm{m},0} + \hat{k}_{\mathrm{m},1}\right) N, \tag{6.1}$$

where $\hat{k}_{\mathrm{m},0}$ is the permeability of the undeformed and unfouled membrane, given by a Kozeny–Carman relation (2.35) for the membrane, and $\hat{k}_{\mathrm{m},1}$ is a correction to the permeability accounting for the deformation.

6.4.1 Fluid flow inside the void

The fluid flow within the central void of the filter ($\hat{r} < R - d_{\mathrm{c}}$) is given by the axisymmetric Stokes equations in polar coordinates

$$\frac{1}{\hat{r}}\frac{\mathrm{d}(\hat{r}\hat{v})}{\mathrm{d}\hat{r}} = 0, \tag{6.2a}$$

$$\frac{1}{\hat{r}}\frac{\mathrm{d}}{\mathrm{d}\hat{r}}\left(\hat{r}\frac{\mathrm{d}\hat{v}}{\mathrm{d}\hat{r}}\right) - \frac{\hat{v}}{\hat{r}^2} = \frac{1}{\mu}\frac{\mathrm{d}\hat{p}}{\mathrm{d}\hat{r}}. \tag{6.2b}$$

We consider the case of constant fluid flux through each cross-section

$$\int_0^{2\pi} \hat{v}\hat{r}\,\mathrm{d}\theta = Q, \tag{6.3}$$

which immediately gives that

$$\hat{v} = \frac{Q}{2\pi\hat{r}}. \tag{6.4}$$

When substituted into (6.2b), we find that

$$\hat{p} = \hat{P}, \tag{6.5}$$

a constant. A constant radial pressure is consistent with flow in a long and thin tube. We take the pressure datum outside the membrane to be zero, meaning that this pressure, $\hat{P}$, is the pressure difference between the centre of the annulus and the outside. It is the driving pressure for the system, and must be determined by considering the resistance to flow through the membrane.

6.4.2 Fluid flow in a cake layer

The flow in the porous cake layer is given by the Darcy equations (2.15) in polar coordinates

$$\frac{1}{\hat{r}}\frac{\mathrm{d}(\hat{r}\hat{v})}{\mathrm{d}\hat{r}} = 0, \tag{6.6a}$$

$$\hat{v} = -\frac{\hat{k}_\mathrm{c}}{\mu}\frac{\mathrm{d}\hat{p}}{\mathrm{d}\hat{r}}, \tag{6.6b}$$

for $R - d_\mathrm{c} < \hat{r} < R$, where $\hat{k}_\mathrm{c}$ is the permeability of the cake layer.

The pressure and velocity are continuous at the void–cake layer boundary

$$[\hat{p}]_{\hat{r}=R-d_\mathrm{c}} = 0, \tag{6.7a}$$

$$[\hat{v}]_{\hat{r}=R-d_\mathrm{c}} = 0. \tag{6.7b}$$

As pointed out earlier, $\hat{v}$ is the fluid velocity in the void. Imposing that the Darcy velocity in the membrane matches $\hat{v}$ is consistent for conservation of mass, but really there is a discontinuity in fluid velocity at $\hat{r} = R - d_\mathrm{c}$.

6.4.3 Fluid flow in membrane

The flow in the membrane is given by the Darcy equations (2.15) in polar coordinates

$$\frac{1}{\hat{r}}\frac{\mathrm{d}(\hat{r}\hat{v})}{\mathrm{d}\hat{r}} = 0, \tag{6.8a}$$

$$\hat{v} = -\frac{\hat{k}_\mathrm{m}N}{\mu}\frac{\mathrm{d}\hat{p}}{\mathrm{d}\hat{r}}, \tag{6.8b}$$

for $R < \hat{r} < R + d_\mathrm{m}$, where $\hat{k}_\mathrm{m}N$ is the effective permeability of a membrane (6.1) that has a fraction of open pores, N.

The pressure and velocity are continuous at the cake layer–membrane boundary

$$[\hat{p}]_{\hat{r}=R} = 0, \tag{6.9a}$$

$$[\hat{v}]_{\hat{r}=R} = 0. \tag{6.9b}$$

6.4.4 Outside the membrane

As already stated we take the pressure outside the membrane to be zero

$$\hat{p}(R + d_\mathrm{m}) = 0. \tag{6.10}$$

The pressure and velocity are continuous at the membrane–outside boundary

$$[\hat{p}]_{\hat{r}=R+d_\mathrm{m}} = 0, \tag{6.11a}$$

$$[\hat{v}]_{\hat{r}=R+d_\mathrm{m}} = 0. \tag{6.11b}$$

6.4.5 Solution for the flow profile

As shown in §6.4.1, the fluid velocity in the void has solution

$$\hat{v} = \frac{Q}{2\pi\hat{r}}. \tag{6.12}$$

The same conservation of mass equations (6.6a,6.8a) apply in the cake layer and membrane, with boundary conditions of continuity of velocity. This means that (6.12) holds in all regions.

The fluid pressure required to drive this flow may be found by substituting the velocity field (6.12) into the Darcy equations (6.6b,6.8b), with boundary conditions of continuity of pressure, to get

$$\hat{p} = \begin{cases} \hat{P} = \dfrac{Q\mu}{2\pi\hat{k}_\mathrm{m}N}\log\left(1+\dfrac{d_\mathrm{m}}{R}\right) - \dfrac{Q\mu}{2\pi\hat{k}_\mathrm{c}}\log\left(1-\dfrac{d_\mathrm{c}}{R}\right), & \hat{r} < R - d_\mathrm{c}, \\ -\dfrac{Q\mu}{2\pi\hat{k}_\mathrm{c}}\log\left(\dfrac{\hat{r}}{R}\right) + \dfrac{Q\mu}{2\pi\hat{k}_\mathrm{m}N}\log\dfrac{R+d_\mathrm{m}}{R}, & R - d_\mathrm{c} < \hat{r} < R, \\ \dfrac{Q\mu}{2\pi\hat{k}_\mathrm{m}N}\log\left(\dfrac{R+d_\mathrm{m}}{\hat{r}}\right), & R < \hat{r} < R + d_\mathrm{m}, \\ 0, & \hat{r} > 1 + \delta_\mathrm{m}. \end{cases} \tag{6.13}$$

Note that this calculation determines the driving pressure, $\hat{P}$, in the void region. Furthermore, we note the pressure on the membrane ($\hat{r} = R$) and cake ($\hat{r} = R - d_\mathrm{c}$) inner surfaces as

$$\hat{P}_1 = \frac{Q\mu}{2\pi\hat{k}_\mathrm{m}N}\log\left(1+\frac{d_\mathrm{m}}{R}\right), \tag{6.14a}$$

$$\hat{P} = \hat{P}_2 = \frac{Q\mu}{2\pi\hat{k}_\mathrm{m}N}\log\left(1+\frac{d_\mathrm{m}}{R}\right) - \frac{Q\mu}{2\pi\hat{k}_\mathrm{c}}\log\left(1-\frac{d_\mathrm{c}}{R}\right), \tag{6.14b}$$

respectively. These will be significant in the next section when we consider the deformation of each layer due to the fluid stress.

6.5 Solid Mechanics

6.5.1 Poroelasticity

The steady-state linear elastic deformation of a solid material is governed by the steady Navier–Cauchy equation with no body forces (Howell et al., 2009),

$$\nabla \cdot \hat{\boldsymbol{\sigma}}^t = 0, \tag{6.15}$$

where $\hat{\boldsymbol{\sigma}}^t$ is the total stress in the material. For a poroelastic material, the total stress is given according to Terzaghi's principle (Coussy, 2011; MacMinn et al., 2015) by,

$$\hat{\sigma}^{\mathrm{t}}_{ij} = \hat{\sigma}_{ij} - \hat{p}\delta_{ij}, \tag{6.16}$$

where $\hat{\boldsymbol{\sigma}}$ is the elastic stress of the material (due to strain), and $-\hat{p}I$ is the contribution due to the fluid pore pressure (where I denotes the identity matrix). Hence, the excess of stress over pore pressure drives the deformation.

Since the elastic stress is a response to the TMP (which we have assumed is independent of z), the elastic displacement of the cake and membrane must be independent of the z-direction as the strain is planar: this is known as *plane strain* (Howell et al., 2009). Furthermore, we assume that the displacement is axisymmetric. The polar-coordinate components of the strain tensor, e_{rr} and $e_{\theta\theta}$, may be written in terms of the radial displacement, $\hat{u}$, of the porous medium,

$$e_{rr} = \frac{1}{E}\left[(1-\nu^2)\hat{\sigma}_{rr} - \nu(1+\nu)\hat{\sigma}_{\theta\theta}\right] = \frac{\mathrm{d}\hat{u}}{\mathrm{d}\hat{r}}, \tag{6.17a}$$

$$e_{\theta\theta} = \frac{1}{E}\left[-\nu(1+\nu)\hat{\sigma}_{rr} + (1-\nu^2)\hat{\sigma}_{\theta\theta}\right] = \frac{\hat{u}}{\hat{r}}, \tag{6.17b}$$

where E is the Young's modulus, and ν is the Poisson ratio of the solid porous material (Howell et al., 2009). It is simpler to solve for the displacement, $\hat{u}$, and so we write

$$\hat{\sigma}_{rr} = \frac{E}{(1+\nu)(1-2\nu)}\left((1-\nu)\frac{\mathrm{d}\hat{u}}{\mathrm{d}\hat{r}} + \nu\frac{\hat{u}}{\hat{r}}\right), \tag{6.18a}$$

$$\hat{\sigma}_{\theta\theta} = \frac{E}{(1+\nu)(1-2\nu)}\left(\nu\frac{\mathrm{d}\hat{u}}{\mathrm{d}\hat{r}} + (1-\nu)\frac{\hat{u}}{\hat{r}}\right). \tag{6.18b}$$

The $\hat{r}$-component of the steady Navier–Cauchy equation (6.15), which reads

$$\frac{1}{\hat{r}}\frac{\mathrm{d}\left(\hat{r}\hat{\sigma}_{rr}\right)}{\mathrm{d}\hat{r}} - \frac{\hat{\sigma}_{\theta\theta}}{\hat{r}} = \frac{\mathrm{d}\hat{p}}{\mathrm{d}\hat{r}}, \tag{6.19}$$

combined with Eq. (6.18) gives

$$\frac{E(1-\nu)}{(1+\nu)(1-2\nu)}\frac{\mathrm{d}}{\mathrm{d}\hat{r}}\left(\frac{1}{\hat{r}}\frac{\mathrm{d}}{\mathrm{d}\hat{r}}\left(\hat{r}\hat{u}\right)\right) = \frac{\mathrm{d}\hat{p}}{\mathrm{d}\hat{r}}. \tag{6.20}$$

This is an ODE describing the elastic displacement in response to an imposed pressure gradient. Since $\hat{p}$ is already known (from (6.13)), $\hat{u}$ may now be determined. Since $\hat{u}$ depends on the pressure gradient of the fluid, it is not uniform in the material.

6.5.2 Boundary conditions

The deformation problem is made up of two parts: when no cake layer is present (at the beginning of the filtration process or after a backflush is performed) and when a cake layer is present. These two scenarios must be treated separately as we will see. Furthermore, the solution without a cake layer feeds into the case with a cake layer.

When the filtration process begins (originally or after a backflush) there is no cake layer present. The membrane deforms elastically, by $\hat{u}_{\mathrm{m}}^{0}$, solely due to the fluid stress. When a cake layer is present, the cake layer is deformed, by $\hat{u}_{\mathrm{c}}$, by the fluid stress and retained by the membrane. Due to this interaction, the cake layer exerts a mechanical stress on the membrane and this, together with the fluid stress, deforms the membrane by $\hat{u}_{\mathrm{m}}$. (This is fundamentally different to the case with no cake layer.) As a result there is a continuity of effective stress at the cake–membrane interface. Since the fluid stress is continuous here, the elastic stress must also be continuous.

The additional pressure caused by fouling in turn induces greater deformation. The membrane surface has already been deformed by the the fluid flow before the cake builds up on this surface (shown schematically in Figure 6.1). We therefore impose continuity of deformation at the cake–membrane interface, that is, we mean continuity of the additional deformation due to further fouling of the membrane during the build up of the cake layer, so that

$$\hat{u}_{\mathrm{c}} = \hat{u}_{\mathrm{m}} - \hat{u}_{\mathrm{m}}^{0}, \qquad \text{at} \qquad \hat{r} = R. \tag{6.21}$$

6.5.2.1 The deformed membrane with no cake layer

In this case, the Navier–Cauchy equation (6.20) for the deformation of the membrane with no cake, $\hat{u}_{\mathrm{m}}^0$, takes the form

$$\frac{E_{\mathrm{m}}(1-\nu_{\mathrm{m}})}{(1+\nu_{\mathrm{m}})(1-2\nu_{\mathrm{m}})}\frac{\mathrm{d}}{\mathrm{d}\hat{r}}\left(\frac{1}{\hat{r}}\frac{\mathrm{d}}{\mathrm{d}\hat{r}}\left(\hat{r}\hat{u}_{\mathrm{m}}^0\right)\right)=\frac{\mathrm{d}\hat{p}}{\mathrm{d}\hat{r}}, \tag{6.22}$$

for $R<\hat{r}<R+d_{\mathrm{m}}$, with $\hat{p}$ given by (6.13). We note that R is the internal radius of the membrane, which is equivalent to the deformed internal radius in linear elasticity.

The flow in the membrane determines the boundary conditions for (6.22). The stresses on the inner ($\hat{r}=R$) and outer ($\hat{r}=R+d_{\mathrm{m}}$) walls of the membrane are given by the fluid pressure at the boundaries, *i.e.*,

$$\hat{\sigma}_{rr}(\hat{r}=R)=\frac{E_{\mathrm{m}}}{(1+\nu_{\mathrm{m}})(1-2\nu_{\mathrm{m}})}\left((1-\nu_{\mathrm{m}})\frac{\mathrm{d}\hat{u}_{\mathrm{m}}^0}{\mathrm{d}\hat{r}}+\nu_{\mathrm{m}}\frac{\hat{u}_{\mathrm{m}}^0}{\hat{r}}\right)\Bigg|_{\hat{r}=R}=-\hat{P}_1, \tag{6.23a}$$

$$\hat{\sigma}_{rr}(\hat{r}=R+d_{\mathrm{m}})=\frac{E_{\mathrm{m}}}{(1+\nu_{\mathrm{m}})(1-2\nu_{\mathrm{m}})}\left((1-\nu_{\mathrm{m}})\frac{\mathrm{d}\hat{u}_{\mathrm{m}}^0}{\mathrm{d}\hat{r}}+\nu_{\mathrm{m}}\frac{\hat{u}_{\mathrm{m}}^0}{\hat{r}}\right)\Bigg|_{\hat{r}=R+d_{\mathrm{m}}}=0, \tag{6.23b}$$

where $\hat{P}_1=\hat{p}(R)$ (6.14a) is the fluid pressure at the inner boundary, and the negative sign is because the fluid pressure is acting in the opposite direction to the normal of the surface.

6.5.2.2 The deformed membrane and cake layer

When a cake layer is present, the Navier–Cauchy equations (6.20) for the membrane and cake layer deformations, $\hat{u}_{\mathrm{m}}$ and $\hat{u}_{\mathrm{c}}$ respectively, take the form

$$\frac{E_{\mathrm{m}}(1-\nu_{\mathrm{m}})}{(1+\nu_{\mathrm{m}})(1-2\nu_{\mathrm{m}})}\frac{\mathrm{d}}{\mathrm{d}\hat{r}}\left(\frac{1}{\hat{r}}\frac{\mathrm{d}}{\mathrm{d}\hat{r}}\left(\hat{r}\hat{u}_{\mathrm{m}}\right)\right)=\frac{\mathrm{d}\hat{p}}{\mathrm{d}\hat{r}}, \tag{6.24a}$$

$$\frac{E_{\mathrm{c}}(1-\nu_{\mathrm{c}})}{(1+\nu_{\mathrm{c}})(1-2\nu_{\mathrm{c}})}\frac{\mathrm{d}}{\mathrm{d}\hat{r}}\left(\frac{1}{\hat{r}}\frac{\mathrm{d}}{\mathrm{d}\hat{r}}\left(\hat{r}\hat{u}_{\mathrm{c}}\right)\right)=\frac{\mathrm{d}\hat{p}}{\mathrm{d}\hat{r}}, \tag{6.24b}$$

for $R<\hat{r}<R+d_{\mathrm{m}}$ and $R-d_{\mathrm{c}}<\hat{r}<R$, respectively; again $\hat{p}$ is given by (6.13).

We use the flow in the cake and membrane to determine the inner ($\hat{r}=R-d_{\mathrm{c}}$) boundary condition for (6.24b) and the outer ($\hat{r}=R+d_{\mathrm{m}}$) boundary condition for (6.24a),

$$\frac{E_{\mathrm{c}}}{(1+\nu_{\mathrm{c}})(1-2\nu_{\mathrm{c}})}\left((1-\nu_{\mathrm{c}})\frac{\mathrm{d}\hat{u}_{\mathrm{c}}}{\mathrm{d}\hat{r}}+\nu_{\mathrm{c}}\frac{\hat{u}_{\mathrm{c}}}{\hat{r}}\right)\Bigg|_{\hat{r}=R-d_{\mathrm{c}}}=-\hat{P}_2, \tag{6.25a}$$

$$\frac{E_{\mathrm{m}}}{(1+\nu_{\mathrm{m}})(1-2\nu_{\mathrm{m}})}\left((1-\nu_{\mathrm{m}})\frac{\mathrm{d}\hat{u}_{\mathrm{m}}}{\mathrm{d}\hat{r}}+\nu_{\mathrm{m}}\frac{\hat{u}_{\mathrm{m}}}{\hat{r}}\right)\Bigg|_{\hat{r}=R+d_{\mathrm{m}}}=0, \tag{6.25b}$$

where $\hat{P}_2 = \hat{p}(R - d_c)$ (6.14b) is the fluid pressure at the cake inner boundary. However, at the cake–membrane interface ($\hat{r} = R$), the membrane retains the cake (*i.e.*, the membrane rejects the particles). We therefore impose continuity in radial stress and further deformation due to caking,

$$\frac{E_c}{(1+\nu_c)(1-2\nu_c)}\left((1-\nu_c)\frac{\mathrm{d}\hat{u}_c}{\mathrm{d}\hat{r}} + \nu_c\frac{\hat{u}_c}{\hat{r}}\right)\bigg|_{\hat{r}=R} = \frac{E_m}{(1+\nu_m)(1-2\nu_m)}\left((1-\nu_m)\frac{\mathrm{d}\hat{u}_m}{\mathrm{d}\hat{r}} + \nu_m\frac{\hat{u}_m}{\hat{r}}\right)\bigg|_{\hat{r}=R}, \quad (6.26a)$$

$$\hat{u}_c = \hat{u}_m - \hat{u}_m^0, \qquad \text{at} \quad \hat{r} = R. \quad (6.26b)$$

6.6 Non-dimensionalization

6.6.1 Scaling

We scale the radial coordinate, r, and the deformations, $\hat{u}_m$ and $\hat{u}_c$, with R, the undeformed inner membrane radius, and the fluid velocity, $\hat{v}$, with Q/R. We denote the thickness ratios of the membrane and cake layer thicknesses to the inner radius of the annulus to be $\delta_m = d_m/R \ll 1$ and $\delta_c = d_c/R \ll 1$, respectively. Darcy's equation motivates the pressure scaling $Q\mu/\hat{k}_{m,0}$, with $\hat{k}_{m,0}$ given by the Kozeny–Carman relation (2.35). The stresses in the membrane and cake are scaled with the stress due to the fluid pressure at the membrane–cake-layer interface ($\hat{r} = R$), $\hat{P}_1$. These are summarized below,

$$\begin{aligned} &\hat{r} = Rr, && \hat{u}_m^0 = Ru_m^0, && \hat{u}_m = Ru_m, && \hat{u}_c = Ru_c, \\ &\hat{v} = \frac{Q}{R}v, && \hat{p} = \frac{Q\mu}{\hat{k}_{m,0}}p, && \hat{\sigma}_{rr} = \hat{P}_1\sigma_{rr}, && \hat{\sigma}_{\theta\theta} = \hat{P}_1\sigma_{\theta\theta}, \end{aligned} \quad (6.27)$$

We scale our reference pressures, $\hat{P}$, $\hat{P}_1$ and $\hat{P}_2$ (6.14), with the above pressure scaling,

$$\hat{P} = \left(Q\mu/\hat{k}_{m,0}\right)P, \qquad \hat{P}_1 = \left(Q\mu/\hat{k}_{m,0}\right)P_1, \qquad \hat{P}_2 = \left(Q\mu/\hat{k}_{m,0}\right)P_2. \quad (6.28)$$

We note that the problem is scaled with the material parameters of the membrane as this is a well defined material, unlike the cake. We assume that the Young's modulus, E, and Poisson ratio, ν, of both the membrane and cake layer, and the permeability of the cake layer, remain constant to leading order (deformation enters only at higher order).

6.6.2 Dimensionless governing equations

The governing equations are non-dimensionalized via (6.27). The solution to the fluid flow problem can be written down immediately as

$$v = \frac{1}{2\pi r}, \tag{6.29a}$$

$$p = \begin{cases} P = \dfrac{1}{2\pi N}\log(1+\delta_\mathrm{m}) - \dfrac{1}{2\pi\kappa}\log(1-\delta_\mathrm{c}), & r < 1-\delta_\mathrm{c}, \\ -\dfrac{1}{2\pi\kappa}\log r + \dfrac{1}{2\pi N}\log(1+\delta_\mathrm{m}), & 1-\delta_\mathrm{c} < r < 1, \\ -\dfrac{1}{2\pi N}\log r + \dfrac{1}{2\pi N}\log(1+\delta_\mathrm{m}), & 1 < r < 1+\delta_\mathrm{m}, \\ 0, & r > 1+\delta_\mathrm{m}, \end{cases} \tag{6.29b}$$

where

$$\kappa = \frac{\hat{k}_{\mathrm{c},0}}{\hat{k}_{\mathrm{m},0}}, \tag{6.30}$$

is the ratio of permeabilities between the cake and membrane (at zero deformation). The pressure (6.29b) forms a piecewise continuous function. At small κ, the pressure difference across the cake layer is large: the cake is restricting the flow of fluid. Fouling (decreasing N and hence $\hat{k}_\mathrm{m}$) increases the pressure difference across the membrane as it reduces the permeability of the membrane to the point that the membrane becomes limiting.

The reference pressures, P_1 at the membrane–cake-layer interface ($r = 1$), and P_2 at the internal-cake interface ($r = 1-\delta_\mathrm{c}$), are given by

$$P_1 = \frac{1}{2\pi N}\log(1+\delta_\mathrm{m}), \tag{6.31a}$$

$$P_2 = P = -\frac{1}{2\pi\kappa}\log(1-\delta_\mathrm{c}) + \frac{1}{2\pi N}\log(1+\delta_\mathrm{m}). \tag{6.31b}$$

We can now consider the dimensionless elastic problem. For convenience, we define the following dimensionless numbers

$$\Omega = \frac{E_\mathrm{m}}{\hat{P}_1(1+\nu_\mathrm{m})(1-2\nu_\mathrm{m})} = \frac{2\pi E_\mathrm{m}\hat{k}_{\mathrm{m},0}}{Q\mu(1+\nu_\mathrm{m})(1-2\nu_\mathrm{m})\log(1+\delta_\mathrm{m})}, \tag{6.32a}$$

$$\Gamma = \frac{2\pi}{(1-\nu_\mathrm{m})\log(1+\delta_\mathrm{m})}, \tag{6.32b}$$

using $\hat{P}_1$ from (6.31a). These dimensionless parameters apply to the unfouled ($N = 1$) membrane, for reference. Although each dimensionless number is defined in terms of

several physical parameters of the system, it is instructive to note the following; Ω is a parameter related to the physics of the system, it depends on $E_\mathrm{m}/\hat{P}_1 \propto E_\mathrm{m}/Q$, and hence it represents a stiffness; Γ is a purely geometrical parameter. As our scalings (6.27) and dimensionless parameters (6.32) are defined with reference to the membrane parameters, it is also convenient to define the following dimensionless parameter ratios between the cake layer and membrane,

$$\omega = \frac{E_\mathrm{c}}{(1+\nu_\mathrm{c})(1-2\nu_\mathrm{c})}\Big/\frac{E_\mathrm{m}}{(1+\nu_\mathrm{m})(1-2\nu_\mathrm{m})}, \qquad \gamma = \frac{1-\nu_\mathrm{m}}{1-\nu_\mathrm{c}}. \tag{6.33}$$

The Navier–Cauchy equation (6.22) for the membrane with no cake layer takes the form

$$\frac{\mathrm{d}}{\mathrm{d}r}\left(\frac{1}{r}\frac{\mathrm{d}}{\mathrm{d}r}\left(ru_\mathrm{m}^0\right)\right) = \frac{\Gamma}{\Omega}\frac{\mathrm{d}p}{\mathrm{d}r} = -\frac{\Gamma}{\Omega}\frac{1}{2\pi N r}, \tag{6.34}$$

for $1 < r < 1+\delta_\mathrm{m}$, with p given in (6.29b), and boundary conditions (6.23)

$$\Omega\left((1-\nu_\mathrm{m})\frac{\mathrm{d}u_\mathrm{m}^0}{\mathrm{d}r} + \nu_\mathrm{m}\frac{u_\mathrm{m}^0}{r}\right)\Big|_{r=1} = -1, \tag{6.35a}$$

$$\Omega\left((1-\nu_\mathrm{m})\frac{\mathrm{d}u_\mathrm{m}^0}{\mathrm{d}r} + \nu_\mathrm{m}\frac{u_\mathrm{m}^0}{r}\right)\Big|_{r=1+\delta_\mathrm{m}} = 0. \tag{6.35b}$$

The Navier–Cauchy equations when a cake layer is present (6.24) take the form

$$\frac{\mathrm{d}}{\mathrm{d}r}\left(\frac{1}{r}\frac{\mathrm{d}}{\mathrm{d}r}\left(ru_\mathrm{m}\right)\right) = \frac{\Gamma}{\Omega}\frac{\mathrm{d}p}{\mathrm{d}r} = -\frac{\Gamma}{\Omega}\frac{1}{2\pi N r}, \tag{6.36a}$$

$$\frac{\mathrm{d}}{\mathrm{d}r}\left(\frac{1}{r}\frac{\mathrm{d}}{\mathrm{d}r}\left(ru_\mathrm{c}\right)\right) = \frac{\Gamma}{\Omega}\frac{\gamma}{\omega}\frac{\mathrm{d}p}{\mathrm{d}r} = -\frac{\Gamma}{\Omega}\frac{\gamma}{\omega}\frac{1}{2\pi\kappa r}. \tag{6.36b}$$

for $1 < r < 1+\delta_\mathrm{m}$ and $1-\delta_\mathrm{c} < r < 1$ respectively, with p given in (6.29b) and boundary conditions from (6.25) and (6.26) now reading:

$$\Omega\,\omega\left((1-\nu_\mathrm{c})\frac{\mathrm{d}u_\mathrm{c}}{\mathrm{d}r} + \nu_\mathrm{c}\frac{u_\mathrm{c}}{r}\right)\Big|_{r=1-\delta_\mathrm{c}} = -\frac{P_2}{P_1} = -\left(1 - \frac{N}{\kappa}\frac{\log\,(1-\delta_\mathrm{c})}{\log\,(1+\delta_\mathrm{m})}\right), \tag{6.37a}$$

$$\Omega\left((1-\nu_\mathrm{m})\frac{\mathrm{d}u_\mathrm{m}}{\mathrm{d}r} + \nu_\mathrm{m}\frac{u_\mathrm{m}}{r}\right)\Big|_{r=1+\delta_\mathrm{m}} = 0, \tag{6.37b}$$

$$\Omega\,\omega\left((1-\nu_\mathrm{c})\frac{\mathrm{d}u_\mathrm{c}}{\mathrm{d}r} + \nu_\mathrm{c}\frac{u_\mathrm{c}}{r}\right)\Big|_{r=1} = \Omega\left((1-\nu_\mathrm{m})\frac{\mathrm{d}u_\mathrm{m}}{\mathrm{d}r} + \nu_\mathrm{m}\frac{u_\mathrm{m}}{r}\right)\Big|_{r=1}, \tag{6.37c}$$

$$u_\mathrm{c}(r=1) = u_\mathrm{m}(r=1) - u_\mathrm{m}^0(r=1), \tag{6.37d}$$

where $P_1 = p(r=1)$ and $P_2 = p(r=1-\delta_\mathrm{c})$ are given by (6.31).

6.6.3 Material properties

6.6.3.1 Porosity

We shall assume that the solid portion of the membrane and cake are incompressible: any volume change suggested by the displacement must be accommodated by a change in porosity. Here, we wish to quantify this change in porosity. In the reference undeformed configuration the total (areal) volume of the material, $\hat{V}_0^{\mathrm{t}}$, may be decomposed into the volume of solid material, $\hat{V}_0^{\mathrm{s}}$, and volume of the pore space, $\hat{V}_0^{\mathrm{p}}$, with

$$\hat{V}_0^{\mathrm{s}} + \hat{V}_0^{\mathrm{p}} = \hat{V}_0^{\mathrm{t}}, \tag{6.38}$$

where the solid material is either the membrane material or the particles that make up the porous cake layer. After deformation, the total volume has changed by a factor $1 + \Delta$, where Δ is the the local (areal) relative volume change, known as the *dilation* (Howell et al., 2009), given by

$$\Delta := \nabla \cdot \boldsymbol{u} = e_{rr} + e_{\theta\theta} = \frac{\mathrm{d}u}{\mathrm{d}r} + \frac{u}{r}, \tag{6.39}$$

The dilation describes the variation of the deformation of a porous medium, specifically whether the medium is expanding ($\Delta > 0$) or compressing ($\Delta < 0$), with $\Delta = \Delta(r)$. When referring the membrane or cake layer specifically, we use Δ_{m} and Δ_{c}, respectively.

After deformation, the volume of the solid material is unchanged, whereas the volume of the pore space is now $\hat{V}_1^{\mathrm{p}}$, with

$$\hat{V}_0^{\mathrm{s}} + \hat{V}_1^{\mathrm{p}} = \hat{V}_0^{\mathrm{t}}(1 + \Delta). \tag{6.40}$$

Defining the undeformed porosity as $\varphi_0 = \hat{V}_0^{\mathrm{p}}/\hat{V}_0^{\mathrm{t}}$ and the deformed porosity $\varphi_{\mathrm{d}} = \hat{V}_1^{\mathrm{p}}/\hat{V}_0^{\mathrm{t}}(1 + \Delta)$, the deformed porosity can be written in terms of the undeformed porosity as

$$\varphi_{\mathrm{d}} = \varphi_0 + \frac{\Delta}{1 + \Delta}(1 - \varphi_0). \tag{6.41}$$

For small deformations (consistent with our assumption of linear elasticity), $\Delta \ll 1$, the deformed porosity can be approximated as a linear function of the dilation,

$$\varphi_{\mathrm{d}} \approx \varphi_0 + \Delta(1 - \varphi_0). \tag{6.42}$$

Hence, when the deformation results in an expansion ($\Delta > 0$) or a contraction ($\Delta < 0$) of a porous medium, its porosity increases or decreases linearly. However, we emphasize that, in general, $\Delta = \Delta(r)$, so that the initially uniform porosity becomes inhomogeneous. (It is also possible that the permeability becomes anisotropic as a result of this deformation, but we neglect such possibilities here.)

6.6.3.2 Poresize

Suppose that in the undeformed reference state either porous media is composed of M pores per unit area, each with equal size $\hat{a}_0$. The porosity, φ_0, is the volume fraction of the pores,

$$\varphi_0 = M\pi\hat{a}_0^2. \tag{6.43}$$

After deformation, the pores have a new radius, $\hat{a}_d$. If we assume that the number of pores is unchanged following deformation then the new poresize is related to the original poresize via (6.42), with $\varphi_\mathrm{d} = M\pi\hat{a}_d^2$, by

$$\hat{a}_d = \hat{a}_0\sqrt{1 + \Delta\left(\frac{1}{\varphi_0} - 1\right)}. \tag{6.44}$$

Scaling the poresize by its undeformed value, $\hat{a}_d = \hat{a}_0 a_d$, and using $\Delta \ll 1$ we have

$$a_d \approx 1 + \frac{1}{2}\Delta\left(\frac{1}{\varphi_0} - 1\right). \tag{6.45}$$

As expected, the poresize increases for $\Delta > 0$ and decreases for $\Delta < 0$ (recalling that $0 < \varphi_0 < 1$).

The poresize (6.45) is a function of position, r, since $\Delta = \Delta(r)$ (6.39). The most important poresize is that at the surface of the membrane at the membrane–cake interface ($r = 1$). If this poresize is larger than the radius of the particles, then fouling of the membrane should occur. This is consistent with the observed increase in fouling of a membrane as filtration progresses.

6.6.3.3 Permeability

The permeability, $\hat{k}$, of a porous medium is related to its porosity, φ, and poresize, $\hat{a}_\mathrm{pore}$, by the Kozeny–Carman relation (2.35). Hence, changes to both of these properties, as discussed in §6.6.3.1 and 6.6.3.2, result in a combined elastic response for

the permeability. We assume that the tortuosity does not change. The deformed permeability of the membrane and cake takes the form

$$\begin{aligned}\hat{k}_{\mathrm{d}} &= \frac{\varphi_{\mathrm{d}}^3}{(1-\varphi_{\mathrm{d}})^2}\frac{\hat{a}_d^2}{36\tau},\\ &\approx \hat{k}_0\Big(1+k_1\Delta(r)\Big),\end{aligned} \tag{6.46}$$

by (6.42) and (6.45), neglecting $\mathcal{O}(\Delta^2)$ terms, where

$$\hat{k}_0 = \frac{\varphi_0^3}{(1-\varphi_0)^2}\frac{\hat{a}_0^2}{36\tau}, \tag{6.47a}$$

$$k_1 = \frac{2\,(2-\varphi_0)}{\varphi_0}. \tag{6.47b}$$

The dimensional parameter in (6.47a) for the membrane, given by

$$\hat{k}_0 = \hat{k}_{\mathrm{m},0} = \frac{\varphi_{\mathrm{m},0}^3}{(1-\varphi_{\mathrm{m},0})^2}\frac{\hat{a}_{\mathrm{m},0}^2}{36\tau_{\mathrm{m}}}, \tag{6.48}$$

is the material parameter for the permeability of the undeformed membrane and is used for the non-dimensionalization (6.27) of our system. The actual leading-order membrane permeability, accounting for fouling, is taken to be $\hat{k}_{\mathrm{m},0}N$.

We non-dimensionalize the permeabilities by scaling with $\hat{k}_{\mathrm{m},0}$ so that

$$k_{\mathrm{m}} = N\,(1+k_{\mathrm{m},1}\Delta_{\mathrm{m}})\,, \tag{6.49a}$$

$$k_{\mathrm{c}} = \kappa\,(1+k_{\mathrm{c},1}\Delta_{\mathrm{c}})\,, \tag{6.49b}$$

where Δ_{m} and Δ_{c} are the membrane the cake layer dilations characterizing their deformation, obtained via Eq. (6.39).

An increase in the permeability ($\Delta > 0$) due to elastic effects means that the fluid flows through the material with less resistance, and reduces the pressure gradient across the medium, *cf.*, Darcy's law (2.15). In this way, elastic expansion of the membrane can increase fouling via an increase in the poresize (6.45), but reduces the pressure required for filtration. Conversely, a decrease in the permeability ($\Delta < 0$), as we will see is the case for the cake layer, means that there is more resistance to flow, increasing the pressure gradient in the medium.

6.7 Elastic Deformation

Using the typical parameter values from §6.3, we find that

$$\Omega \approx 6.05 \times 10^3, \qquad \Gamma \approx 94.18, \qquad \omega \approx 0.012, \qquad \gamma \approx 0.875, \qquad \kappa = 1. \tag{6.50}$$

We note that Ω takes a large value, indicating a stiff material (consistent with our assumption of small strains and use of linear elasticity). Furthermore, to a reasonable approximation, $\Gamma \approx 1/\omega$, is also large, and $\Gamma/\Omega \approx \omega/\gamma$. We note that we may exploit these large and small values to perform an asymptotic analysis of the elastic deformation system given by (6.34), (6.35), (6.36), and (6.37). Here, at order $\mathcal{O}(1/\Omega) \ll 1$, the membrane is undeformed, and the cake layer deforms as a porous medium on top of a rigid surface. The membrane deforms at the next order ($\mathcal{O}(1/\Omega^2) \ll 1$), with a membrane–cake layer interaction occurring.

However, we want the membrane to deform by a small degree, but not so small that we do not observe a change in pressure due to fouling. We now solve the equations developed in §6.6.2 analytically for the elastic deformations of the cake layer and membrane caused by the flow in (6.29). The elastic response perturbs the fluid flow and we discuss the consequences for membrane filtration.

We shall analyse the effect a small deformation has on the properties of the membrane and cake layer, such as porosity, poresize and permeability, as described in §6.6.3. The effect we wish to capture here is the change in the permeability of the membrane due to elasticity, $\hat{k}_\mathrm{m} = \left(\hat{k}_{\mathrm{m},0} + \hat{k}_{\mathrm{m},1}\right) N$ (6.1), where $\hat{k}_{\mathrm{m},0}$ is the undeformed and unfouled membrane permeability and $\hat{k}_{\mathrm{m},1}$ is the elasticity correction that we must determine. A key quantity of interest is the pressure, P, required to maintain a constant flux as fouling and caking proceed. To do this, we must determine the deformation itself.

6.7.1 Membrane deformation with no cake layer

The solution to the Navier–Cauchy equation (6.34) for the membrane deformation with no cake layer, u_m^0, along with the stress boundary conditions (6.35), reads

$$u_\mathrm{m}^0 = -\frac{\Gamma}{8\pi\Omega N}\left(-r + 2r\log r\right) + A_\mathrm{m}^0\, r + \frac{B_\mathrm{m}^0}{r}, \tag{6.51}$$

for $1 < r < 1 + \delta_{\mathrm{m}}$, where

$$A^0_{\mathrm{m}} = \frac{8\pi N + \Gamma\left\{\left[(1+\delta_{\mathrm{m}})^2 - 1\right](1-2\nu_{\mathrm{m}}) + 2(1+\delta_{\mathrm{m}})^2 \log\left(1+\delta_{\mathrm{m}}\right)\right\}}{8\pi N\Omega\left[(1+\delta_{\mathrm{m}})^2 - 1\right]}, \tag{6.52a}$$

$$B^0_{\mathrm{m}} = \frac{(1+\delta_{\mathrm{m}})^2\left[4\pi N + \Gamma \log\left(1+\delta_{\mathrm{m}}\right)\right]}{4\pi N\Omega(1-2\nu_{\mathrm{m}})\left[(1+\delta_{\mathrm{m}})^2 - 1\right]}. \tag{6.52b}$$

Note that A^0_{m} and B^0_{m} are both positive as $\nu_{\mathrm{m}} < 1/2$ for the porous membrane, and hence $u^0_{\mathrm{m}} > 0$ for $1 < r < 1 + \delta_{\mathrm{m}}$; the membrane is pushed outwards by the flow, as expected. Crucially, the deformation (6.51) depends on the parameter $1/\Omega$ (6.32): since $1/\Omega$ is small (6.50), the deformation is small.

The deformation with no cake layer for an unfouled and partially fouled membrane is shown in Figure 6.3(a). The membrane deformation decreases with position, r, but increases with the amount of fouling (as N decreases). This is because the fluid pressure (6.29b), which stresses the membrane, increases with fouling to maintain a constant flux. This effect appears in the governing equations (6.34a) for the elastic response. Naively, we ought to expect that $u^0_{\mathrm{m}} \propto 1/N$, but inspection of Figure 6.3 reveals this is not the case.

The local dilation (6.39) of the membrane, that characterizes the deformation by the fluid, is given by

$$\begin{aligned}\Delta^0_{\mathrm{m}} &= -\frac{\Gamma}{2\pi\Omega N}\log r + 2A^0_{\mathrm{m}}, \\ &= \frac{1}{4\pi N\Omega\left[(1+\delta_{\mathrm{m}})^2 - 1\right]}\Bigg[8\pi N + \\ &\qquad \Gamma\left\{(1-2\nu_{\mathrm{m}})\left[(1+\delta_{\mathrm{m}})^2 - 1\right] + 2(1+\delta_{\mathrm{m}})^2 \log\frac{1+\delta_{\mathrm{m}}}{r} + 2\log r\right\}\Bigg],\end{aligned} \tag{6.53}$$

using (6.51) and (6.52a). This local dilation is positive for $1 < r < 1 + \delta_{\mathrm{m}}$ and $\nu_{\mathrm{m}} < 1/2$. Hence, the deformation is an expansion of the porous membrane, scaling with $1/\Omega$ as expected.

The dilation in this case is shown in Figure 6.3(b) (derived from the deformations shown in Figure 6.3(a)). The local dilation (6.53) is a decreasing function of position, r: expansion of the membrane is greater at the membrane surface and decays further into the membrane. This is as expected since the stresses are due to the fluid pressure (6.29b), which falls with position.

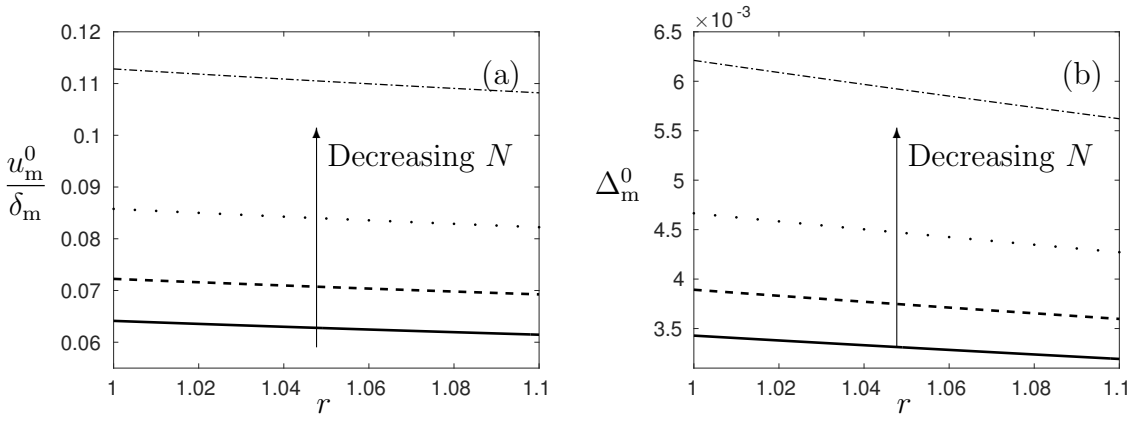

Figure 6.3: (a) The membrane deformation with no cake (6.51), as a fraction of membrane thickness. (b) The membrane dilation with no cake (6.53). The additional fouling increases the membrane deformation and dilation. The fouling corresponds to $N = 1$ (solid), $N = 0.8$ (dashed), $N = 0.6$ (dotted), and $N = 0.4$ (dot-dashed).

6.7.2 Membrane and cake deformation

The solution to the Navier–Cauchy equations (6.36) for the membrane and cake layer deformation, with boundary conditions (6.37), reads

$$u_{\mathrm{m}} = -\frac{\Gamma}{8\pi\Omega N}\left(-r + 2r\log\, r\right) + A_{\mathrm{m}}\, r + \frac{B_{\mathrm{m}}}{r}, \qquad 1 < r < 1 + \delta_{\mathrm{m}}, \tag{6.54a}$$

$$u_{\mathrm{c}} = -\frac{\Gamma\gamma}{8\pi\Omega\omega\kappa}\left(-r + 2r\log\, r\right) + A_{\mathrm{c}}\, r + \frac{B_{\mathrm{c}}}{r}, \qquad 1 - \delta_{\mathrm{c}} < r < 1, \tag{6.54b}$$

where A_{m}, B_{m}, A_{c}, and B_{c} are constants determined by substituting the general solutions (6.54) into the boundary conditions (6.37). These constants may be determined explicitly, but for brevity we show their expressions in matrix form,

$$\begin{pmatrix} A_{\mathrm{m}} \\ B_{\mathrm{m}} \\ A_{\mathrm{c}} \\ B_{\mathrm{c}} \end{pmatrix} = \begin{pmatrix} (1+\delta_{\mathrm{m}})^2 & -1+2\nu_{\mathrm{m}} & 0 & 0 \\ 0 & 0 & (1-\delta_{\mathrm{c}})^2 & -1+2\nu_{\mathrm{c}} \\ 1 & -1+2\nu_{\mathrm{m}} & -\omega & \omega(1-2\nu_{\mathrm{c}}) \\ -1 & -1 & 1 & 1 \end{pmatrix}^{-1} \Xi, \tag{6.55}$$

where

$$\Xi = \begin{pmatrix} \dfrac{\Gamma(1+\delta_{\mathrm{m}})^2}{8\pi N\Omega}\left[1-2\nu_{\mathrm{m}}+2\log\left(1+\delta_{\mathrm{m}}\right)\right] \\ \dfrac{(1-\delta_{\mathrm{c}})^2}{8\pi\kappa\Omega\omega}\left[-8\pi\kappa+\Gamma\gamma(1-2\nu_{\mathrm{c}})+2\dfrac{\log\left(1-\delta_{\mathrm{c}}\right)}{\log\left(1+\delta_{\mathrm{m}}\right)}\left(4\pi N+\Gamma\gamma\log\left(1+\delta_{\mathrm{m}}\right)\right)\right] \\ \dfrac{\Gamma}{8\pi\kappa\Omega}\left[\gamma(-1+2\nu_{\mathrm{c}})+\dfrac{\kappa(1-2\nu_{\mathrm{m}})}{N}\right] \\ -u_{\mathrm{m}}^{0}(1)+\dfrac{\gamma}{8\pi\Omega}\left[\dfrac{1}{N}-\dfrac{\gamma}{\kappa\omega}\right] \end{pmatrix}. \tag{6.56}$$

When the cake thickness is zero, A_{m} and B_{m} reduce to (6.52), obtained in the absence of a cake. We note that the solution incorporates the deformation with no cake layer, u_{m}^{0}, after the last backflush or at the beginning of the experiment.

The membrane and cake deformations are plotted in Figure 6.4 for various cake thicknesses, δ_{c}. Here, we have chosen an initially unfouled membrane ($N=1$), but plot the deformations for fouling corresponding to $N=0.75$ for various cake thicknesses. This means that the deformation of the membrane before any cake development, u_{m}^{0} (6.51), is calculated with $N=1$. The deformations decrease with position, r, but increase with the cake layer thickness, δ_{c}, as seen in Figure 6.4. Again, this may be attributed to the decreasing hydrodynamic pressure within the membrane.

The local dilations (6.39) of the membrane and cake layer, due to the deformation (6.54), are given by

$$\Delta_{\mathrm{m}} = -\frac{\Gamma}{2\pi\Omega N}\log r + 2A_{\mathrm{m}}, \qquad 1 < r < 1+\delta_{\mathrm{m}}, \tag{6.57a}$$

$$\Delta_{\mathrm{c}} = -\frac{\Gamma\gamma}{2\pi\Omega\omega\kappa}\log r + 2A_{\mathrm{c}}, \qquad 1-\delta_{\mathrm{c}} < r < 1, \tag{6.57b}$$

respectively, where A_{m} and A_{c} are given in (6.55). The small dilations of the membrane and cake layer are shown in Figure 6.4, where we vary the cake thickness.

The membrane deformations correspond to an expansion (6.57a) that decays with radial position, r (Figure 6.4(d)). This means that, like the case with no cake layer, the deformation (expansion) is greater at the membrane surface, and less so further in. However, the magnitude of dilation increases with cake size, due to the additional mechanical stress exerted.

The cake layer deformations correspond to a compression (6.57b) that is an increasing function of position, r (Figure 6.4(c)). This means that the deformation (compression) is smaller at the membrane surface than inside the cake region. This makes sense since the membrane is retaining (confining) the cake layer so that it is being squeezed here. The cake compression increases with cake thickness.

Observing that the membrane expands ($\Delta_{\mathrm{m}} > 0$) and the cake compresses ($\Delta_{\mathrm{c}} < 0$) has interesting consequences for the filtration process. In particular the expansion and contraction affects the respective material properties, such as porosity, poresize and permeability, as we shall see in §6.8, and perturbs the fluid flow in the system, as we shall see in §6.9. Furthermore the results of our model, that the membrane expands and the cake layer contracts, explains the experimental observations as in Chou et al. (2013), Guo et al. (2012), Hwang and Hsueh (2003), and She et al. (2012).

6.7.3 Deformation of a fouled membrane with a cake

Previously we considered deformation of a cake layer and membrane when the cake layer is assumed to have developed on an initially unfouled membrane, *i.e.*, $N = 1$. Although we do not discuss the rate of fouling here (see Chapter 7), we recognize that some degree of fouling occurs (*i.e.*, $N = N_1 < 1$) during filtration. Furthermore, a backflush may be performed, removing the cake layer but not the fouling particles. As a result, when filtration resumes, $N = N_1$. Here, we consider the elastic effects in the system with a membrane that is, initially, partially fouled before the cake layer develops. The deformation with no cake layer, u_{m}^0 via (6.34) and (6.35), now corresponds to this partially fouled membrane: as observed in Figure 6.3(a), u_{m}^0 increases with decreasing N.

We take $N = 0.8$ and re-calculate the deformations and dilations of the membrane and cake layers via (6.36) and (6.37) that have developed on the partially fouled membrane where further fouling has resulted in $N = 0.75$. This means that we can compare the result to the deformations in Figure 6.4 where $N = 0.75$ but no intermediate backflush was performed. In Figure 6.5, we show the resulting deformation and dilation for the cake thickness, $\delta_{\mathrm{c}} = 0.1 = \delta_{\mathrm{m}}$ (the blue curves in Figure 6.4). The behaviour is similar for other thicknesses. The deformation and dilation has decreased for the cake layer but increased for the membrane, as expected since the partially fouled membrane requires a higher driving pressure to maintain a constant flux.

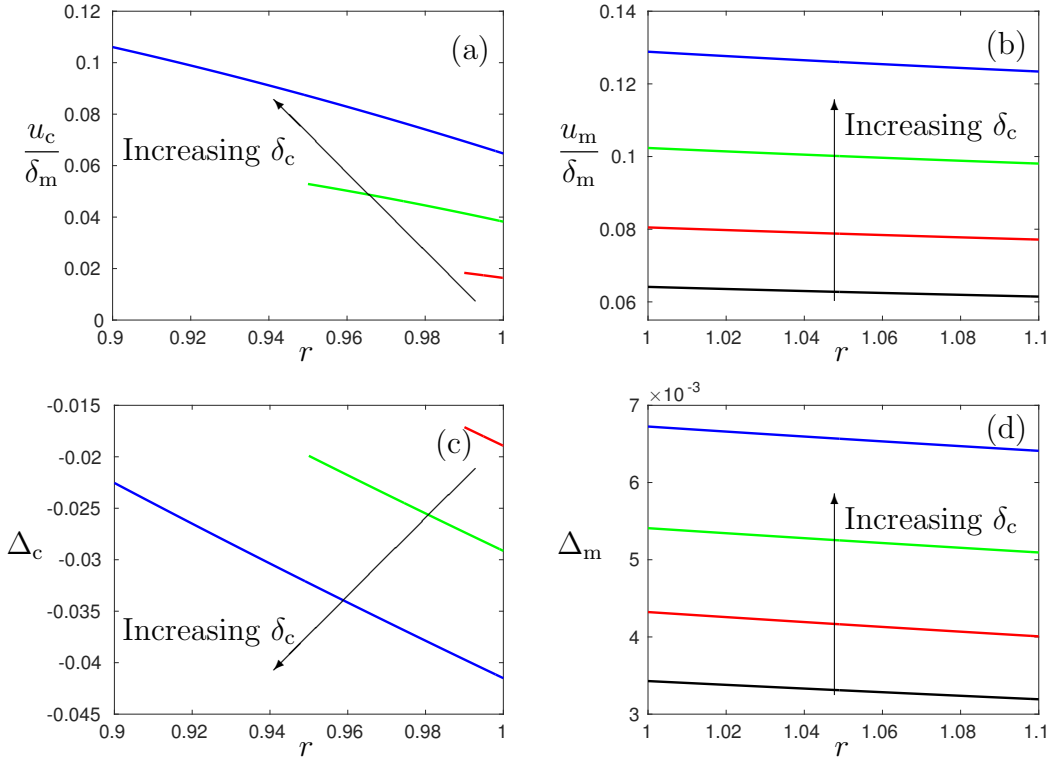

Figure 6.4: A plot of the deformations of the (a) cake, u_c, and (b) membrane, u_m, and the dilations of the (c) cake layer, Δ_c, and (d) membrane, Δ_m. These are shown as functions of position, with the deformation scaled as fractions of the membrane thickness. Initially the membrane is unfouled ($N = 1$) resulting in a membrane deformation and dilation with no cake layer (6.51) given by the black curves in (b) and (d). Plotted here are the deformations for fouling corresponding to $N = 0.75$. Results are shown for $\delta_c = 0.01$ (red), $\delta_c = 0.05$ (green), and $\delta_c = 0.1$ (blue) in each case, and $\delta_m = 0.1$. The deformations decrease with position, r, but also increase with the cake layer thickness, δ_c. The dilations tell us that the membrane deformations correspond to an expansion, but the cake layer deformations correspond to a compression.

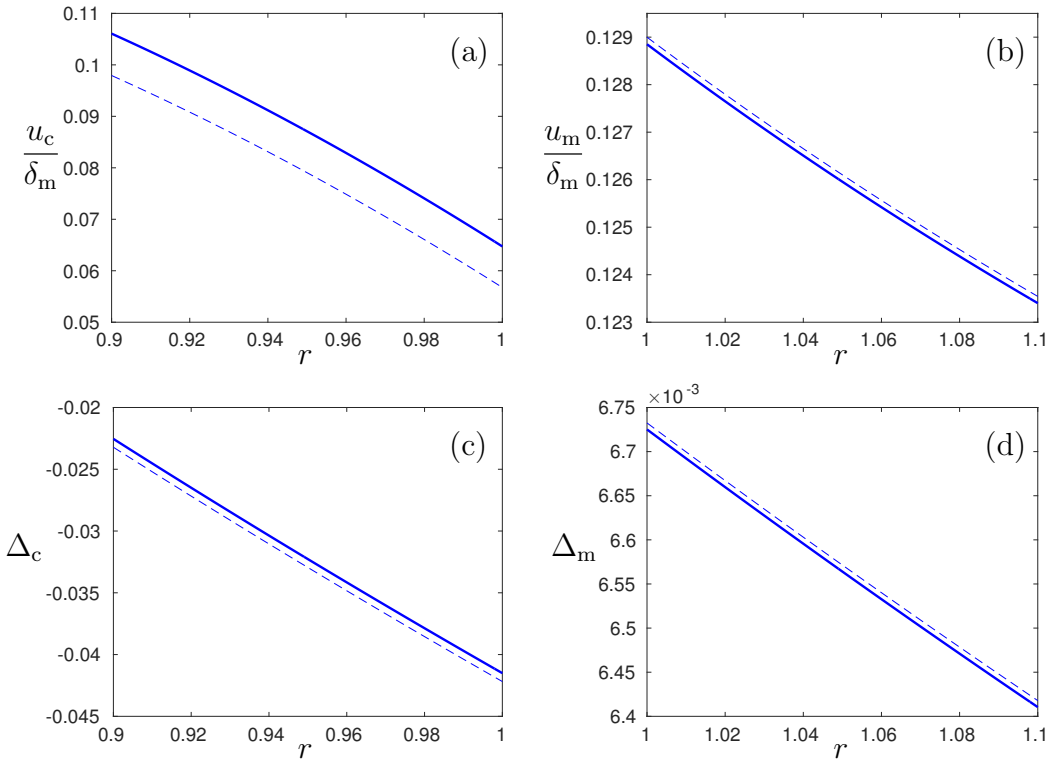

Figure 6.5: A plot of the deformation of the (a) cake, u_c, and (b) membrane, u_m, and the dilation of the (c) cake layer, Δ_c, and (d) membrane, Δ_m. These are shown as functions of position, with the deformation scaled as fractions of the membrane thickness. These deformations are for a cake thickness of $\delta_c = 0.1 = \delta_m$. This cake has developed on an unfouled ($N = 1$) membrane (solid) and on a membrane after a backflush was performed with $N = 0.8$ (dashed). The membrane deformation increases and the cake deformation decreases.

The only change to the system is that a backflush has occurred at an intermediate fouling stage, increasing the deformation with no cake layer when filtration resumes u_{m}^0. This, and the additional mechanical stress of the cake, accounts for the increased membrane deformation. However, an increased u_{m}^0 affects the cake deformation via the boundary condition (6.37d), where it will reduce the cake deformation.

6.8 Elastic effects on material properties

The deformation of both the membrane and cake layer alters their material properties. In the case of small deformation, with dilation $\Delta \ll 1$, the material properties such as porosity, poresize and permeability that we will discuss here depend linearly on the dilation, Δ. This linear dependence on the dilation means that the changes in porosity, poresize and permeability for each medium are represented by a factor of the expressions given in Eq. (6.57), whose dependence on position, r, fouling, N, cake thickness, δ_{c}, and backflush properties are represented in Figures 6.4 and 6.5.

6.8.1 Porosity

The porosity of a porous medium was discussed in §6.6.3.1. For our system, the deformed membrane and cake porosities, $\varphi_{\mathrm{m,d}}$ and $\varphi_{\mathrm{c,d}}$ respectively, may be written in terms of their undeformed porosities, $\varphi_{\mathrm{m},0}$ and $\varphi_{\mathrm{c},0}$ respectively, via (6.42),

$$\varphi_{\mathrm{m,d}} \approx \varphi_{\mathrm{m},0} + \Delta_{\mathrm{m}}(1 - \varphi_{\mathrm{m},0}), \tag{6.58a}$$

$$\varphi_{\mathrm{c,d}} \approx \varphi_{\mathrm{c},0} + \Delta_{\mathrm{c}}(1 - \varphi_{\mathrm{c},0}), \tag{6.58b}$$

where $\Delta_{\mathrm{m}} > 0$ (6.57a) is the membrane expansion and $\Delta_{\mathrm{c}} < 0$ (6.57b) is the cake layer compression. The dilations are functions of position, meaning that the porosity is altered non-uniformly by elastic effects.

The linear dependence on the dilation means that the changes in porosity for each medium may be directly inferred from Figures 6.4 and 6.5. The porosity of the membrane increases, meaning there is more free space for the fluid in the membrane pore space. Conversely, the cake porosity decreases, meaning there is less free space for the fluid in the cake pore space. Porosity also plays an important role in the permeability of a porous medium, *cf.*, Kozeny–Carman relation (2.35); we will discuss this further in §6.8.3.

6.8.2 Poresize

The poresize of a porous medium was discussed in §6.6.3.2. The membrane poresize increases since $\Delta_{\mathrm{m}} > 0$, and the cake poresize decreases since $\Delta_{\mathrm{c}} > 0$. As with the porosity, the poresize plays an important role in the permeability of each medium. However, from a practical point of view, in membrane filtration we are most interested in the poresize of the membrane as this determines the particle sizes that will be rejected. The poresize in the undeformed membrane is uniform. However, Δ_{m} is a function of r that is positive and decreasing with position (Figure 6.4(d)). This means that the pores have expanded, but are now asymmetric (larger on the inner surface of the membrane and continuously narrowing with depth).

Although larger particles may enter the membrane, the pores may constrain and capture them further into the membrane. Hence the particles may enter the membrane and foul it irreversibly. Many membranes are manufactured to have such an asymmetry even in the absence of flow; here we see that initially uniform membranes naturally deform to an asymmetric state.

However, we are most concerned with the membrane poresize at the cake layer–membrane interface ($r = 1$), where the particles are retained. Here, if the deformed membrane poresize, $a_{\mathrm{m,d}}(r = 1)$, is greater than the particle size, then particles may enter into the membrane, leading to fouling. Now,

$$\begin{aligned} a_{\mathrm{m,d}}(r = 1) &= 1 + \frac{1}{2}\Delta_{\mathrm{m}}(r = 1)\left(\frac{1}{\varphi_{\mathrm{m},0}} - 1\right), \\ &= 1 + A_{\mathrm{m}}\left(\frac{1}{\varphi_{\mathrm{m},0}} - 1\right), \end{aligned} \tag{6.59}$$

using (6.57a) at $r = 1$ where the constant A_{m} is given in (6.55). The surface poresize of the membrane is shown in Figure 6.6 as a function of the cake thickness, δ_{c}, for various amounts of fouling, N. The poresize increases with δ_{c}, as expected due to the additional stress it exerts on the membrane. Interestingly, the rate of poresize increase is larger for less fouling, and there is a crossover point at which the less fouled membrane is deformed to a larger poresize than the more fouled membrane, with the same cake layer. Although not shown here, we note that the stresses in the membrane and cake layer are dependent on N and δ_{c}. We do not fully understand this behaviour but suggest, from calculations of the stress, that perhaps the more a membrane is fouled, the more it resembles a rigid wall; the stress distribution in the

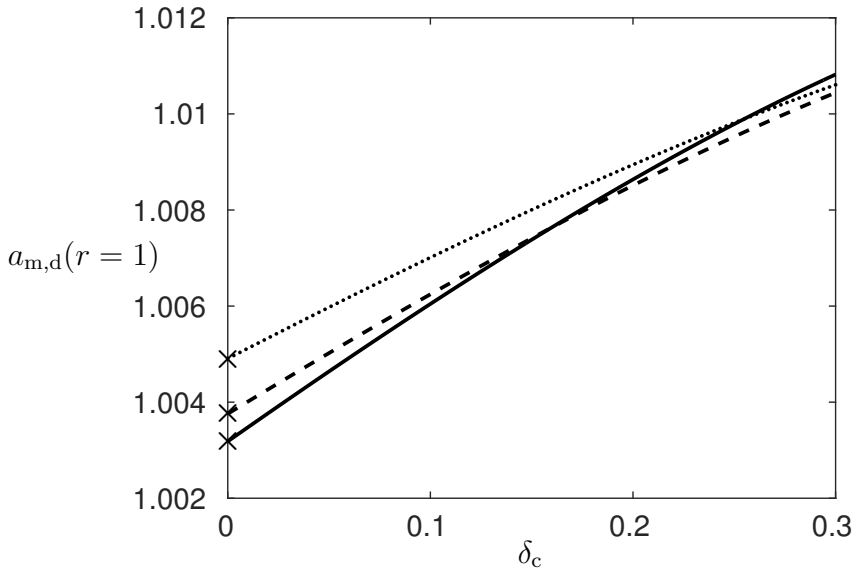

Figure 6.6: The membrane surface poresize, $a_{\mathrm{m,d}}(r=1)$ via (6.59), as a function of the cake thickness, δ_{c}, for various amounts of fouling, N. The membrane thickness is taken to be $\delta_{\mathrm{m}} = 0.1$. We take $N = 1$ (solid), $N = 0.75$ (dashed), $N = 0.5$ (dotted). The "×" marking is the poresize for the deformed membrane with no cake layer, computed using the dilation in (6.53).

cake layer may then reconfigure within the medium and, with continuity of stress at the cake–membrane interface, the pores do not expand to the expected extent.

The cake layer poresize is also deformed asymmetrically, again with the pores becoming smaller with depth. However, since the cake is being compressed, this poresize is smaller than its undeformed state.

6.8.3 Permeability

The permeability of a porous medium was discussed in §6.6.3.3. The fluid flow through the membrane and cake layer deforms the porous media (6.54), with dilations of the form (6.57). As the permeability is given by the Kozeny–Carman relation (6.46), the permeability increases with the porosity and poresize, and hence with their deformations. For each porous medium, the permeabilities of the deformed membrane and cake layer are given by (6.49).

Specifically, the elastic effects mean that the membrane permeability increases ($\Delta_{\mathrm{m}} > 0$ as in Figure 6.4(d)) and the cake permeability decreases ($\Delta_{\mathrm{c}} < 0$ as in Fig-

ure 6.4(c)). Furthermore, the permeability, like the porosity and poresize, is asymmetric in each porous medium.

6.8.4 Young's modulus and Poisson ratio

The above elastic effects on porosity, poresize and permeability result in first-order changes to the fluid flow and membrane fouling. Other parameters such as the Young's modulus, E, and Poisson ratio, ν, are also likely to be affected. However, these deformed parameters alter the fluid flow and membrane fouling by way of a second-order deformation (caused by the perturbed flow) and we neglect such considerations here.

Furthermore, our assumption that the fouled pores do not allow more particles inside (as the cake layer builds up on top of the blocked region) means that only a single layer of particles foul the membrane internally. We do not account for depth in the fouling (multiple particles fouling the same pore at different depths as in Griffiths et al. (2014)), and so the changes to the Young's modulus and Poisson ratio will not be significant.

6.9 Flow Perturbation

We have seen in §6.8 that elastic deformations of the membrane and cake layer affect the material properties of the porous medium, especially the permeability (§6.8.3). As the system we consider operates at constant flux, the fluid velocity is unperturbed (6.29a). The flow variable that is perturbed by these elastic effects is the pressure. Here we analyse the pressure perturbation in each porous medium, and the overall driving pressure across the whole system.

6.9.1 Pressure perturbation

Consider the pressure scaling in (6.27), $\hat{p} = (Q\mu/\hat{k}_{\mathrm{m}})p$. We take the permeability to scale like the undeformed membrane permeability, $\hat{k}_{\mathrm{m}} \sim \hat{k}_{\mathrm{m},0}$, and so modifying the Darcy equation (6.8b) for the pressure in the membrane to account for the permeability perturbation $1 + \Delta_{\mathrm{m}} k_{\mathrm{m},1}$ (6.46), via Darcy's law (2.15), gives

$$v = -\left(1 + \Delta_{\mathrm{m}}(r)\ k_{\mathrm{m},1}\right) N \frac{\mathrm{d}p}{\mathrm{d}r}, \tag{6.60}$$

where $k_{\mathrm{m},1}$ (6.47b) is a constant and $\Delta_{\mathrm{m}} = 2A_{\mathrm{m}} - (\Gamma/2\pi\Omega N)\log r$ (6.57a). Substituting the velocity from (6.29a) and rearranging, the pressure gradient reads

$$\frac{\mathrm{d}p}{\mathrm{d}r} = -\frac{1}{2\pi N\left(1+\Delta_{\mathrm{m}}(r)\ k_{\mathrm{m},1}\right)r} \approx -\frac{1}{2\pi N r} + \frac{A_{\mathrm{m}}k_{\mathrm{m},1}}{\pi N r} - \frac{\Gamma k_{\mathrm{m},1}\log r}{4\pi^2\Omega N^2 r}, \tag{6.61}$$

with A_{m} (6.55), Γ, Ω (6.32), $k_{\mathrm{m},1}$ (6.47b) all constant and $\Delta_{\mathrm{m}}(r) \ll 1$ a function of r. Note that the additional term is such that the pressure gradient is less negative than in the rigid (inelastic) undeformed case. This makes sense as the membrane is expanding, *i.e.*, more permeable meaning that less force is required to drive the fluid through. Integrating for the pressure, with $p(r = 1+\delta_{\mathrm{m}}) = 0$, results in a pressure field,

$$p = \frac{1}{2\pi N}\log\left(\frac{1+\delta_{\mathrm{m}}}{r}\right) + \frac{k_{\mathrm{m},1}}{\pi N}\log\left(\frac{1+\delta_{\mathrm{m}}}{r}\right)\left[\frac{\Gamma}{8\pi\Omega N}\log\left[r(1+\delta_{\mathrm{m}})\right] - A_{\mathrm{m}}\right], \tag{6.62}$$

for $1 < r < 1+\delta_{\mathrm{m}}$, where the first term is the pressure in the membrane without deformation (6.29b). The second term is negative for $1 < r < 1+\delta_{\mathrm{m}}$ meaning that the pressure difference across the membrane has been reduced, as just discussed.

As with the membrane expansion, the deformed permeability caused by compression of the cake modifies the Darcy equation (6.6b) to read

$$v = -\kappa\left(1+\Delta_{\mathrm{c}}(r)\ k_{\mathrm{c},1}\right)\frac{\mathrm{d}p}{\mathrm{d}r}, \tag{6.63}$$

where $k_{\mathrm{c},1}$ (6.47b) is a constant and $\Delta_{\mathrm{c}} = 2A_{\mathrm{c}} - (\Gamma\gamma/2\pi\Omega\omega\kappa)\log r$ (6.57b). Substituting the velocity from (6.29a) and rearranging, the pressure gradient reads

$$\frac{\mathrm{d}p}{\mathrm{d}r} = -\frac{1}{2\pi\kappa\left(1+\Delta_{\mathrm{c}}(r)\ k_{\mathrm{c},1}\right)r} \approx -\frac{1}{2\pi\kappa r} + \frac{A_{\mathrm{c}}k_{\mathrm{c},1}}{\pi\kappa r} - \frac{\Gamma\gamma k_{\mathrm{c},1}\log r}{4\pi^2\Omega\omega\kappa^2 r}, \tag{6.64}$$

with A_{c} (6.55), Γ, Ω (6.32), γ, ω (6.33), κ (6.30) and $k_{\mathrm{c},1}$ (6.47b) all constants and $\Delta_{\mathrm{c}}(r) \ll 1$ a function of r. Note that in this case the additional term due to deformation is such that the pressure gradient is more negative than the inelastic undeformed case. This makes sense as the cake layer is being compressed, *i.e.*, it is less permeable meaning that more force is required to drive the fluid through. This contrasts with the membrane layer, which is expanding and, as such, requires a larger pressure gradient. Integrating for the pressure, with continuity of pressure at the membrane-cake layer interface, $[p(r=1)] = 0$, with $p(r=1)^+$ from (6.62) at $r = 1$,

results in a pressure field

$$p = \frac{1}{2\pi N}\log\,(1+\delta_{\mathrm{m}}) + \frac{k_{\mathrm{m},1}}{\pi N}\log\,(1+\delta_{\mathrm{m}})\left[\frac{\Gamma}{8\pi\Omega N}\log\,(1+\delta_{\mathrm{m}}) - A_{\mathrm{m}}\right] - \frac{1}{2\pi\kappa}\log\,r - \frac{k_{\mathrm{c},1}}{\pi\kappa}\log\,r\left[\frac{\Gamma\gamma}{8\pi\Omega\omega\kappa}\log\,r - A_{\mathrm{c}}\right], \tag{6.65}$$

for $1-\delta_{\mathrm{c}} < r < 1$. The terms on the first line are from the pressure required in the membrane (Eq. (6.62) with $r = 1$). The first terms on both the first and the second lines give the leading-order pressure required for the cake layer, *i.e.*, without deformation (6.29b). The final term is positive for $1-\delta_{\mathrm{c}} < r < 1$ meaning that the pressure difference across the cake layer has been increased, as just discussed.

6.9.2 Driving pressure

The driving pressure, P, required to maintain a constant flux through the membrane and cake layers, is the (constant) pressure found within the device ($r < 1-\delta_{\mathrm{c}}$). At leading order, this driving pressure reads

$$P = P_2 = \frac{1}{2\pi N}\log\,(1+\delta_{\mathrm{m}}) - \frac{1}{2\pi\kappa}\log\,(1-\delta_{\mathrm{c}}), \tag{6.66}$$

as in (6.29b). This includes the effect of the fouling, N, and the ratio of permeabilities, κ (6.33). However, elastic deformation modifies the permeabilities of each layer, altering each porous region differently, as discussed in §6.9.1.

The driving pressure, P, accounting for elastic deformation, may be calculated analytically. Since the pressure in the internal region is constant (6.29b), the driving pressure, P, is the pressure, (6.65), at the inner cake boundary ($r = 1-\delta_{\mathrm{c}}$).

$$\begin{aligned} P \;=\; & \frac{1}{2\pi N}\log\,(1+\delta_{\mathrm{m}}) - \frac{1}{2\pi\kappa}\log\,(1-\delta_{\mathrm{c}}) \\ & + \frac{k_{\mathrm{m},1}}{\pi N}\log\,(1+\delta_{\mathrm{m}})\left[\frac{\Gamma}{8\pi\Omega N}\log\,(1+\delta_{\mathrm{m}}) - A_{\mathrm{m}}\right] \\ & - \frac{k_{\mathrm{c},1}}{\pi\kappa}\log\,(1-\delta_{\mathrm{c}})\left[\frac{\Gamma\gamma}{8\pi\Omega\omega\kappa}\log\,(1-\delta_{\mathrm{c}}) - A_{\mathrm{c}}\right]. \end{aligned} \tag{6.67}$$

Fouling, characterized by N, and the cake thickness, δ_{c}, appear explicitly as parameters or within expressions such as the constants from the deformation (6.55). The first two terms represent the leading-order pressure without any deformation, P_2, as in (6.66). The remaining two terms represent the first-order corrections to the

pressure due to the expansion of the membrane, reducing the driving pressure, and compression of the cake, increasing the driving pressure.

The driving pressure in Eq. (6.67) is a key result. As already discussed, the amount of fouling and caking influence the result in opposing ways. In the next chapter, we study the coupled evolution of fouling and cake development (with periodic backflushing). We will determine conditions for which the elastic deformation can result in a decreased driving pressure, *i.e.*, less energy required than the rigid case.

6.10 Conclusions

We have modelled the elastic deformation of a membrane and cake layer during filtration. The model agrees with experimental observations that the membrane expands and the cake layer compresses (Guo et al., 2012; She et al., 2012; Chou et al., 2013; Hwang and Hsueh, 2003). We have analysed and quantified the results with respect to the parameters of the system: the deformations increase with the cake thickness, the degree of fouling, and with backflushing (here we have compared the deformation of an initially clean membrane with a cake to that of an initially partially fouled membrane with the same cake). We have determined the effect on material parameters of the membrane, and the effect on the fluid flow.

The effects of elastic deformations of a membrane and cake layer during water filtration provide many interesting considerations for the filtration industry, including a dilemma in the choice of poresize that maximizes permeability without compromising on fouling. The membrane's porosity, poresize and permeability are all increased by deformation. This membrane expansion may improve the filtration rate but also reduce its effectiveness at rejecting contaminants: these changes allow larger particles to enter the membrane, fouling it irreversibly or, in the worst case scenario, passing completely through the membrane.

The membrane permeability depends on its porosity and poresize, via the Kozeny–Carman relation (2.35). In practice, the poresize is restricted with an upper bound the size of the particles to be filtered. However, the poresize can be tuned for the flow and material parameters so that, even after expansion, its maximum size remains just below the particle size. This means that the permeability can be maximized without compromising filtration effectiveness.

A certain amount of fouling is expected in the membrane industry, with the membrane's effectiveness decreasing over time. The filtration process efficiency (energy cost via the driving pressure required), however, increases due to elastic effects. As the membrane permeability increases due to expansion, it is easier to drive a flow through the membrane, *i.e.*, it requires a smaller pressure difference, and hence less energy to operate. However, the cake permeability decreases due to elastic deformation, and so the flow in this porous medium requires a larger pressure difference. Performing more frequent backflushes would reduce the size and influence of the cake layer.

This raises the question of whether a balance exists for operating the filtration process. The decrease in pressure drop (and hence driving pressure) from membrane expansion, the increase in pressure drop from cake contraction, and the loss of operating time via regularly stopping the process to perform a backflush, may cancel out. It is not just a question of more water filtered (operating for longer, with fewer backflushes, at higher permeabilities) versus less energy use (operating at lower pressures): the lifetime of the membranes must also be considered. In the next chapter, we will consider some of these questions by modelling the fouling and cake development in the system with time.

Chapter 7

Fouling and Cake Development

Summary

The rates of fouling and caking depend on the particle size in relation to the poresize. We combine the elasticity model of the previous chapter, accounting for the quasi-static increase of the poresize during filtration, and couple this to a model for fouling and cake development. Furthermore, we study the effects of backflushing on the relative importance of caking and fouling. The evolution of the driving pressure in this model is consistent with the observed gradual increase over time. A strategy is proposed to maximize the membrane permeability without fouling occurring, by increasing the number of backflushes that are performed.

7.1 Introduction

In the previous chapter we considered the effect of elasticity on a porous membrane and cake layer. We determined the deformations of a cross-sectional annulus of each medium under the influence of the hydrodynamic pressure and analysed how elastic deformations modify the material parameters of the porous media, feeding back to the pressure required to drive the flow.

The results of the previous chapter are largely illustrative, however. In particular, we studied the deformation with given values of fouling and cake thickness. In reality, the fouling rate and cake development are coupled processes, and are strongly influenced by the frequency of backflushing. This means that we cannot simply pick convenient values for the fouling, N, and cake thickness, δ_c. In this chapter, we develop a model

that couples and quantifies the evolution of fouling and cake development to both elasticity and the backflush frequency.

During filtration at constant flux, a constant number of particles reach the membrane surface. If the size of a particle, $\hat{a}_{\text{part}}$, is larger than the poresize, $\hat{a}_{\text{pore}}$, then the particle is sterically prevented from entering a pore and so cannot cause fouling. Instead it must become part of a cake layer, adding resistance to the flow and exerting a mechanical stress on the membrane. However, if the particle size is less than the poresize, then the particle may enter the pore only to be caught and retained in the tortuous path of the pores within the membrane. This form of membrane fouling is generally irreversible. In particular, fouling is not reversed by backflushing since, in a backflush, the pores compress, holding the particles in position more tightly. Studies have shown that backflushing can return the membrane permeability to its initial state, but the number of particles removed can be as low as 25% (Remize et al., 2010). For simplicity, we assume that backflushing removes the cake layer completely but does not affect the internal fouling of the membrane.

Fouling and caking have been modelled extensively (Field and Wu, 2011; Griffiths et al., 2014; Hermia, 1982; Ho and Zydney, 2000), with fouling typically subcategorized as either complete, intermediate or internal blocking (as discussed in §1.3.3). Here we are concerned with the interaction of the fluid, fouling, and caking with the elastic response of the membrane and cake layer, and how this affects the development of fouling and caking. As such, for simplicity, we consider a model in which fouling occurs via internal pore blocking only: we assume that a single particle plugs a single pore, and any particle that reaches, but does not enter, the membrane pores instead forms part of a cake.

We assume that the cake layer is stable (not easily broken up during filtration, as opposed to a backflush), as the irreversibility of particle attachment to the cake layer was shown in microfiltration experiments with monodisperse particles (Altmann and Ripperger, 1997). This attachment is due to adhesive forces caused by van der Waals and electrostatic interactions. However, as the shear stress increases with cake thickness, eventually the cake reaches an equilibrium thickness (a balance between shear stress and adhesive forces where incident particles are ripped off the surface). Microfiltration experiments report this cake threshold thickness as a significant fraction of the tube radius, up to 38% (Benkahla et al., 1995).

We first show that the poroelastic response timescale is much shorter than the fouling rate so that a quasi-static approximation can be used to decouple the fouling and caking evolution from their elastic responses: the elastic effects may be assumed to occur instantaneously. As fouling proceeds, a higher pressure is needed to drive a constant flux, exerting a higher stress on the membrane, and hence causing further expansion of the membrane. As a result, the pores get larger, permitting larger particles to enter and foul the membrane. This cycle repeats until the membrane is completely fouled. In this chapter we investigate this and the extent to which it may be exacerbated by cake buildup; the process is shown in the flow chart in Figure 7.1. We then study how the design of the membranes and the operation procedure may be tweaked to mitigate the observed pressure and fouling increases over time (Figure 5.1).

7.2 Setup

We assume that the membrane consists of equal sized and equidistributed pores, of radius $\hat{a}_{\text{pore}}$. That is, in the undeformed state, $\hat{a}_{\text{pore}} = \hat{a}_{\text{m,0}}$. In the deformed state, $\hat{a}_{\text{pore}} = \hat{a}_{\text{m,d}}$, a function of the parameters of the system (6.45). In general, $\hat{a}_{\text{pore}} = \hat{a}_{\text{pore}}(\hat{t})$, as the dynamic nature of the fouling and cake growth changes the parameters over time.

Particles in the flow to be filtered are, in general, of varying sizes, and we assume that these reach the membrane at a constant rate. We assume that a (normalized) distribution of particle sizes, $\hat{f}(\hat{s})$, exists where $\hat{s} \in [\hat{a}^{\text{min}}_{\text{part}}, \hat{a}^{\text{max}}_{\text{part}}]$. The minimum particle size is $\hat{a}^{\text{min}}_{\text{part}}$, and maximum particle size is $\hat{a}^{\text{max}}_{\text{part}}$. The distribution may be assumed to be uniform, truncated Gaussian, *etc.* If $\hat{a}_{\text{pore}} < \hat{a}^{\text{min}}_{\text{part}}$ then particles do not foul the membrane and instead only contribute to cake growth; if $\hat{a}_{\text{pore}} > \hat{a}^{\text{max}}_{\text{part}}$ then all the particles enter to foul the membrane. In general, the particles that contribute to fouling are those in the size range $[\hat{a}^{\text{min}}_{\text{part}}, \hat{a}_{\text{pore}}]$ and particles that contribute to cake growth are those in the size range $[\hat{a}_{\text{pore}}, \hat{a}^{\text{max}}_{\text{part}}]$. As such, the fraction of incoming particles that may enter the pore, f_p, is given by

$$f_p(\hat{a}_{\text{pore}}(\hat{t})) = \int_{\hat{a}^{\text{min}}_{\text{part}}}^{\hat{a}_{\text{pore}}(\hat{t})} \hat{f}(\hat{s})\,\mathrm{d}\hat{s}, \tag{7.1}$$

and the fraction that contributes to cake growth is $f_c = 1 - f_p$. The ratio of these contributions to fouling and caking changes with time. Furthermore, we assume that when a cake layer is present, particles deposited on the cake may contribute to fouling

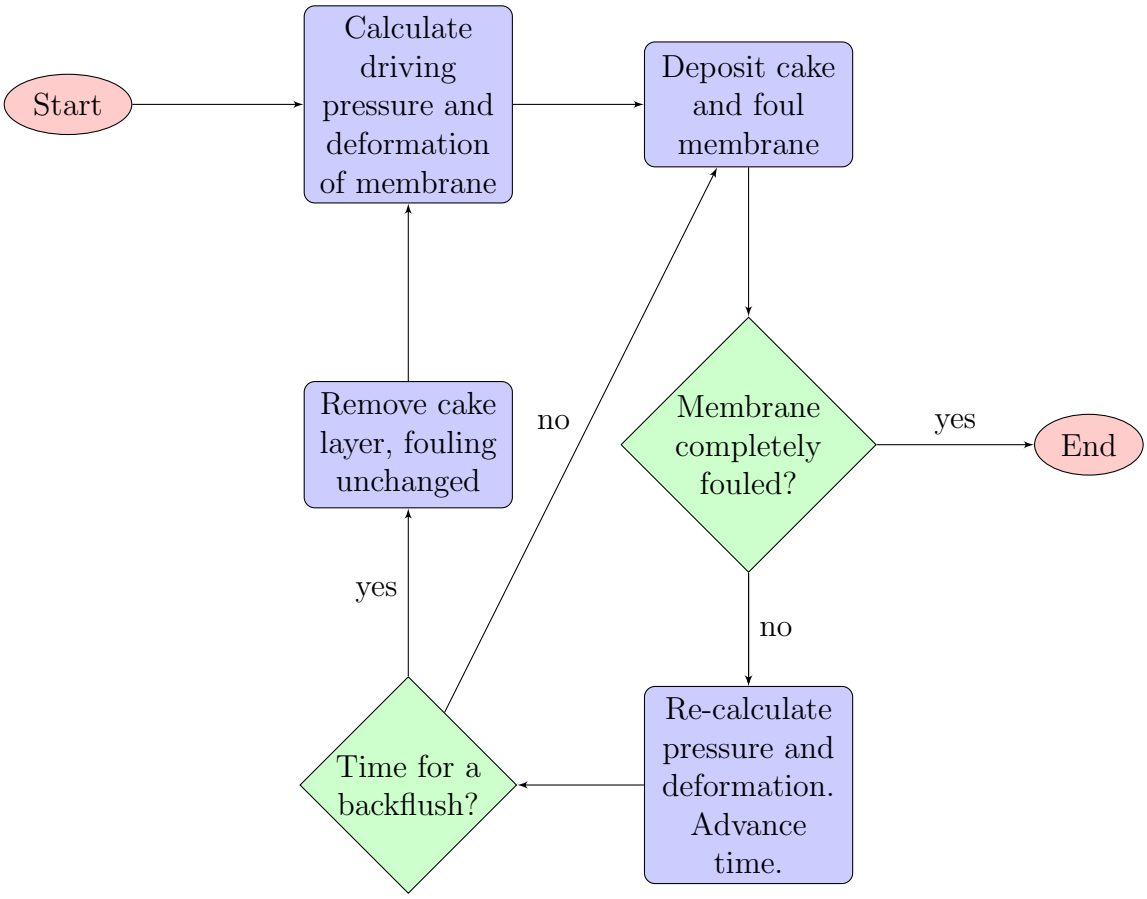

Figure 7.1: Flow chart mapping out the model for fouling and cake development. We start the process with no fouling or cake layer. As particles reach the membrane surface, a cake layer develops and fouling occurs. This changes the flow pressure and elastic deformations. A backflush is periodically performed, removing the cake layer, but the fouling remains unchanged. The system ends when the membrane is completely fouled. We calculate the flow pressure and elastic deformations from our analysis in Chapter 6, and the rates of fouling and caking are derived in this chapter.

despite the cake being in their way to reaching the membrane surface. We justify this by assuming that the cake layer itself may experience dynamic behaviour involving the movement of particles. In some re-ordering the appropriate portion of incoming particles may enter into the membrane.

We use the parameter values given in §6.3, unless otherwise stated.

7.3 Quasi-static Coupling

We can solve for the time evolution of the stresses with the fouling and cake development. However, the rate at which caking develops is on a timescale of the order of minutes (with backflushes performed approximately every 20 minutes). The poroelastic timescale, T_{pe}, reflects the material's control over the storage and release of elastic energy: the diffusion and dissipation of fluid pressure. The timescale T_{pe} may be derived via a combination of conservation of mass, Darcy's law, the Navier equation with Terzaghi's principle, and a stress that is Hertzian elastic and linearly viscous in the volumetric strain (MacMinn et al., 2015). A balance of the strain rate and elastic stress, for the membrane, gives the timescale as

$$T_{\mathrm{pe}} = \frac{\mu R^2}{E_{\mathrm{m}} k_{\mathrm{m},0}} \approx 0.1\,\mathrm{s}. \tag{7.2}$$

As the poroelastic timescale is much shorter than the caking and fouling, changes in the deformation of the porous media occur quasi-statically compared to the rate of fouling and cake growth. Hence, we will solve for the fouling of the membrane and the size of the cake layer, and use an elastic model to determine the quasi-static deformations that occur.

7.4 Fouling

We present a simple model that accounts for the contribution of the incoming particles to fouling. We assume that the fraction of open pores at a time $\hat{t}$ is given by $N(\hat{t})$. A particle only enters a pore if its size is at most that of the pore. We will also assume that any particle smaller than a pore is equally likely to occupy the hole. This means that the first sufficiently small particle to reach an open pore enters it and blocks it. (This is a simplification as the particle just has to be smaller than the pore to fit in and may not in general block it completely.) If $\lambda\Delta\hat{t}$ particles, where λ is the

rate of incoming particles, with size distribution $\hat{f}(\hat{s})$ reach the membrane surface in time $\Delta\hat{t}$, the number of pores that are blocked instantaneously is proportional to the fraction of particles in the distribution with size below the poresize,

$$\Delta\hat{t}\lambda f_p(\hat{a}_{\text{pore}}), \tag{7.3}$$

where $f_p(\hat{a}_{\text{pore}})$ is given in (7.1). Hence, for a fraction of unblocked pores, $N(\hat{t})$, the rate of fouling, assuming that each particle blocks only one pore, is

$$\frac{\mathrm{d}N(\hat{t})}{\mathrm{d}\hat{t}} = -\frac{\lambda}{N_0} f_p(\hat{a}_{\text{pore}}), \tag{7.4}$$

where N_0 is the number of pores initially. Eq. (7.4) is an ODE for the degree of fouling which is to be solved with the initial condition,

$$N(0) = 1, \tag{7.5}$$

corresponding to an initially unfouled membrane.

7.5 Cake Growth

We present a simple model that accounts for the growth of a cake layer from the particles that are rejected by the membrane. The cake layer itself is an array of packed particles. Assuming that particles are added to the cake at a rate proportional to λ, we determine an evolution equation for the increase in cake thickness.

Each layer of the cake contributes a height of $2\hat{a}_{\text{part}}/\varphi_c$; that is, the average diameter of the particle, $2\hat{a}_{\text{part}}$, scaled with the porosity of the cake layer, φ_c. For a membrane surface with circumference $2\pi R$, each layer of particles consists of $\varphi_c \pi R/\hat{a}_{\text{part}}$ particles; that is, the perimeter of the surface divided by the diameter of a particle scaled by the porosity of the cake layer. This of course is a first approximation; since the surface is curved, each layer has a smaller surface area, so that $R \to R - 2\hat{a}_{\text{part}}/\varphi_c$, but such variations are insignificant due to the small cake thicknesses. The increase in thickness of the cake layer, Δd_{c}, in time $\Delta\hat{t}$, is given by

$$\begin{aligned}\Delta d_{\text{c}} &= \text{height gained} \times \frac{\#\text{ particles arriving}}{\#\text{ particles needed for one layer}}, \\ &= \frac{2\hat{a}_{\text{part}}^2}{\varphi_c^2 \pi R}\lambda\Delta\hat{t}\Big(1 - f_p(\hat{a}_{\text{pore}})\Big),\end{aligned} \tag{7.6}$$

since only $1 - f_p(\hat{a}_{\text{pore}})$ of the particles contribute to caking. The cake thickness, d_{c}, is given by an accumulation of these particle layers over time. Taking the limit $\Delta\hat{t} \to 0$ in (7.6) we find that

$$\frac{\mathrm{d}d_{\text{c}}}{\mathrm{d}\hat{t}} = \frac{2\hat{a}_{\text{part}}^2}{\varphi_c^2 \pi R}\lambda\Big(1 - f_p(\hat{a}_{\text{pore}})\Big). \tag{7.7}$$

We note that $\hat{a}_{\text{pore}} = \hat{a}_{\text{pore}}(\hat{t})$ and changes due to the elastic response during fouling and cake development. After each backflush, the cake layer is completely removed. If the backflushes are performed periodically at intervals of $\hat{t}_{\text{bf}}$, then at the beginning of the n^{th} filtration cycle, the initial condition on the cake layer is

$$d_{\text{c}}(n\hat{t}_{\text{bf}}) = 0. \tag{7.8}$$

7.6 Non-dimensionalization

We non-dimensionalize the ODEs for cake growth (7.7) and fouling (7.4) by scaling the cake thickness with R as in Eq. (6.27), and the time $\hat{t}$ so that it reflects the timescale that emerges from the rate of incoming particles in the problem. In particular, we have

$$d_{\text{c}} = R\delta_{\text{c}} \qquad\qquad \hat{t} = \frac{1}{\lambda}t. \tag{7.9}$$

The ODEs for fouling (7.4) and cake growth (7.7) may then be written

$$\frac{\mathrm{d}N}{\mathrm{d}t} = -\frac{1}{N_0} f_p\left(a_{\text{pore}}(t)\right), \qquad N(0) = 1, \tag{7.10a}$$

$$\frac{\mathrm{d}\delta_{\text{c}}}{\mathrm{d}t} = \beta\left[1 - f_p\left(a_{\text{pore}}(t)\right)\right], \qquad \delta_{\text{c}}(nt_{\text{bf}}) = 0, \tag{7.10b}$$

where $\hat{f}_p$ is given in (7.1), and

$$\beta = \frac{2\hat{a}_{\text{part}}^2}{\varphi_c^2 \pi R^2}, \tag{7.11}$$

represents the cake growth per particle arriving, and N_0 is the initial number of open pores. We can relate N_0 to the parameters of the system, estimating it as the number of pores that can fit into the circumference, scaled with the porosity of the membrane, φ_{m}, *i.e.*,

$$N_0 = \varphi_{\text{m}} \times \frac{\text{perimeter of surface}}{\text{diameter of pore}} = \varphi_{\text{m}} \frac{\pi R}{\hat{a}_{\text{pore}}}. \tag{7.12}$$

The quasi-static elastic response results in time-dependent parameters for the system. The poresize, $a_{\text{pore}}(t)$, that appears in the ODEs (7.10) takes the form given by (6.59),

$$a_{\text{pore}}(t) = 1 + A_{\text{m}}(t)\left(\frac{1}{\varphi_{\text{m},0}} - 1\right), \tag{7.13}$$

where the constant, A_{m}, from the quasi-static membrane deformation solution (6.55), is now a time-dependent parameter, $A_{\text{m}}(t)$ (which depends on the parameters of the system Ω, Γ from (6.32), ω, γ from (6.33), κ from (6.30), material parameters δ_{m}, ν_{m}, ν_{c}, from §6.3, and crucially on $\delta_{\text{c}}(t)$ and $N(t)$).

7.7 Results

We solve for the evolution of membrane fouling and cake thickness (7.10), with the fluid flow and elastic responses of the porous media adjusting quasi-statically to the changes brought about by fouling. These quasi-static responses result in time-dependent parameters in the ODEs for the membrane fouling and cake growth. We are interested in the evolution of fouling, cake buildup, poresize and the driving pressure.

7.7.1 Fouling and cake development

The fouling and cake development model is given by the ODEs in (7.10). To estimate the parameters β and N_0, we consider the values given in §6.3. We note that the poresize is approximately equal to the particle size, $\hat{a}_{\text{part}} \approx \hat{a}_{\text{pore}}$, and the membrane and cake porosities are approximately equal, $\varphi_{\text{m}} \approx \varphi_c$. For simplicity, we can rescale time in the ODEs (7.10) with the dimensionless number $\hat{a}_{\text{pore}}/\varphi_c \pi R$, with the remaining factor given by $2\hat{a}_{\text{part}}/\varphi_c R \approx 0.02$, so that the fouling and caking rates are now given by,

$$\frac{\mathrm{d}N}{\mathrm{d}t} = -f_p(a_{\text{pore}}), \qquad N(0) = 1, \tag{7.14a}$$

$$\frac{\mathrm{d}\delta_{\text{c}}}{\mathrm{d}t} = 0.02\Big(1 - f_p(a_{\text{pore}})\Big), \qquad \delta_{\text{c}}(nt_{\text{bf}}) = 0, \tag{7.14b}$$

for $0 \le t \le nt_{\text{bf}}$ and $n = 1, 2, 3, \ldots$. Here a backflush is performed at regular intervals of t_{bf} removing the cake layer, hence the initial condition in (7.14a). We solve the system (7.14) numerically, with a particle size distribution, f, and the membrane surface poresize, $a_{\text{pore}}(t)$, given by Eq. (7.13).

The ODEs (7.14) are solved in MATLAB using `ode45`. At each time step, Δt, the deformed poresize, $a_{\text{pore}}(t)$ (7.13), is updated for the current values of $N(t)$ and $\delta_{\text{c}}(t)$ that determine its elastic deformation. As t passes through nt_{bf}, δ_{c} is reset to 0 (representing a backflush), but $N(t)$ remains unchanged.

For illustration, we first assume that the particle distribution, f, is uniform, with minimum particle size $\hat{a}_{\text{part}}^{\min} = 4\,\mu$m and maximum particle size $\hat{a}_{\text{part}}^{\max} = 5\,\mu$m. The undeformed poresize is taken to be $4.1\,\mu$m so that initially 10% of the particles may foul the membrane. In Figure 7.2, we show the evolution of the fouling, cake development and poresize where we perform zero, one, or two backflushes during the operation. Microparticles are used so that the cake can build to an appreciable size whilst still neglecting osmotic pressure (Bowen and Jenner, 1995a).

The system (7.14) can be solved when elastic effects are neglected. Here, a_{pore} remains constant, *i.e.*, as the original undeformed poresize of the membrane (as in the dashed curves in Figure 7.2(a)). The rate of fouling and cake buildup (7.14) are now decoupled. The right-hand side of each ODE is constant and, hence, the system has solutions that are linear with time. The fouling follows a linear progression that remains unchanged with the number of backflushes (Figure 7.2(b)), whereas the cake grows linearly until a backflush removes it to start over again (Figure 7.2(c)).

Now we consider the additional effect of elasticity perturbing the solutions. The poresize increases with cake thickness (Figure 6.6), and hence so too does $F(\hat{a}_{\text{pore}}(t))$ in (7.14). The rate of fouling increases (Figure 7.2(b)), and the cake layer development slows down (Figure 7.2(c)). This is a consequence of conservation of particles, *i.e.*, if more particles are fouling the membrane, then fewer are adding to the cake layer. Note that the fouling deviates more from the rigid case with time. This shows that the rate of fouling increases with time, an observation that is acknowledged in the membrane industry, *e.g.*, Hong et al. (2005).

The number of backflushes also alters the elastic response of the system. The poresize increases with cake thickness (Figure 6.6) as the cake exerts a mechanical stress on the membrane. Due to additional fouling, the poresize after each subsequent backflush is larger, but the contribution of the cake layer is much more significant than fouling: when the cake is removed, the poresize drops dramatically (Figure 7.2(a)). Since fewer particles can foul the membrane, the rate of fouling is reduced when more backflushes are performed (Figure 7.2(b)), as expected.

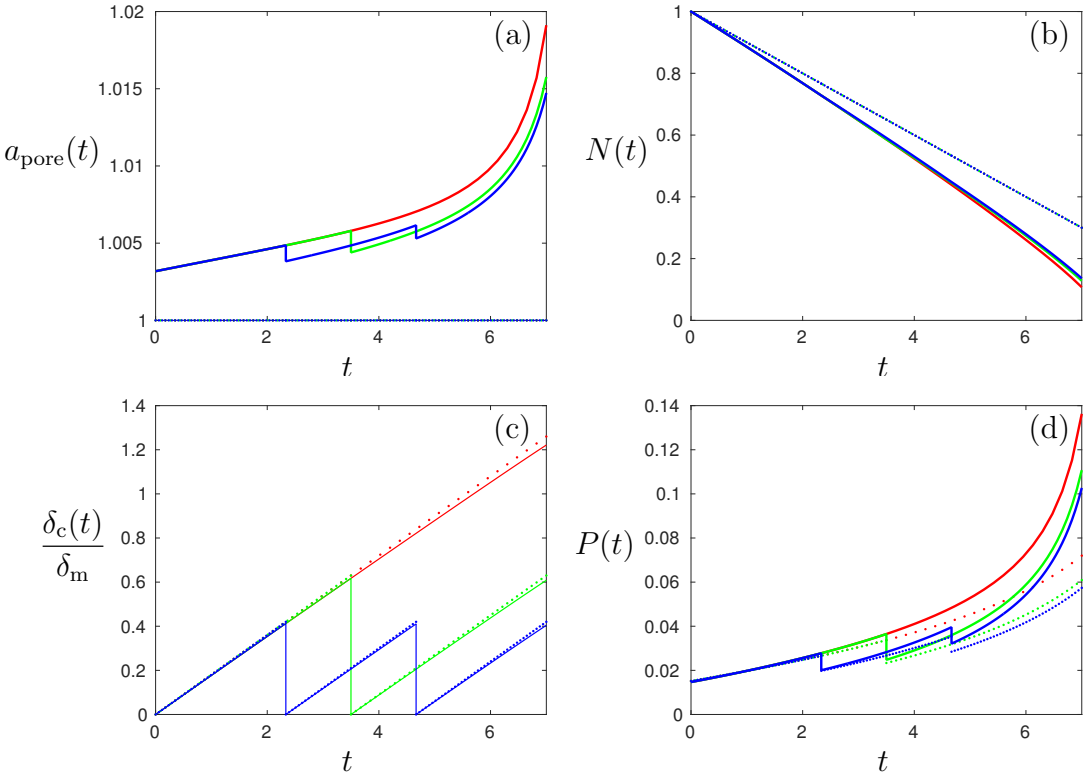

Figure 7.2: The evolution of (a) poresize, (b) fouling, (c) cake thickness (as a fraction of membrane thickness) and (d) driving pressure, P (6.67), with varying numbers of backflushes, and both with (solid) and without (dotted) elasticity. Red denotes no backflushes, green is one backflush, and blue is two backflushes. Here the membrane thickness is $\delta_m = 0.1$.

As the filtration process generally operates at constant flux, its efficiency is measured by the driving pressure, P (6.67), required to maintain that fixed flux. Since we assume that P responds quasi-statically to changes in N and δ_c, Eq. (6.67) can be used to determine P at any instant. However, the terms are now time-dependent.

In Figure 7.2(d) we show the evolution of the driving pressure for the system solved in §7.7.1. This figure resembles the schematic figure of the driving pressure in a typical membrane filtration operation (Figure 5.1) used to motivate this study. We plot the driving pressure for no backflush, and one and two backflushes during the operation, both with and without elastic effects. We note that when the fouling of the membrane is near complete, $N \ll 1$, its permeability will be near zero and P (6.67) diverges, as expected (Figure 7.2(d)). At this point the membrane must be replaced by a clean membrane.

Performing a backflush significantly reduces the driving pressure in the system. Furthermore, the difference between the driving pressures with and without elastic effects decreases as the number of backflushes performed increases. This difference is quite small until the membrane is mostly fouled (Figure 7.2(b,d)). This will be significant in the next section as we will find that elastic effects can improve the efficiency (allowing for smaller driving pressures) of the system compared to the rigid system.

If the poresize is initially smaller than all the particles, then no fouling occurs until the fluid and cake stresses deform the membrane so that particles can foul the membrane. The system then behaves as described above. We will discuss this, in the context of a strategy to prevent fouling, in §7.7.3.

7.7.2 Competing mechanisms

There are competing elastic effects in the membrane and cake layer that both increase and decrease the driving pressure, P (6.67). We observed that the membrane expands and, as such, its permeability increases (§6.8.3); this reduces the driving pressure of the system (§6.9.1). However, the increased permeability is a result of larger poresizes, meaning more particles can foul the membrane thereby increasing the fouling rate (Figure 7.2(b)). The resulting increase in driving pressure from further fouling competes with the decrease due to the higher permeability.

Analogously, the cake layer deformation results in a competition between these mechanisms. The decreased permeability due to compression (§6.8.3) increases the driv-

ing pressure (§6.9.1), but its development slows down with increased fouling (Figure 7.2(c)), to decrease the driving pressure. The most significant alteration to the driving pressure is by a backflush (Figure 7.2(d)).

Hence, in both the membrane and cake layer, we observe a competition between the elastic effects of fouling, membrane expansion and cake compression that affects the driving pressure of the system. The effect of this competition is embedded in the driving pressure, P (6.67). Without elastic effects, the driving pressure is given by $P_2(t)$ (6.31b),

$$P_2(t) = \frac{1}{2\pi N(t)} \log\,(1+\delta_{\mathrm{m}}) - \frac{1}{2\pi\kappa} \log\,(1-\delta_{\mathrm{c}}(t))\,. \tag{7.15}$$

We can consider the net effect of elasticity on the driving pressure by comparing the solutions with and without elastic effects at a given time. We vary the number of backflushes performed during that time and also the ratio of permeabilities of the cake to membrane, κ. In each case, we solve (7.14) to determine the evolution of the system.

We show the net result of elastic effects on the driving pressure in Figure 7.3. For more backflushes, and larger permeability ratios, κ, the elastic effect has a net reduction on the driving pressure. This means that the cake layer is more conducive to flow so the pressure gradient is lower, and the cake cannot build up significantly. The smaller cake thickness reduces the mechanical stress it exerts on the membrane, thereby reducing pore expansion to reduce the rate of fouling.

7.7.3 A strategy for fouling prevention

Pore fouling, which tends to have severe consequences, will not occur if the poresize is smaller than the particle size. Without pore fouling, cake buildup can still occur (linearly with time for a constant flux of particles), and in this way increases the poresize (elastic deformations from the stress due to the cake). We envisage operating with a poresize that is just large enough to prevent fouling even after expansion by the fluid passing through (with no cake layer). However, as a cake is deposited and grows, the poresize in turn increases. If we can perform backflushes fast enough that the deformed poresize remains smaller than the particle size, then we can prevent any fouling of the system. Here we aim to show that this can be achieved.

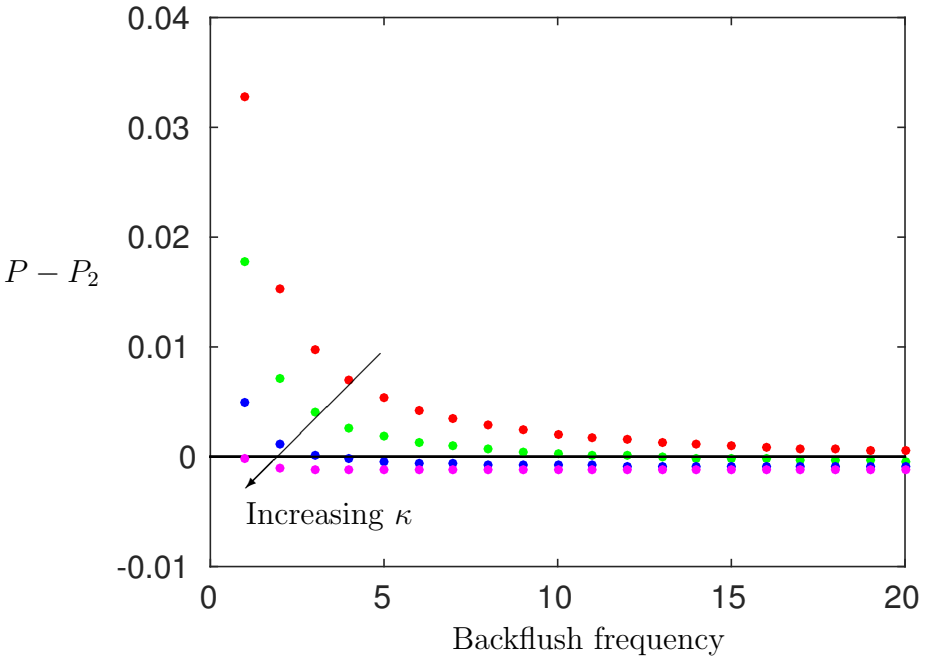

Figure 7.3: Difference in driving pressure with elastic effects, P (6.67), and without elastic effects, P_2 (7.15), against backflush frequency, during a time length of 2 for various ratios of cake to membrane permeability, $\kappa = 1$ (red), 2 (green), 5 (blue) and 10 (magenta). A positive value means that the driving pressure is larger with elastic effects, and negative means that it is lower.

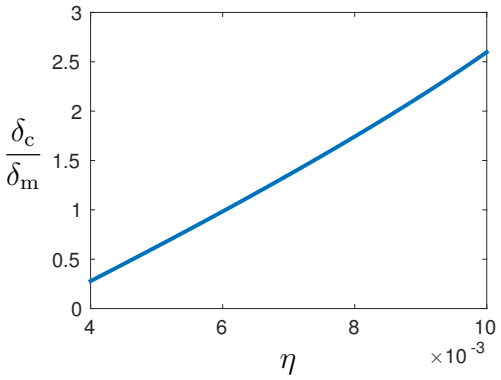

Figure 7.4: The cake thickness, δ_c, required to increase the poresize by a fraction η without fouling occurring. If this poresize is less than the smallest particle, then fouling will not occur.

Suppose the smallest particle is a fraction η greater than the undeformed poresize. Then fouling will begin to occur when

$$\eta = a_{\text{pore}} - 1 = A_m \left(\frac{1}{\varphi_0} - 1 \right), \tag{7.16}$$

using (7.13), where A_m (6.55) depends on δ_c. The idea is to perform a backflush just before this condition is met. The frequency at which a backflush must be performed will depend on the initial difference η. In principle, Eq. (7.16) can be solved for the thickest cake that can be allowed to develop before backflushing. However, a closed analytical expression is not possible; it must be computed numerically, as in Figure 7.4.

The backflush frequency may be calculated using the ODEs in (7.14). While the poresize is less than any particle size, no fouling can occur, *i.e.*, $N = 1$. The cake growth ODE (7.14b) can then be solved independently, where the time at which the value of δ_c is large enough to extend the pores by a fraction η determines the minimum backflush frequency.

The proof of concept of this strategy is shown in Figure 7.5. Dimensionally, the pores are initially $3.986\,\mu$m, with the particle size ranging uniformly from 4–5 μm. Fouling corresponds to $\eta = 0.0035$ and the cake thickness required to achieve this is $\delta_c = 0.1074\,\delta_m$, via (7.16). The solution to (7.14b) is linear in time (until the poresize increases sufficiently to allow fouling, *i.e.* when $\delta_c = 0.1074\,\delta_m$), and we find that in half a time unit, the cake can grow to $\delta_c = 0.1\,\delta_m$ so that operating at a backflush frequency of 2 per unit time will prevent fouling. We demonstrate this by backflushing at two different frequencies: once and twice per unit time over 400 time

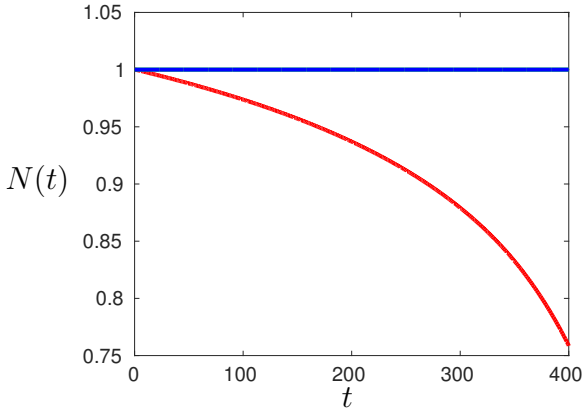

Figure 7.5: The time evolution of fraction of open pores, N, with a backflush frequency of 1 (red), 2 (blue) per time unit. For sufficiently high frequencies of backflushing, the deformed poresize does not expand to a size that permits fouling (blue curve).

units (that is, 400 and 800 total backflushes, respectively). As the cake develops, fouling eventually occurs for the lower backflushing frequency (where the cake grows to a larger size). Once fouling occurs, it increases with time. However, we show that there is a backflush frequency beyond which fouling does not occur (the blue curve). The fluid and cake contributions to the elastic deformation at the higher backflush frequency do not deform the membrane sufficiently to the point when irreversible internal fouling may occur.

7.8 Conclusions

In this chapter, we have developed a model for the evolution of fouling and cake development in membrane filtration. A constant flux of particles reaches the membrane, which may enter and foul the membrane or be deposited as a cake layer. The model incorporates the effect of a small elastic deformation to the membrane and cake layer; the two phenomena of fouling and caking are coupled by a quasi-static elastic response of the porous media that we quantified in Chapter 6.

The model requires knowledge of the particle size distribution, f. If the particles can enter the pores, fouling begins to occur. This initiates a cycle of increasing the pressure to maintain a constant flux, causing further deformation of the pores, leading to more fouling. The observation made in the the membrane industry is that the rate of fouling increases with time. We have shown that this can be explained by considering elastic effects in the system, as in Figure 7.2(b).

It is shown that elastic effects may reduce the efficiency of the filtration process by increasing the rate of fouling. However, strategic planning of backflushing can result in the gains of increased permeability of the membrane outweighing the losses through increased fouling. Indeed, the driving pressure can be reduced overall in comparison to the inelastic case. This means that the membrane has a shorter life time, as it fouls at a faster rate, but it can be operated at a lower energy cost.

We also propose a strategy that allows operation without fouling. The industry could choose the fluid flux and frequency of backflushing, and other parameters such as membrane porosity, Young's modulus, Poisson ratio, *etc.* With this information, the permeability (*i.e.*, poresize) of the membrane could be maximized without allowing fouling to occur.

Chapter 8

Discussion

8.1 Conclusions

In this thesis we studied crossflow and directflow filtration processes operating at constant flux. We began by addressing questions related to concentration polarization (CP) in crossflow systems: its influence on the viscosity of the filtrate and the effect thereof (Chapter 3), and improving the filtration efficiency by tailoring the wall permeability to reduce the effects of osmosis (Chapter 4). We then addressed questions regarding the development of membrane fouling and caking in directflow systems: the transmembrane pressure difference (TMP) (Chapter 5), the effect of elastic deformations during filtration (Chapter 6), and the influence of elasticity and backflushing on the development of fouling (Chapter 7).

In Chapter 3 we analysed the effects of a concentration-dependent viscosity on a crossflow system. The modification of the flow profile, under the condition of constant flux, was quantified in the asymptotic limit of a dilute suspension. We considered an inlet particle distribution that varied with distance from the axis according to a Gaussian distribution. We varied the width of this Gaussian to investigate the relative benefits of stirring the suspension to having a uniform distribution. We found that the pressure gradient required to drive the flow depends on the width of the inlet particle distribution, due to changes in viscosity. Surprisingly we found that there is a pessimal (worst possible) distribution width. As the fluid pressure decreases along the channel, we observed that there will in general be a point beyond which the osmotic pressure exceeds the fluid pressure. This results in a backflow by osmosis of clean water from the permeate side into the channel. Backflow occurs near the end of the channel where the fluid pressure is lowest. Furthermore, we varied the (constant)

pressure on the permeate side, and showed that when this pressure is sufficiently negative (relative to the exit pressure), we are able to suppress the osmosis-driven backflow in the system.

In Chapter 4 we addressed the problem of backflow due to osmosis more directly. As backflow occurs towards the end of the channel, we considered the effect of simply blocking the walls of the end section of the channel. This inevitably changes the fluid flow in the channel, altering the net flux of fluid filtered (permeate flux). We optimized the permeate flux (via a numerical search) by varying the length of the wall that remains permeable. We found that the optimal permeable length decreases with wall permeability and increases with Péclet number. However, the permeate flux at these optimal conditions has a surprising dependence on the Péclet number: it is maximized by an intermediate Péclet number. This is due to the increasing CP boundary layer that develops at the wall for large Péclet numbers: the permeate flux increases with Péclet number at a faster rate than the osmotic pressure until a critical Péclet number, beyond which the permeate flux decreases. The setup was explored further by considering a series of striped permeable/impermeable regions, in both symmetric and asymmetric configurations. The idea was to reduce the size of the CP layer via repeated advection and diffusion from an impermeable wall. CP would then not be as pronounced further down the channel. However, we showed that the permeate flux is lower for these setups, due to a reduction in permeable membrane area where the fluid pressure is largest. We found a similar result for the energy required to operate the system. Since we envisaged operating at constant influx, this energy is reduced by reducing the inlet pressure, with a minimum occurring for a particular Péclet number. We thus provide an insight into operating strategies that maximize either permeate flux or the energy required to produce a fixed volume of clean water.

The models in Chapters 3 and 4 are suitable for the early stages of fouling, before pore blocking and caking occur. We showed that it is possible to increase the efficiency of the filtration process at this stage, and that changes in design can greatly improve performance by minimizing energy cost and adverse effects such as backflow due to osmosis. We expect this to have favourable repercussions later on in the process by delaying irreversible fouling and significantly reducing the amount of filtering to be performed at higher pressures. The remainder of this thesis was concerned with these later stages of filtration.

Chapter 5 marked the first steps in developing a model to explain the observed increase in TMP over time during filtration when operating at constant flux. We studied a directflow system for microfiltration, where osmotic pressures are not so significant. Our ultimate aim was to use elasticity theory to explain an observed increase in fouling and hence driving pressure. First, we analysed the flow for a single directflow device, and exploited symmetry in the system due to the other other modules that make up an array in a directflow device. We found that often in such scenarios the TMP is approximately constant along the length of the membrane. This both confirms an empirical observation and simplified the elasticity problem considered in Chapter 6.

In Chapter 6 we quantified the elastic deformation of a porous membrane and cake layer. We showed that during filtration the membrane expands, increasing its permeability, but the cake layer contracts, decreasing its permeability. These effects result in a decrease (via membrane expansion) and increase (via cake contraction) to the fluid pressure drop across the membrane and cake, respectively. The effects are exacerbated by greater membrane fouling.

In Chapter 7, we modelled the evolution of fouling and caking over time. The poroelastic deformations were shown to occur quasi-statically, and hence could be decoupled as parameters in the model. We illustrated the potential that elasticity has to increase the rate of fouling, using the model of Chapter 6 to quantify the changes in membrane poresize and the increase in pressure caused by both fouling and caking. Furthermore, we considered the effect of backflushing, and demonstrated that it is possible to tune the frequency of backflushing to give several operating advantages. In particular, it is possible to maximize the poresize, and hence permeability, without fouling occurring; the membrane expansion from the fluid and cake stresses do not alter the poresize enough to allow particles to foul the pores internally. If fouling is considered inevitable, as it is in the membrane technology industry, then backflushing can be performed at a sufficiently high frequency that the pressure drop increases from cake contraction are exceeded by decreases from membrane expansion; this allows filtration to operate at a lower overall pressure, reducing energy costs.

The models in Chapters 5, 6 and 7 demonstrate the adverse effects of internal fouling and caking on filtration. We showed how the elastic properties of the membrane during filtration increase both the rate of fouling and the driving pressure required to operate at constant flux, as observed experimentally. However, we demonstrated that

by tuning the frequency of backflushing, we could reduce operating pressures and, in some circumstances, even prevent fouling while maximizing efficiency.

8.2 Future directions

In this thesis we have developed models grounded in well established assumptions and operating conditions for membrane filtration. However, these assumptions do not always hold and the operating conditions can change during the process. Here, we consider some possible extensions to our models.

Chapters 3 and 4 considered the precursor of fouling in which a CP layer is present. Here, we assumed a dilute suspension of particles. This is a reasonable assumption until cake formation begins, a frequent occurrence during operation. A numerical study for non-dilute suspensions, where appropriate functional forms for the viscosity and diffusivity are chosen, may provide additional insight for the fluid and transport properties of the system, as well as the transition to cake formation. Furthermore, the models could be extended to include a cake layer on the membrane surface. Firstly, this would add a resistance to the permeate flow. Secondly, the cake layer would reduce the diffusivity of, say, a second smaller species of particles in the flow that may pass through the cake. As a result, the osmotic pressure increases, an effect known as *cake-enhanced osmotic pressure* (Hoek and Elimelech, 2003).

The particles in a feed solution are often not the same species and so may have different transport properties (*e.g.*, diffusivity): different filtration methods may need to be used for each species. As such, a model for two (or more) different sized species in a channel would be of great interest. Concentration-dependent diffusivities become more important when considering multiple particle species in a flow. Each species then has its own diffusivity as well as cross-diffusion terms for the motion of one species under a concentration gradient of another (Bruna and Chapman, 2012).

In the elasticity model (Chapter 6) we used the observation that in certain directflow operating regimes the TMP is approximately constant along the membrane. This allowed us to model the elastic deformation as plane strain. However, if we were to generalize this to all crossflow systems (with an open exit), the TMP would, in general, be a monotonically decreasing function of position. As such, the strain would vary with position along the membrane, with consequences that merit further study.

However it is not just the feed flow that exerts stress on the membrane. In a hollow fibre or capillary membrane module, each long and thin membrane unit experiences stress from the feed flow inside the unit and the permeate flow from other membrane units. A representative from the membrane industry has suggested that this can cause buckling of the module. It would be interesting to determine the conditions under which this buckling occurs.

In the fouling and caking models (Chapter 7), we made assumptions that show only part of a bigger and more complicated picture. In the fouling model, we simplified the model so that a single particle enters and blocks a single pore. In reality, there are many types of fouling: complete, partial and internal. Our model could be generalized to incorporate more details specific to these types of fouling, as well as allowing for more than one particle to enter a pore before completely blocking the pore, *e.g.*, Griffiths et al. (2014). In the caking model, we assumed that the incoming particles that are deposited on top of a cake layer may contribute to fouling, via a re-ordering of particles in the cake layer. The structure of the cake layer during filtration is an interesting aspect of the problem for further study.

These are just a few of many possible extensions for further study in this field.

Appendix A

Testing of Numerical Scheme

A.1 The problem

In this appendix we consider the numerical solution of the advection–diffusion equation (3.29) with symmetry and no-flux boundary conditions (3.30) and inlet condition (3.31). For convenience, we recall these equations here:

$$\mathrm{Pe}\left(u_0\frac{\partial\phi_1}{\partial x}+v_0\frac{\partial\phi_1}{\partial y}\right)=\frac{\partial^2\phi_1}{\partial y^2}, \tag{A.1a}$$

$$\left.\frac{\partial\phi_1}{\partial y}\right|_{y=0}=0, \tag{A.1b}$$

$$\mathrm{Pe}\,v_0\,\phi_1-\left.\frac{\partial\phi_1}{\partial y}\right|_{y=1}=0, \tag{A.1c}$$

$$\phi_1|_{x=0}=\Phi(y), \tag{A.1d}$$

where the velocities, u_0 and v_0, are known in terms of the (unknown) pressure field (*cf.* §3.4 or Probstein (1989)),

$$u_0(x,y)=\frac{\mathrm{d}p_0}{\mathrm{d}x}\frac{(y^2-1)}{2}, \tag{A.2a}$$

$$v_0(x,y)=\frac{\mathrm{d}^2p_0}{\mathrm{d}x^2}\frac{(3y-y^3)}{6}. \tag{A.2b}$$

The function $\Phi(y)$ in (A.1d) is a Gaussian with mean zero and standard deviation, σ, and normalized so that $\int_{-\infty}^{\infty}\Phi\,\mathrm{d}y=1$. We therefore have:

$$\phi(0,y)=\Phi(y)=\frac{\exp\left(\dfrac{-y^2}{2\sigma^2}\right)}{\sqrt{\dfrac{\pi}{2}}\,\sigma\,\mathrm{erf}\left(\dfrac{1}{\sqrt{2}\sigma}\right)}. \tag{A.3}$$

A.2 Discretization

To solve (A.1a)–(A.1d), we use a finite difference scheme that is second-order accurate. We exploit the symmetry about the y-axis by considering only the domain $(x, y) \in [0, 1] \times [0, 1]$, and discretize this domain by introducing grid points:

$$x_i = hi, \qquad i = 0, 1 \ldots N, \tag{A.4a}$$

$$y_j = kj, \qquad j = 0, 1 \ldots M, \tag{A.4b}$$

for grid spacings h and k where $h = \Delta x = 1/N$ and $k = \Delta y = 1/M$. We index the variable ϕ_1 as follows

$$\phi_{i,j} = \phi_1(x_i, y_j). \tag{A.5}$$

We use forward differences for first derivatives and centre differences for second derivatives (*cf.* Morton and Mayers (2005)). A standard second-order accurate forward-centre finite difference scheme for (A.1) is given by:

$$\phi_{i+1,j} = \phi_{i,j} + \frac{2h}{p'(x_i)(y_j^2 - 1)}\bigg(- p''(x_i)\frac{3y_j - y_j^3}{6}\frac{\phi_{i,j+1} - \phi_{i,j-1}}{2k} + \frac{1}{\mathrm{Pe}}\frac{\phi_{i,j+1} - 2\phi_{i,j} + \phi_{i,j-1}}{k^2}\bigg), \tag{A.6a}$$

$$\phi_{i+1,1} = \frac{4\phi_{i+1,2} - \phi_{i+1,3}}{3}, \tag{A.6b}$$

$$\phi_{i+1,M} = \frac{2\phi_{i+1,M-1} - \frac{1}{2}\phi_{i+1,M-2}}{\frac{3}{2} - k\,\mathrm{Pe}\,v_{i+1,M}}, \tag{A.6c}$$

$$\phi_{1,j} = \Phi(y_j), \tag{A.6d}$$

for $i = 1, 2, \ldots N - 1$ and $j = 2, 3, \ldots M - 1$.

A.3 Convergence

For a constant-coefficient convection–diffusion equation

$$f_x + af_y = bf_{yy}, \tag{A.7}$$

with $b > 0$, there are two mesh size parameters to consider

$$\nu = \frac{a\Delta x}{\Delta y}, \qquad \eta = b\frac{\Delta x}{\Delta y^2}. \tag{A.8a,b}$$

Implementing a stable forward-in-x, central-differences-in-y finite-differences scheme, it is required that (Morton and Mayers, 2005)

$$0 < \nu \leq 1, \qquad 0 < \eta \leq \frac{1}{2}. \tag{A.9}$$

In our governing equations, the advection–diffusion equation (A.1a) for the volume fraction ϕ_1 does not have constant coefficients, but the coefficients are well behaved, with no singularities. We ensure that the scheme is stable by requiring $\Delta x/\Delta y^2 = 1/50 \ll 1/2$ for stability: we typically use $\Delta y = 2 \times 10^{-2}$ and $\Delta x = 8 \times 10^{-6}$.

A test of the accuracy of our numerical scheme is to compute the total flux of fluid and particles in and out of the channel. Since the system operates in steady state, any deviation from equality may indicate errors such as numerical diffusion. We require the ratio of particle influx to the fluid influx to be equal to the ratio of particle outflux to the fluid outflux (noting that in some cases the fluid may pass through the channel wall but particles cannot), *i.e.*,

$$\frac{\displaystyle\int_0^1 \left[\mathrm{Pe}\, u_0\, \phi_1\right]_{x=0} \,\mathrm{d}y}{\displaystyle\int_0^1 \left[u_0\right]_{x=0} \,\mathrm{d}y} = \frac{\displaystyle\int_0^1 \left[\mathrm{Pe}\, u_0\, \phi_1\right]_{x=1} \,\mathrm{d}y}{\displaystyle\int_0^1 \left[u\right]_{x=1} \,\mathrm{d}y + \int_0^1 \left[v\right]_{y=1} \,\mathrm{d}x}. \tag{A.10}$$

The ratio of the right-hand side to the left-hand side of (A.10) is computed for different values of $k = \Delta y^2$ while satisfying the relationship

$$\frac{h}{k^2} = \frac{\Delta x}{\Delta y^2} = \frac{1}{50}, \tag{A.11}$$

ensuring that the stability condition is always satisfied.

For all three cases (no permeation, constant permeation and permeation proportional to the pressure through the walls, where the required pressures, p, are given in §3.4), the ratio (A.10) approaches unity linearly as $k^2 = \Delta y^2$ is reduced with h/k^2 held constant. This is seen in Figure A.1 for $\mathrm{Pe} = 3$, $\sigma^2 = 0.05$ and $\kappa = 1$. This quadratic decay in Δy^2 is expected because our numerical scheme (A.6) is second-order accurate.

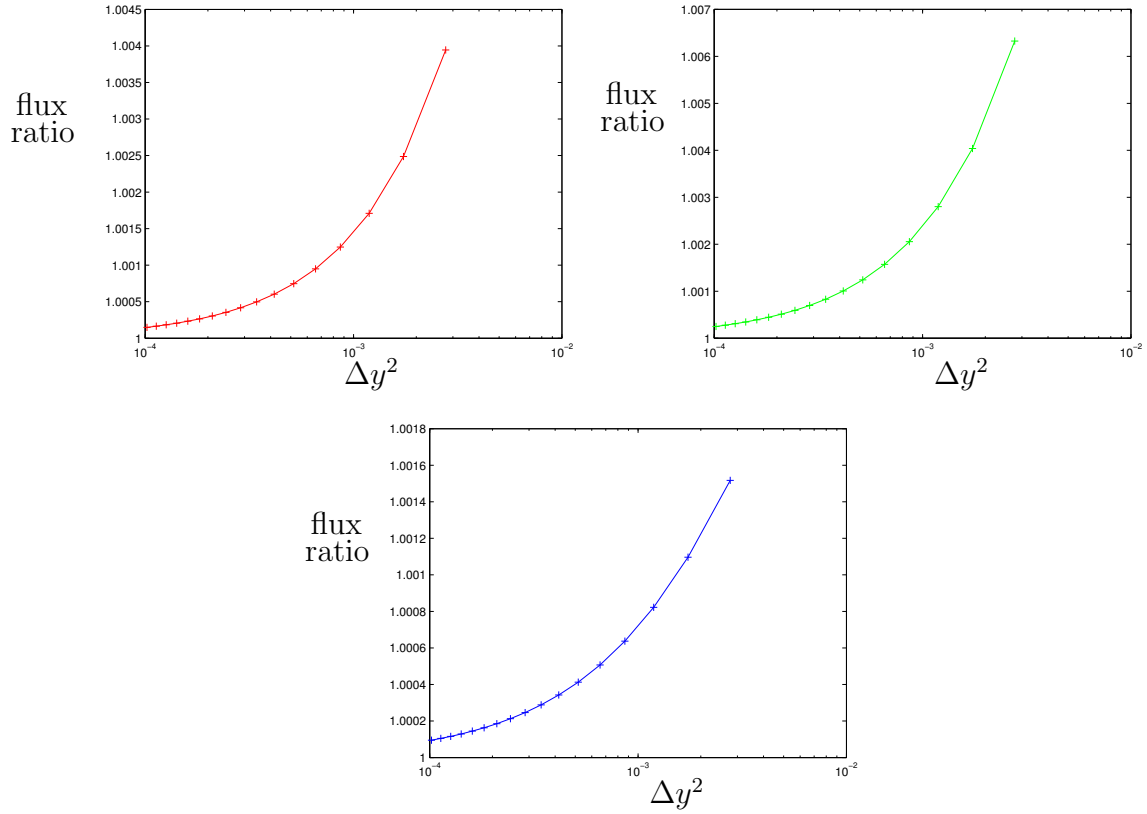

Figure A.1: Ratio of the right-hand side to the left-hand side of flux condition (A.10) for (a) no permeation through the walls, $v_0(x, 1) = 0$, (b) constant permeation through the walls, $v_0(x, 1) = 0.1$, and (c) permeation through the walls proportional to the pressure, $v_0(x, 1) = p_0$. The ratio approaches 1 in all cases as $\Delta y^2 \to 0$ with h/k^2 constant. The points (+) are fitted by linear least-squares method. We take the parameters values: $\mathrm{Pe} = 3$, $\sigma^2 = 0.05$ and $\kappa = 1$.

Bibliography

D. J. Acheson. *Elementary Fluid Dynamics*. Oxford University Press, 1990.

P. Aimar, J. A. Howell, M. J. Clifton, and V. Sanchez. Concentration polarisation build-up in hollow fibers: a method of measurement and its modelling in ultrafiltration. *Journal of Membrane Science*, 59(1):81–99, 1991.

F. W. Altena and G. Belfort. Lateral migration of spherical particles in porous flow channels: application to membrane filtration. *Chemical Engineering Science*, 39 (2):343–355, 1984.

J. Altmann and S. Ripperger. Particle deposition and layer formation at the crossflow microfiltration. *Journal of Membrane Science*, 124(1):119–128, 1997.

M. Amiji and B. Sandmann. *Applied Physical Pharmacy*. McGraw Hill Professional, 2003.

N. W. Arnell. Climate change and global water resources. *Global Environmental Change*, 9:S31–S49, 1999.

P. Bacchin. A possible link between critical and limiting flux for colloidal systems: consideration of critical deposit formation along a membrane. *Journal of Membrane Science*, 228(2):237–241, 2004.

P. Bacchin, D. Si-Hassen, V. Starov, M. J. Clifton, and P. Aimar. A unifying model for concentration polarization, gel-layer formation and particle deposition in cross-flow membrane filtration of colloidal suspensions. *Chemical Engineering Science*, 57:77–91, 2002.

S. Badalov, Y. Oren, and C. J. Arnusch. Ink-jet printing assisted fabrication of patterned thin film composite membranes. *Journal of Membrane Science*, 493: 508–514, 2015.

S. Banerjee, S. Murad, and I. K. Puri. Preferential ion and water intake using charged carbon nanotubes. *Chemical Physics Letters*, 434(4):292–296, 2007.

G. Batchelor, H. Moffatt, and M. Worster. *Perspectives in Fluid Dynamics*. Cambridge University Press, 2002.

G. K. Batchelor. *An Introduction to Fluid Dynamics*. Cambridge University Press, 1967.

G. K. Batchelor. Brownian diffusion of particles with hydrodynamic interaction. *Journal of Fluid Mechanics*, 74:1–29, 1976.

G. K. Batchelor and J. T. Green. The determination of the bulk stress in a suspension of spherical particles to order c^2. *Journal of Fluid Mechanics*, 56(03):401–427, 1972.

G. S. Beavers and D. D. Joseph. Boundary conditions at a naturally permeable wall. *Journal of Fluid Mechanics*, 30:197–207, 1967.

B. J. Bellhouse and R. W. H. Lewis. A high efficiency membrane separator for donor plasmapheresis. *ASAIO Journal*, 34(3):747–754, 1988.

Y. K. Benkahla, A. Ould-Dris, M. Y. Jaffrin, and D. Si-Hassen. Cake growth mechanism in cross-flow microfiltration of mineral suspensions. *Journal of Membrane Science*, 98(1):107–117, 1995.

A. S. Berman. Laminar flow in channels with porous walls. *Journal of Applied Physics*, 24:1232–1235, 1953.

M. S. H. Boutilier, J. Lee, V. Chambers, V. Venkatesh, and R. Karnik. Water filtration using plant xylem. *PLOS ONE*, 9, 2014.

W. R. Bowen and F. Jenner. Theoretical descriptions of membrane filtration of colloids and fine particles: an assessment and review. *Advances in Colloid and Interface Science*, 56:141–200, 1995a.

W. R. Bowen and F. Jenner. Dynamic ultrafiltration model for charged colloidal dispersions: a wigner-seitz cell approach. *Chemical Engineering Science*, 50(11): 1707–1736, 1995b.

W. R. Bowen and P. M. Williams. Prediction of the rate of cross-flow ultrafiltration of colloids with concentration-dependent diffusion coefficient and viscosity – theory and experiment. *Chemical Engineering Science*, 56:3083–3099, 2001.

W. R. Bowen, A. Mongruel, and P. M. Williams. Prediction of the rate of cross-flow membrane ultrafiltration: a colloidal interaction approach. *Chemical Engineering Science*, 51(18):4321–4333, 1996.

J. F. Brady. Brownian motion, hydrodynamics, and the osmotic pressure. *The Journal of Chemical Physics*, 98(4):3335–3341, 1993.

P. L. T. Brian. Concentration polarization in reverse osmosis desalination with variable flux and incomplete salt rejection. *Industrial & Engineering Chemistry Fundamentals*, 4(4):439–445, 1965.

M. Bruna and S. J. Chapman. Diffusion of multiple species with excluded-volume effects. *The Journal of Chemical Physics*, 137(20):204116, 2012.

E. F. Casassa and H. Markovitz. Statistical thermodynamics of polymer solutions. I. Theory of the second virial coefficient for a homogeneous solute. *The Journal of Chemical Physics*, 29(3):493–503, 2004.

T. Y. Cath, A. E. Childress, and M. Elimelech. Forward osmosis: principles, applications, and recent developments. *Journal of Membrane Science*, 281(1):70–87, 2006.

K. Chamsri. Derivation of darcys law using homogenization methods. *International Journal of Computing Science and Mathematics*, 7,9:94–98, 2013.

V. Chen, A. G. Fane, S. Madaeni, and I. G. Wenten. Particle deposition during membrane filtration of colloids: transition between concentration polarization and cake formation. *Journal of Membrane Science*, 125(1):109–122, 1997.

Y.-L. Cheng, D.-J. Lee, and J.-Y. Lai. Filtration blocking laws: Revisited. *Journal of the Taiwan Institute of Chemical Engineers*, 42:506–508, 2011.

S. Chou, R. Wang, and A. G. Fane. Robust and high performance hollow fiber membranes for energy harvesting from salinity gradients by pressure retarded osmosis. *Journal of Membrane Science*, 448:44–54, 2013.

D. A. Clifford. Ion exchange and inorganic adsorption. *Water Quality and Treatment*, 4:561–564, 1999.

M. J. Clifton, N. Abidine, P. Aptel, and V. Sanchez. Growth of the polarization layer in ultrafiltration with hollow-fibre membranes. *Journal of Membrane Science*, 21 (3):233–245, 1984.

O. Coussy. *Mechanics and Physics of Porous Solids*. John Wiley & Sons, 2011.

R. G. Cox and H. Brenner. The lateral migration of solid particles in Poiseuille flow - I Theory. *Chemical Engineering Science*, 23(2):147–173, 1968.

Data 360. Average Water Use Per Person Per Day. http://www.data360.org/dsg.aspx?Data_Set_Group_Id=757, July 2015.

R. H. Davis. Modelling of fouling of crossflow microfiltration membranes. *Separation and Purification Methods*, 21:75–126, 1992.

R. H. Davis and D. T. Leighton. Shear-induced transport of a particle layer along a porous wall. *Chemical Engineering Science*, 42:275–281, 1987.

R. H. Davis and J. D. Sherwood. A similarity solution for steady-state crossflow microfiltration. *Chemical Engineering Science*, 45:3203–3209, 1990.

A. Deboeuf, G. Gauthier, J. Martin, Y. Yurkovetsky, and J. F. Morris. Particle pressure in a sheared suspension: a bridge from osmosis to granular dilatancy. *Physical Review Letters*, 102(10):108301, 2009.

N. Delgrange-Vincent, C. Cabassud, M. Cabassud, L. Durand-Bourlier, and J. M. Laine. Neural networks for long term prediction of fouling and backwash efficiency in ultrafiltration for drinking water production. *Desalination*, 131(1):353–362, 2000.

D. Di Carlo, J. F. Edd, K. J. Humphry, H. A. Stone, and M. Toner. Particle segregation and dynamics in confined flows. *Physical Review Letters*, 102(9):094503, 2009.

A. J. DiLeo, A. E. Allegrezza, and S. E. Builder. High resolution removal of virus from protein solutions using a membrane of unique structure. *Nature Biotechnology*, 10 (2):182–188, 1992.

J. Duan, E. Litwiller, and I. Pinnau. Solution-diffusion with defects model for pressure-assisted forward osmosis. *Journal of Membrane Science*, 470:323–333, 2014.

A. Einstein. *Investigations on the Theory of the Brownian Movement*. Courier Corporation, 1956.

S. B. Elbaz and A. D. Gat. Dynamics of viscous liquid within a closed elastic cylinder subject to external forces with application to soft robotics. *Journal of Fluid Mechanics*, 758:221–237, 2014.

M. Elimelech, J. Gregory, X. Jia, and R. A. Williams. *Particle Deposition and Aggregation. Measurement, Modelling and Simulation*. Butterworth-Heinemann, 1995.

A. Fakhrul-Razi, A. Pendashteh, L. C. Abdullah, D. R. A. Biak, S. S. Madaeni, and Z. Z. Abidin. Review of technologies for oil and gas produced water treatment. *Journal of Hazardous Materials*, 170(2):530–551, 2009.

R. W. Field. University of Oxford. Private communication, 2015.

R. W. Field and G. K. Pearce. Critical, sustainable and threshold fluxes for membrane filtration with water industry applications. *Advances in Colloid and Interface Science*, 164:38–44, 2011.

R. W. Field and J. J. Wu. Modelling of permeability loss in membrane filtration: Re-examination of fundamental fouling equations and their link to critical flux. *Desalination*, 283:68–74, 2011.

R. W. Field, D. Wu, J. A. Howell, and B. B. Gupta. Critical flux concept for microfiltration fouling. *Journal of Membrane Science*, 100:259–272, 1995.

Free Drinking Water. Different water filtration methods explained. http://www.freedrinkingwater.com/water-education/quality-water-filtration-method.htm, January 2015.

A. Gabelman and S.-T. Hwang. Hollow fiber membrane contactors. *Journal of Membrane Science*, 159(1):61–106, 1999.

A. Gadgil. Drinking water in developing countries. *Annual Review of Energy and the Environment*, 23(1):253–286, 1998.

E. P. Garmash, Y. N. Kryuchkov, and V. N. Pavlikov. Ceramic membranes for ultra- and microfiltration (review). *Glass and Ceramics*, 52(6):150–152, 1995.

N. Ghaffour, T. M. Missimer, and G. L. Amy. Technical review and evaluation of the economics of water desalination: current and future challenges for better water supply sustainability. *Desalination*, 309:197–207, 2013.

W. N. Gill, D. E. Wiley, C. J. D. Fell, and A. G. Fane. Effect of viscosity on concentration polarization in ultrafiltration. *AIChE Journal*, 34(9):1563–1567, 1988.

P. H. Gleick. Basic water requirements for human activities: Meeting basic needs. *Water International*, 21(2):83–92, 1996.

P. H. Gleick. The human right to water. *Water Policy*, 1(5):487–503, 1998.

P. H. Gleick, N. Ajami, et al. *The World's Water Volume 8: The Biennial Report on Freshwater Resources*, volume 8. Island Press, 2014.

P. S. Goh, A. F. Ismail, and B. C. Ng. Carbon nanotubes for desalination: performance evaluation and current hurdles. *Desalination*, 308:2–14, 2013.

I. M. Griffiths, P. D. Howell, and R. J. Shipley. Control and optimization of solute transport in a thin porous tube. *Physics of Fluids*, 25(3):033101, 2013.

I. M. Griffiths, A. Kumar, and P. S. Stewart. A combined network model for membrane fouling. *Journal of Colloid and Interface Science*, 432:10–18, 2014.

E. Guazzelli and J. F. Morris. *A Physical Introduction to Suspension Dynamics*. Cambridge University Press, 2012.

W. Guo, H.-H. Ngo, and J. Li. A mini-review on membrane fouling. *Bioresource Technology*, 122:27–34, 2012.

K. R. Hall. Another hard-sphere equation of state. *The Journal of Chemical Physics*, 57(6):2252–2254, 1972.

J. Hermia. Constant pressure blocking filtration laws – application to power-law non-Newtonian fluids. *Transactions of the Institution of Chemical Engineers*, 60: 183–187, 1982.

N. Hilal. University of Swansea. Private communication, 2015.

N. Hilal, O. O. Ogunbiyi, N. J. Miles, and R. Nigmatullin. Methods employed for control of fouling in MF and UF membranes: a comprehensive review. *Separation Science and Technology*, 40(10):1957–2005, 2005.

C.-C. Ho and A. L. Zydney. A combined pore blockage and cake filtration model for protein fouling during microfiltration. *Journal of Colloid and Interface Science*, 232:389–399, 2000.

E. M. V. Hoek and M. Elimelech. Cake-enhanced concentration polarization: a new fouling mechanism for salt-rejecting membranes. *Environmental Science & Technology*, 37(24):5581–5588, 2003.

E. M. V. Hoek, A. S. Kim, and M. Elimelech. Influence of crossflow membrane filter geometry and shear rate on colloidal fouling in reverse osmosis and nanofiltration separations. *Environmental Engineering Science*, 19(6):357–372, 2002.

S. Hong, P. Krishna, C. Hobbs, D. Kim, and J. Cho. Variations in backwash efficiency during colloidal filtration of hollow-fiber microfiltration membranes. *Desalination*, 173(3):257–268, 2005.

K. Hood, S. Lee, and M. Roper. Inertial migration of a rigid sphere in three-dimensional Poiseuille flow. *Journal of Fluid Mechanics*, 765:452–479, 2015.

K. J. Howe and M. M. Clark. *Coagulation Pretreatment for Membrane Filtration*. American Water Works Association, 2002.

P. Howell, G. Kozyreff, and J. R. Ockendon. *Applied Solid Mechanics*. Number 43. Cambridge University Press, 2009.

S. Howison. *Practical Applied Mathematics: Modelling, Analysis, Approximation*. Cambridge University Press, 2005.

M. Hurwitz. Proceedings from Mathematical Problems in Industry Workshop. 1989.

K.-J. Hwang and C.-L. Hsueh. Dynamic analysis of cake properties in microfiltration of soft colloids. *Journal of Membrane Science*, 214(2):259–273, 2003.

Hyflux Membranes. Filtration types. http://www.hyfluxmembranes.com/filtration-types.html, August 2012.

S. Ilias and R. Govind. A study on concentration polarization in ultrafiltration. *Separation Science and Technology*, 28(1-3):361–381, 1993.

Institute Water for Africa. Water Consumption. http://www.water-for-africa.org/en/water-consumption.html, July 2015.

A.-S. Jönsson and B. Jönsson. Ultrafiltration of colloidal dispersionsa theoretical model of the concentration polarization phenomena. *Journal of Colloid and Interface Science*, 180(2):504–518, 1996.

S. Karode. Laminar flow in channels with porous walls, revisited. *Journal of Membrane Science*, 191(1-2):237–241, 2001.

O. Kedem and A. Katchalsky. Thermodynamic analysis of the permeability of biological membranes to non-electrolytes. *Biochimica et Biophysica Acta*, 27:229–246, 1957.

J. P. Keener. *Principles of Applied Mathematics*. Westview, 2000.

G. Keir and V. Jegatheesan. A review of computational fluid dynamics applications in pressure-driven membrane filtration. *Reviews in Environmental Science and Bio/Technology*, 13(2):183–201, 2014.

J. Kim and B. Van der Bruggen. The use of nanoparticles in polymeric and ceramic membrane structures: review of manufacturing procedures and performance improvement for water treatment. *Environmental Pollution*, 158(7):2335–2349, 2010.

M. Kostoglou and A. J. Karabelas. Mathematical analysis of fluid flow and mass transfer in a cross flow tubular membrane. *Industrial & Engineering Chemistry Research*, 48:5885–5893, 2009.

S. K. Lateef, B. Z. Soh, and K. Kimura. Direct membrane filtration of municipal wastewater with chemically enhanced backwash for recovery of organic matter. *Bioresource Technology*, 150:149–155, 2013.

P. Le-Clech, V. Chen, and A. G. Fane. Fouling in membrane bioreactors used in wastewater treatment. *Journal of Membrane Science*, 284(1):17–53, 2006.

D. Leighton and A. Acrivos. The shear-induced migration of particles in concentrated suspensions. *Journal of Fluid Mechanics*, 181:415–439, 1987.

T. Leiknes. The effect of coupling coagulation and flocculation with membrane filtration in water treatment: A review. *Journal of Environmental Sciences*, 21(1): 8–12, 2009.

H.-Y. Li, C. D. Bertram, and D. E. Wiley. Mechanisms by which pulsatile flow affects cross-flow microfiltration. *AIChE Journal*, 44(9):1950–1961, 1998.

H. K. Lonsdale. The growth of membrane technology. *Journal of Membrane Science*, 10(2):81–181, 1982.

H. Ma, J. Zeng, M. L. Realff, S. Kumar, and D. A. Schiraldi. Processing, structure, and properties of fibers from polyester/carbon nanofiber composites. *Composites Science and Technology*, 63(11):1617–1628, 2003.

Y. J. Ma, X. F. Yao, Q. S. Zheng, Y. J. Yin, D. J. Jiang, G. H. Xu, F. Wei, and Q. Zhang. Carbon nanotube films change Poissons ratios from negative to positive. *Applied Physics Letters*, 97(6):061909, 2010.

C. W. MacMinn, E. R. Dufresne, and J. S. Wettlaufer. Fluid-driven deformation of a soft granular material. *Physical Review X*, 5(1):011020, 2015.

S. S. Madaeni. The application of membrane technology for water disinfection. *Water Research*, 33(2):301–308, 1999.

A. Matilainen, M. Vepsäläinen, and M. Sillanpää. Natural organic matter removal by coagulation during drinking water treatment: A review. *Advances in Colloid and Interface Science*, 159(2):189–197, 2010.

M. Mayhew and T. Stephenson. Low biomass yield activated sludge: a review. *Environmental Technology*, 18(9):883–892, 1997.

M. Meireles, M. Prat, and G. Estachy. Analytical modeling of steady-state filtration process in an automatic self-cleaning filter. *Chemical Engineering Research and Design*, 2015.

T. Mezher, H. Fath, Z. Abbas, and A. Khaled. Techno-economic assessment and environmental impacts of desalination technologies. *Desalination*, 266(1):263–273, 2011.

E. Mintz, J. Bartram, P. Lochery, and M. Wegelin. Not just a drop in the bucket: expanding access to point-of-use water treatment systems. *American Journal of Public Health*, 91(10):1565–1570, 2001.

A. K. Mishra and S. Ramaprabhu. Functionalized graphene sheets for arsenic removal and desalination of sea water. *Desalination*, 282:39–45, 2011.

K. W. Morton and D. F. Mayers. *Numerical Solution of Partial Differential Equations*. Cambridge University Press, 2005.

Q. T. Nguyen and J. Neel. Characterization of ultrafiltration membranes.: Part iv. influence of the deformation of macromolecular solutes on the transport through ultrafiltration membranes. *Journal of Membrane Science*, 14(2):111–127, 1983.

H. Ockendon. Proceedings from Mathematical Problems in Industry Workshop. 1991.

J. R. Ockendon, S. Howison, A. Lacey, and A. Movchan. *Applied Partial Differential Equations*. Oxford University Press, 2003.

A. Oron, S. H. Davis, and S. G. Bankoff. Long-scale evolution of thin liquid films. *Reviews of Modern Physics*, 69(3):931, 1997.

L. Oxarango, P. Schmitz, and M. Quintard. Laminar flow in channels with wall suction or injection: a new model to study multi-channel filtration systems. *Chemical Engineering Science*, 59(5):1039–1051, 2004.

K. Parameshwaran, A. G. Fane, B. D. Cho, and K. J. Kim. Analysis of microfiltration performance with constant flux processing of secondary effluent. *Water Research*, 35(18):4349–4358, 2001.

G. K. Pearce. *UF/MF Membrane Water Treatment: Principles and Design*. Water Treatment Academy, 2011.

G. K. Pearce. Membrane Consultancy Associates Limited. Private communication, 2013.

R. F. Probstein. *Physicochemical Hydrodynamics. An Introduction*. Butterworths, 1989.

J. Qin and T.-S. Chung. Effect of dope flow rate on the morphology, separation performance, thermal and mechanical properties of ultrafiltration hollow fibre membranes. *Journal of Membrane Science*, 157(1):35–51, 1999.

A. M. Ravazzini, A. F. Van Nieuwenhuijzen, and J. H. M. J. Van Der Graaf. Direct ultrafiltration of municipal wastewater: comparison between filtration of raw sewage and primary clarifier effluent. *Desalination*, 178(1):51–62, 2005.

P. J. Remize, C. Guigui, and C. Cabassud. Evaluation of backwash efficiency, definition of remaining fouling and characterisation of its contribution in irreversible fouling: Case of drinking water production by air-assisted ultra-filtration. *Journal of Membrane Science*, 355(1):104–111, 2010.

O. Reynolds. On the theory of lubrication and its application to Mr. Beauchamp Tower's experiments, including an experimental determination of the viscosity of olive oil. *Proceedings of the Royal Society of London*, 40(242-245):191–203, 1886.

S. B. Sadr Ghayeni, P. J. Beatson, A. G. Fane, and R. P. Schneider. Bacterial passage through microfiltration membranes in wastewater applications. *Journal of Membrane Science*, 153(1):71–82, 1999.

P. G. Saffman. On the boundary condition at the surface of a porous medium. *Studies in Applied Mathematics*, 50:93–101, 1971.

R. M. Sandblom. Alfa-Laval. Filtering Process, Patent, August 1978.

P. Schmitz and M. Prat. 3-d laminar stationary flow over a porous surface with suction: Description at pore level. *AIChE Journal*, 41(10):2212–2226, 1995.

G. Segre and A. Silberberg. Behaviour of macroscopic rigid spheres in Poiseuille flow Part 2. experimental results and interpretation. *Journal of Fluid Mechanics*, 14 (01):136–157, 1962.

M. A. Shannon, P. W. Bohn, M. Elimelech, J. G. Georgiadis, B. J. Marinas, and A. M. Mayes. Science and technology for water purification in the coming decades. *Nature*, 452(7185):301–310, 2008.

Q. She, X. Jin, and C. Y. Tang. Osmotic power production from salinity gradient resource by pressure retarded osmosis: Effects of operating conditions and reverse solute diffusion. *Journal of Membrane Science*, 401:262–273, 2012.

R. J. Shipley and S. L. Waters. Fluid and mass transport modelling to drive the design of cell-packed hollow fibre bioreactors for tissue engineering applications. *Mathematical Medicine and Biology*, 2011.

R. J. Shipley, S. L. Waters, and M. J. Ellis. Definition and Validation of Operating Equations for Poly(Vinyl Alcohol)-Poly(Lactide-Co-Glycolide) Microfiltration Membrane-Scaffold Bioreactors. *Biotechnology and Bioengineering*, 107:382–392, 2010.

L. Song and M. Elimelech. Theory of concentration polarization in crossflow filtration. *Journal of the Chemical Society, Faraday Transactions*, 91:3389–3398, 1995.

R. W. Style and S. S. L. Peppin. Crust formation in drying colloidal suspensions. *Proceedings of the Royal Society of London A: Mathematical, Physical and Engineering Sciences*, 467(2125):174–193, 2011.

United Nations. Millennium Development Goals and Beyond 2015. http://www.un.org/millenniumgoals/environ.shtml, August 2015.

United Nations General Assembly. Resolution A/RES/64/292. http://www.un.org/en/ga/search/view_doc.asp?symbol=A/RES/64/292, July 2010.

United States Geological Survey. The World's Water. http://water.usgs.gov/edu/earthwherewater.html, August 2015.

J. Van Brakel and P. M. Heertjes. Analysis of diffusion in macroporous media in terms of a porosity, a tortuosity and a constrictivity factor. *International Journal of Heat and Mass Transfer*, 17(9):1093–1103, 1974.

B. Van der Bruggen and C. Vandecasteele. Distillation vs. membrane filtration: overview of process evolutions in seawater desalination. *Desalination*, 143(3):207–218, 2002.

B. Van der Bruggen, C. Vandecasteele, T. Van Gestel, W. Doyen, and R. Leysen. A review of pressure-driven membrane processes in wastewater treatment and drinking water production. *Environmental Progress*, 22(1):46–56, 2003.

S. S. Vasan and R. W. Field. On maintaining consistency between the film model and the profile of the concentration polarisation layer. *Journal of Membrane Science*, 279(1):434–438, 2006.

R. J. Wakeman and C. J. Williams. Additional techniques to improve microfiltration. *Separation and Purification Technology*, 26(1):3–18, 2002.

D. M. Wang and J. M. Tarbell. Nonlinear analysis of flow in an elastic tube (artery): steady streaming effects. *Journal of Fluid Mechanics*, 239:341–358, 1992.

R. Wang, L. Shi, C. Y. Tang, S. Chou, C. Qiu, and A. G. Fane. Characterization of novel forward osmosis hollow fiber membranes. *Journal of Membrane Science*, 355 (1):158–167, 2010.

Y. Wang, J. A. Howell, R. W. Field, and M. R. Mackley. Oscillatory flow within porous tubes containing wall or central baffles. *Chemical Engineering Research & Design*, 72(5):686–694, 1994.

K. Watkins. Human development report 2006-beyond scarcity: Power, poverty and the global water crisis. *UNDP Human Development Reports*, 2006.

R. J. Whittaker, M. Heil, O. E. Jensen, and S. L. Waters. A rational derivation of a tube law from shell theory. *The Quarterly Journal of Mechanics and Applied Mathematics*, 63(4):465–496, 2010.

J. G. Wijmans and R. W. Baker. The solution-diffusion model: a review. *Journal of Membrane Science*, 107:1–21, 1995.

F. A. Williams. A nonlinear diffusion problem relevant to desalination by reverse osmosis. *SIAM Journal on Applied Mathematics*, 17:59–73, 1969.

World Health Organization. *Guidelines for Drinking-Water Quality: Recommendations*, volume 1. World Health Organization, 2004.

World Health Organization. *Global Health Risks: Mortality and Burden of Disease Attributable to Selected Major Risks*. World Health Organization, 2009.

W. Xi and S. Geissen. Separation of titanium dioxide from photocatalytically treated water by cross-flow microfiltration. *Water Research*, 35(5):1256–1262, 2001.

P. Xu and B. Yu. Developing a new form of permeability and Kozeny–Carman constant for homogeneous porous media by means of fractal geometry. *Advances in Water Resources*, 31(1):74–81, 2008.

K. M. Yao, M. T. Habibian, and C. R. O'Melia. Water and waste water filtration. concepts and applications. *Environmental Science & Technology*, 5(11):1105–1112, 1971.

Y. Ye, V. Chen, and P. Le-Clech. Evolution of fouling deposition and removal on hollow fibre membrane during filtration with periodical backwash. *Desalination*, 283:198–205, 2011.

A. L. Zydney. Stagnant film model for concentration polarization in membrane systems. *Journal of Membrane Science*, 130(1):275–281, 1997.